ASPECTS OF STELLAR ATMOSPHERES AND STAR FORMATION

Sílvia Helena Paixão Alencar

May 2000

SILVIA HELENA PAIXÃO ALENCAR

ASPECTS OF STELLAR ATMOSPHERES AND STAR FORMATION

Thesis submitted to the UNIVERSIDADE FEDERAL DE MINAS GERAIS as a partial requirement for obtaining the Ph.D. degree in Physics.

Concentration area: ASTROPHYSICS
Thesis advisor: Prof. Dr. Luiz Paulo Ribeiro Vaz (UFMG)
Thesis co-advisor: Prof. Dr. Gibor Basri (UC Berkeley)

Departamento de Física - ICEx - UFMG
2000

Acknowledgements

Many people have helped me in different ways during this very pleasant and interesting work and I am afraid I will undoubtly forget someone.

I had the pleasure to work with two awesome advisors in the last years, they were patient and helped me grow as a researcher in my own rythm. They showed me that hard work compensates and that stellar astrophysics is an astonishing field where surprises are always bound to happen. Luiz Paulo is known for his terrible temper but most people simply get him wrong and miss his critic humour, funny comments and encyclopedic knowledge of every imaginable subject. He has been my advisor for so long that I am forever indebted to him for most of my knowledge in astronomy. He is also a good friend and was always ready to calm me down when I thought that nothing made sense, which was quite often :-) Gibor welcomed me at Berkeley with his usual smile and positive way of looking at every small progress as a conquest. I sincerely hope I grew up to the expectations of both.

I have enjoyed the last four years immensely and had a great time with my friends from Brazil and Berkeley. My special thanks go to Andrea Gilbert whom, as my officemate in Campbell Hall, frequently helped me with fruitful discussions about physics, books and desserts. She does the best cookies ever.

My family has always supported my decision to pursue an academic career and although they actually don't know what my work is about, everybody thinks it is great.

Finally I must thank Eddie, the sweetest person I know, for all the love.

Contents

List of Figures

List of Tables

Abstract

We initially investigate some processes that affect the stellar atmosphere, such as the gravity-brightening and limb-darkening, and the influence of the reflection effect on them. We study the gravity-brightening exponents using the Uppsala Model Atmospheres. In non-illuminated convective atmospheres the exponent value ($\beta = 0.32$) proposed by Lucy was confirmed only for $T_{\rm eff} \sim 6500$ K. The exponent depends upon $T_{\rm eff}$, being rather insensitive to variations of the mixing-length parameter, the stellar mass and the use of grey or non-grey atmospheres. We demonstrate the influence of the mutual illumination in a close binary on the gravity-brightening exponent. The external illumination increases the value of β, the larger the amount of incident flux the larger the value of the exponent. This effect is caused by the "quenching" of convection as the external illumination heats the surface layers of the illuminated star, bringing it closer to radiative equilibrium, where β is close to unity.

We determine monochromatic, bolometric and passband-specific limb-darkening coefficients for illuminated atmospheres. Our results show that illuminated coefficients are significantly different from the non-illuminated ones. We test different methods to calculated the coefficients and showed that in the illuminated case the method proposed by Van Hamme is recommended in order to obtain coefficients that preserve the total emergent flux from the atmosphere.

In the second part of this work we study Classical T Tauri stars. We discuss the many processes acting in the forming star-disk system and test the predictions of magnetospheric accretion models. We present a spectral analysis of 30 T Tauri stars observed with the Hamilton echelle spectrograph over more than a decade. We discuss the relation between different line-forming regions and search for good accretion rate indicators. We confirm several important points of the models, such as the correlation between accretion and outflow, broad emission components that are mostly central or slightly blueshifted, and only the occasional presence of redshifted absorption. We also show, however, that the broad emission components supposedly formed in the magnetospheric accretion flow only partially support the models. Unlike the predictions, they are sometimes redshifted and are mostly found to be symmetric. The published theoretical profiles do not have a strong resemblance to our observed ones.

We also present the analysis of 103 spectra of the Classical T Tauri star DR Tau. The star exhibits strong emission lines that show a wide variety and variability in profile shapes. These lines show both outflow and infall signatures which change on a variety of timescales. The system shows quasiperiodic variations in line intensities

and position, but a unique period that describes all of the data could not be found. The Balmer line profiles are generally strongly peaked in the red, and do not resemble published theoretical magnetospheric accretion profiles. We suggest that the system is seen nearly pole-on. This can explain the highly asymmetric Balmer lines if the line emissivity increases strongly near the star. The Ca II and He I emission line components are found to be very symmetric and that they could be produced by magnetic turbulence.

Resumo

Estudaram-se inicialmente processos que afetam a atmosfera estelar como o brilho por gravidade e o escurecimento de bordo e a influência do efeito reflexão nestes processos. Os expoentes de brilho por gravidade foram determinados usando o Modelo de Atmosferas de Uppsala. Para atmosferas convectivas não iluminadas o valor do expoente proposto por Lucy ($\beta = 0.32$) foi confirmado apenas para $T_{\rm ef} \sim 6500$ K. O expoente depende de $T_{\rm ef}$, sendo bastante insensível a variações do parâmetro de comprimento de mistura, à massa da estrela e ao uso de atmosferas cinzas ou não cinzas. Mostrou-se a influência da iluminação mútua de binárias próximas no expoente de brilho por gravidade. A iluminação externa aumenta o valor de β, quanto maior o fluxo incidente maior o valor do expoente. Esse efeito é causado pela diminuição da convecção a medida que a iluminação externa aquece as camadas superficiais da estrela iluminada, levando-a em direção ao equilíbrio radiativo, onde β é próximo da unidade.

Determinaram-se coeficientes de escurecimento de bordo monocromáticos, bolométricos e de bandas fotométricas para atmosferas iluminadas. Nossos resultados mostram que os coeficientes iluminados são significativamente diferentes dos não iluminados. Foram testados diferentes métodos de cálculo dos coeficientes e mostrou-se que, no caso iluminado, o método proposto por Van Hamme é recomendado para que se obtenha coeficientes que preservam o fluxo total emergente da atmosfera.

Na segunda parte deste trabalho foram estudadas estrelas T Tauri Clássicas. Discutiram-se vários processos que atuam no sistema de estrela e disco em formação e testaram-se as previsões dos modelos de acresção magnetosférica. Realizou-se a análise espectral de 30 estrelas T Tauri observadas com o espectrógrafo echelle Hamilton durante mais de uma década. Foram discutidas as relações entre diferentes regiões de formação de linha e procuraram-se bons indicadores de taxa de acresção de massa. Foram confirmados vários pontos importantes dos modelos, como as correlações entre acresção e perda de massa, componentes largas em emissão que se encontram quase sempre centradas ou levemente desviadas para o azul, e a presença ocasional de absorção desviada para o vermelho. Entretanto, mostrou-se também que as componentes largas em emissão que se formam supostamente no fluxo de acresção magnetosférico dão apenas suporte parcial aos modelos. Diferentes das previsões, elas aparecem às vezes desviadas para o vermelho e são quase sempre simétricas. Além disto, os perfis teóricos publicados não se parecem muito com os que observamos.

Apresenta-se também a análise de 103 espectros da estrela T Tauri Clássica DR Tau. Esta estrela exibe linhas intensas em emissão que apresentam uma grande va-

riedade e variabilidade de perfis. Estas linhas possuem características de acresção e perda de massa que mudam em várias escalas de tempo. As intensidades e posições das linhas de emissão mostram variações quase periódicas, mas não se obteve um período único que as descrevesse. Os perfis das linhas de Balmer mostram um pico intenso desviado para o vermelho e não se parecem com os perfis dos modelos magnetosféricos teóricos. Sugere-se que o sistema é visto quase de face. Isto pode explicar a asimetria das linhas de Balmer se a emissividade das linhas aumentar fortemente perto da estrela. As componentes das linhas de Ca II e He I em emissão são bastante simétricas e podem ter origem na turbulência magnética.

Chapter 1

—

Introduction

Star formation and evolution are very active research fields that have benefitted from the study of young stellar objects and binary star systems. A few years ago most of the tests of evolutionary models were performed with Main Sequence (MS) stars. The results were very interesting and, in the last decade, high quality data showed the importance of effects such as core overshooting in the traditional convection formulation, the influence of the chemical composition in stellar evolution, they encouraged a revision of theories of tidal evolution in binary star systems and the development of better opacity tables (Andersen, 1991).

Recently, several Pre-Main Sequence (PMS) systems, many of them binary, were discovered with the development of high quality Infra Red (IR) detectors. The test of evolutionary models could then start to be extended to the early stages of star formation. In the PMS phase the star is often surrounded by an envelope and also a disk that interacts with the star and alters its spectral and photometric characteristics. It is very important to understand how the several processes related to the formation of the young star show up in the photometry and spectroscopy to be able to distinguish them from the changes related to a possible binarity of a system. It is also very interesting to investigate the formation of stars with disks that are the most plausible source of planetary formation and evolution.

In the beginning of this work we studied some processes that affect the stellar atmosphere, such as the reflection effect, the gravity-brightening and the limb-

darkening, making an effort to describe these effects in a suitable way in order to apply the results to light curve synthesis models of Eclipsing Binary Systems (EBS). We improved classical theoretical results like those by Lucy (1967) (gravity-brightening of convective atmospheres) and by Van Hamme (1993) (limb-darkening), extending these results to illuminated atmospheres, a much more realistic scenario in the case of binary systems.

In the second part of this work we studied Classical T Tauri Stars (CTTSs), in order to better understand the many processes acting in the forming star-disk systems, and to test magnetospheric accretion models. We investigated the general characteristics of these stars, analysing several spectral lines of 30 T Tauri stars (TTSs), and studied more than a decade of spectra of a specific CTTS, DR Tau.

The main goal of this work was to improve both theoretically and empirically the methods of analysis of precise stellar dimensions and to contribute to a better understanding of the several processes taking place in the formation of T Tauri stars.

In Chapter 2 we give a brief introduction to stellar atmospheres, the gravity-brightening exponent results are presented in Chapters 3 (non-illuminated atmospheres) and 4 (illuminated atmospheres). The limb-darkening results are shown in Chapter 5. In Chapter 6 we give an introduction to T Tauri stars, in Chapter 7 we show a spectral analysis of 30 TTSs and in Chapter 8 we study the Classical T Tauri star DR Tau. The conclusions of this work are outlined in Chapter 9. Part of this work was carried out in Brazil at UFMG and part in the USA at UC Berkeley. In order to make it easily accessible to Brazilian readers, we make a synthesis of the results in Portuguese in Chapter 10. Finally in Chapter 11 we present the published papers that resulted from the present work.

Chapter 2

—

Stellar atmospheres

Due to the high opacity of the stellar interior, the light emitted by a star has the characteristics of its most external surface layers, the photosphere.

We can analyse that light by measuring the stellar magnitude which corresponds to the integrated flux of radiation in a given wavelength range. We can also study the stellar spectrum, the energy liberated as a function of the frequency or wavelength. These analyses are fundamental to the study of a stellar atmosphere, since they can help constrain its physical parameters such as temperatures, pressures and densities. They also give insight on the presence of turbulence, convection and magnetic fields and allow the determination of the atmosphere's chemical composition.

The energy flux through the most external stellar layers must be correctly described in order to predict the observable characteristics of the emergent radiation. This is achieved by applying fundamental physical laws to describe the interaction of radiation with matter, and by constructing mathematical models in order to calculate theoretical predictions of the observable physical characteristics.

The atmosphere models must describe the physical structure of an atmosphere and its spectrum. It is a highly complex problem to analyse the physical phenomena that are taking place in a stellar atmosphere and to perform the necessary calculations to compute them. The following approximations are usually made to simplify the problem.

The geometry of a star is essencially spherical, but some models assume that the

atmosphere is composed of plane-parallel homogeneous layers. The plane-parallel approximation is valid only when the atmosphere depth is small compared to the stellar radius (Mihalas, 1978) and the homogeneity consideration reduces the problem to one dimension.

Local thermodynamical equilibrium (LTE) is another important simplification often adopted. The LTE hypothesis implies that the occupation numbers of the free and bound states of the material, the opacity, the emissivity and all the thermodynamic proprieties are described by the pressure and temperature's local values. This is a strong assumption, as we have a local theory, which does not take into account the interaction of a gas element and its neighbors, nor the gradients commonly present in an atmosphere. Grey atmospheres, where the opacity does not depend on the frequency, can be used as a starting point in the studies. The final goal however is to describe applicable results to non-grey, and consequently more realistic, atmospheres.

Atmospheres in hydrostatic and radiative equilibrium are commonly adopted, but sometimes our interest lies on convective atmospheres and the latter simplification does not apply. In stellar atmospheres, the energy transport occurs through the most efficient process between convection and radiation. In general, radiative equilibrium prevails in early-type stars while convection becomes important in F stars and dominates the late-type ones. The convective flux is turbulent and unfortunately there is no final theory of convection yet. The mixing-length theory, which is the mostly used, includes several basic physical parameters and provides a scenario at least illustrative of the effects of convection. In this theory a convective cell with an average density difference $\Delta\rho$ with the surroundings will travel a distance ℓ, called the mixing-length, before dissolving into the local medium. ℓ is an arbitrary free parameter that must be adjusted in the model. The convective flux, Φ, can be expressed in terms of the temperature excess compared to the surroundings ΔT, the specific heat at constant pressure C_P, the cell density, ρ and velocity, v as:

$$\Phi = \rho C_P v \Delta T \tag{2.1}$$

The cell velocity can be obtained through the energy conservation equation:

$$\frac{1}{2}\rho v^2 = g\Delta\rho\ell \tag{2.2}$$

Assuming pressure equilibrium and constant mean molecular weight $\Delta\rho/\rho = \Delta T/T$ and

$$v = (2g\ell\Delta T/T)^{1/2} \tag{2.3}$$

which gives

$$\Phi = \rho C_P (2g\ell/T)^{1/2} \Delta T^{3/2} \tag{2.4}$$

in terms of the mixing-length parameters (Gray, 1992). In most models the mixing-length is reduced to a parameter $\alpha = \ell/H_P$, where $H_P = (-d\ln P/dr)^{-1} = P/\rho g$ is the local scaleheight of the stars's atmosphere.

In EBS one component illuminates the other, affecting the temperature distribution in both atmospheres. This effect of mutual irradiation, called the "reflection effect", is correctly described for atmospheres in radiative equilibrium. Eddington (1926) and Milne (1927) showed that in this case the bolometric reflection albedo is unity, i.e. all the incident energy is necessarily radiated/scattered locally by the external atmospheric layers (Vaz, 1985). Vaz & Nordlund (1985) showed it is possible, for the grey non-convective atmospheres, to express as a polynomial an "effective reflection albedo" that takes into account the reemission dependence on the wavelength. For convective atmospheres they obtained approximate numerical expressions to determine an effective reflection albedo dependent on the frequency. However the model dependence on various parameters as the mixing length, the incident flux and the direction of incidence did not allow a generalization as that obtained with non-convective atmospheres. These results were later extended to non-grey atmospheres (Nordlund & Vaz, 1990). Claret & Giménez (1992) studied bolometric reflection albedoes in the case of mutual irradiation of Algol-like systems. They showed the importance of taking into account the illumination in order to avoid errors when analysing stellar spectra, showing that, for example, some spectral regions of an irradiated spectrum can be very similar to a non-irradiated spectrum of an atmosphere with a lower metallicity, what could lead to wrong conclusions about the components' metallicity.

Stellar atmosphere models are an important tool to study phenomena like the reflection albedoes, as described above, and others, like the gravity-brightening and the limb-darkening. In order to ensure a correct and precise determination of absolute parameters (masses and radii) of EBS it is essencial to understand those effects since they are generally parametrized through exponents and coefficients that are forced to follow certain laws (or are kept fixed at their theoretical values determined with atmosphere or evolutionary models) in the light curves synthesis programs. The more accurate (in terms of the physical approximation) the values we use the more trustful will be the final absolute parameters that are freely ajusted by the programs.

2.1 The Uppsala Model Atmospheres (UMA)

The UMA code is described in detail by Nordlund (1974) and Gustafsson *et al.* (1975). Here we will only give a very brief explanation of the model. In order to obtain a closed system of equations to compute an atmosphere model we need temperature and pressure equations. The temperature is determined by the equation of total flux constancy

$$\int_0^\infty \mathcal{F}_\nu d\nu + \Phi = F_{\rm tot} = \sigma T_{\rm eff}^4 \tag{2.5}$$

where $\mathcal{F}_\nu$ is the monochromatic radiative flux, $F_{\rm tot}$ is the total flux at effective temperature $T_{\rm eff}$, and σ is the Stefan-Boltzmann constant. The radiative flux and pressure depend on the temperature and electron pressure distributions through the solution of the transfer equation (see Section 5.1) which is solved by the Feautrier method (Mihalas, 1978). The total pressure is determined by the hydrostatic equilibrium equation

$$\frac{dP_{\rm tot}}{d\tau} = \frac{g}{\kappa}, \tag{2.6}$$

with the boundary conditions $P_{\rm tot}(\tau = 0) = P_{\rm rad}(\tau = 0)$, where κ is the opacity at optical depth τ and $P_{\rm rad}$ is the radiation pressure. The turbulent pressure is calculated with the expression

$$P_{\rm turb} = \beta \rho v^2 \tag{2.7}$$

where β is a constant of order unity and v is the average velocity of a turbulent element. The electron pressure is determined by the pressure balance equation

$$P_g(P_e, T) = P_{\rm tot} - P_{\rm rad} - P_{\rm turb} \tag{2.8}$$

where P_g is the gas pressure and P_e is the electron pressure. Finally, the convective flux is calculated with Eq. 2.4. Now that we have a closed system of equations for the temperature and pressure, the solution consists of obtaining the distribution of all the parameters as a function of optical depth. The equations are solved with a Newton-Raphson linearization method on τ and λ, but are not linearized on the angular dependence, that is considered in an indirect way through the variable Eddington factors described by Mihalas (1978).

A modified version by Vaz & Nordlund (1985) of the Uppsala Model Atmospheres (UMA) that takes into account external illumination was used in our analysis. The program was designed for cool stars ($T_{\rm eff} < 8000$K), plane-parallel atmospheres in hydrostatic equilibrium with LTE and using a mixing-length theory to describe convection.

Non-illuminated models are defined by the star's effective temperature $T_{\rm eff}$, surface gravity g and mass M, the mixing-length parameter $\alpha = l/H_P$ and the chemical composition (fixed at the solar value in our works). Illuminated models also need the illumination direction ω ($= \cos(\theta)$, where θ is the incidence angle measured relative to the surface normal), the effective temperature of the illuminating flux (the heating temperature) T_h and the apparent radius of the illuminating star r_h. The apparent radius is the ratio between the source star radius and the distance from its center to a point on the surface of the reflecting star. Figure 10.1 of Chapter 10 (also reproduced as Fig. 1 of Paper 3, presented in Chapter 11) shows the geometry of illumination in a double star system. A more detailed description of the boundary conditions in the illuminated and non-illuminated models is given in Chapter 5.

Stellar models (Claret, 1995, X=0.70, Z=0.02) were used to associate $T_{\rm eff}$ with M in order to describe a non-deformed ZAMS star. We call the models with and without line opacities "non-grey" and "grey" respectively, including in the grey ones the continuum opacity variation with frequency (as in Nordlund & Vaz, 1990). We investigated grey and non-grey illuminated atmospheres in convective equilibrium. The line opacities were described using Opacity Distribution Functions (ODFs) which limited the temperature range of our studies to those corresponding to ZAMS stars with masses ranging from $0.6 M_\odot$to $1.5 M_\odot$.

Chapter 3

—

Gravity-brightening - non-illuminated models

3.1 Gravity-brightening exponents

When the components of a binary system are close enough to each other, tidal forces coupled to rotation cause important deformations in the star's atmospheres. These geometry distortions produce a non-uniform gravity distribution in the stellar surface, which affects the brightness distribution, making the aparent stellar disk brighter at the poles than the equator.

von Zeipel (1924) showed that the radiative flux ($\mathcal{F}$) distribution on a stellar surface distorted by rotation or tidal force varies with gravity according to

$$\mathcal{F} \ \alpha \ g^{\beta} \tag{3.1}$$

where β, the gravity-brightening exponent, is equal to 1.0 for atmospheres in radiative equilibrium. In 1967 Lucy calculated β for convective atmospheres and obtained a mean value of 0.32 coupling convective envelopes of models with different surface gravities at depths where the temperature gradient was adiabatic. He recognized that the entropy at the bottom of different models should be the same, in order to represent the same star.

Anderson & Shu (1977) presented another formulation for convective atmospheres arguing that, for a contact star in hydrostatic equilibrium having a common convective envelope (the contact discontinuity model, Shu *et al.*, 1976; Lubow & Shu, 1977), the convective flux depends on the effective gravitational potential alone, and not on its gradient (i.e. the local acceleration of gravity). As for late-type stars $F_{\rm conv} \sim F_{\rm total}$ and the photosphere must ultimately radiate $\sigma T_{\rm eff}^4$, this flux should be constant on equipotentials, with consequently $\beta = 0$.

Rafert & Twigg (1980) determined β by analysing a uniform sample of detached, semi-detached and contact EB with the WD (Wilson, 1979) program. They found $\beta \approx 0.31$ for convective envelopes ($5\,400$ K $< T_{\rm eff} < 7\,100$ K) and $\beta \approx 0.96$ for the radiative ones ($T_{\rm eff} > 7\,900$ K). For $7\,100$ K $< T_{\rm eff} < 7\,900$ K they found empirically $0.31 < \beta < 1$.

Hilditch (1981) found very small values of β for four contact eclipsing binaries, and that imposing $\beta = 0.32$ yields a photometric mass ratio which is significantly different from the spectroscopic one, what does not happen with $\beta = 0$. However, the obvious presence of star spots in all 4 systems may render very difficult, and even spoil, attempts to determine temperature variations over the surfaces (Ruciński, 1989).

Nakamura & Kitamura (1992, and references therein) did empirical studies on the β exponent (their distortion theory extended to a second order treatment, Kitamura & Nakamura, 1983). For detached EB their values agree with those of von Zeipel (1924) and Lucy (1967), but for early-type both semi-detached (Kitamura & Nakamura, 1987; Nakamura & Kitamura, 1992) and contact EB (Kitamura & Nakamura, 1988a,b) they obtained $\beta > 1.0$.

Sarna (1989), with a model of convective envelope for Roche lobe filling stars (W UMa-type), computed the distribution of effective temperatures and surface gravities for the stars and directly determined $\beta \approx 0.32$.

The most adopted theoretical values (1.0 for radiative and 0.32 for the convective atmospheres) do not always agree with the ones obtained with observational data (Alencar *et al.*, 1997) and a careful study applied to EBS was still needed. Unfortunately there are only a few binary systems with high quality data (yielding, for example, to the determination of absolute parameters with errors of 1-2%) that have been systematically analysed in order to determine reliable values of parameters such as the gravity-brightening exponents (Alencar, 1995) from the observations.

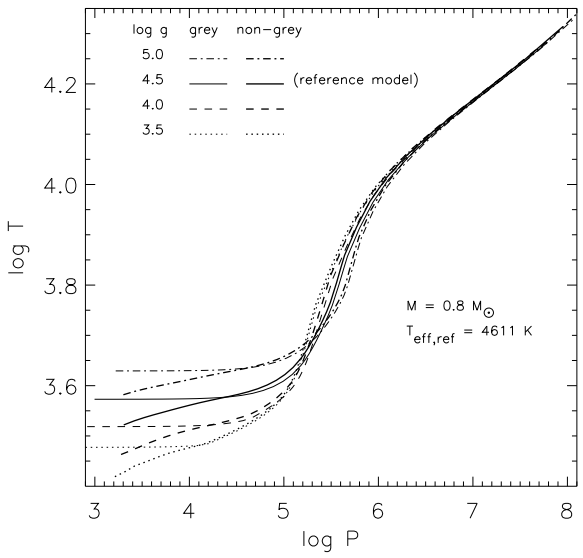

Figure 3.1: $\log T$ vs. $\log P$ for convective grey (thin lines) and non-grey (thick lines) models.

3.2 Method

Using the UMA code, we initially studied the gravity-brightening exponent of grey and non-grey atmospheres without external illumination in the temperature range $3\,700\,\mathrm{K} < T_{\mathrm{eff}} < 7\,000\,\mathrm{K}$.

Starting from a reference model ($\log g = 4.5$), adjust T_{eff} for models having another $\log g$ (distorted) until the adiabat at the bottom of the distorted model becomes equal to that of the reference one, i.e. these models must represent the same star by having the same entropy at the bottom of the atmosphere. We then examine how the total flux varies with g, determining β by linear regression. Some adjusted models are shown in Fig. 3.1.

Equation (3.1) was valid to a high degree in all the models. The β values were determined by linear regression with correlation coefficients very close to 1.0; the smallest value was $r^2 = 0.994$.

Table 3.1: Coefficients of Eq. (3.2) for convective models.

	a_0	a_1	a_2	a_3
grey	-5.00784	27.9838	-46.9701	25.5398
non-grey	-5.61111	31.6225	-54.0000	29.7779

3.3 Results

We calculated grey and non-grey models varying the values of $\alpha(= l/H_P)$, but β did not show a strong dependence on α as shown in Fig. 3.2. The β values obtained with non-grey models turned out to be very similar to the those for grey models (Fig. 3.2, bottom panel), showing that the phenomenon is more related to the constitutive equations than to the ODF table used. The β values calculated by Lucy (1967) are also shown in the bottom panel. Although the procedure used to compute β was the same, our opacity tables and atmosphere model were different from those he used. Even then, our results are in very close agreement. In Fig. 3.2 we also show the third order polynomial adjusted with our theoretical β values given by the equation:

$$\beta = \sum_{i=0}^{3} a_i t_e^i \tag{3.2}$$

with $t_e = T_{\rm eff} \times 10^{-4}$ and the values of a_i given in Table 3.1. We recommend the use of double precision and all the digits given in Table 3.1 when computing the polynomial approximations in order to minimize the errors in the calculation of the exponent values.

The maximum in $\beta(T_{\rm eff})$ is caused by changes in the convection and opacity properties of the models. For low $T_{\rm eff}$, convection is rather efficient, because of the high mass densities and low total energy fluxes. The entropy jump at the surface is correspondingly small and its changes even smaller, yielding small β when we force the entropy at the bottom of the models to be constant. This can be observed in Fig. 3.3, where we show $\log T$ vs. $\log P$ for a set of 5 values of $T_{\rm eff}$ and 4 values of $\log g$. The effective temperature may be approximated by $T_{\tau=1}$ (marked in Fig. 3.3). In its turn, $T_{\tau=1}$ is influenced by both convection and the physics of the absorption coefficient. On the other hand, the total flux is proportional to $\sigma T_{\tau=1}^4$ and, using Eq. (3.1), β is proportional to the total extension of $\Delta T_{\tau=1}$ obtained for each $T_{\rm eff}$ and models with $\log g$ varying between 3.5 and 5.0 (shown as vertical bars in Fig. 3.3).

The $T_{\rm eff}$=3900 K models are so adiabatic that β is small (the points at $T_{\tau=1}$ almost follow one adiabat). For intermediate $T_{\rm eff}$, convection becomes less efficient,

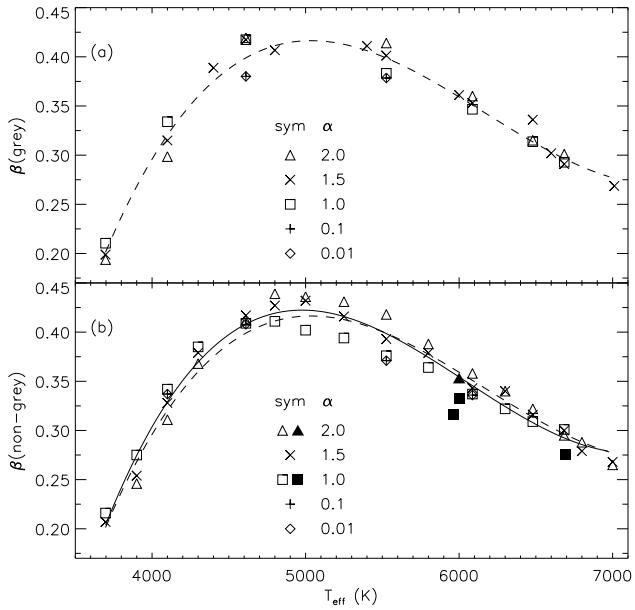

Figure 3.2: β vs. $T_{\rm eff}$ - non-illuminated grey (**a**) and non-grey (**b**) models. The filled symbols correspond to Lucy's values for a similar chemical composition. We overplot the third order polynomials obtained with the grey (dashed lines) and non-grey (solid line) results.

with a correspondingly larger entropy jump near the surface. The stabilizing influence of convection thus diminishes, and the values of β increase (as can be seen by the increase of the extension of the vertical bars in Fig. 3.3 for $T_{\rm eff} \leq 5500\,{\rm K}$).

For even higher $T_{\rm eff}$ the influence of the opacity becomes significant. The temperature dependence of κ (i.e. $\partial \log \kappa / \partial \log T$) is much larger than κ's pressure dependence ($\partial \log \kappa / \partial \log P$). This is clear from Fig. 3.3, which shows that the contour levels of constant $\log \kappa$ tend to run parallel to the $\log P$ axis, especially as $\log T$ increases. The physical reason for this is that $T_{\rm eff}$ enters the regime where H is the dominant electron contributor and where, consequently, hydrogen ionization implies that the opacity (predominantly H^-) increases very rapidly with temperature. To appreciate how the temperature sensitivity of κ influences β it is useful to consider the approximation $\tau \sim \kappa P/g$, according to which, if g is increased, it does not take much of an increase in T to compensate for the change. One may derive

$$\beta \approx \frac{\Delta \log T^4}{\Delta \log g} \approx \frac{4}{[\frac{\partial \log \kappa}{\partial \log T}]_P + [1 + [\frac{\partial \log \kappa}{\partial \log P}]_T] / \frac{d \log T}{d \log P}}, \tag{3.3}$$

where $d \log T / d \log P$ is the logarithmic temperature gradient of the model at $\tau = 2/3$, and the dependence of $d \log T / d \log P$ on g has been ignored. Eq. (3.3) shows that β does indeed become small for large values of $[\frac{\partial \log \kappa}{\partial \log T}]_P$.

Some time after this work Claret (1998) performed calculations of the gravity brightening exponent and of limb-darkening coefficients using a completely different approach. He computed β values of non-illuminated models using stellar interior parameters from evolutionary tracks for a $T_{\rm eff}$ interval larger than ours. His results are presented as a function of the logarithm of the model masses, starting at the Solar mass. Considering values at the ZAMS, the temperature interval of $3.56 < \log T_{\rm eff} < 3.85$, covered in our work, corresponds to $-0.222 < \log(m/{\rm M}_\odot) < 0.176$. Claret (1998) results are in remarkable agreement with those presented here with respect to the behaviour of β in the common region ($3.81 < \log T_{\rm eff} < 3.85$) covered by both works. Curiously enough our work, published before the one by Claret (1998) was submitted, is not in their reference list.

The lower limit in $\log T_{\rm eff}$ of Claret's models (3.81) is hotter than the value for which we found a maximum in β (at $\log T_{\rm eff} \approx 3.74$, $F_{\rm rel}=0$). But his calculations of the evolution of β with the age of 2 models do confirm the existence of such a feature (see both his Fig. 5, for the evolution of a $2\,M_\odot$ model off the Main Sequence, and his Fig. 6. for the evolution of a $1\,M_\odot$ model from the Pre-Main Sequence phase). Claret (1998) interprets the general trends in β changes in terms of convection only, however, as explained above, this behaviour is due to the interplay between the convection and opacity properties of the models.

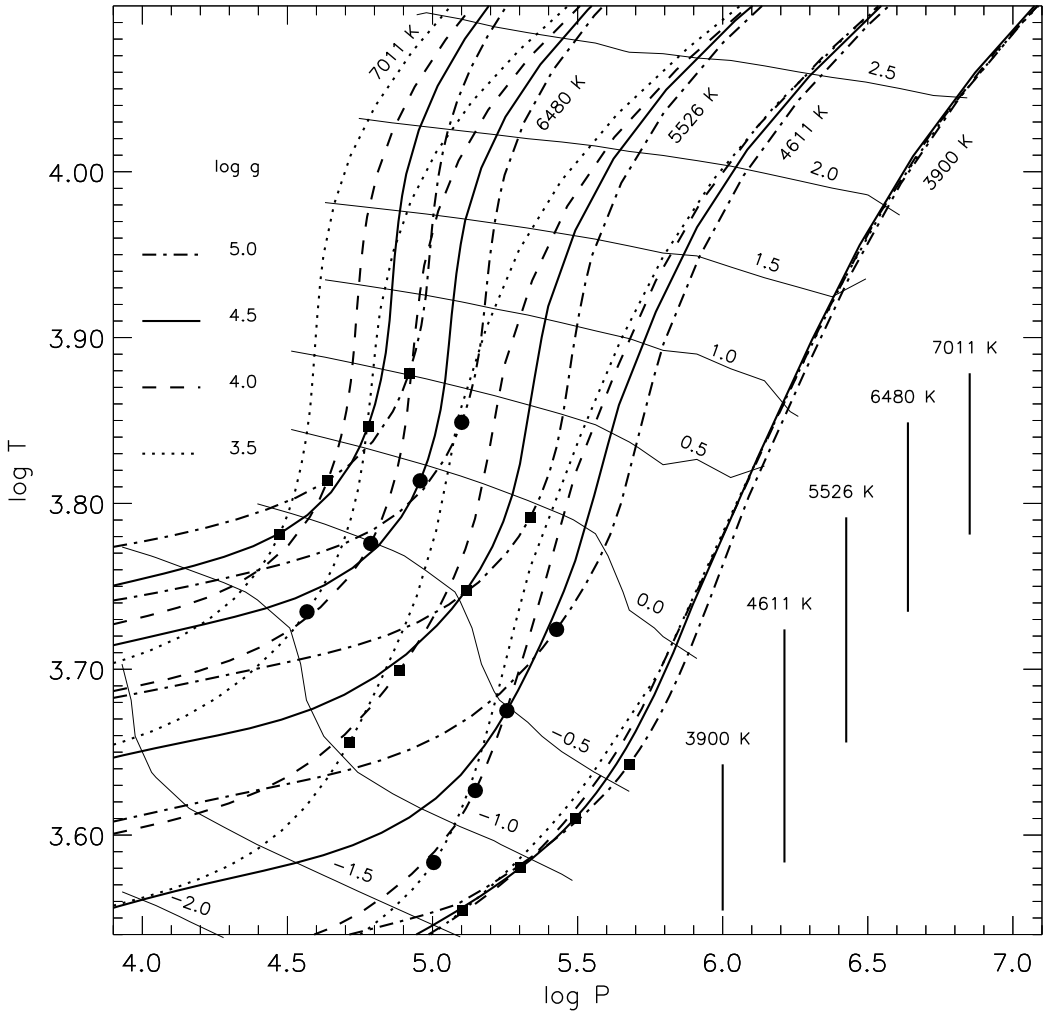

Figure 3.3: $\log T$ vs. $\log P$ for convective non-grey non-illuminated models with $\alpha = 1.5$, $\mu = 0.93$ and different values of $T_{\rm eff}$. $\mu = cos(\gamma)$ and γ is the angle between the line of sight and the normal to the surface of the star. For each value of $T_{\rm eff}$ there are 4 models with different values of $\log g$, which match the entropy of the reference model ($\log g$=4.5) at the bottom. The ■ and • symbols mark the $\tau_{\rm Ross}$=1 (Rosseland mean) layers. The vertical bars mark the extension of the temperature variation with the different $\log g$ for each $T_{\rm eff}$ at $\tau_{\rm Ross}$=1. The length of these bars is proportional to β. The thin continuous lines are contours of $\log \kappa$ (again shown as Rosseland mean) constant, marked from $\log \kappa$=-2.0 to 2.5 in equal steps of 0.5 dex.

3.3.1 One first observational test

Equation (3.2), with the non-grey coefficients of Table 3.1, was implemented in the WD light curve synthesis model (Wilson & Devinney, 1971; Wilson, 1993) described by Vaz *et al.* (1995). The triple PMS eclipsing system TY CrA (Casey *et al.*, 1993, 1995) has its eclipsing secondary component early in the PMS evolutionary phase, at the very end of the Hayashi track. The light curves were analysed (Casey *et al.*, 1998) with the WD model using both Lucy's and our approximation for β. For the secondary's effective temperature (4 800 K) our value is 0.41, about 28% larger than Lucy's value. The results obtained with our β were more consistent than when using $\beta = 0.32$, yielding a (B8-9 ZAMS) primary star with absolute dimensions closer to what theoretically expected for a star in such phase. The reason was the increase of surface brighteness in the secondary polar regions, requiring a lower inclination to reproduce the minimum depth and, consequently, larger stellar radii to reproduce the minima duration.

3.4 Conclusions

The gravity-brightening law, Eq. (3.1), is valid to a high degree for all models generated in this work with a modified version of the UMA code. The β exponents for convective atmospheres were calculated theoretically by forcing the entropy at the bottom of the atmosphere to be equal in models that should represent the same star. Our model reproduces the mean result of Lucy (1967) for the convective regime, and we extend his results (obtained only for three values of $T_{\rm eff}$) to the range 3 700 K$< T_{\rm eff} <$ 7 000K. We found that β practically only depends on $T_{\rm eff}$, being rather insensitive to the value of the mixing length parameter and to the use of grey or non-grey atmospheres. A third order polynomial, $\beta(T_{\rm eff})$, was given as a convenient way to use the results in the analysis of eclipsing binary light curves. We showed that the existence of a maximum in the $\beta(T_{\rm eff})$ relation is due to the interplay between the convection and opacity properties of the models.

This work was published in Astronomy and Astrophysics, Volume 326, pp. 257-262 (1997)

Chapter 4

—

Gravity-brightening - illuminated models

In Chapter 3 it was shown that the gravity-brightening exponent of a non-illuminated convective atmosphere depends mostly on the star's effective temperature, Lucy's result being a good approximation only as a mean value. In many eclipsing binary systems, however, the external illumination is significant, as evidenced by the conspicuous "reflection effect" (mutual illumination in a close binary) in their light curves. But, until now, no particular attention has been paid to its influence on the β exponent. Our goal in the present study is to clarify the dependence of β on external illumination.

4.1 Method

Using the UMA code, we studied the gravity-brightening exponent of grey and non-grey atmospheres in the temperature range $3\,700\,\mathrm{K}<T_{\mathrm{eff}}<7\,000\,\mathrm{K}$ illuminated by grey and non-grey fluxes with heating temperatures ranging from $7\,000\,\mathrm{K}$ to $12\,000\,\mathrm{K}$.

Starting from a reference ($\log g = 4.5$) non-illuminated model we adjust T_{eff} for illuminated models with the same $\log g$ until the adiabat at the bottom of the illuminated model becomes equal to that of the reference model. These models represent the illuminated and the non-illuminated sides of the same star, by having the same entropy at the bottom. We then use the illuminated model with $\log g$=4.5 as a reference and follow the procedure described in Chapter 3 to determine β, by

examining how the total flux of the illuminated models varies with g (Eq. 3.1).

Note that our method gives β as a function of parameters that were chosen primarily for convenience of computing stellar atmosphere models, rather than for their direct applicability to binary systems. The parameters $\log g$, $r_{\rm h}$, and ω, for example, are interrelated through the value of the radius of the star. When applying these results to the study of a particular binary system, it is necessary to interpolate in our parameter space to the particular combination of parameter values appropriate to a given point on the stellar surface. The resulting values of the gravity brightening exponent will vary between points on the reflecting stellar surface, a property that is shared with the limb-darkening coefficients, which are also affected by external illumination (Alencar & Vaz, 1999).

Equation 3.1, proposed by von Zeipel (1924) for atmospheres in radiative equilibrium and applied by Lucy (1967) to stars with convection, proved to be a good approximation for all the $\log g$ intervals used, like in the non-illuminated case. The correlation coefficients in the linear regressions used to determine β were always close to unity (the smallest one found was 0.987).

We calculated models with relative fluxes,

$$F_{{\rm rel},\omega} = [T_{\rm h}/T_{\rm eff}]^4 r_{\rm h}^2 \omega \tag{4.1}$$

ranging from 0 to 2, whenever possible ($r_{\rm h} < 1$). Those values are easily found in the literature amongst many types of binary systems. Using ω=1 we find $F_{\rm rel}$=0.446 for V Pup (detached, Andersen *et al.*, 1983), 0.338 for LZ Cen (detached, Vaz *et al.*, 1995), 0.386 for RY Aqr (semi–detached, Helt, 1987), 0.660 for DH Cep (detached, Hilditch *et al.*, 1996), 1.35 for AT Peg (algol, Maxted *et al.*, 1994), 2.39 for HU Tau (algol, Maxted *et al.*, 1995) and 2.72 for TV Cas (algol, Khalesseh & Hill, 1992).

Many of the binary systems above also have temperatures that fall in our selected ranges: RY Aqr ($T_{\rm eff}$=4 500 K and $T_{\rm h}$=7 600 K), AT Peg (4 898 K and 8 395 K), HU Tau (5 495 K and 12 022 K) and TV Cas (5 248 K and 10 471 K).

As with $T_{\rm h}$ close to $T_{\rm eff}$ we could not get large values of $F_{\rm rel}$ with reasonable values of $r_{\rm h}$, we studied models mostly ranging in the interval 7 000 K$<T_{\rm h}<$12 000 K. The illuminating non–grey fluxes with $T_{\rm h}\leq$7 000 K were generated with the UMA code, while for higher $T_{\rm h}$ we took the fluxes from Kurucz (1979).

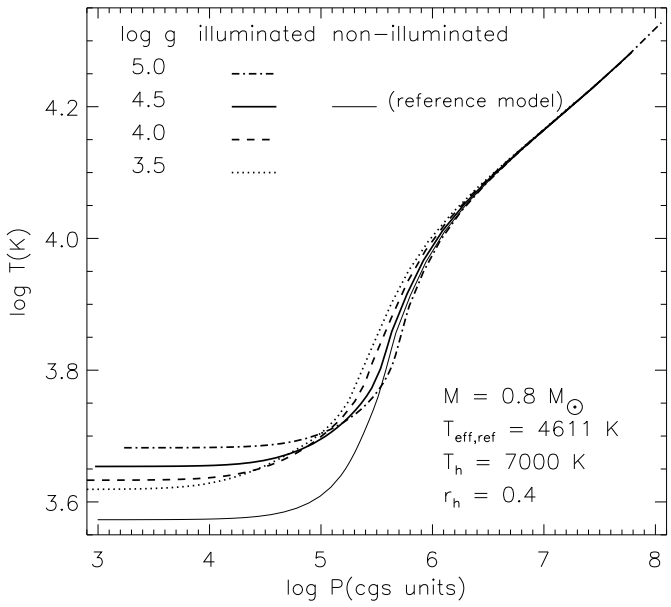

Figure 4.1: $\log T$ vs. $\log P$ for convective grey non-illuminated (solid thin line) and illuminated models with $\alpha = 1.5$, $\omega = 0.93$.

4.2 Results

4.2.1 Convective grey (continuum-only) atmospheres

Some of the models obtained with this method are shown in Fig. 4.1. The solid lines represent our reference models (with $\log g$=4.5); the thin line represents the non-illuminated model, while the thick line is the illuminated one. The other models are the illuminated and distorted ones. The relation of $\log T$ to $\log P$ is the same at the bottom of the atmospheres so that the different models have the same entropy there.

We calculated models by varying $r_{\rm h}$ and $T_{\rm h}$ for different values of $T_{\rm eff}$ (illuminated atmosphere), and four values of the angle of incidence of the radiation ($\omega = \cos\theta =$ 0.06943, 0.33001, 0.66999 and 0.93057). The corresponding β values are shown in Fig. 4.2, where $F_{{\rm rel},\omega}$ (Eq. 4.1), represents the influence of the parameters related to the illuminating flux, and $t = T_{\rm eff} \times 10^{-3}$ is the relevant parameter of the illuminated atmosphere. Note that in all panels of Fig. 4.2 the curve for $F_{{\rm rel},\omega}$=0 corresponds to the non-illuminated results of Chapter 3. Note also that β depends strongly on the

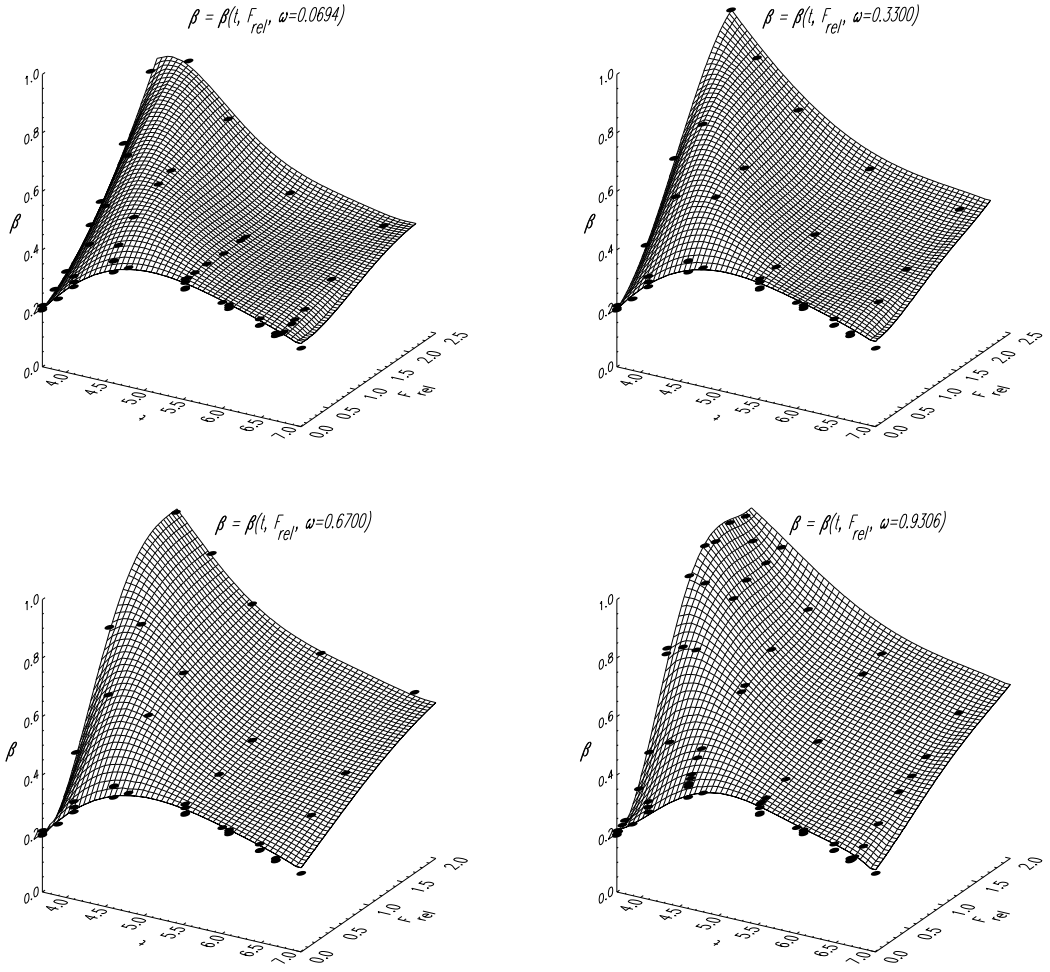

Figure 4.2: $\beta(t, F_{\mathrm{rel},\omega}, \omega)$, 4 values of ω, grey models. The curved grids represent the parametrization whose coefficients are shown in the Table 1 of Alencar *et al.* (1999), and the points represent the calculations.

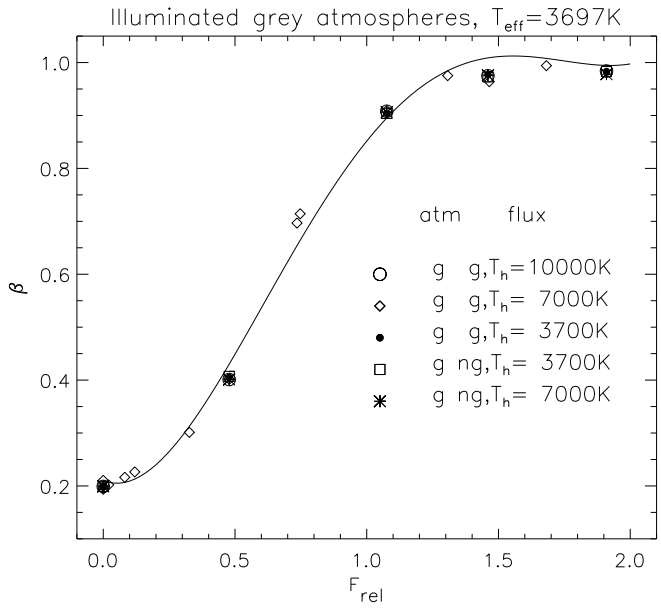

Figure 4.3: $\beta(F_{\rm rel}), \omega = 0.9306$, for grey atmospheres illuminated with grey (g) and non–grey (ng) fluxes with different values of $T_{\rm h}$. The solid line corresponds to our parameterization given by Eqs. (4.2) to (4.4) and the coefficients in Table 1 of Alencar *et al.* (1999).

amount of external illumination, represented by $F_{{\rm rel},\omega}$. A weaker dependence on the angle of incidence of the external radiation, ω, is also visible.

The β exponent increases with the incident flux, represented by $F_{{\rm rel},\omega}$ and saturates when β reaches its value for radiative atmospheres. When a model atmosphere is heated by a large external flux, a significant part of the convection is extinguished and the model practically becomes one in radiative equilibrium, obeying the von Zeipel law asymptotically. This is most noticeable for models computed with incidence direction close to the surface normal (ω=0.93 and 0.67) in Fig. 4.2. The general trend revealed in the last Chapter of β having a maximum for a certain value of $T_{\rm eff}$ is repeated here for all values of $F_{{\rm rel},\omega}$. The maximum shifts to lower $T_{\rm eff}$ with increasing values of $F_{{\rm rel},\omega}$.

The variation of β for illuminated grey atmospheres is primarily a function of $T_{\rm eff}$, $F_{{\rm rel},\omega}$ and ω. In order to easily account for this dependence in light curve synthesis programs, we separate each variable using polynomials:

$$\beta = \sum_{n=0}^{4} a_n(t,\omega) F_{{\rm rel},\omega}^n \qquad (4.2)$$

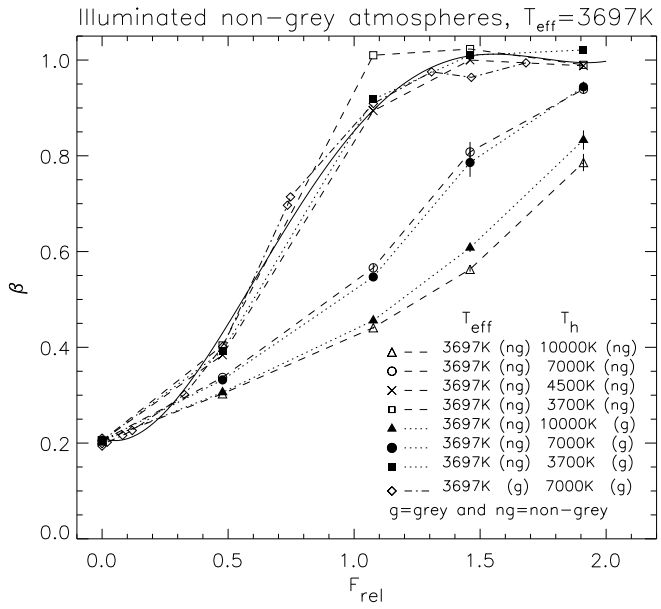

Figure 4.4: $\beta(t, F_{\rm rel})$, $\omega = 0.9306$, for non–grey atmospheres illuminated by grey (g) and non–grey (ng) fluxes with different values of $T_{\rm h}$. The solid line has the same meaning as in Fig. 4.3.

$$\text{where} \quad a_n(t,\omega) = \sum_{l=0}^{5} b_{nl}(\omega) t^l \tag{4.3}$$

$$\text{and} \quad b_{nl}(\omega) = \sum_{m=0}^{3} c_{nlm} \omega^m, \ \text{with } t = T_{\rm eff} \times 10^{-3} \tag{4.4}$$

The theoretical grid obtained is shown in Fig. 4.2, with the values determined from the atmosphere model overplotted. The 120 c_{nlj} coefficients obtained with grey models are listed in Table 1 of Alencar *et al.* (1999), that is available electronically at `http://www.fisica.ufmg.br/~silvia/thesis/beta2/tables`, also. The standard deviation of the parametric fit is σ=0.022 (26 models), with no systematic tendency of σ with the incidence angle.

In Fig. 4.3 we show β calculated for grey atmospheres ($T_{\rm eff}$=3697 K, ω=0.9306) illuminated by grey and non–grey fluxes for different values of $T_{\rm h}$ (3 700 K, 4 500 K, 7 000 K and 10 000 K). Our parametric approximation (Eqs. 4.2– 4.4) is also included. One can see that β does not depend significantly on $T_{\rm h}$ for grey illuminated models. Similar results are obtained for grey models with other values of ω and of $T_{\rm eff}$.

4.2.2 Convective non–grey (line-blanketed) atmospheres

Using the same procedure as in Sects. 4.1 and 4.2.1 we constructed non–grey atmosphere models illuminated by grey and non–grey fluxes. The gravity brightening exponent values obtained are close to the grey ones for effective temperatures of the illuminating stars ($T_{\rm h}$) close to those of the illuminated stars ($T_{\rm eff}$). However, for a given illuminated star and a fixed incident flux, β decreases with the increase of the effective temperature of the illuminating star, showing that there is a dependence of β on $T_{\rm h}$, beyond the dependence on the incident flux ($\propto T_{\rm h}^4$).

The differences between atmosphere models illuminated by grey and non–grey fluxes are small relative to the differences between the grey and non–grey illuminated models. Thus, significant changes of β are not related to the use of line-blanketed illuminating fluxes, but rather to the interaction between a line-blanketed illuminated atmosphere and the overall spectral distribution of the illuminating flux. Representative results are shown in Fig. 4.4, for a particular line-blanketed illuminated atmosphere ($T_{\rm eff} = 3\,697\,{\rm K}$) and different illuminating fluxes. We also show a result obtained with a grey illuminated model for comparison.

It is clear from Fig. 4.4 that at least one more parameter is influencing the results in the case of non–grey illuminated models. By comparing the illuminated grey and non–grey models, we realized that the main difference between them is that the spectral line opacity prevents part of the incident flux from reaching the continuum formation layers in the non–grey models. Because most of the spectral line opacity occurs in the UV, an increasing amount of the incident flux is intercepted for increasing effective temperatures of the illuminating star. The more of the incident flux that is intercepted, the smaller is the influence of the illumination on the convection. As a consequence, the increase of β with increasing illumination is reduced in non–grey models relative to grey models, following nevertheless a similar behavior as a function of the relative flux, as can be seen in Fig. 4.4. An immediate consequence is that line-blanketed illuminated atmospheres have β values which must depend on the metal abundance [Fe/H] of the model.

The results for grey models obtained in Sect. 4.2.1 are nevertheless more general than they might seem at first sight. The relative fluxes in the non–grey case should be regarded as the effective amount of flux that penetrates to the continuum formation layers. We may describe this effect through a "penetration" factor, f, that, multiplied by the incident flux, would give a new corrected flux that could be used to interpolate β with the grey parameterization coefficients given in Table 1 of Alencar *et al.* (1999) ($F_{{\rm rel},\omega} = f F_{{\rm rel},\omega,{\rm Total}}$). For grey illuminated atmospheres $f = 1$, while $f < 1$ for line-blanketed illuminated models. This interpretation is strictly correct

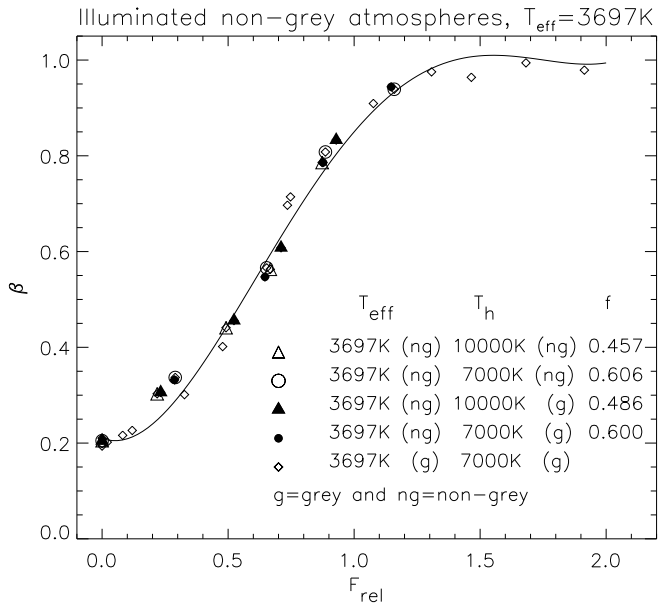

Figure 4.5: $\beta(t, F_{\rm rel})$, $\omega = 0.9306$. We applied the penetration factors (f) shown in the figure above to the fluxes presented in Fig. 4.4. The symbols are the same as in Fig. 4.4, the larger symbols correspond to the corrected relative fluxes. The solid line has the same meaning as in Fig. 4.3.

only if there exists a unique "penetration" factor for each set of parameters ($T_{\rm eff}$, $T_{\rm h}$ and ω). In principle there are, of course, differences in detail between different cases, but, in practice, the differences may be small. Figure 4.5 shows the models presented in Fig. 4.4. B It illustrates that it is indeed possible to find a factor f that brings together all the points, for each set of parameters $T_{\rm eff}$, $T_{\rm h}$ and ω to be fitted by the parametric curves given by Eqs. (4.2) to (4.4) and the coefficients of Table 1 of Alencar *et al.* (1999).

It can be seen from Fig. 4.5 that f differs between cases where the incident flux is a continuum–only (g) or a line-blanketed (ng) one. This is due to minor differences in the amount of flux in the UV region. However, to a good approximation we may assume that the penetration factor is related only to opacity distribution of the illuminated model. The surfaces presented in Fig. 4.2 may then be used to determine β even in the non–grey case, using appropriate values for the incident flux and the penetration factor.

In the present work we have concentrated on establishing the existence of such a penetration factor, by empirically calculating it and proving that it is the same

for each family of models. However, it should be possible to calculate f from the knowledge of the effective temperature of the incident flux (in order to know its amount of UV) and of the opacity properties of the atmosphere model at the upper layers (which determine how much of the UV flux will be blocked).

As stressed both in Alencar & Vaz (1997) and by Claret (1998), the comparison between the theoretical calculations and the empirical determinations of β available in the present is problematic and inconclusive, although promising (see Fig. 3 of Alencar *et al.* 1999 and Fig. 7 of Claret 1998). A possible test of the results presented here is to fit the light curves of Algol-type stars using our predicted β values, to test if it is possible to improve upon earlier results. Such tests are currently underway, with our results (of this chapter and the previous, for β, and of the next chapter for the limb-darkening coefficients) being implemented in a version of the WD model for light curve synthesis and solution of eclipsing systems (Wilson & Devinney, 1971; Wilson, 1993; Vaz *et al.*, 1995; Casey *et al.*, 1998).

4.3 Conclusions

The most general result, of the work presented in this chapter, is that we demonstrated for the first time the influence of external illumination on the gravity-brightening exponent, showing that external illumination increases the value of β. This suggests that the classical value of $\beta = 0.32$ may be too small for binary systems with close components.

The results presented here extend our results from the previous chapter for illuminated convective atmospheres, providing β in the range $3\,700\,\mathrm{K} < T_{\mathrm{eff}} < 7\,000\,\mathrm{K}$, for varying amounts of external illumination and angles of incidence. For illuminated convective grey atmospheres the gravity-brightening exponent may be calculated from the effective temperature of the illuminated star, the external radiation angle of incidence, and the incident flux of radiation that reaches the continuum forming layers in the illuminated star. The general trend, of β having a maximum in the T_{eff} range covered in this work, is interpreted as being caused by an interplay between the convection and opacity properties of the atmosphere model.

For illuminated non–grey atmospheres the gravity-brightening exponent also depends on the spectral distribution of the incident flux. When T_{h} does not differ by more than $\sim 25\%$ from T_{eff}, the results obtained with illuminated grey atmospheres may be used. For larger relative temperature differences, one needs to correct the relative incident flux with a penetration factor, corresponding to the absorption of UV flux in the upper layers of the illuminated model. The penetration factor is

necessarily a function of the metal abundance of the atmosphere, but this aspect has not yet been investigated.

This work was published in Astronomy and Astrophysics, Volume 346, pp. 556-563 (1999).

Chapter 5

—

Limb-darkening

5.1 Limb-darkening coefficients

The apparent stellar disk is normally brighter in the center than at the borders. This effect, easily observed in the Sun, is called limb-darkening. Although we see the same optical depth along the line of sight in both cases, it corresponds to deeper, and consequently hotter, layers in the center than at the limb. It is a well known and frequently studied effect in non-illuminated atmospheres, and various laws have been proposed to describe the intensity distribution of the stellar disk (Van Hamme, 1993; Díaz-Cordovés *et al.*, 1995).

The change in the specific intensity at a frequency ν over an increment of path length ds, in the time dt, in the direction $\hat{n}$ is equal to the intensity created by emission subtracted by the amount lost due to absorption:

$$\left[\frac{1}{c}\frac{\partial}{\partial t} + \frac{\partial}{\partial s}\right] I_\nu(\vec{r},\hat{n},t) = j_\nu(\vec{r},\hat{n},t) - \kappa_\nu(\vec{r},\hat{n},t) I_\nu(\vec{r},\hat{n},t) \tag{5.1}$$

where $j_\nu(\vec{r},\hat{n},t)$ and $\kappa_\nu(\vec{r},\hat{n},t)$ are the emission and absorption coefficients. In plane parallel atmospheres

$$\frac{\partial I}{\partial s} = \frac{\partial z}{\partial s}\frac{\partial I}{\partial z} = \cos\gamma \frac{\partial I}{\partial z}$$

In this case and for a time independent problem Eq. (5.1) becomes

$$\cos\gamma \frac{dI_\nu}{dz} = j_\nu(z) - \kappa_\nu(z) I_\nu(z) \tag{5.2}$$

The optical depth is defined as $d\tau_\nu(z) = -\kappa_\nu(z)dz$, where the minus sign appears since τ_ν increases inwards, and the source function is $S_\nu(z) = j_\nu(z)/\kappa_\nu(z)$. Making the above substitutions in Eq. (5.2), and omitting the reference to the τ_ν dependence, we get the basic equation of transfer for a plane-parallel atmosphere

$$\cos\gamma \frac{dI_\nu}{d\tau_\nu} = I_\nu - S_\nu \tag{5.3}$$

The solution of this equation at the surface of a non-illuminated atmosphere is

$$\begin{cases} I_\nu^{\text{in}} = 0 \\ I_\nu^{\text{out}} = \int_0^\infty S_\nu \exp\left(-\tau_\nu \sec\gamma\right) \sec\gamma d\tau_\nu \end{cases} \tag{5.4}$$

The exponential extinction varies as $\tau_\nu \sec\gamma$, so the position of the unit optical depth along the line of sight moves to smaller τ_ν as the line of sight goes from the center to the limb as showed in Fig. 5.1 reproduced from Gray (1992).

For a linear source function $S_\nu = a + b\tau_\nu$ and calling $\mu = \cos\gamma$, Eq. (5.4) will give:

$$\begin{aligned} I_\nu^{\text{out}}(\mu) &= \int_0^\infty \frac{(a + b\tau_\nu)}{\mu} e^{(-\tau_\nu/\mu)} d\tau_\nu \\ &= \frac{a}{\mu}\int_0^\infty e^{(-\tau_\nu/\mu)} d\tau_\nu + \frac{b}{\mu}\int_0^\infty \tau_\nu e^{(-\tau_\nu/\mu)} d\tau_\nu \\ &= a + b\mu \end{aligned} \tag{5.5}$$

The ratio $I_\nu(\mu)/I_\nu(1)$ is called a limb-darkening law. For the case above it is given by:

$$\frac{I_\nu(\mu)}{I_\nu(1)} = \frac{a + b\mu}{a + b} = 1 - x_\nu(1 - \mu), \tag{5.6}$$

where $x_\nu = b/(a + b)$ is the limb-darkening linear coefficient. The linear law gives a good description of the limb-darkening in the solar atmosphere. Mainly due to theoretical studies on stellar atmospheres, other limb-darkening laws have been proposed in the literature, such as the polynomial approximations, that better describe the effect away from the solar temperature range:

$$\frac{I_\nu(\mu)}{I_\nu(1)} = 1 - x_\nu(1 - \mu) - y_\nu(1 - \mu)^n, \tag{5.7}$$

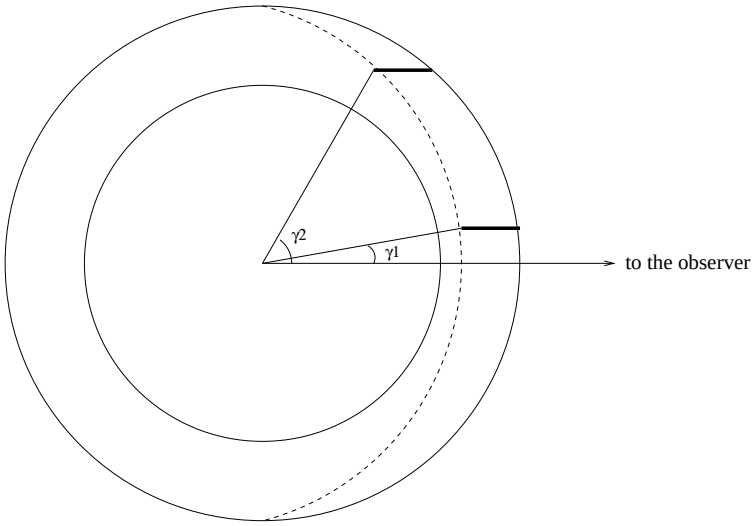

Figure 5.1: Limb-darkening configuration. The top and bottom of the photosphere are indicated by the outer and inner circles (not in scale). The dashed line indicates penetration of our line of sight to unit optical depth. Radiation coming from γ_2 originates in outer and consequently cooler layers than from γ_1.

where y_ν is the non-linear limb-darkening coefficient, $n = 2$ for the quadratic law (Wade & Ruciński, 1985, using the 1979 version of ATLAS by Kurucz, 1979; Manduca *et al.*, 1977 and Claret & Giménez, 1990, using versions of UMA), and $n = 3$ for the cubic law (Van't Veer, 1960, quoted by Díaz-Cordovés *et al.*, 1992). The logarithmic approximation, proposed by Klingesmith & Sobieski (1970), gave very good results fitting their theoretical models, valid in the range $10\,000\text{K} < T_{\text{eff}} < 40\,000\text{K}$:

$$\frac{I_\nu(\mu)}{I_\nu(1)} = 1 - x_\nu(1-\mu) - y_\nu \mu \ln \mu, \tag{5.8}$$

and was confirmed by Van Hamme (1993) with the 1991 version of ATLAS. Díaz-Cordovés *et al.* (1992) proposed a new non-linear approximation, the square-root limb-darkening law:

$$\frac{I_\nu(\mu)}{I_\nu(1)} = 1 - x_\nu(1-\mu) - y_\nu(1-\sqrt{\mu}). \tag{5.9}$$

In subsequent papers Claret *et al.* (1995); Díaz-Cordovés *et al.* (1995) made a comparison between the linear, quadratic and square-root laws. In this case, the square-root approximation seems, almost always, to be the best one. But according to

Van Hamme (1993) the logarithmic law gives the best approximation in the UV, while the square-root law is the best in the IR and longer wavelengths. In the optical region, cooler stars are better represented by the logarithmic law and high temperature stars by the square-root law.

Due to the limb-darkening it is possible to obtain the temperature structure as a function of optical depth of the Sun's atmosphere. Unfortunately, the limb-darkening cannot be measured in most other stars, but it is an important parameter in the determination of stellar angular diameters, radii and effective temperatures using interferometry and lunar occultation methods (Hofmann *et al.*, 1998; Pauls *et al.*, 1998). In EBS the shape of the light curves in the beginning and end of the eclipses is affected by the limb-darkening, whose coefficients are usually bi-linearly interpolated in the light curve synthesis programs from theoretical tabulated values obtained with atmosphere models as a function of $T_{\rm eff}$ and $\log g$.

5.2 Illuminated models

The limb-darkening effect is highly affected by external illumination (Vaz, 1985; Nordlund & Vaz, 1990; Claret & Giménez, 1990) but, until now, the light curve synthesis models have used limb-darkening coefficients calculated with non-illuminated atmospheres. One effect concerns the values of the limb-darkening coefficients, which are changed by the infalling flux. In fact, even the limb-darkening law which best represents the variation of the flux with the line of sight angle may change due to the external illumination. Another important difference, as compared to the normal stellar atmospheres (for which the limb-darkening laws and coefficients are valid over the whole stellar surface), is that the illuminated atmospheres show different limb-darkening coefficients (and laws) for different points on the stellar surface, due to the dependence of these on the incidence angle of the infalling flux. Therefore, the best representation for the center-to-limb variation of the surface brighteness of eclipsing binary components in the synthetic LC generation studies is to use the coefficients calculated for the local configuration (i.e. considering the apparent radius, the direction of illumination and the temperature of the companion).

Vaz & Nordlund (1985) modified the original UMA program introducing an external radiation field in the model. This field is assumed to be a plane parallel beam striking the surface of the atmosphere at an angle $\theta = \cos^{-1}\omega$ with the surface normal and specific intensity (dropping the reference to the frequency dependence):

$$I^{in} = i_0 \delta(\omega - \omega_i)\delta(\eta - \eta_i), \tag{5.10}$$

where $\delta(x)$ is the Dirac delta function and η_i is the azimuthal angle about the normal to the surface corresponding to the direction of the irradiating flux. i_0 is a constant given by:

$$F_r^* = \int_0^{2\pi} d\eta \int_{-1}^{0} I(\omega, \eta)\omega d\omega = \omega_i i_0, \tag{5.11}$$

where F_r^* is the radial component (normal to the surface) of the incident flux per unit area perpendicular to the incident ray, F^* :

$$F^* = \sigma T_{\rm h}^4 r_{\rm h}^2, \tag{5.12}$$

σ is the Stefan's constant, $T_{\rm h}$ is the effective temperature and $r_{\rm h}$ is the apparent radius of the illuminating star . Equation (5.10) substitutes the first part of Eq. (5.4) in the illuminated case.

5.3 Methods

The atmosphere model generates intensities in six different angular directions ($\mu =$ 0.06943, 0.33001, 0.5, 0.66999, 0.93057 and 1.0) and 368 wavelengths ranging from 1500Å to 124000Å. Starting from these data, monochromatic, passband-specific and bolometric limb-darkening coefficients can be calculated.

When calculating the passband coefficients we made a convolution of the intensities with the response functions, $S(\lambda)$, corresponding to the Strömgren filters uvby (Crawford & Barnes, 1970) and the UBVRI passbands (Bessel, 1983). We used in the convolution the atmospheric mean transmission by Allen (1976), the reflection curve of two aluminum coated mirrors (Allen, 1976), the sensitivity of a 1P21 photomultiplier from Kurucz (1979) and for the Strömgren filters, the sensitivity function of the SAT photometer (Florentin-Nielsen 1983, personal communication).

Two different calculation methods were tested. The first one, described by Claret & Giménez (1990) (CG), determines the coefficients by least-square fitting of the integrated and normalized model intensities. The second method follows the procedure outlined by Van Hamme (1993) (VH) where a number of physical constraints, equal to the number of coefficients to be determined, are assumed. The limb-darkening coefficients are obtained by solving the constraint equations. Using a one parameter law, the constraint is the conservation of the total flux and for a two parameters law, the additional constraint that the mean intensity of the approximation and the atmosphere model must be equal is applied.

These methods differ from each other in some important aspects. While CG emphasize the point of using coefficients that best match the relation I(μ)/I(1)

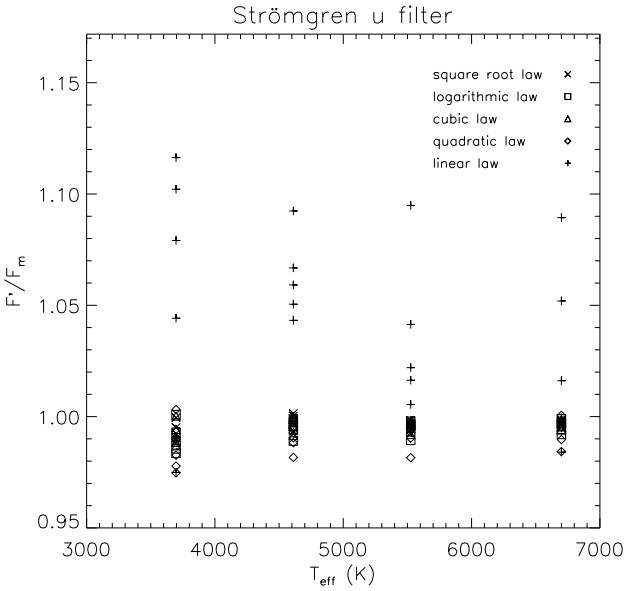

Figure 5.2: $F'/F_{\rm m}$ calculated with the coefficients determined by the CG method. Models used: $\omega = 0.07$, $T_{\rm h}$ =7 000 K.

vs μ, even if the total flux is not perfectly conserved, VH says that the physical constraints of his method are introduced in order to avoid non-physical coefficients. In non-illuminated atmospheres CG find that the total emergent flux obtained by integrating the intensities calculated from the adjusted coefficients (F') does not differ more than 2% from the total flux obtained from the model intensities ($F_{\rm m}$), and that when choosing a non-linear law, the difference vanishes. We calculated the relation ($F'/F_{\rm m}$) for all our illuminated models, and the result for a set of models is shown in Fig. 5.2. As noticed, the linear law is not a good approximation when dealing with illuminated atmospheres. We find that the mean difference between the fluxes is around 4% (with a maximum of 26% in some models) in the case of a linear law and less than 1% (however with a maximum of 6%) for the non-linear ones. These results show that for an illuminated atmosphere the CG method should be used with care, as, for some models, even choosing a non-linear law, the flux is not conserved. Due to that we decided to adopt the VH method in our calculations of all the results presented in Tables 1 and 2 of Alencar & Vaz (1999) that are available electronically at `http://www.fisica.ufmg.br/~silvia/thesis/limb/tables`.

5.4 Results

We noticed that the effect caused by illumination on the limb-darkening was weakly dependent on the $\log g$ of the model. This can be seen in Fig. 5.3. Therefore we did calculations only for $\log = 4.5$, as for this value we achieve a representative mean effect of illumination for the interval $3.5 \leq \log\ g \leq 5.0$.

Figure 5.4 shows that the external illumination strongly affects the limb-darkening laws and coefficients of illuminated atmospheres as compared with the non-illuminated ones. These models are approximately equivalent to those calculated by CG and ω has a mean value between vertical and grazing incidence. In order to be consistent we will show the results for the Strömgren u filter, but the effects are similar for the other calculations done, bolometric, monochromatic and for all the Strömgren filters and the UBVRI filters of the Johnson-Morgan system, as well. As we increase the amount of incident energy, for example by increasing the apparent radius while keeping the other parameters fixed, the law for non-illuminated models no longer represents the calculated intensities, showing that non-illuminated coefficients yield wrong limb-darkening laws when used with illuminated stars.

A first interesting result from Fig. 5.4 is that, depending on the set of parameters chosen, we observe an effect of limb-brightening instead of darkening. This can be understood as follows: as we increase the illumination flux, the temperature

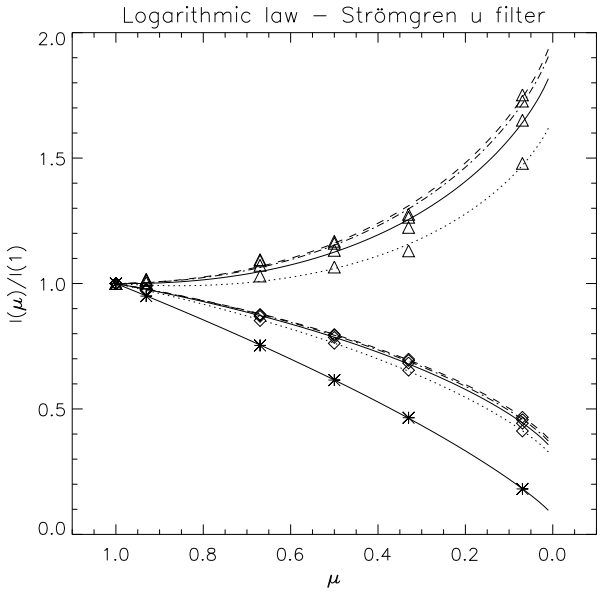

Figure 5.3: Comparison between the effect of the surface gravity and of external illumination on the limb-darkening, here adjusted by the logarithmic law. The * symbols correspond to the non–illuminated model with $T_{\rm eff}$=3 697 K. The $\diamond$ and $\triangle$ symbols correspond to this model illuminated by $T_{\rm h}$ = 3 700 K and 10 000 K, respectively. The dashed lines correspond to models with $\log g$=3.5, the dash-dotted ones to $\log g$=4.0, the solid lines to $\log g$=4.5 and the dotted lines to $\log g$=5.0.

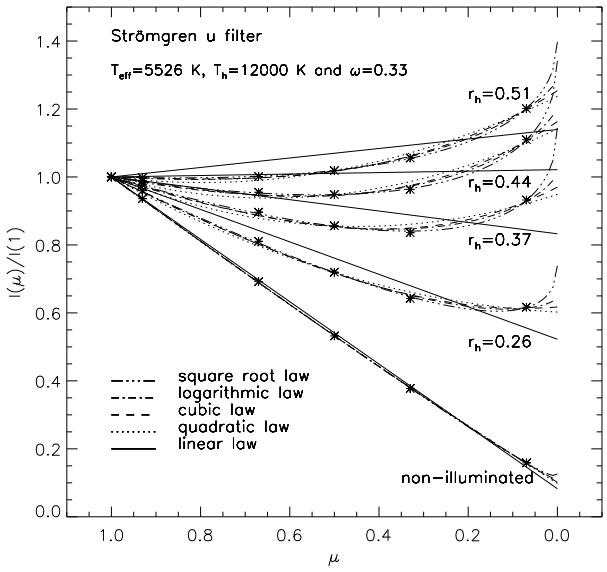

Figure 5.4: Adjusted limb-darkening laws for a non-illuminated model and 4 illuminated models (varying $r_{\rm h}$). The asterisks represent the model results.

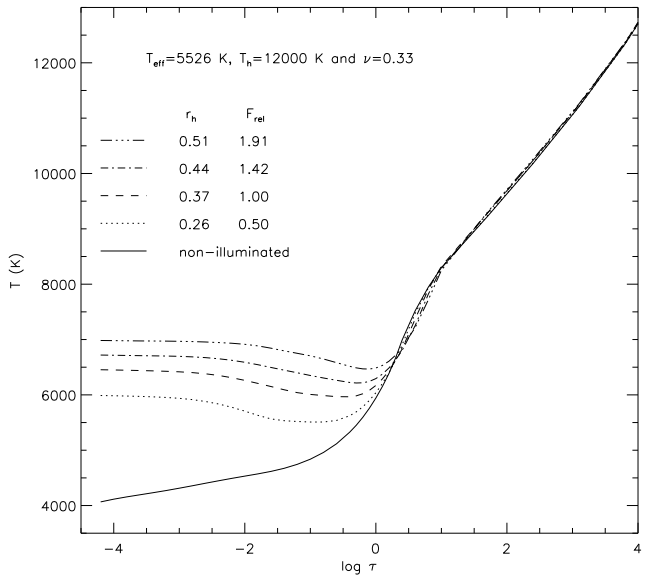

Figure 5.5: The run of the temperature with the optical depth (Rosseland mean) for the models shown in Fig. 5.4.

distribution in the atmosphere of the illuminated star becomes more and more homogeneous, until it reaches a state where there is no center-to-limb darkening and the star's brightness is the same throughout the stellar disk. This can be seen in Fig. 5.5, where we show the temperature structure for the models shown in Fig. 5.4. The larger the amount of infalling flux the higher the temperature of the external layers and the larger the region where it stays approximately constant. If we keep increasing $F_{\rm rel}$, by changing either $r_{\rm h}$, $T_{\rm h}$ or ω, we reach a situation where the most external layers are hotter than the internal ones. As we see more external layers looking at the limb than looking at the center, we have a limb brightening effect.

As already noticed by Claret & Giménez (1990), the limb-darkening coefficients of an illuminated atmosphere strongly depend on many parameters, making it difficult to find a simple function that describes the effect. We propose, for the passband specific coefficients, a solution to easily account for the effect in LC synthesis programs, parametrizing with polynomials the results obtained. In Eq. (5.13) K represents x_λ

or y_λ of Eqs. (5.6) to (5.9) for the different limb-darkening laws:

$$K = a_0(t) + \sum_{n=1}^{3} a_n(t, \omega, t_{\rm h}) F^n, \tag{5.13}$$

$$a_n = \sum_{m=0}^{3} b_{nm}(\omega, t_{\rm h}) t^m, \tag{5.14}$$

$$b_{nm} = \sum_{l=0}^{3} c_{nml}(t_{\rm h}) \omega^l, \tag{5.15}$$

$$\text{and} \quad c_{nml} = \sum_{k=0}^{2} d_{nmlk} t_{\rm h}^k, \tag{5.16}$$

with $F = F_{\rm rel}$, $t = T_{\rm eff} \times 10^{-3}$ and $t_h = T_{\rm h} \times 10^{-3}$

A sample of the adjusted polynomial coefficients obtained are given in Table 3 of Alencar & Vaz (1999) where is also shown the adjusted polynomial surface for one chosen model. A complete version of Table 3 with the adjusted polynomial coefficients for the 9 chosen photometric filters can be accessed in electronic form at the CDS archive (`http://cdsweb.u-strasbg.fr/htbin/Cat?J/A+AS/135/555`) and also at `http://www.fisica.ufmg.br/~silvia/thesis/limb/tables`.

5.5 Conclusion

We determined monochromatic, bolometric and passband specific limb-darkening coefficients for illuminated atmospheres. Our results show that illuminated coefficients are significantly different from the non-illuminated ones and that illuminated atmospheres may present limb-brightening instead of darkening, depending on the set of parameters chosen. We tested two different methods (Claret & Giménez, 1990; Van Hamme, 1993) to calculate the coefficients and showed that in the illuminated case the method proposed by Van Hamme is recommended in order to obtain coefficients that preserve the total emergent flux from the atmosphere. For the passband specific coefficients we also present our results in a polynomial form, which is convenient for implementation of these "illuminated" coefficients in the analysis of eclipsing binary light curves.

This work was published in the Astronomy and Astrophysics Supplement, Volume 135, pp. 555-564 (1999).

Chapter 6

T Tauri stars

6.1 Star formation

Star formation is one of the most challenging subjects in stellar astrophysics nowadays. Although this area of research has progressed immensely during the last decades, many fundamental questions are still under discussion. What triggers star formation is still unknown. Many factors are thought to play important roles like dust, turbulence and magnetic fields but there is no way to predict up to now if a cloud core that has not yet collapsed ever will. It is still unclear if the mass of a star is determined by the mass of its original cloud core, or if the star itself is mainly responsible for determining its mass through accretion and outflow processes. When and how binary stars form is still an open question. Very young embedded stars are already found to be binaries so the answer may lie in the physics of protostars that only recently became accessible observationally. What makes a star loose its angular momentum is not clear either. Main-sequence stars are generally much slower rotators than the slowest T Tauri stars that are still contracting and accreting and would be expected to spin further up and not down. Magnetic winds are the main mechanism accepted nowadays to brake down these rapidly rotating young stars, but they still can not explain the transition from the period distributions observed in the PMS to the ones present in the MS. The role of jets and molecular outflows in Pre-Main Sequence evolution is far from being understood and there is a long way

to go in the study of disk evolution and planetary formation. Finally, little is known about the formation of high mass stars: they evolve so rapidly that newly forming ones are consequently very rare. Most of what will be described here may not apply to them, as most of the work so far has naturally concentrated on low mass stellar formation and evolution.

The advances in a number of observational techniques has permitted in the last decade the study of many aspects of the initial states of stellar formation and evolution. Infrared detectors allow us to extend the study to very embedded sources and to disks as well. Better radio wavelength interferometers, with high sensitivity and spatial resolution, are now available to precisely investigate the distribution of molecular material around young stars. High resolution echelle spectrographs provide simultaneous observation of a large number of lines, and help constrain the nature of line forming regions. On the theoretical front, many different models have been proposed (and many refuted also) to explain the observations. We may certainly say that the theory of star formation has evolved as much as the observational results, and a theoretical picture of the main processes taking place in the early stages of a star's life is gradually reaching a consensus, although much is still to be done.

Stars are thought to be born mostly in Giant Molecular Clouds (GMCs). These large scale structures have typically masses of the order of 2-3$\times 10^5$ $M_\odot$ and sizes $\sim 50-100$ pc. They are cold (kinetic temperatures ~ 10 K) and dense (n(H_2) $\sim 200-300\,\mathrm{cm}^{-3}$) interstellar regions. Molecular clouds of various masses and sizes have been observed to be marginally bound, a necessary although not sufficient condition for star formation to occur. Because they are so cold, thermal pressure alone cannot prevent them from collapsing and support against gravity is also thought to be due to magnetic fields and turbulence. GMCs are not uniform but constitute of many filamentary structures and high density ($\sim 10^4\,\mathrm{cm}^{-3}$) clumps and cores. At such densities the core collapse may occur in only a few hundred thousand years. But the star formation process is very inefficient and, according to observations, roughly 2-3% of the molecular gas in a GMC end up forming stars. Part of the reason may be that when very massive stars are formed they rapidly ionize and disrupt the molecular gas. Dust is also thought to play an important role in star formation. Dust extinction in molecular clouds may enhance the star formation by lowering the temperature of cloud cores (McKee, 1999). The external radiation absorption by dust may reduce the ionization of the molecular cloud decreasing the coupling of ions and neutrals in the cores and permitting the gas to diffuse across magnetic field lines. This reduces the magnetic support of the cloud and accelarates the star formation process.

When a cloud core becomes gravitationally unstable the collapse begins at nearly free-fall velocities. It is thought to proceed initially from inside-out, the central and densest part of the cloud core collapsing first. Any small initial rotational velocity, that the cloud core might have, implies that its angular momentum will have to be transferred to the forming star. Due to the rapidity of the process, and to the difference in size between the cloud and the star, it is likely that material will end up forming a disk, a multiple star system or both instead of falling directly to the central mass.

The protostar and disk are formed deeply embedded in the remaining collapsing cloud. From there on, in the case of low-mass stars, most of the stellar mass will be acquired through accretion from the disk. Initially material is still falling from the surrouding envelope to the disk while the disk accretes material into the star. As these accretion rates may not be the same, material may pile up in the disk that is thought to undergo rapid outbursts. This could explain the FU Ori outbursts currently observed and poorly understood, but they could also be caused by disk instabilities.

Winds, jets and molecular outflows are driven by the young star-disk system and help dissipating the surrounding cloud. When the Pre-Main Sequence star becomes optically visible it is called a T Tauri star in the low-mass case (M <2 $M_\odot$) or a Herbig AeBe star for intermediate masses (2 $M_\odot$< M < 8 $M_\odot$). It still accretes from the disk, but at lower accretion rates than in the protostellar phase. It is not actually known what causes the end of the disk. It can be just mostly accreted to the star but can also be disrupted by tidal instabilities and gaps created by planet formation. Some T Tauri stars, known as weak-lined T Tauri stars (WTTSs) do not exhibit disks at very early ages ($\sim 10^6$ years) while others, the Classical T Tauri Stars (CTTSs), at the same ages and spectral types still do.

It is currently believed that there are two basic modes of star formation (Lada, 1999). A clustered mode, like the Orion complex, where stars are formed in rich and dense clusters and the mass range goes up to very massive O stars. And a distributed mode, like the Taurus complex, where low mass stars form in individual low mass cores. Although the clustered mode seems to be dominant, Taurus is the most studied star formation site, mostly due to its proximity ($\sim$ 140 pc) to us and for being visible in the northern hemisphere.

6.2 Classical T Tauri Stars

T Tauri stars were first discovered by Joy (1945) as variable stars associated with nebulosities and presenting strong emission lines. Later Herbig (1962) proposed a spectroscopic selection criteria for TTSs based on their hydrogen and calcium lines in strong emission. The term Classical T Tauri Star came recently to distinguish the standard TTSs from a new population of young low-mass stars discovered in X-ray emission surveys and named Weak-Lined T Tauri Stars. The WTTSs showed only weak Hα emission and due to that had escaped detection in previous Hα surveys used to search for TTSs. They are thought to be PMS stars that have already lost their disks. The weak emission lines are supposed to be due to chromospheric activity, caused by strong magnetic fields at the stellar surface that commonly shows large cold spots, which give support to that idea.

CTTSs are now known to be optically visible low-mass PMS stars surrounded by an accretion disk. They exhibit IR excesses associated to the reprocessing of stellar radiation by the disk. They also show UV continuum excess (known as veiling), produced in hot spots at the stellar surface, where the infalling material hits the star in the accretion process. CTTSs present many permitted and forbidden emission lines and show lithium (6707.8 Å) in absorption. They are photometrically variable, mainly due to the presence of hot and cold spots at their surface. The cold spots are due to magnetic acivity that is also responsible for flares and X-ray emission.

Their youth is confirmed observationally by the presence of lithium in their spectra, the association with OB association (which are naturally short lived), or dark clouds. Theoretically, their young age is inferred from their position in the HR diagram: TTSs lie above the Main Sequence along the Hayashi tracks (see Fig. 6.1).

A star appears in the HR diagram as soon as it becomes visible, or equivalently, reaches the birthline. TTSs at that point have not yet reached temperatures in the core center to start burning hydrogen and are fully convective. They evolve contracting quasi-estatically to mantain hydrostatic equilibrium. This happens almost without changing their temperature and they approach the Main Sequence following steep Hayashi tracks. Stars less massive than 0.8 $M_\odot$ remain fully convective up to the MS, while the more massive ones develop a radiative core still in the PMS phase. In the radiative regime a star's luminosity depends mainly on its mass and it evolves following the almost horizontal radiative tracks. Only very low mass TTSs (M<0.3 $M_\odot$) escape the protostellar phase with their initial deuterium intact. In this case, at ~ 1 My the contraction slows as their cores reach the deuterium burning temperatures, proceeding later through the convective paths. For all masses the

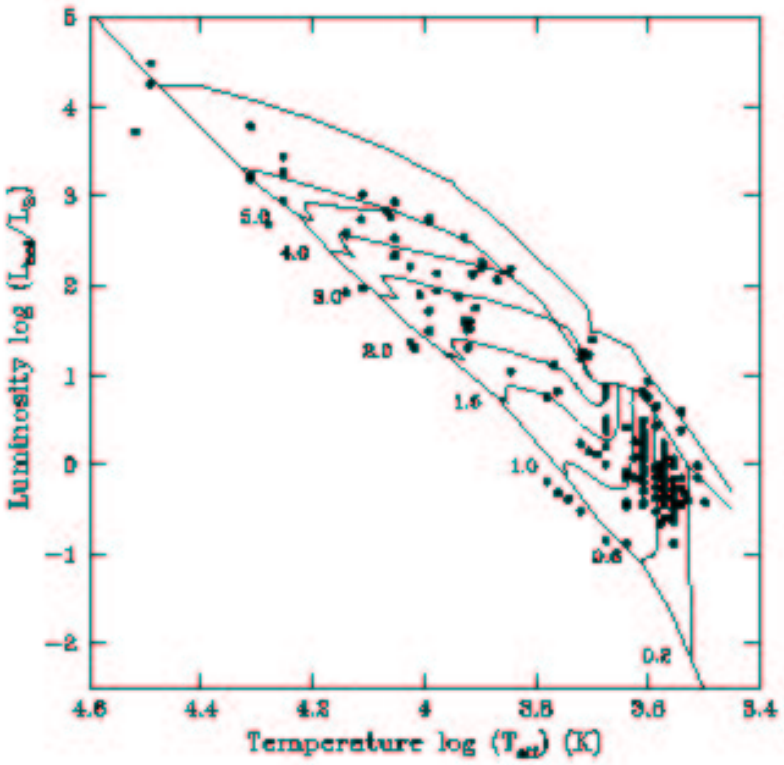

Figure 6.1: T Tauri stars in the HR diagram (Palla , 1999). The filled circles give the position of young PMS stars. PMS evolutionary tracks are labeled according to the stellar masses. The 2 upper lines are birthlines for different accretion rates and the lower line is the Main Sequence location.

contraction continues until the TTS starts burning hydrogen where it reaches the Main Sequence and ends its youth.

6.2.1 Accretion Models

Many models have been proposed to explain the observational characteristics of CTTSs. The pioneer work of Lynden-Bell & Pringle (1974) presented the idea that viscous dissipation in disks might be responsible for the IR excess. They also proposed that the UV excess could be produced in a boundary layer between the rapidly rotating disk and the slowly rotating star. However, these models cannot

explain the inverse P Cygni profiles commonly present in the CTTSs emission lines, which show a redshifted absorption component at 200-300 km s^{-1}. In the boundary layer, material is supposed to slow down from the disk to the star producing small radial velocities. The boundary layer model could not easily explain the spectral energy distribution (i.e. the observed flux distribution λF_λ) of many CTTSs that is better fitted by disks without the inner part, disks with holes. The maximum disk temperature to fit the observations needs to be smaller than it would be expected for a disk reaching close to the stellar surface. These models also had trouble explaining why CTTSs are often found to be slow rotators ($v \sin i \sim 10$ km s^{-1}) since the accretion process should spin up the star.

Outflowing wind models were suggested to explain the CTTSs' emission line spectra (Hartmann *et al.*, 1982, 1990; Natta & Giovanardi , 1990). But they tend to predict upper Balmer lines (Hβ , Hγ , Hδ) with strong wind absorption components and cannot explain the spectra of many CTTSs that show these lines with very faint or even without blueshifted absorptions. They also cannot justify the presence of hot spots inferred from photometric variations and, like the boundary layer models, cannot produce the observed inverse P Cygni profiles.

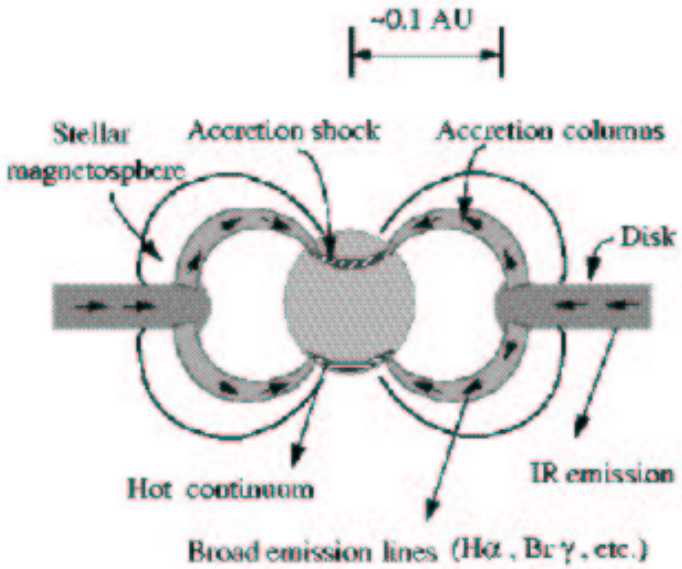

Figure 6.2: Simplified magnetospheric accretion model configuration with the regions where many observed features are thought to originate (from Hartmann , 1999).

In recent years magnetospheric accretion models were proposed (Shu *et al.*, 1994; Hartmann *et al.*, 1994; Muzerolle *et al.*, 1998a) and are the current consensus to describe CTTSs. A simplified picture of the magnetospheric accretion configuration is shown in Fig. 6.2 and a view close to the star according to Shu's model is shown in Fig. 6.3. In these models a strong stellar magnetic field truncates the circumstellar disk at the Alfvén radius and locks the star to the disk. Material is accreted through closed magnetic field lines from the disk to the star, while angular momentum is transferred from the star to the disk. Open field lines originating close to the corrotation radius drive away a wind, and may spiral up to create a jet. Open field lines from the star itself also contribute to the outflow. The permitted emission lines are thought to be produced in the magnetic funnel flow, where material is accelerated. When the accretion material hits the stellar surface a hot spot or a ring is formed and the strong UV and optical continuum excess (known as veiling) is produced. Forbidden emission lines originate in the outflow or jet and should be blueshifted, as observed, due to the occultation of the receding part of the flow by the disk.

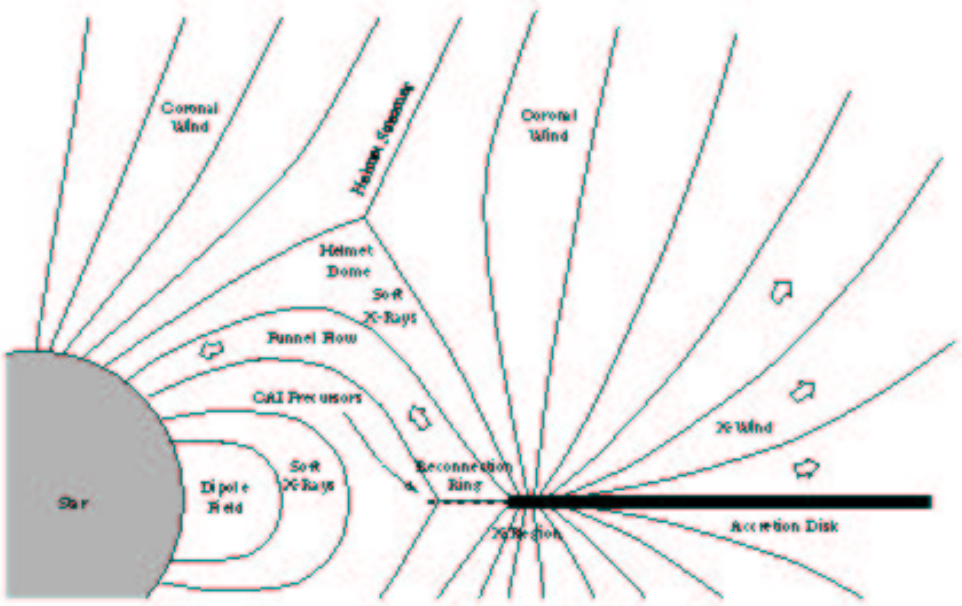

Figure 6.3: Magnetospheric accretion model configuration (Shu *et al.*, 1999).

The models naturally predict the inverse P Cygni profiles since material falls onto the star at nearly free-fall velocities, which corresponds to the observed redshifted

absorption values for a typical Classical T Tauri star ($\sim$0.5 $M_\odot$ and r=2-3 $R_\odot$). They also agree with the SED's results since the disk is supposed to be disrupted by the stellar magnetic field.

In addition, the disk-locking mechanism may explain why CTTSs are mostly found to be slower rotators than WTTSs that do not have disks. Some years ago Choi & Herbst (1996) found a bimodal distribution of rotational periods among the TTSs in the Orion Nebula Cluster (ONC). The stars with the longer periods also exhibited IR excess (an indication of disks) that the ones rotating faster did not have. Recently Stassun *et al.* (1999) studying a larger region around the ONC apparently did not find any indication of a bimodal distribution. However their results may be biased towards low mass stars, where deuterium burning is still occuring and help slow down the rotational period evolution around the ONC age, filling up the gap in the period distribution.

The magnetospheric accretion models assume dipolar strong (up to 10 kG) magnetic fields. A few magnetic field strength measurements of CTTSs are avaliable. Mean fields of order of 2-3 kG were obtained by Johns-Krull *et al.* (1999) from Zeeman broadening of infrared line profiles for 4 CTTSs but the measured values do not correlate with the predicted field strengths from magnetospheric theories. However, magnetic field measurements in the accretion shock, determined with circular polarization in the emission lines of CTTSs, apparently show values that correlate with those predicted by the theory (Johns-Krull & Valenti, 1999).

The magnetospheric accretion model presented by Shu *et al.* (1994) was a new version of their X-celerator mechanism whose natural period is the rotational period of the star. Lines formed in the magnetospheric accretion flow that is controlled by the stellar field should show periodicity at the stellar rotation period in the presence of an inclined dipole field. SU Aur presented this kind of variations in Hβ and Hα (Johns & Basri, 1995b)

In general, however, the line variations do not seem to be related to orbital motion, as they do not usually correlate with the stellar rotational period. Different parts of a line may vary differently, as Johns & Basri (1995a) showed by analysing time variations of Hα for several CTTSs. They suggest the line emission region is composed of discrete, stochastically varying blobs with a range of velocities and turbulence, which the Sobolev treatment used in the actual magnetospheric models does not take into account.

Hartmann *et al.* (1994) and Muzerolle *et al.* (1998b) presented emission line profiles calculated with their magnetospheric accretion models that can be compared to the observed ones. The theoretical profiles are generally found to be centered at the stellar rest frame or slightly blueshifted. They tend to present blueward asym-

metry due to occultation by the disk of part of the receding flow. They may exhibit reshifted absorption at free-fall velocities in some favored geometrical configurations: the accreting material must be projected against the hot spot (or ring).

Edwards *et al.* (1994) showed observational evidence, in a sample of 15 CTTSs, that they claimed confirm some of the magnetospheric predictions, like blueward asymmetric emission lines and inverse P Cygni profiles in almost all the stars' spectra. The line profiles of several other stars were also well reproduced by magnetospheric calculations (Muzerolle *et al.*, 1998b; Najita *et al.*, 1996), but often the theoretical profiles are more asymmetric and always less broadened than the observed ones. However, we must keep in mind that the models of Hartmann *et al.* (1994) do not include rotation and winds that would certainly influence both the asymmetry and the broadening of the theoretical profiles. Another difficulty to model CTTSs is that the accretion process is dynamic and the line profiles may change drastically in a few hours. The fact that a certain star shows a line profile that agrees with the theory does not mean that it will always be the case and is not necessarily a strong support for the models. The real challenge for the models is to reproduce all the profiles a line of a certain star may exhibit and the many profiles of a line shown by various CTTSs.

One way to test the magnetospheric accretion model predictions is to look at simultaneously observed lines of various T Tauri stars. From the relation between the lines equivalent widths and their components one can infer many of the model characteristics. We can also investigate the line profile symmetry and shape and help calibrate the models providing values for parameters such as wind velocities and line broadening. Another way to make the test is to gather synoptic observations of a single CTTS. These are critical to understanding the full range of profiles produced by a single star, where some underlying parameters do not change but others do, and many structures are dynamic. We decided to do both.

6.3 Observations and reduction

Part of the observations were obtained in several new observing runs during 1998 and 1999. The total set of observations, which span over a decade, were carried out at Lick Observatory with the 3m Shane reflector or the 0.6m Coudé Auxiliary Telescope (CAT) and the Hamilton Echelle Spectrograph (Vogt , 1987) coupled either to a TI 800x800 CCD or a FORD 2048x2048 CCD. With the smaller detector two settings were established: a red setting covering 52 orders from 4900 Å up to 8900 Å and a blue setting covering 38 orders from 3900 Å up to 5200 Å. The spectral coverage,

however, is not complete, with a gap of a few dozens of angstroms between orders. Whenever possible, blue and red observations were obtained in the same night or within 1 night of difference. The bigger CCD installed in 1992 permits a full spectral coverage of ~ 92 orders ranging from 3900 Å to 8900 Å. The mean resolution of the spectrograph is $\lambda/\Delta\lambda \approx 48,000$ and the exposure times varied from 15min to 1h15min, depending on the target and the CCD used.

The Hamilton spectrograph is optimized for high resolution and broad spectral coverage where multiple spectral orders are simultaneously recorded. The orders overlap one another after being formed at the grating and are separated by the cross-dipersing prisms. The echelle spectrum that results is composed of slightly curved orders as shown in Fig. 6.4 in the case of the Sun.

The reduction was performed in a standard way described by Valenti (1994) which includes flatfielding with an incandescent lamp exposure, background subtraction and removal of cosmic rays. A narrow flat exposure is used to find the exact position of each order in the CCD. These positions are fit with polynomials that are later used to extract the orders in the stellar spectra. Wavelength calibration is made by observing a Thorium-Argon comparison lamp and performing a 2-D solution to the position of the Thorium lines. Radial and barycentric velocity corrections are applied and all the data shown are in the stellar rest frame. The spectra are not flux calibrated, so each spectrum has been continuum normalized. Due to differences in weather conditions, exposure times and efficiency between different chips there is a wide range of signal to noise in the data.

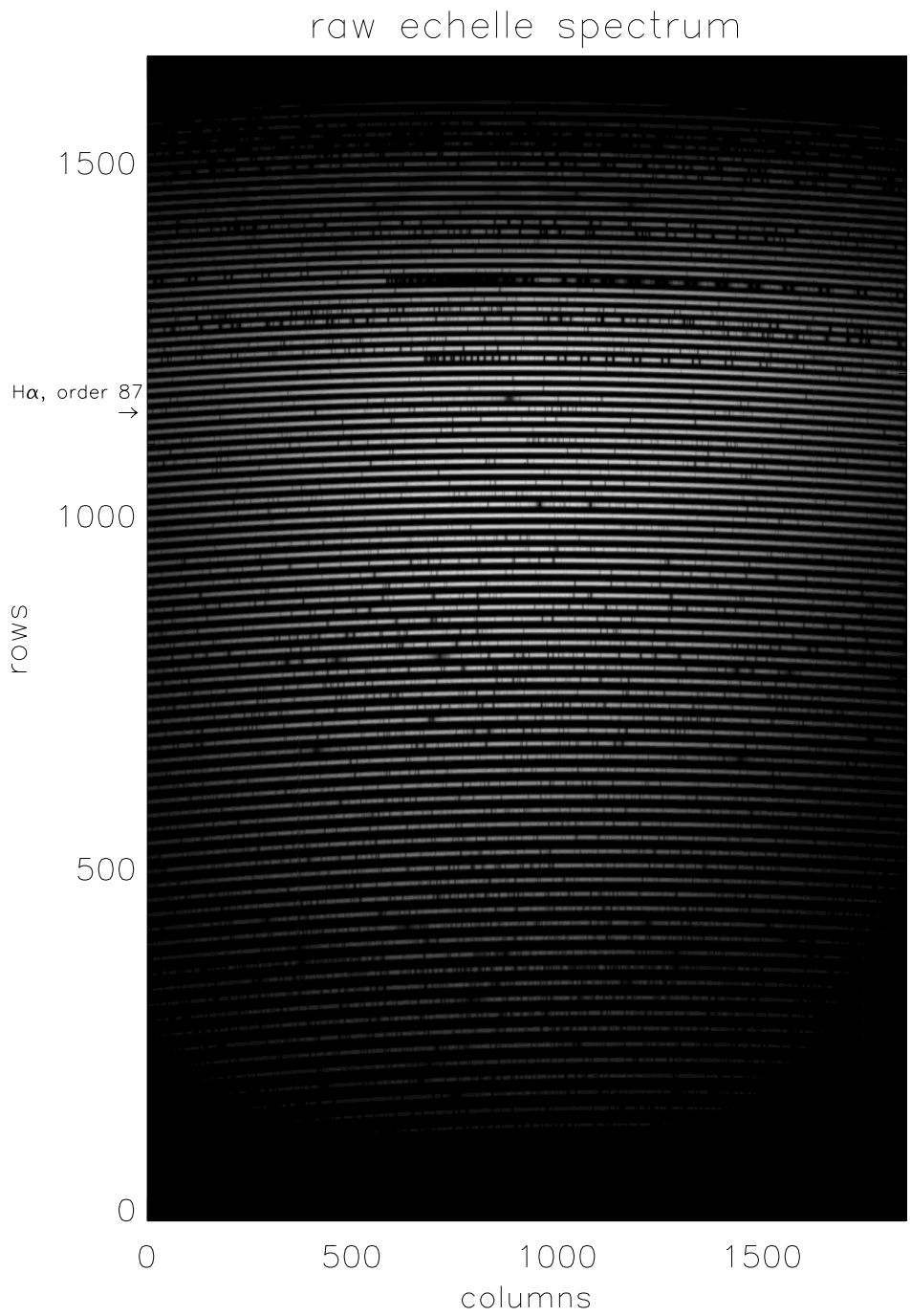

Figure 6.4: Raw echelle spectrum of the Sun. Absolute order 87 where Hα is located almost in the center is indicated by the arrow.

Chapter 7

—

Profiles of strong permitted lines in Classical T Tauri stars

We analyse the spectra of 30 T Tauri stars observed with the Hamilton echelle spectrograph. The line profiles are shown in Fig. 1 and the journal of observations in Table 1 of Paper 4 of Chapter 11. One goal is to test magnetospheric accretion model predictions. Observational evidence previously published supporting the model, such as emission line asymmetry and a high frequency of redshifted absorption components, are considered. We also discuss the relation between different line forming regions and search for good accretion rate indicators.

7.1 Equivalent widths and profile decomposition

We first measured the equivalent width of all the lines presented in Paper 4 of Chapter 11 that could be reliably identified. The results are presented in Table 1 of that paper and will be used in the following sections to study the relations between "fluxes" (veiling corrected equivalent widths) from different lines and between "fluxes" and parameters such as the mass accretion rate.

The line profiles were also decomposed with a multiple gaussian procedure based on the Marquardt method, so that we could also study correlations between line components. Most of the lines were very well fitted by 1 or 2 gaussians and only

sometimes required a third component. Some exceptions are the flat topped profiles of T Tau, SU Aur and DE Tau that are clearly non-gaussians (see Fig. 1 of Paper 4 of Chapter 11). The fitting procedure was not always straightforward, since some lines are contaminated by non-stellar emission, some are blended by other lines and some can be fitted with more than one gaussian combination (like 2 emissions instead of 1 emission and 1 absorption, for example). We explain below how we dealt with those problems.

The Hα line often exhibits a double peaked profile which was, in most cases, better fitted by a broad emission and a blue absorption than 2 emissions. The Hα wings are not steep and seem to belong to a very broad emission line rather than to 2 narrow ones. It is often possible to confirm that a true absorption is present by looking at the upper Balmer lines where the feature is enhanced relatively to the emission and dips below the continuum.

The Na D lines are strongly contaminated by the vapor lamps of the city of San Jose but our decomposition procedure was able to reliably subtract that contamination with a simultaneous gaussian fit while decomposing the line profiles.

The Ca II infrared triplet (IRT) and He I (λ5876) lines exhibit profiles typically with narrow and broad emission components; some lines show only one of the components. In some Ca II lines the narrow component is present inside a photospheric absorption core and, in that case, the emission-line equivalent width was measured considering the base of the absorption core as the continuum at 1. The Ca II IRT lines are also blended with a Paschen emission line that has usually strengths less than 20% of the IRT, as also noted by Hamann & Persson (1992). Whenever the Ca II lines are weak or narrow, the Paschen contamination is significant and has been extracted from the equivalent width measurements.

Finally, the Fe II equivalent widths were only measured when the line was in strong emission and could surely be distinguished from the lines nearby.

7.2 Veiling

The veiling (V) is the excess UV and optical continuum produced in the accretion shock. When normalizing the stellar spectrum to unity, the effect on an absorption line of adding the veiling, defined as a fraction of the stellar continuum, is to change the normalized profile to

$$P' = \frac{P + V}{1 + V}, \tag{7.1}$$

where P is the normalized unveiled line profile and P' is the normalized veiled one (Fig 7.1 and Basri & Batalha , 1990). A veiled spectrum will therefore present shallower lines than an unveiled spectrum.

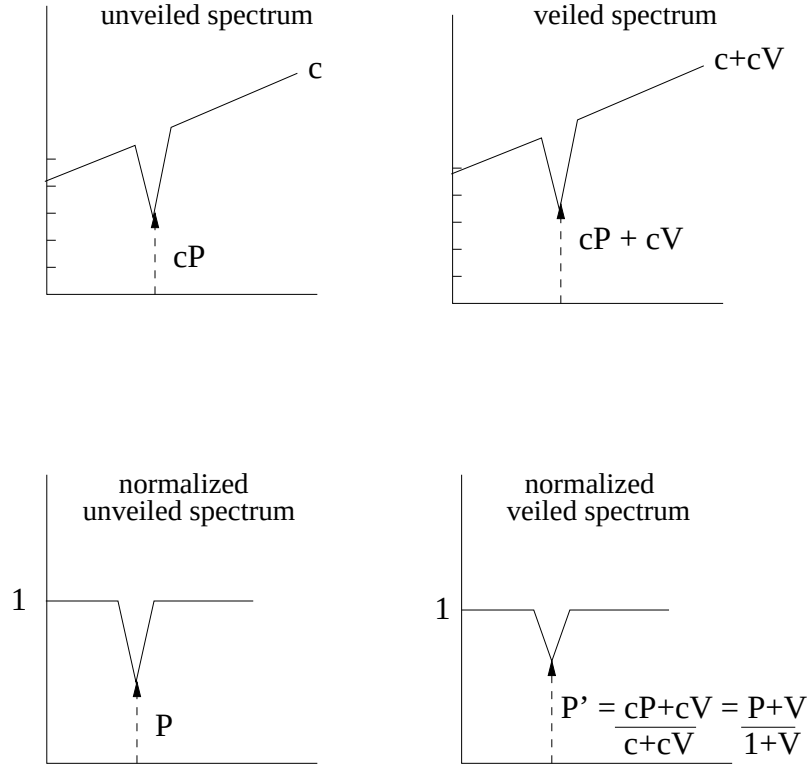

Figure 7.1: The effect of adding veiling on an absorption profile. c is the stellar continuum and V is the veiling. On the left side we show the normalization of an unveiled spectrum and on the right side the normalization of a veiled one. The absorption line appears shallower in the normalized veiled spectrum than in the unveiled one ($P' > P$).

The line equivalent widths obtained are contaminated by the variable continuum against which they were measured. They need to be corrected for the veiling in order to represent a true emission strength that can be regarded as a "flux" measurement. Some of our spectra have measured veilings in previous papers (Basri & Batalha , 1990; Johns-Krull & Basri, 1997) but in order to be consistent we decided to measure all the veilings again. The new values are presented in the last columns of Table 1 of Paper 4 of Chapter 11 and the common measurements agree, within the errors, with the previously published ones.

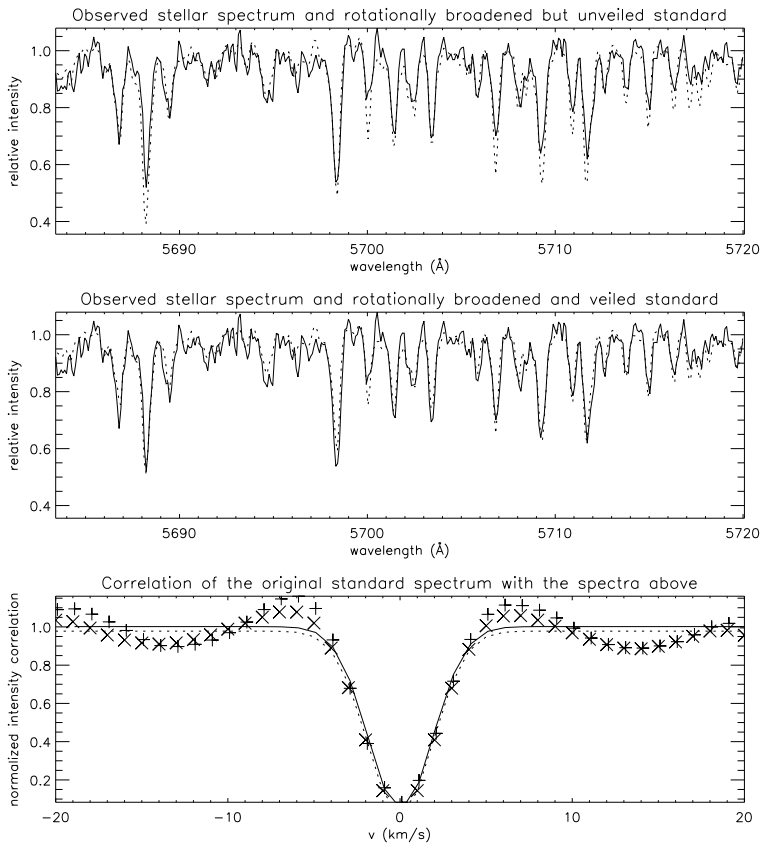

Figure 7.2: Veiling determination process. In this figure we have the CTTS AA Tau (solid line) and VA 622 (dotted line) as a standard. Top pannel: the standard spectrum is rotated to the same velocity as the CTTS. Middle pannel: the standard spectrum is rotated and veiled to match the CTTS spectrum. Bottom pannel: the symbols represent the cross-correlation function of the original standard spectrum with the rotated and veiled standard spectrum and with the CTTS spectrum. The lines are gaussians adjusted to them.

In order to calculate the veilings we chose spectral orders with many photospheric absorption lines both in the blue and red settings. The red orders correspond to the wavelength ranges 5557Å$< \lambda <$ 5642Å and 5668Å$< \lambda <$ 5755Å and the blue orders to 4571Å$< \lambda <$ 4641Å and 4763Å$< \lambda <$ 4836Å. The idea is to compare the spectrum of a CTTS with that of a standard star with the same spectral type that has been broadened to the CTTS rotational velocity and veiled. The choice of suitable standard stars is important and we followed, whenever possible, the suggestion of Basri & Batalha (1990) to use the Hyades dwarfs as reliable standards.

We also used the standard and CTTS spectral types determined by them.

We first rotationally broadened the continuum normalized spectrum of the standard star (Fig. 7.2, top) and then applied the veiling to the standard's spectrum (Fig. 7.2, middle), comparing it with the observed CTTS spectrum until a good match was found. The best adjustment was determined by eye, but a unique veiling value did not perfectly match all the photospheric lines and the results presented correspond to a mean value obtained with all the lines in the selected orders. The errors in the veiling determination are bigger for the higher veiling values, as the photospheric lines of highly veiled stars are extremely shallow and hard to match. Typically we have errors of 0.1 for veilings smaller than 1.0 and up to 0.5 for the higher ones. Most of the rotational velocities were taken from Basri & Batalha (1990), although we verified them by checking the match between the FWHM of the cross-correlation normalized profiles of the original standard with the CTTS spectra and of the original standard with the broadened and veiled standard (Fig. 7.2, bottom).

The veiling values obtained are used to search for correlations between veiling corrected line equivalent widths, defined as in Johns-Krull & Basri (1997):

$$W_{\rm eq}^{0} = W_{\rm eq}(V+1), \tag{7.2}$$

where $W_{\rm eq}$ is the measured equivalent width and V is the veiling.

7.3 Line Strengths

The study of the correlations between the "fluxes" of different lines is an important tool that gives insight on the relations between different line formation regions. Correlations can indicate common forming regions, but can also mean that a common process is affecting both regions at the same time. In this section we discuss the correlations that appear and also those that do not in our data.

The Balmer lines emission components are well correlated with each other, as are the IRT lines with each other, which is expected as they should be formed in regions with the same physical characteristics. The difference between them should arise mainly due to differences in line optical depths. The reality of a correlation can be estimated calculating the linear correlation coefficient and the false alarm probability (FAP) that the correlation occurs just by chance (Bevington, 1969; Johns-Krull & Basri, 1997). In the Balmer lines case, the correlation seems to decrease as we compare lines that are further apart in the series, e.g. Hα and Hβ show a strong correlation with each other (Fig. 7.3, top) with a false alarm probability of 3.24×10^{-7},

but Hα and Hδ do not (FAP=0.168). This behavior is biased by stars with strong wind contribution, where the emission component is sometimes almost absent due to large absorption components and/or a hot underlying photosphere. Eliminating those stars the good correlations are partially recovered (Fig. 7.3, bottom), the FAP of the Hα and Hδ emission components decreasing to 3.55×10^{-4} and presenting a linear correlation coefficient r=0.880.

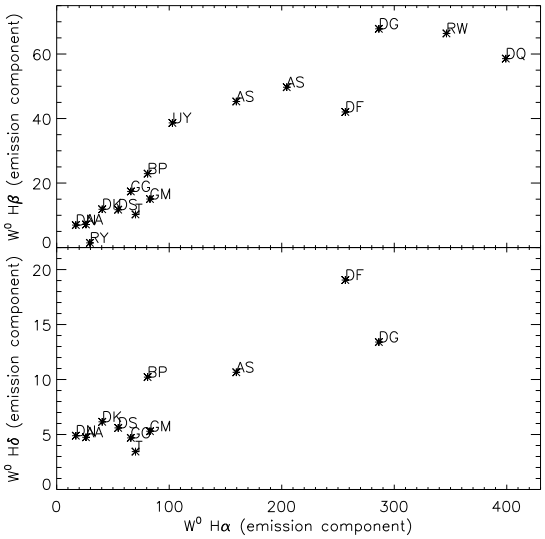

Figure 7.3: Veiling corrected equivalent widths of the emission components: $W^0_{\mathrm{H}\alpha}$(Å) vs. $W^0_{\mathrm{H}\beta}$(Å) and vs. $W^0_{\mathrm{H}\delta}$(Å).

The entire Hα and He I lines are also well correlated (Fig. 7.4 ; FAP=1.26×10^{-6}), except for DQ Tau which has a very high Hα equivalent width in the outburst spectra we chose and CW Tau which has a high uncertainty in the veiling measurement (we get FAP=4.65×10^{-10} without DQ Tau and CW Tau). The same kind of correlation is verified with Hβ, but Hγ and Hδ do not show a well defined correlation with He I. The apparent lack of correlation with Hγ and Hδ may be due to the small number of spectra where those lines could be reliably measured and the lower S/N present in our spectra in that region. Apart from the correlation with the entire lines, we also verified some good correlation between the Hα emission component and the He I broad component (BC, FAP=4.68×10^{-4} with DQ Tau and CW Tau and FAP=8.32×10^{-6} without them). The He I line is believed to form in high

temperature regions (20,000K to 50,000K) and together with the large width of its BC it suggests that the BC comes either from the highly turbulent shock region or the magnetospheric flow, where the broad emission component of the Balmer lines is also supposed to be formed. Due to their larger optical depths, the Balmer lines probe a much larger volume of gas than the He I lines, but the correlations between the entire lines and the components show that their formation regions are strongly related to each other.

Also thought to be formed in the accretion flow because of its large widths and blueshifted center, the broad IRT component does not strongly correlate with the He I BC (FAP=1.97×10^{-3} and r=0.678 for λ8498) or with the Hα emission (FAP=6.12×10^{-3} and r=0.590 for λ8498). For the He I BC, no correlation is found for small equivalent width values and a tendency for the equivalent widths to increase together exists, although with much scatter. For the Hα, however, a correlation seems to exist except for the higher Hα "flux" values (where the scatter is really large). Although the Ca II line is formed at much lower temperatures, it is expected to strongly correlate with Hα and He I if the accretion flow is sufficiently organized that a global change in accretion rate is felt by all diagnostics.

Batalha *et al.* (1996) showed that the narrow components (NC) of CTTSs have a flux excess when compared to the WTTSs and this was attributed to the reprocessing of radiation produced in accretion shocks as the accreting material hits the stellar atmosphere. However, neither the He I NC nor the Ca II NC correlate with the Balmer emission, which implies that although both the NCs and the Balmer lines are related to accretion, they are probably probing regions that are far away from each other and consequently not equally influenced by the same physical processes, or the time delay for changes that affect one region to reach the other is too large for the changes to show up in simultaneous spectra of both components.

We also confirmed the trend noticed by Batalha *et al.* (1996) that the IRT and the He I NCs are positively correlated (Fig. 7.5 and FAP=1.41×10^{-5}), (unsurprisingly, since we have a lot of data in common), while Muzerolle *et al.* (1998a) found that they were uncorrelated. Those lines are generally thought to sample quite different temperature regions – the He I is formed in high temperatures ($> 20,000$K) while the IRT is a chromospheric line formed at $4,000\text{K} < \text{T} < 7,000$K. The correlation found is probably related to the excess emission due to the influence of the accretion shock on the stellar atmosphere, a common feature in both of them.

Another important aspect of the correlation measurements is the quest for good accretion rate indicators that would later provide an easy way to obtain these rates for other stars. Using the mass accretion rates in Hartmann *et al.* (1998), there is a very good correlation between the IRT veiling corrected equivalent widths (Ca

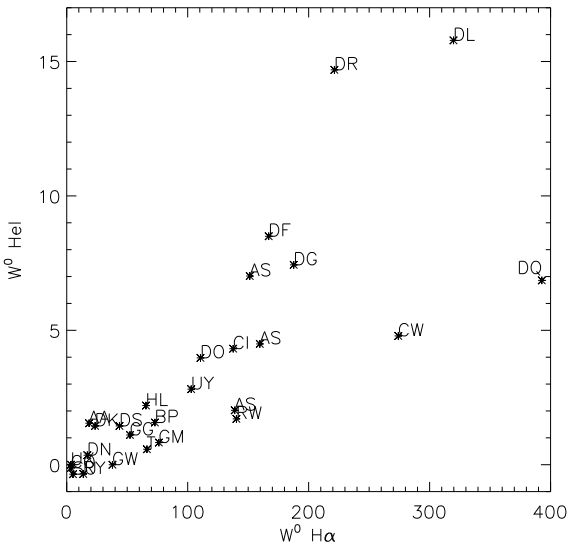

Figure 7.4: $W^0_{\rm H\alpha}$(Å) vs. $W^0_{\rm HeI}$(Å).

II λ8498 and λ8662) and mass accretion rates (Fig. 7.6 (top) and FAP=1.80×10^{-4}), as in Muzerolle *et al.* (1998a) for Ca II (λ8542). The only exception is DQ Tau, that has a $\log \dot{M} = -9.4\ M_\odot {\rm yr}^{-1}$ according to Hartmann *et al.* (1998) but $-7.3\, M_\odot {\rm yr}^{-1}$ according to Hartigan *et al.* (1995) (the largest discrepancies between their values). DQ Tau is known to have a variable accretion rate that depends on the orbital phase of the binary system and on events such as outbursts that may occur when the stars approach each other (Basri *et al.*, 1997). We decided not to use this star.

The Balmer lines and their components are also correlated to the mass accretion rates (Fig. 7.6, middle and bottom, with FAP=3.40×10^{-4} and 7.09×10^{-3} respectively). The results for the absorption component are not as reliable as the others, mainly due to the small number of stars that exhibit a clear absorption and for which there are published mass accretion rates. The "flux" of the emission and absorption components increases as the accretion rate increases, showing that the accretion may be powering both the emission and the outflow. This would be consistent with theoretical results (Shu *et al.*, 1994) that suggest that the wind mass loss rate and the disk accretion rate are directly proportional (but see below for caveats).

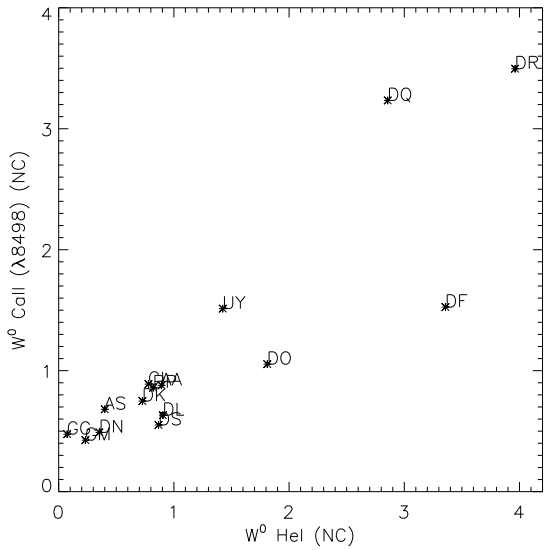

Figure 7.5: $W^0_{\rm HeI}$(NC) (Å) vs. $W^0_{\rm CaII(\lambda 8498)}$(NC) (Å)

7.4 Evidence for Outflows

Winds are expected to be present in CTTS and help carry away angular momentum. If cool, they should appear mainly as absorption components. Due to the presence of the disk the absorption is expected to be blueshifted, the receding part of the wind is blocked by the disk from the observer's line of sight. The emission components of CTTS were thought for some time to be produced in optically thick winds, but these models also generated upper Balmer line profiles with very deep absorptions that were not consistent with observations.

The Balmer and Na D blueshifted absorption components are the most clear evidence in our data that a strong wind is present in our sample of CTTSs. Almost 80% of our stars show blueshifted absorption components in at least one line, the most common being Hα. The number of blueshifted components decrease as we look at the upper Balmer lines, appearing only in $\sim$ 35% of the Hδ profiles (where they tend to be weak). This suggests that the blueshifted absorptions arise from a region that is optically thin at least in the upper Balmer lines, and distinct from the emission component that is believed to arise mainly in the optically thick accretion flow. Some stars, like DR Tau and AS 353, present P Cygni profiles in all the Balmer

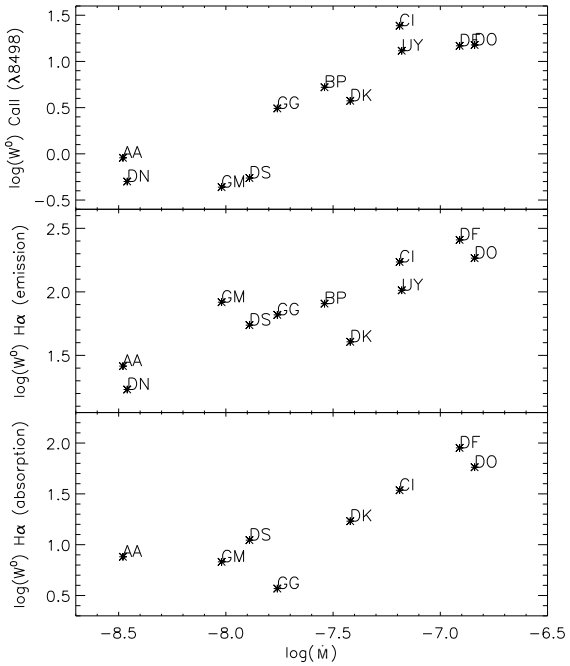

Figure 7.6: $\dot{M}$ ($M_{\odot}yr^{-1}$) vs. $W^0_{\mathrm{CaII}(\lambda 8498)}$ (Å) and vs. $W^0_{\mathrm{H}\alpha}$ (emission and absorption components) (Å).

lines. These are normally associated with strong winds, and other stars, like CO Ori, RW Aur, SU Aur and RY Tau, have such a strong absorption component that it sometimes suppresses the emission in the upper Balmer lines of the stars with the hottest underlying photospheres. A number of these stars are known to be jet sources.

The 8 stars in our sample that exhibit blueshifted absorption components in the Na D lines (presumably indicating high mass loss rates; Hartmann , 1998), also do in Hα. The lack of P Cygni profile in the Na D lines does not necessarily mean low mass loss rates, as the star may present a deep photospheric absorption that prevents the detection of the blue absorption due to the wind (Natta & Giovanardi , 1990). Due to the difference in their optical depths, the Balmer and Na lines will sample different wind volumes. As resonance lines, the sodium probes the coolest part of the wind. The blueshifted components of both lines tend to be centered

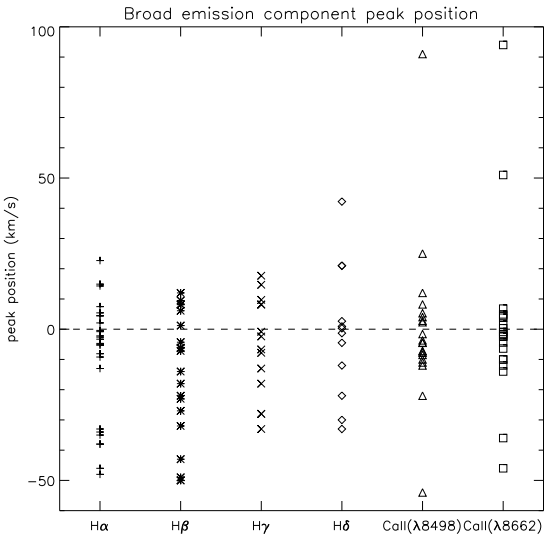

Figure 7.7: Blueshifted absorption component's peak position.

at approximately the same velocities, likely meaning that different wind regions share some common kinematic component. The Na D blueshifted absorptions bear no other resemblance to the Hα ones, being much weaker in intensity and width. The position of blueshifted absorption centers in these lines vary from star to star, suggesting that the wind velocities can occur with a wide range of values (from 0 to –270 km s^{-1} in our sample, see Fig. 7.7). There may well be projection effects that must be taken into account; these would imply that the outflow is not spherical.

After decomposing the profiles, we can also investigate the correlations that appear between different wind components and between wind components and other features, in order to better understand the wind forming region. The Hα and Hβ blueshifted absorptions are very well correlated (FAP=2.39×10^{-8}), showing that they both probe the same wind region, and although there is apparently no correlation with the blueshifted absorptions of Hγ and Hδ, this may be due to the small number of observations where Hγ and Hδ present blueshifted absorptions. Where the absorption does appear in the upper lines the wind component is often very weak and consequently hard to fit.

The Hα and Hβ blueshifted absorptions also show some correlation with their line's emission components: the stronger the emission, the stronger the absorption.

Unfortunately, that does not have a unique interpretation. One possibility is that the same mechanism that is powering the emission is also powering the wind in the sense that, when more material is accreted there is more to outflow. This is predicted by the accretion model and also means that the absorption region is outside the emission region. A second possibility is that, if both emission and absorption were formed in winds, the absorption component would be due only to the decay of the source function in the outer regions of the atmosphere and not to the accretion itself. If the first possibility is correct, this relation could also explain the trend seen between the Hα emission and absorption components and the mass accretion rates.

Finally, the present result may also be an effect of line optical depth; if the wind is optically thick the central depth of the blueshifted absorption is fixed and the changes that appear are in fact only due to the emission component variations, as shown by Johns & Basri (1995b) in the case of SU Aur. Johns-Krull & Basri (1997) also found that the Hα absorption and emission strengths of many DF Tau spectra were correlated and that the absorption component strength correlated with the veiling.

A curious fact about the absorption components can be noticed in the stars that show an absorption component in the 4 analysed Balmer lines. This component tends to be shifted towards the red as we go from Hα to Hδ and in Fig. 7.8 we plot the absorption centers vs. the Balmer lines oscillator strengths for those stars. It seems that we may be seeing the acceleration of the flow. This shift of the absorption component can also be noticed in Edwards *et al.* (1994) in the residual profiles of DK Tau and in Appenzeller *et al.* (1988) in the DR Tau spectra, showing that this behavior may be quite common among CTTSs.

Another feature that is associated with strong activity, presumably both inflow and outflow, are the iron lines in strong emission. These lines are often in absorption in our sample, but Fe II (λ4923) is also found in emission in $\sim$ 40% of our stars. When this happens, a wind component is present at least in Hα, sometimes also in the other Balmer lines and in the Na D lines, and the IRT lines always show a BC. The Fe lines in emission seem to be related to both the presence of outflow and high veiling, as some stars that show blueshifted absorption in Hα but no BC in the IRT do not present Fe II (λ4923) in emission. DG Tau, AS 353 and RW Aur, that also exhibit Fe I (λ6192) and Fe II (λ4352) in strong emission, also have associated jets (Edwards *et al.*, 1994; Mundt & Eislöffel , 1998). The iron lines when in emission are centered at the stellar rest frame. They are probably not produced in the outflow (wind or jet), since the occultation of the receding part of the flow by the disk would yield a blueshifted line as observed in the case of forbidden lines. The forbidden lines originate in metastable transitions in low density regions far

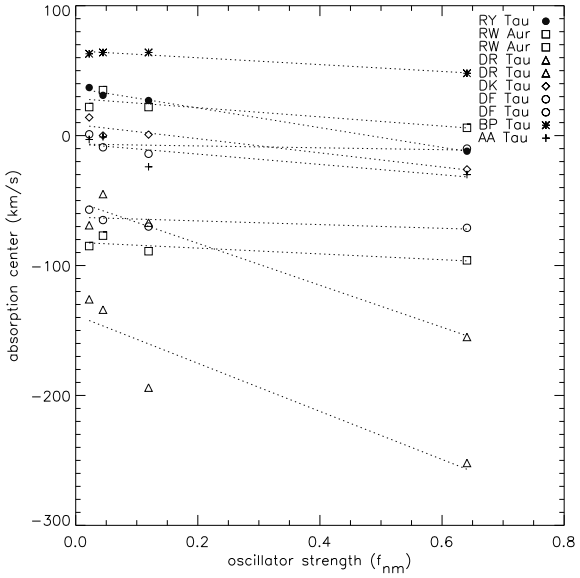

Figure 7.8: Balmer line absorption center vs. oscillator strength. RW Aur, DR Tau and DF Tau are plotted twice as 2 wind components were measured.

away from the star and often appear blueshifted due to occultation effects.

7.5 Evidence for Infall

Redshifted absorption components in the line profiles (inverse P Cygni profiles), can be the clearest spectral evidence that infall of material is occurring, and are naturally predicted by the magnetospheric accretion models. These models, however, require special conditions for the redshifted absorption component to be visible, such as low line thermalisation, low emission damping wings, and proper inclination values. The inclination dependence arises from the contrast of the line source function of the infalling gas and the continuum source function where the gas stream is projected (Hartmann *et al.*, 1994). If the projection is against the cool photosphere (low inclinations) no absorption is found, but if it is against the hot shock material, like a ring or spots, (higher inclinations) the absorption can be produced.

Edwards *et al.* (1994) presented an analysis of 15 CTTSs included in our sample, and showed that 87% of their stars had redshifted absorption components in at least one line at $\sim$ 200 to 300 km s^{-1}, a range of velocities that is consistent with the

ballistic infall predicted by the magnetospheric models for a typical CTTS. Only $\sim$ 40% of our stars have redshifted absorption components in at least one line, and generally not at $\sim$ 200 to 300 km s^{-1}. BP Tau, for example, shows redshifted absorption in many lines at $\sim$ 50 km s^{-1} and UX Tau has a strong redshifted absorption in Hα at 43 km s^{-1}. The difference in the absorption centroid position of the stars from the values predicted by the models could partially be due to inclination effects. The difference in the number of redshifted absorption occurrences found in the two different analysis could be due to the fact that Edwards *et al.* (1994) analysed residual profiles instead of the original ones. This gives, according to them, a high sensitivity in defining features such as the Balmer lines wings, where the redshifted absorption lies. However, in the residual profiles showed by Muzerolle *et al.* (1998a) of 11 CTTSs, redshifted absorption at typical free-fall velocities can be found in less than half of their sample, which is more in agreement with the predictions of the magnetospheric accretion models.

In order to compare our results with the ones cited above we decided to generate residual profiles from our sample, choosing 8 lines commonly found in emission: Hα, NaD, He I, CaII (λ8498 and λ8662), Hβ, Hγ and FeII (λ4352). Hδ was excluded as most of our spectra present low signal to noise in that region, making it hard to obtain reliable information about small absorption features. We generated the residual profiles by subtracting from each observation a broadened and veiled standard spectrum, using as standard stars the ones previously selected for the veiling calculations.

Although the residual method often enhances features like weak emission lines (see Fig. 7.9, top), care must be taken during the subtraction, as a small difference in continuum normalization between the two spectra can also introduce false features. The uncertainty in the veiling determination and the difficulty of choosing suitable standard stars are other factors that can introduce errors in the process.

The residual profile calculation suppresses, in principle, all the photospheric contribution that is present in the spectra, generating smoother profiles, as the broad lines are no longer superimposed with narrow absorption ones. However, we noticed that it did not a priori enhance the redshifted absorptions present in our unsubtracted spectra; indeed some of the redshifted absorption components turned out to be mainly photospheric (for example, the Na D lines of BP Tau, DF Tau, DQ Tau and RY Tau, see Fig. 7.9, bottom). In general, most of the redshifted absorptions became shallower, although less noisy, and we did not find many new ones. Our residual profiles show that $\sim$ 50% of our stars present at least one line with a redshifted absorption component, a result in agreement with the original (unsubtracted) data, with the magnetospheric models, with the results by Muzerolle

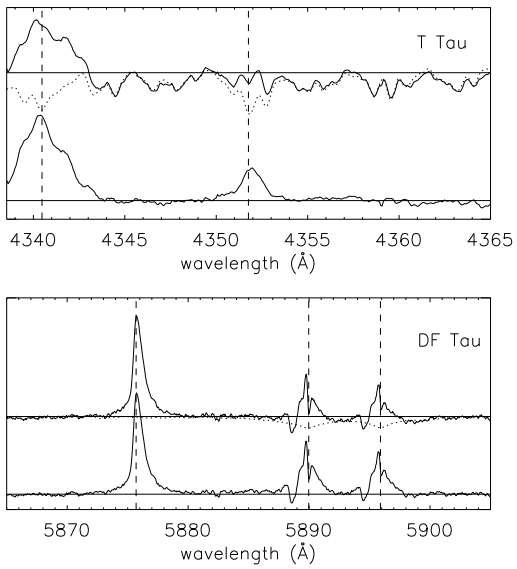

Figure 7.9: Residual profile determination, the thin solid line corresponds to the original spectrum, the dotted line to the standard spectrum and the thick solid line to the residual CTTS profile. Top: Fe II (λ4352) is dramatically enhanced by the residual method. Bottom: the redshifted absorption that appears in the unsubtracted spectrum in the Na D lines turns out to be mainly photospheric.

et al. (1998a) but not with Edwards *et al.* (1994). Although very weak features such as the iron emission lines and the redshifted absorptions at free-fall velocities are strongly affected by the underlying photospheric spectrum, one may notice that the general characteristics of the line profiles discussed in this work are weakly affected by the subtraction of the photospheric features, and that our results are also valid for residual profiles.

Finally, in agreement with both the model predictions and with Edwards *et al.* (1994), we see less evidence of redshifted absorption in Hα at high velocities than in the upper Balmer lines, probably due to thermalisation effects and the Stark damping of the Hα wings.

7.6 Profile Symmetry

The magnetospheric accretion models predict that the BC emission is formed in the magnetospheric infalling material. It should, then, exhibit a central or slightly blueshifted peak and blueward asymmetry due to occultation, by the disk and the star, of part of the flow moving slowly away from the observer. By blueward asymmetry we mean that there is an excess of blue emission compared to the red emission. Some theoretical profiles published by Hartmann *et al.* (1994) also show redshifted absorption at free-fall velocities, while others show extended red wings caused by the occultation of the high velocity blueshifted material by the star; both effects add up to enhance the line asymmetry.

One way to search for asymmetries is to reflect one of the line wings about the broad emission centroid, as done by Johns-Krull & Basri (1997) for DF Tau. If the wings match each other, the line is considered symmetric, and this avoids a confusion between lines that are only shifted and lines that are really asymmetric. P Cygni profiles are more difficult to evaluate, since the blue emission wing is sometimes completely absent and it may be hard to determine the correct shift to be applied.

The BCs that showed blueward asymmetry comprise only $\sim 20\%$ of the analysed lines. Most of the BCs are symmetric (well fitted by a Gaussian) and $\sim 75\%$ of them have a central or slightly blueshifted peak. In Fig. 7.10 we show the velocity position of the broad emission peak for several lines and we notice that, although most of them are indeed blueshifted, a substantial number present a redshifted peak. This is not seen in the published theoretical magnetosphere profiles. Lines with P Cygni profiles and those where the emission component was not reliably extracted are not included in this plot.

Among the lines that presented asymmetries, some have symmetric low velocity material and a blueward excess of high velocity emission, and others show redward asymmetries. Neither type is predicted by the magnetospheric model. Some lines however do present profiles with the characteristics described by the magnetospheric models. Examples of profiles in agreement and opposite to the magnetospheric symmetry predictions are shown in Fig. 7.11 with the reflected wings overplotted.

Each Ca II IRT line is blended with a Paschen emission line and this could lead to a wrong asymmetry classification. However, from the thirteen stars that presented IRT asymmetries only four could be due to the Paschen contribution, which affects the high velocity wing redward of the line center.

In general the symmetry predictions of the magnetospheric model cannot be strongly confirmed with our sample. Contrary to them, most of the BCs are found to be symmetric; among the asymmetric ones many are not blueward asymmetric,

and $\sim 20\%$ of the broad emission components present centroids redshifted by more than 5km s^{-1} .

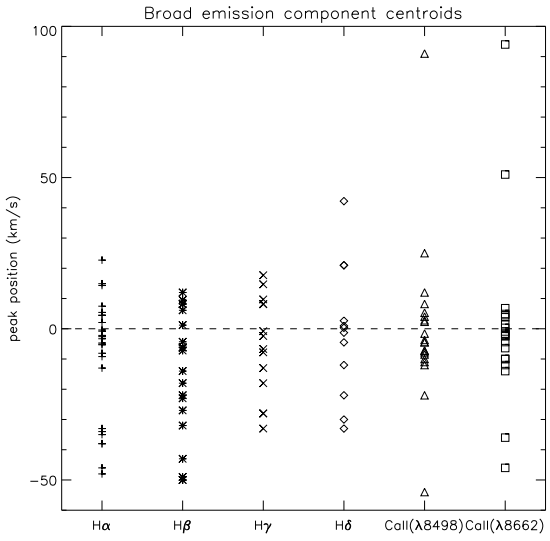

Figure 7.10: Broad emission component's peak position. Lines with P Cygni profiles and those not reliably measured are not included.

7.7 Discussion

Many aspects of the line formation of a CTTS can be inferred from the correlations found with the veiling corrected equivalent widths in the previous sections.

We showed that lines coming from a common lower level are very well correlated, like Hβ with Hα and the IRT lines with each other. This is expected, as they need the same physical conditions to be produced and tend to be affected by the same physical processes. As previous studies also showed, most lines have more than one component (BC and NC for the He I and the Ca II and emission and absorption components for the Balmer and Na D lines). These are likely formed in distinct regions, as the characteristics of those components are very different from each other throughout our sample and many correlations found were valid for one of the components but not for the other. According to our data the Balmer emission, the

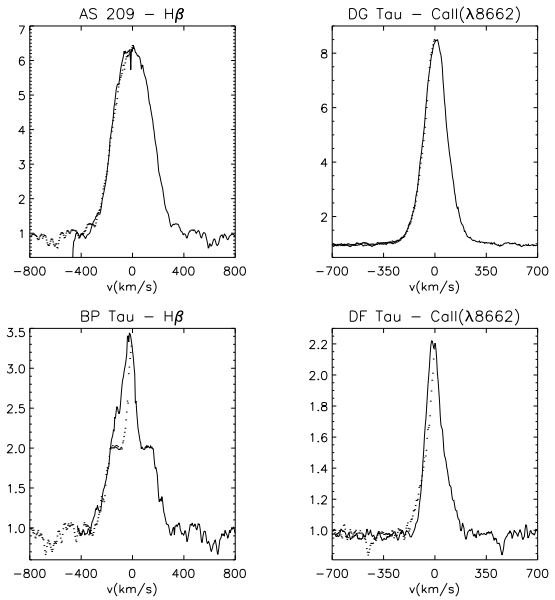

Figure 7.11: Emission lines with the red wings (dotted lines) reflected. The top lines are symmetric and the bottom ones are asymmetric and in agreement with the magnetospheric model predictions.

He I BC, the IRT BC and the iron lines (when in strong emission) are mainly formed in the magnetospheric flow due to the correlations they exhibit. Alternatively, the He I BC may also come from the shock region, where the temperatures are high and more appropriate for the formation of that line instead of the magnetospheric flow itself. The NCs of the Ca and He I lines are thought to be formed at the stellar surface where it is perturbed by the infall of material and partly in the normal stellar chromosphere. The wind is the origin of the blueshifted absorption commonly seen in the Na D and Balmer lines.

We also verified that the effect of accretion on the line components sometimes probably produces the correlations, as lines formed in regions with physically distinct properties (very different temperatures, for example) but both affected by accretion can be found to correlate very well, like the He I and the IRT NCs.

Somewhat puzzling is the lack of strong correlation between the IRT BCs and the Hα emission or the He I BCs, if all broad emission lines are supposed to share a common forming region. Johns-Krull & Basri (1997), analysing DF Tau, confirm the lack of correlation found between the IRT BC and the Hα emission, but they

found a correlation between the He I BC and the IRT that neither we nor Muzerolle *et al.* (1998a) confirm in our samples of various CTTSs.

We showed that the IRT lines and Hα are good mass accretion indicators in our sample. We also confirmed that the same mechanism that powers the accretion also seems to influence the outflow, as the emission and absorption components of Hα are well correlated both with the mass accretion rates and with each other. Other good evidence for the accretion-wind connection is that the Fe lines in strong emission seem to be related to both processes, occurring when the wind and the veiling are prominent.

The blueshifted absorption components are thought to be formed in low density winds. There is strong evidence that the NCs are formed at the stellar surface (Batalha *et al.*, 1996). Although they are both influenced by the accretion process, they should not be compared to the theoretical magnetospheric profiles.

Some of the observations tend to support the fact that the accretion affects the relatively quiet stellar atmosphere, and lines produced in that region suffer the influence of such changes. The models also predict that accretion and outflow should be related to each other – the former occurring through closed magnetic field lines that connect the disk to the star and the latter through the open field lines escaping from the disk itself.

However, the results presented in the previous sections show, also, that some of the general characteristics of the magnetospheric accretion models are not always confirmed by our data. The idea that the broad emission components mainly arise from a common emitting region, the infalling magnetospheric gas according to those models (Hartmann *et al.*, 1994), must be taken with care, as the observational evidence is not yet conclusive. We must also keep in mind that the magnetospheric predictions do not do particularly well for the broad emission components that they primarily apply to. We find observed profiles to be generally fairly symmetric with centroids distributed through a range of blueshifted to redshifted velocities. Sometimes they have redshifted absorption components, but often not at free-fall velocities. Only about 20% of the BC profiles support the specific predictions of the models.

Hartmann *et al.* (1994), Muzerolle *et al.* (1998b) and Muzerolle *et al.* (1998a) presented line profiles generated with magnetospheric models and compared them with observational ones. They obtained good agreement between the observed and theoretical profiles of many lines for some stars, like BP Tau. But comparing their BP Tau observed profiles to ours, many differences can be seen. This is expected, as CTTSs are known to exhibit line profile variability sometimes even within a few hours (Johns & Basri , 1995a), and Gullbring *et al.* (1996) showed that this is the

case for BP Tau, a typical CTTS. The problem that arises with the rapid profile variation is that, even if the magnetospheric models can reproduce one of the profile types of a star, it does not mean that all the profiles that a line may exhibit will be reproduced without changing basic model characteristics. As an example, the model used to compare the observed and theoretical profiles of BP Tau cited above does not fit our observations of that star well.

Some years ago, Shu *et al.* (1994) proposed a new version of their X-celerator mechanism whose natural period was the rotational period of the star. Lines formed in magnetospheric accretion flows that are controlled by the stellar field might, also, show periodicity at the stellar rotation period in the presence of an inclined dipole field. In this case, the line variations would certainly be due to geometrical effects, and a model with the same basic parameters should be able to describe the various line profiles. SU Aur presented this kind of variations in Hβ and Hα (Johns & Basri, 1995b), but unfortunately its profiles do not resemble the published theoretical ones very much.

In general, however, the line variations do not seem to be related to orbital motion, as they do not usually correlate with the stellar rotational period. Different parts of a line may vary differently, as Johns & Basri (1995a) showed by analysing time variations of Hα for several CTTSs. They suggest the line emission region is composed of discrete, stochastically varying blobs with a range of velocities and turbulence, which the Sobolev treatment used in the actual magnetospheric models does not take into account.

Najita *et al.* (1996), analysing Brγ emission profiles, showed that WL 16, an obscured low-luminosity YSO, presented profiles that were remarkably similar to the theoretical Balmer line calculations by Hartmann *et al.* (1994). Later, Muzerolle *et al.* (1998b) calculated profiles for the Brγ emission and showed that, in fact, the WL 16 Brγ emission line was very well reproduced. However, some of the stars in the sample of Najita *et al.* (1996) also present very symmetric emission profiles, like AS 353, DG Tau and SVS 13, that cannot be explained only by magnetospheric accretion. Although the magnetospheric model can generically explain part of the large line widths and the occasional redshifted line absorptions, it does not predict symmetric profiles, because the magnetospheric infalling material is subjected to occultation effects by the star-disk system.

Most of our broad emission profiles were found to be symmetric, and the few asymmetries occur on both the blue and the red side. Due to these differences, the profiles presented in the theoretical papers generally do not match our observed ones. Many authors have speculated on the origin of the rather symmetric broad line wings in TTS profiles. Basri (1990) suggested that the wings were formed in

a turbulent region near the star and Edwards *et al.* (1994) pointed out that Alfvén waves could generate the necessary turbulent broadening. Johns & Basri (1995b) managed to reproduce some of the Balmer line symmetric features of SU Aur by adding a range of turbulent high velocity components at the base of spherically symmetric wind models, and Johns & Basri (1995a) could also fit the DF Tau wings with a similar procedure.

Most of the stars discussed here rotate slowly ($v \sim 10$km s^{-1}) at velocities that are much smaller than the velocities of the infalling material ($v \sim 200 - 300$ km s^{-1}), and the inclusion of rotation in the theoretical models will not significantly alter the profiles in this case. Even in the case of a stiff magnetosphere, material coming from a disk at $3R\star$ would have $v \sim 30$ km s^{-1} and would not influence the entire line. The addition of winds to the theoretical models will certainly change the line shapes but stars like AS 209 and DE Tau, that do not always exhibit blueshifted absorption and are rather slow rotators, will still need some further explanation of their broad symmetric line profiles.

Stark broadening may explain the low very broad far wings in Hα (Hartmann *et al.*, 1994; Muzerolle *et al.*, 1998b), but will not produce the main Gaussian shape commonly present in many different lines. A better treatment of the radiative transfer (actually done with the Sobolev method) could also alter the theoretical line profiles and would properly take into account Stark and opacity broadening effects.

Magnetospheric accretion probably does occur in CTTS. Evidence for it includes hot spots at the stellar surface of these stars, thought to be due to the magnetic accretion shock, redshifted absorption components at free-fall velocities that would be hard to explain without magnetospheric infall, as well as cases like SU Aur and WL 16, that give more explicit support to the theory. However, it may not be the only important mechanism. The symmetry of the line profiles and the lack of correlation of the variation among different line regions suggest that an important turbulent process may be occurring together with the magnetospheric infall.

7.8 Conclusions

We have presented the spectral analysis of a sample of CTTSs covering a wide range of optical wavelengths and veilings. We tested the predictions of the magnetospheric accretion model and previously published results supporting them. We confirm that many CTTSs exhibit central or blueshifted broad emission lines but a substantial minority show redshifted centroids. The accretion and outflow seem to be related

and redshifted absorption components are sometimes present in the spectra. We found that the analysis and interpretation of these is not straightforward. We could not reproduce the observational results that showed a very high frequency of redshifted absorption in the lines of CTTSs. We also show that most of our emission components are symmetric, instead of blueward asymmetric as predicted by the theory or suggested by previous observational studies. We saw that the broad components of different atomic lines are not strongly correlated to each other, while we would expect them to be if they were all formed in the accretion flow.

Our results do not refute the general magnetospheric accretion scenario, but rather indicate that is only part of the important processes which produce the strong permitted line emission in CTTSs. Our intent is to point out that the case has not yet been strongly made, and that much more observational and theoretical work is required. Part of the emission line profiles may also be produced in winds, and rotation and turbulence must be added to the models.

This work was published in the Astronomical Journal, Volume 119, Issue 4, pp. 1881-1900 (2000).

Chapter 8

—

The spectral variability of the Classical T Tauri star DR Tau

DR Tau is one of the best studied CTTSs. Its visual brightness increased in an outburst by several magnitudes in the early 70's (Chavarria-K. , 1979) and since then it has remained relatively bright ($V \sim$ 11-12) although extremely variable. It shows strong (1-3 mag) photometric variability attributed both to cool and hot spots (e.g. Bertout *et al.*, 1977; Bouvier *et al.*, 1993; Kenyon *et al.*, 1994; Ultchin *et al.*, 1997) and high veiling values in the optical (Basri & Batalha , 1990; Valenti , 1994). The photospheric absorption lines are almost absent and the continuum is dominated by the veiling radiation at optical wavelengths. DR Tau shows [OI] (λ6300) in emission with a double peak (Hartigan *et al.*, 1995; Hirth *et al.*, 1997) suggesting the presence of a collimated outflow. The star seems to exhibit quasiperiodic variabilities, several periods being reported from photometric and spectroscopic studies ranging from 4 to 9 days. It has strong emission lines that show a wide variety and variability of profiles (Appenzeller *et al.*, 1988; Guenther & Hessman , 1993; Johns & Basri , 1995a; Hessman & Guenther , 1997; Smith *et al.*, 1999).

We present the analysis of a sample of 103 spectra of the CTTS DR Tau, which span over more than a decade. The journal of observations is shown in Table 8.1. We intend to investigate the nature of the emission line region, to give insight on the relation between different line forming regions and to test the predictions of magnetospheric accretion models.

Table 8.1: DR Tau journal of observations. The blanks correspond to veiling values that could not be reliably measured.

Obs.	UT Date and Time	JD (-2400000)	Tel.	veiling
1.....	1989 Jan 03, 03:55	47529.664	CAT	
2.....	1989 Jan 03, 07:32	47529.812	CAT	
3.....	1989 Jan 17, 04:03	47543.668	3m	5.5
4.....	1989 Jan 17, 10:00	47543.918	3m	4.5
5.....	1989 Jan 20, 07:13	47546.801	CAT	
6.....	1989 Jan 21, 03:46	47547.656	CAT	
7.....	1989 Jan 22, 08:05	47548.836	CAT	
8.....	1989 Oct 07, 07:26	47806.809	CAT	
9.....	1989 Oct 07, 12:09	47807.008	CAT	
10....	1989 Oct 08, 07:31	47807.812	CAT	3:
11....	1989 Oct 08, 12:16	47808.012	CAT	3:
12....	1989 Oct 09, 06:58	47808.789	CAT	4:
13....	1989 Oct 14, 09:15	47813.887	3m	6.0
14....	1989 Oct 26, 08:56	47825.871	CAT	5:
15....	1989 Oct 26, 12:28	47826.020	CAT	
16....	1989 Oct 27, 05:43	47826.738	CAT	
17....	1989 Oct 28, 12:34	47828.023	CAT	
B 18....	1989 Oct 29, 11:49 B	47828.992	CAT	
19....	1989 Oct 30, 05:31	47829.730	CAT	4.9:
20....	1989 Oct 30, 12:32	47830.023	CAT	
21....	1989 Oct 31, 05:28	47830.727	CAT	
22....	1989 Oct 31, 11:42	47830.988	CAT	
23....	1989 Nov 01, 05:30	47831.730	CAT	
24....	1989 Nov 01, 12:38	47832.027	CAT	4:
25....	1989 Nov 02, 06:02	47832.750	CAT	4.5:
26....	1989 Nov 02, 12:24	47833.016	CAT	2.8:
27....	1989 Dec 01, 04:53	47861.703	CAT	
28....	1989 Dec 01, 11:21	47861.973	CAT	5:
29....	1989 Dec 02, 04:38	47862.691	CAT	
30....	1989 Dec 02, 11:11	47862.965	CAT	
31....	1989 Dec 03, 04:20	47863.680	CAT	5:
32....	1989 Dec 04, 04:23	47864.684	CAT	
33....	1989 Dec 04, 10:25	47864.934	CAT	
34....	1989 Dec 05, 10:52	47865.953	CAT	

Table 8.1: (Continued)

Obs.	UT Date and Time	JD (-2400000)	Tel.	veiling
35....	1989 Dec 06, 04:14	47866.676	CAT	4.9
36....	1989 Dec 08, 11:24	47868.977	3m	
37....	1990 Oct 21, 10:56	48185.957	CAT	4.7:
38....	1990 Oct 22, 09:36	48186.898	CAT	5:
39....	1990 Oct 24, 10:54	48188.953	CAT	
40....	1990 Oct 25, 11:11	48189.965	CAT	
41....	1990 Oct 27, 11:04	48191.961	CAT	4:
42....	1990 Oct 28, 07:57	48192.832	CAT	
43....	1990 Nov 13, 06:05	48208.754	CAT	
44....	1990 Nov 16, 05:38	48211.734	CAT	
45....	1990 Nov 18, 05:51	48213.742	CAT	5.5:
46....	1992 Jan 02, 05:52	48623.746	CAT	
47....	1992 Jan 12, 07:24	48633.809	CAT	3.4:
48....	1992 Jan 13, 07:45	48634.824	CAT	3.3
49....	1992 Jan 14, 05:41	48635.738	3m	
50....	1992 Jan 15, 07:08	48636.797	3m	4.4
51....	1992 Jan 15, 08:04	48636.836	3m	5.7:
52....	1992 Jan 16, 08:44	48637.863	3m	
53....	1992 Sep 24, 12:01	48890.000	CAT	5.5
54....	1992 Oct 20, 11:39	48915.984	CAT	3.8
55....	1992 Oct 23, 10:37	48918.941	CAT	2.7:
56....	1992 Oct 24, 11:00	48919.957	CAT	3.4
57....	1992 Oct 25, 10:12	48920.926	CAT	4.0
58....	1992 Oct 28, 10:02	48923.918	CAT	3.0
59....	1992 Nov 02, 09:27	48928.895	CAT	6.4
60....	1992 Nov 14, 11:39	48940.984	3m	3.6:
61....	1992 Nov 15, 08:26	48941.852	3m	4.1
62....	1992 Nov 16, 11:19	48942.973	3m	3.6
63....	1992 Nov 23, 08:10	48949.840	CAT	
64....	1992 Nov 23, 12:06	48950.004	CAT	3.7:
65....	1992 Nov 24, 10:39	48950.945	CAT	
66....	1992 Nov 26, 07:23	48952.809	CAT	
67....	1992 Nov 26, 11:29	48952.977	CAT	
68....	1992 Nov 28, 06:06	48954.754	CAT	3.8:

Table 8.1: (Continued)

Obs.	UT Date and Time	JD (-2400000)	Tel.	veiling
69....	1992 Nov 28, 10:58	48954.957	CAT	4.9:
70....	1992 Nov 29, 06:27	48955.770	CAT	5.5:
71....	1992 Nov 30, 07:22	48956.809	CAT	4.0
72....	1992 Nov 30, 11:23	48956.973	CAT	
73....	1992 Dec 01, 07:31	48957.812	CAT	3.7:
74....	1992 Dec 01, 11:53	48957.996	CAT	
75....	1992 Dec 02, 07:50	48958.828	CAT	
76....	1992 Dec 19, 09:01	48975.875	CAT	3.2:
77....	1992 Dec 21, 05:40	48977.734	CAT	3.3:
78....	1992 Dec 21, 08:58	48977.875	CAT	5:
79....	1992 Dec 22, 06:36	48978.773	CAT	4.2:
80....	1992 Dec 23, 06:33	48979.773	CAT	
81....	1992 Dec 24, 06:21	48980.766	CAT	
82....	1994 Feb 02, 06:30	49385.770	CAT	6:
83....	1994 Feb 03, 06:48	49386.785	CAT	
84....	1994 Feb 09, 08:01	49392.836	CAT	
85....	1994 Feb 12, 08:03	49395.836	CAT	3:
86....	1994 Feb 13, 06:35	49396.773	CAT	
87....	1994 Feb 14, 07:37	49397.816	CAT	3:
88....	1994 Feb 15, 07:31	49398.812	CAT	3.3
89....	1998 Nov 03, 07:48	51120.824	3m	
90....	1998 Nov 19, 09:26	51136.895	CAT	3.5:
91....	1998 Nov 21, 05:29	51138.730	CAT	3.8:
92....	1998 Dec 15, 05:18	51162.723	CAT	
93....	1998 Dec 15, 10:09	51162.922	CAT	7:
94....	1998 Dec 16, 04:46	51163.699	CAT	6.4:
95....	1998 Dec 16, 09:13	51163.883	CAT	4.3
96....	1998 Dec 17, 03:53	51164.660	CAT	2.5:
97....	1998 Dec 17, 08:22	51164.848	CAT	
98....	1998 Dec 18, 03:45	51165.656	CAT	
99....	1998 Dec 18, 08:12	51165.844	CAT	7.9:
100...	1998 Dec 19, 03:58	51166.664	CAT	
101...	1998 Dec 19, 08:38	51166.859	CAT	6.1:
102...	1998 Dec 22, 05:11	51169.715	CAT	
103...	1998 Dec 22, 09:30	51169.895	CAT	

8.1 Survey of line profiles

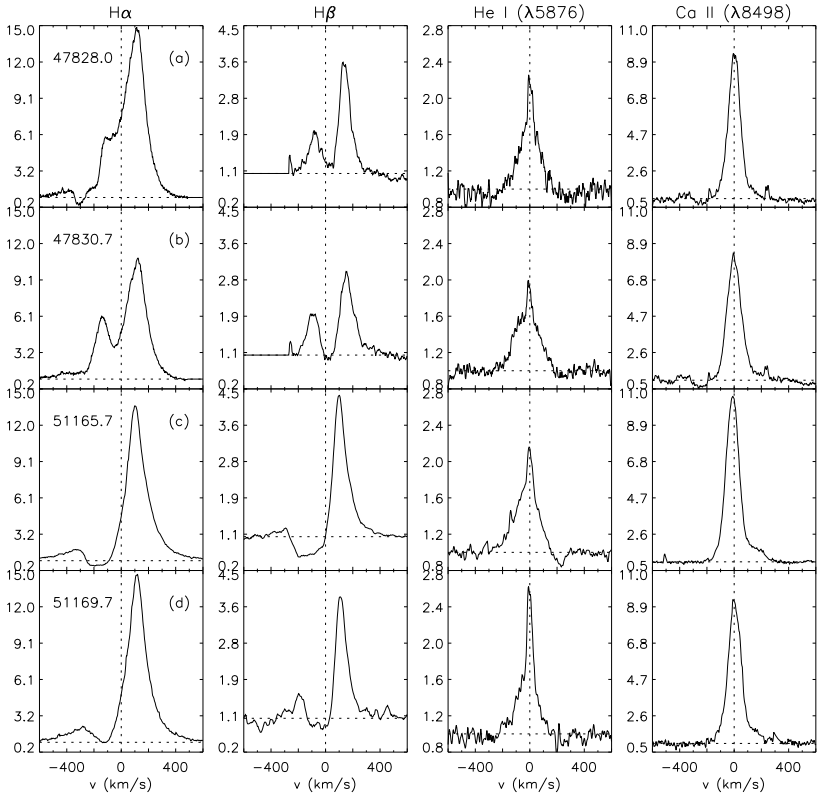

Figure 8.1: Line profiles sample. The horizontal dotted lines represent the continuum level at 1. The vertical dotted lines are the spectral line's center at the stellar rest frame. The numbers in the leftmost pannels are the Julian Dates of the observations minus 2400000.0.

A sample of the various line profiles discussed in the following sections is shown in Fig. 8.1. The first two observations are separated by 3 days in October 1989 and the last two by 2 days in December 1998.

The Hα line presents type I P Cygni profiles in $\sim$ 75% of the observations (Fig. 8.1*c* and *d*). Sometimes, however, a blue shoulder develops (Fig. 8.1*b*) and the Hα line may end up looking like the profiles of stars such as RW Aur: two very

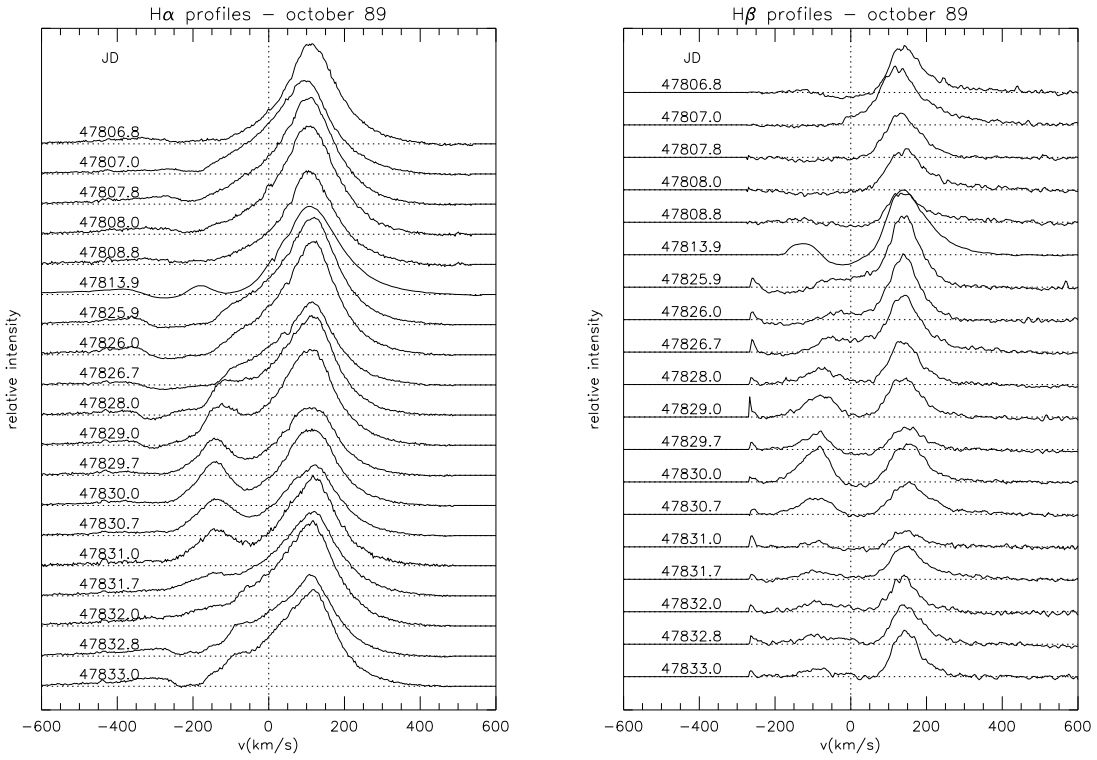

Figure 8.2: Sequence of observations in October 1989. JD is Julian Date - 2400000.0 and the dotted lines have the same meaning as in Fig. 8.1.

symmetric and very separated peaks (Johns & Basri , 1995a; Muzerolle *et al.*, 1998a; Alencar & Basri , 2000). An intermediate situation is shown Fig. 8.1*a*, where a blue bump has just appeared and is still very close to the red emission. The Hβ line mimics the Hα behavior with smaller intensities in the red emission peak.

The He I line characteristics may vary a lot as can be noticed in Fig. 8.1, where the the narrow component (NC) increases from *c* to *d* in 2 days while the broad component (BC) becomes significantly narrower in the same time. The He I profile seems to change simultaneously with the Balmer lines. We can even notice a blue "bump" in the He I BC when the blue emission in the Balmer lines is the most prominent (Fig. 8.1*b*).

The Ca II lines mainly change in intensity but do not seem to show any significant change in shape when the Balmer profiles develop a blue emission. The BCs in this case are much narrower ($\Delta v \sim 300$ km s^{-1}) than the He I BCs ($\Delta v \sim 500$ km s^{-1}), indicating that the He I comes from a more turbulent region, like a hot spot, or a region with higher velocity gradients than the Ca II .

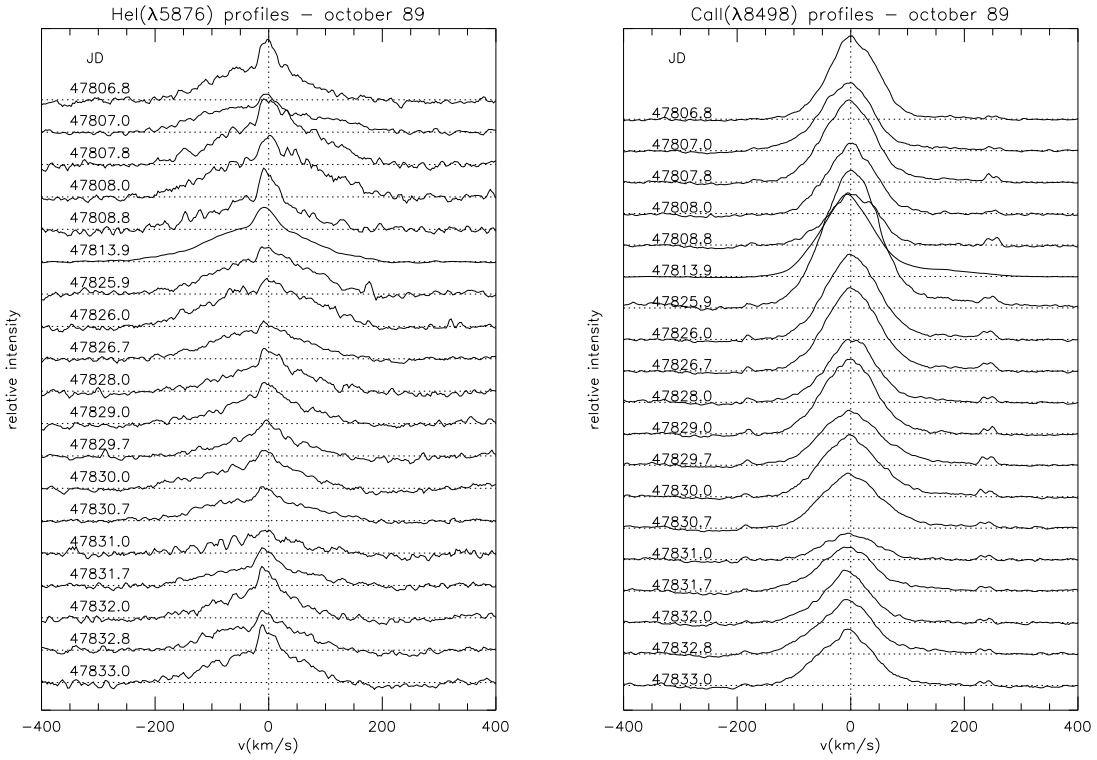

Figure 8.3: Sequence of observations in October 1989. JD is Julian Date - 2400000.0 and the dotted lines have the same meaning as in Fig. 8.1.

In Fig. 8.2 and 8.3 we show a sequence of spectra obtained in October 1989. We notice that the rapid variation in the Hα profile, where a blue bump develops, fades away in less than a week and a that new blue emission appears at low velocities in the last 2 profiles. The Hβ profile shows the same type of variation, the blue bump becoming as strong as the red emission. The He I line displays small changes in

strength and shape, and a redshifted absorption component is barely visible in some of the spectra, while the Ca II line apparently only changes in intensity. Another 1 week series of Hα profiles from December 1998 is shown in Fig. 8.4. This time almost nothing happens to the profile that remains P Cygni during the entire run.

MPEG animation movies showing the variation of each line and the simultaneous variation of many of them can be seen in `http://sprg.ssl.berkeley.edu/~cmj/html/drtau.html`.

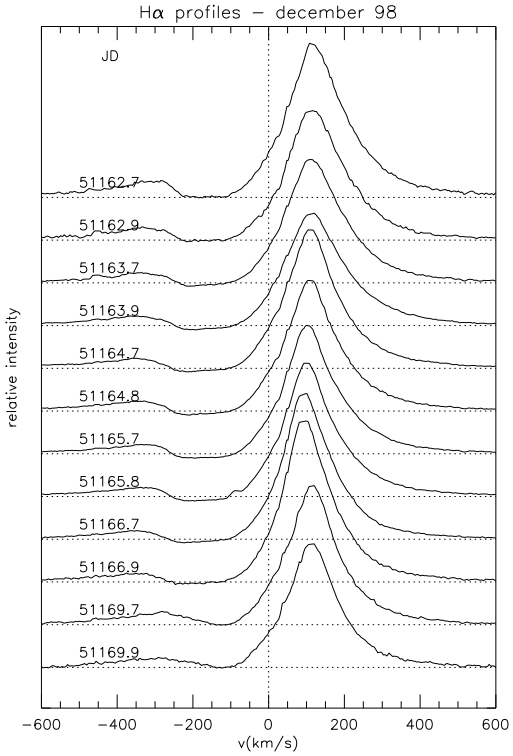

Figure 8.4: Sequence of observations in December 1998. JD is Julian Date - 2400000.0 and the dotted lines have the same meaning as in Fig. 8.1.

8.2 Profile decomposition

Most of the lines present more than one component with different characteristics and variability. We decomposed the line profiles in order to investigate each component's behavior separately and to be able to compare the magnetospheric theoretical profiles only with the components supposedly formed in the accretion flow.

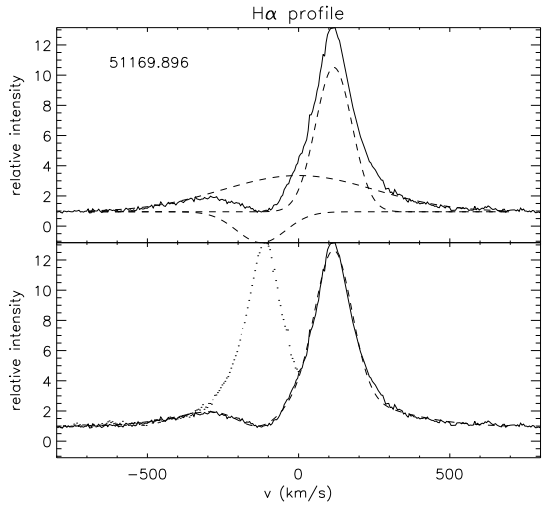

Figure 8.5: Hα decomposition. The dashed lines in the upper panel show the individual components. The dashed line in the lower panel represents the final fit (adding all the individual components). The dotted line is the red side reflected about zero. The number in the upper left corner is the Julian Date of the observation minus 2400000.0.

We decomposed the Hα P Cygni profiles with a strong red emission, a blue absorption and a low gaussian component with large FWHM centered at rest velocity (Fig. 8.5). We favor this decomposition instead of an emission centered at rest velocity and a blueshifted wind component (Fig. 8.6) for several reasons. The equivalent width of a centered emission that fitted the observations would have to be more than twice that of the emission components in Fig. 8.5 and would require a very large emission area. There was always the need in this case for very strong wind absorption components, at least one of them centered at the stellar rest velocity, which would imply that the low velocity receding part of the wind is only partially blocked by the star-disk system. The upper red wing of the observed emission is rather steep and does not seem to belong to a broad Gaussian emission centered

at rest but rather to a redshifted narrower emission. The upper red emission is very symmetric and this would be hard to explain, if each wing were influenced by different processes: accretion for the red side and winds for the blue side. Furthermore, we obtain a better fit with our adopted decompostion (Fig. 8.5: χ^2=0.042) than we do decomposing the profiles with a centered emission component (Fig. 8.6: χ^2=0.093), using the same number of parameters.

When a blue shoulder appears, an extra blue emission component is necessary to fit the profiles (15% of the cases as Fig. 8.1*a* and Fig. 8.7) and the blue absorption may even disappear completely (11% of the cases, as Fig. 8.1*b* and Fig. 8.8).

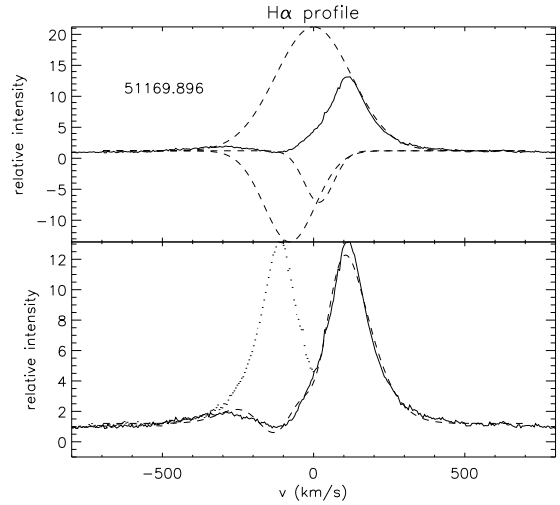

Figure 8.6: Hα decomposition with a very large emission centered at rest. All the lines have the same meaning as in Fig. 8.5. The number in the upper left corner is the Julian Date of the observation minus 2400000.0.

The Hβ profiles resemble the Hα ones, except for the broad and low gaussian contribution, that does not seem to be very important in this case.

The He I lines present a broad component, a narrow component and in $\sim$ 20% of our spectra a redshifted absorption component at $\sim$ 250 km s^{-1} that is easily seen in Fig. 8.1*c*. Both broad and narrow components are generally very symmetric and very well fitted by Gaussians. The NC is normally found centered at the stellar rest velocity while the BC is generally slightly blueshifted.

The Ca II IRT lines show basically only a broad component, although the presence of a small NC cannot be totally discarded due to the somewhat triangular

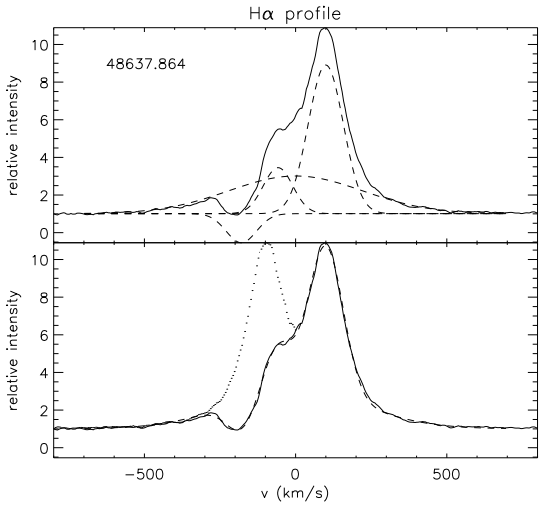

Figure 8.7: Different Hα profile. All the lines have the same meaning as in Fig. 8.5. The number in the upper left corner is the Julian Date of the observation minus 2400000.0.

shape of the profiles. The Ca II lines also have contributions of a Paschen emission line to their high velocity red wings that could be easily subtracted.

The lines were decomposed as described above. The equivalent width measurements and the decomposition parameters are presented in Tables available electronically at `http://www.fisica.ufmg.br/~silvia/thesis/drtau/tables/`.

8.3 Veiling

DR Tau is highly veiled as already noted by several authors (Basri & Batalha , 1990; Valenti *et al.*, 1993; Guenther & Hessman , 1993) with published veiling values ranging from 0.7 to 20. To obtain a good veiling measurement it would require at least a couple of photospheric lines clearly distinct from the continuum. Unfortunately at our S/N the only strong photospheric signature that is present in most of the spectra is the Li I (λ6707) line which is far from being ideal to be used as a probe for veiling. Stout-Batalha *et al.* (2000) showed that in the case of RW Aur the Li I de-veiled line strength is enhanced by accretion by more than a factor of 2 between the lowest ($v = 0.3 \pm 0.3$) and highest ($v = 6.1 \pm 1.7$) veiling values. We confirm a similar trend with our data using only our best spectra, where the veiling could

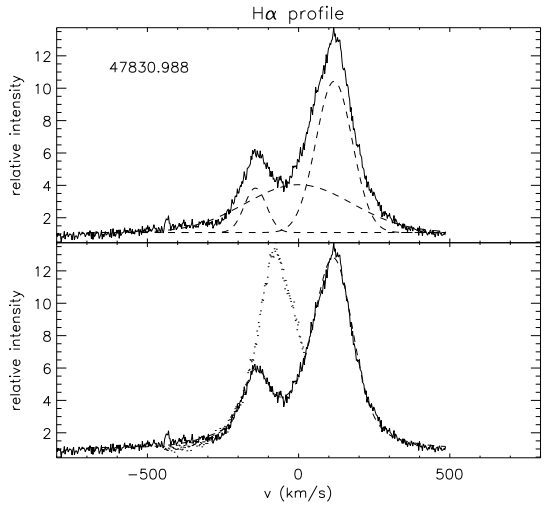

Figure 8.8: Different Hα profile. All the lines have the same meaning as in Fig. 8.5, but the dotted line is the red side reflected about 20 km s^{-1}. The number in the upper left corner is the Julian Date of the observation minus 2400000.0.

also be determined from photospheric lines other than Li I. Nevertheless, since the Li I line is our best option, we used it to measure veiling values between 3 and 6 in the spectra, where they could trustfully be measured (the ones with higher S/N), and checked for consistency with other very faint photospheric lines. We might, in principle, be missing the high veiling values, as they could be confused with low S/N spectra, but in the case of Li I enhancement a highly veiled line may still be visible. The veiling values obtained are listed in the electronic tables.

8.4 Profile variability

We show in Fig. 8.9 the average line profiles for some strong emission lines. Also shown in the shaded area are the normalized variance profiles which measure the amount of variability of each wavelength or velocity bin in the line. As defined by Johns & Basri (1995a), the temporal variance of the line at each wavelength bin is given by

$$\sum_{\lambda} = \left[\frac{\sum_{i=1}^{n} (I_{\lambda,i} - \overline{I}_{\lambda})^2}{(n-1)} \right]^{1/2} \tag{8.1}$$

and the normalized variance profile is obtaineed dividing the variance profile by the average line profile.

Although the spectra are not corrected for veiling, we see that the main variations in the line profiles are not due to the veiling itself. If this were the case, the shape of the variance profile would be the same as the line itself, since the entire line would change together. Most of the changes in Hα are in the blue side, which we interpret as being due to changes in the wind. The red emission peak shows almost no variation if compared to the blue side meaning they are not equally influenced by the same processes. The Hβ variations look like the Hα ones, except that the sharp cuttof in the blue is due to the fact that some Hβ spectra used fall too close to the left edge of the CCD. The He I and Ca II lines do not show strong variations in general, but can vary sporadically. We can easily notice in Fig. 8.9 the redshifted absorption at ~ 250 km s^{-1} in He I probably due to the infall of material at free-fall velocities in the accretion process. The He I line is the weakest line studied and, therefore, the most influenced by veiling variations. Its normalized variance profile is consequently the one that most resembles the average line profile.

8.5 Periodogram

Many attempts have been made in the literature to determine the rotation period of DR Tau. Richter *et al.* (1992) obtained a marginal detection of a 9.0 day period using differential photometry. Bouvier *et al.* (1993), analysing broad band light curves, suggested two periods of 2.8 and 7.3 days. Kenyon *et al.* (1994) found phased optical and near-IR photometric variations with time scales of 5 or 10 days. However, Kenyon *et al.* (1994) argue that neither theirs nor Bertout's sample is long enough in time to demonstrate periodic behavior. Bouvier *et al.* (1995) observed DR Tau again (as part of the COYOTES campaign) and were able to confirm the 7.3 day period they had found earlier. They also reported a 9.0 day period that agrees with the determination by Richter *et al.* (1992), but this value has a larger uncertainty as their light curve covers less than two photometric periods. Johns & Basri (1995a), analysing the Hα profile variations of DR Tau, obtained a period of 5.1 ± 0.2 days and another possible period of 7.85 ± 0.4 days. Hessman & Guenther (1997) analysed a series of spectroscopic and photometric observations and found that the strength of the strong emission lines of DR Tau seemed to be quasi-periodic in time. They obtained a 4.48 day period, mainly due to the Balmer line variations and a 4.5-5.0 day period mostly due to Ca II. As pointed out in Section 7.2, the veiling of this star is high and quite variable and the photometric periods obtained

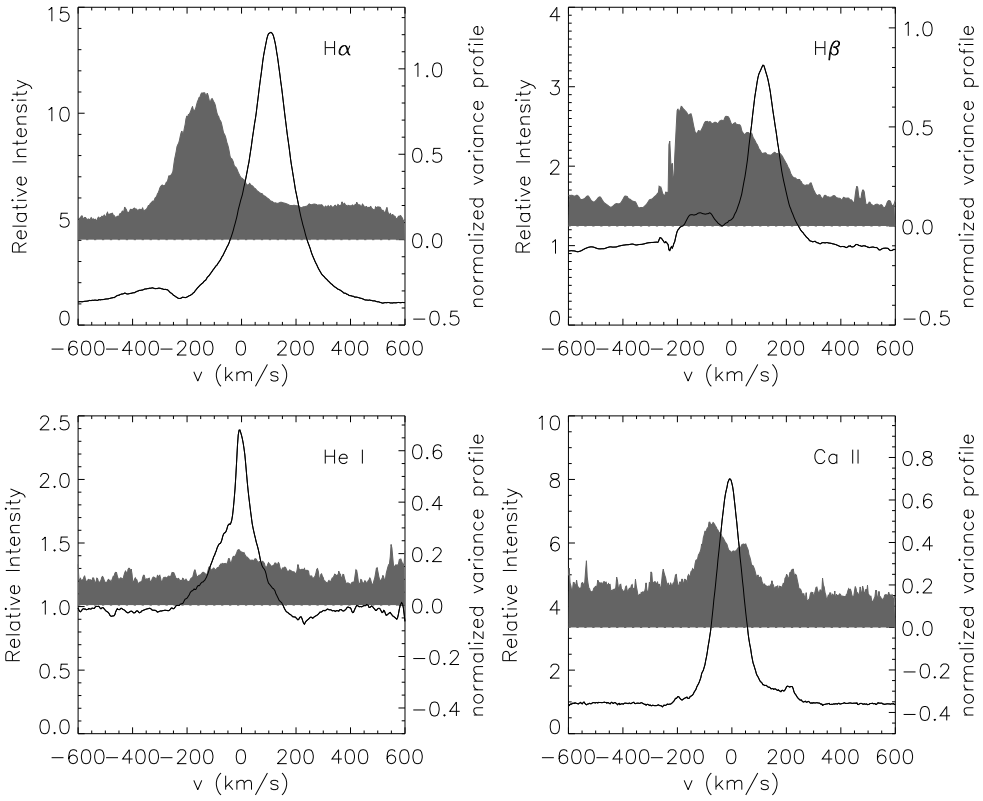

Figure 8.9: Average line profiles (solid lines) and variance profiles (grey shaded areas).

due to hot spots could just be reflecting quasiperiodicities in the accretion source, and not necessarily the stellar rotation itself (Johns & Basri , 1995a).

We performed a periodogram analysis of the line's intensities using the Scargle (1982) periodogram estimator as modified by Horne & Baliunas (1986) that is appropriate to handle irregularly spaced data. We decided to investigate small groups of data instead of the entire set at once since our data sets are sometimes separated by several months. Also due to the fact that so many different periods have been reported for this star, it seems to make more sense to analyse the data on a month-to-month basis. In general, periods of 4 to 9 days were obtained with several different lines, but we could not find a unique period that described the line

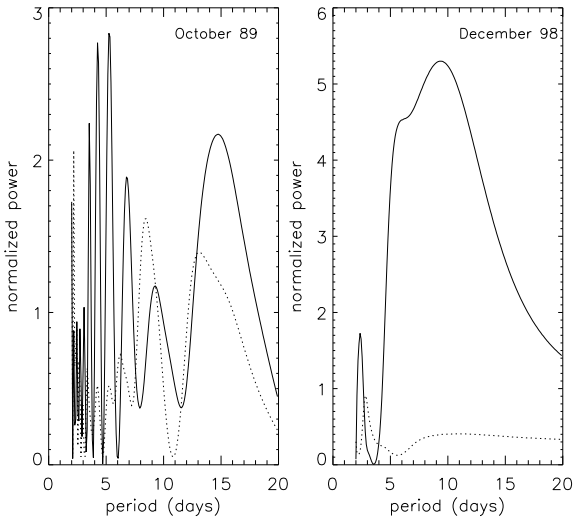

Figure 8.10: Power spectrum of the Hα red emission peak center in October 89 and December 98. The solid lines correspond to the observed data and the dotted lines to random noise sampled at the same times as the data.

variations. We also tried to use the complete data set but we could not retrieve any significant period from it.

We note in Fig. 8.4 that the Hα red emission peak position seems to vary periodically. But like in the intensities case, although the data may look ordered and periodic in certain epochs, most of the times it is quite random. We show in Fig. 8.10 the periodogram results for December 98 and for October 89, which correspond to Fig. 8.3 and 8.4. We overplot with dotted lines the power spectrum of random noise sampled at the same times as the data. We can see that the peaks that appear with the October 89 data are likely to be all due to the sampling rather than real periodicities. However, if we analysed only the December 98 data we would probably conclude that the data revealed a 9.3 day period.

8.6 Correlation matrices

Correlation matrices are 2D plots of linear correlation coefficients. These coefficients are calculated, in this work, correlating the time variation of each velocity bin of a spectral region with the time variation of all the other velocity bins of that region or of a different region. In order to investigate how the profile variations are correlated

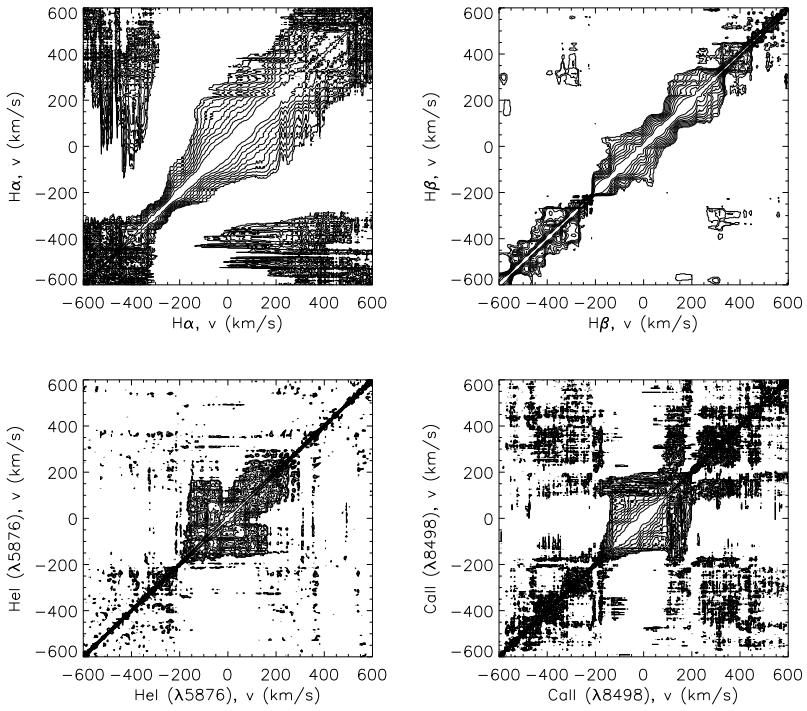

Figure 8.11: Autocorrelation matrices.

across an emission line we calculated correlation matrices for each of the main emission lines of DR Tau. If the veiling is the main source of variability the matrices will appear squarish as all the velocity bins will be correlated. Correlation matrices are shown for each line in Fig. 8.11 where the lowest contour plots correspond to 99.9% confidence level. We did some tests to see how the influence of the veiling would appear in our profiles. We added to the average Hα profile a random veiling value in the range $3 < v < 5$ which corresponds to the mean values we obtained for DR Tau. We did not get any structure along the diagonal except for a square centered at -200 km s$^{-1} < v < 400$ km s^{-1}. The observed Hα profiles on the other hand show lots of structures along the diagonal that are probably not due to veiling. We note that the region corresponding on average to the wind (-300 km s$^{-1} < v < -100$ km s^{-1}) does not correlate with the rest of the profile. This shows that the blueshifted part of the line is produced in a different region than the emission peak. The blue side comes from a region that varies a lot (according to the variance profiles) and

not uniformily, since the correlation matrix is very narrow in this part of the profile. The Hβ matrix shows no squarish part and a real pinch at the red emission peak position. Most of the correlations are along the diagonal showing little relation between the variations of the different line parts. The correlation matrix of the Ca II line is by far the most squarish we obtained and could be mostly due to veiling. However, if the veiling were responsible for the Ca II variations it should also appear in the matrices of the other lines. The Ca II line exhibits a simple profile with just one component and is probably formed in a small region that feels any turbulence altogether. This would also generate a squarish matrix. The He I matrix shows that the emission parts of the line are well correlated, either due to veiling or to the accretion process itself, while the redshifted part of the profile does not show much correlation with the emission components. If the veiling was the main responsible for the correlations the entire line would show a good correlation and not only the emission part of it. From the correlation matrices we conclude that although the veiling is important, for many lines most of the variations are not simply the result of changes in the veiling.

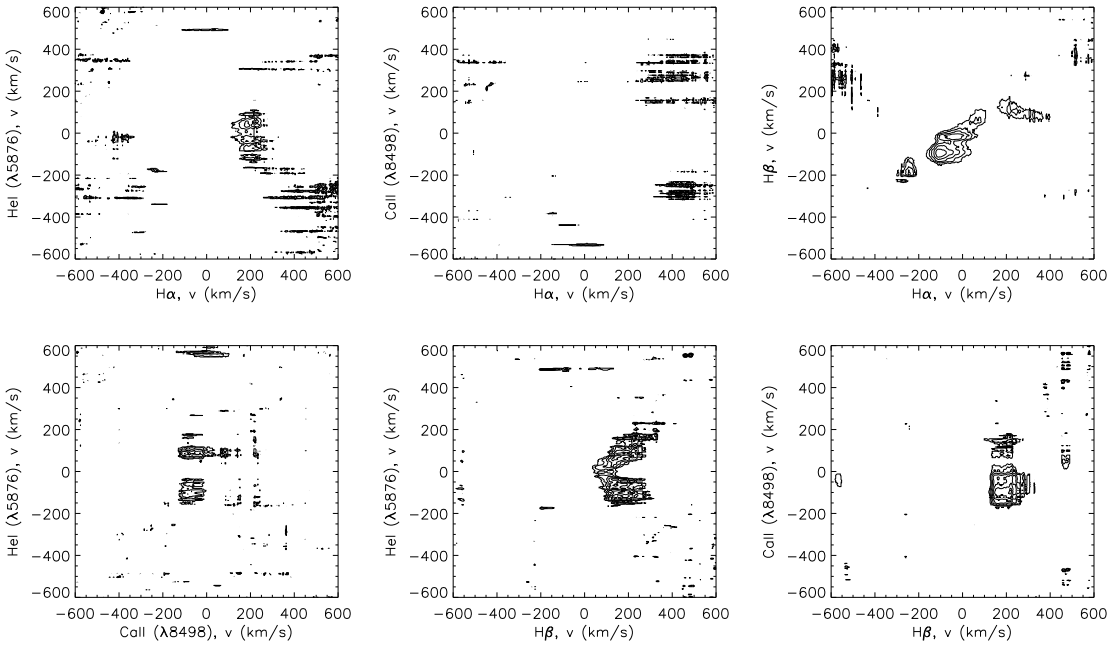

Figure 8.12: Correlation matrices between different lines - no time lag.

We note that the right and left wings of the Hα emission peak are very well correlated, indicating that the same process is affecting both sides simultaneously. It is not likely that the wind is responsible for the left side of the emission and accretion for the right side. In other words, the Hα profile should not be decomposed as a large emission centered at rest frame and several wind components.

Another interesting use of the correlation matrices is to search for common forming regions between different lines. We calculated the matrices between the main emission lines and noticed that Hα and Ca II do not seem to show any correlation at all. The other correlations found are shown in Fig. 8.12. The emission part of the He I shows a good correlation with most of the Hα emission peak, implying that they are both formed, at least partially, in the same region, the accretion flow, according to the magnetospheric models. The He I BC is correlated to the Ca II emission that is basically composed only of a BC. They are both thought to be produced in the accretion flow although in different regions. The He I is formed in high temperature ($T > 20\,000$K) regions while the Ca II is thought to come from low temperatures ($4\,000\text{K} < T < 7\,000\text{K}$). The correlation shows that, despite the different characteristics of their formation regions, there is some common process affecting them both. Hα and Hβ present a strong correlation between each other, as expected, since they are supposed to be formed in regions with the same characteristics. The correlation is mainly along the diagonal, showing that the same components of the 2 lines are well correlated with each other. The He I line correlates with the Hβ emission peak, once again showing that the Balmer lines and the He I must share some commom formation region. It seems from the matrix that the He I NC tends to correlate better with the central part of the Hβ emission peak, while the BC shows a strong correlation with the the peak's red wing. Differing from Hα, the Hβ red emission peak correlates with the Ca II emission line.

We also checked for 1, 2 and 3 day time lagged correlations between different lines. The results are presented in Fig. 8.13. We found that the He I line 1 day later correlates with the Hα emission peak. Hα probes a much larger area than He I line that is thought to originate, at least partially, in the shock region. Both lines show a strong correlation with no time lag, but it seems that the effects of accretion last longer in the region where the He I emission line originates. The shock propagation in the hot spot could be responsible for such effect. No correlation was found between the Hα line 1 day later and the He I line. The Ca II line 1 day later slightly correlates with Hβ . They also correlate with each other with no time lag. Nothing was found between the Ca II and the Hβ line 1 day later. The Hα line 1 day later slightly correlates with the Hβ along the diagonal, the blue absorptions and the red emission of both lines showing some memory of the 1 day changes. The same kind

of correlation is found between the Hβ line 1 day later and Hα . The variation of both lines in time is very similar and they would be expected to show some time lagged correlation with each other. We could not find any correlation with 2 or 3 days time lag. The number of data points suited for that study was not extremely small (36 data pairs in the first case and 32 pairs in the second).

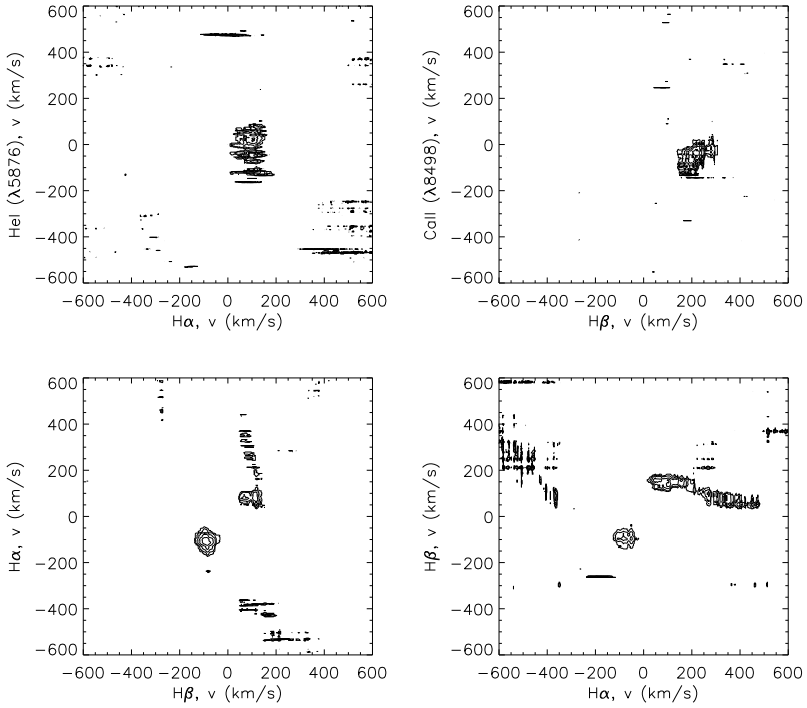

Figure 8.13: Correlation matrices between different lines. The horizontal axis line occurs 1 day before the vertical axis line.

8.7 Discussion

In the previous sections, DR Tau has been shown to display a large array of line profile shapes in its permitted emission lines. The geometry of the DR Tau system, that would allow for such a variability and diversity of profiles, is puzzling. It is very difficult to estimate even the inclination of the system, since we do not know precisely the rotational period of the star. Kenyon *et al.* (1994), using a period of

5 days, $v \sin i \leq 10$ km s^{-1}, and assuming $R_\star = 2\ R_\odot$ estimated that the system inclination should be $i \leq 30°$ (they obtained in fact $i \leq 60°$, but there was an error in their calculations). This also agrees with the SED fits they determined for DR Tau: the system is more likely viewed closer to pole-on than edge-on. They further estimated that $i + \beta \approx 95°$ which would imply that β, the angle between the magnetic and rotation axes, is $\geq 65°$. However, their values for i and β are based on many assumptions, like the position and size of the accretion rings, the disk parameters and the rotation period itself.

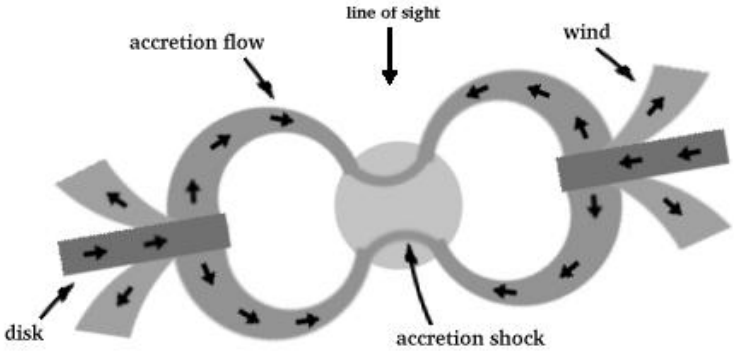

Figure 8.14: Simplified representation of the DR Tau system. The small arrows show the flux of material from the disk.

We agree with Kenyon *et al.* (1994) and favor a more pole-on than edge-on geometry. We assume that, most of the time, the high velocity magnetospheric flow directed away from the observer (redshifted) is visible, while the blueshifted flow is hidden by the star close to the stellar poles (Fig. 8.14). Part of the low velocity redshifted flow is also occulted by the disk in this configuration, which enhances the line redshifted asymmetry. The Hα decomposition we adopted based on this picture provides a better fit to the observed line profiles than one with a very large centered emission component. In this model, the red emission is due to accretion and is produced in the magnetospheric flow, while the variable blue emission peak may arise in a sporadic outflow. The velocity of the blue emission peak is comparable to the terminal outflow velocity measured by the position of the blue emission peak of the [OI] (λ6300) line. This forbidden line supposedly forms many stellar radii from the star and in DR Tau is commonly found in the range -160 km s$^{-1} < v < -120$ km s^{-1} (Appenzeller *et al.*, 1988; Hartigan *et al.*, 1995). The red and blue emissions

do not seem to be related to each other, as can be seen in Fig. 8.11, where there is no sign of correlation between them. Most of the variability in Hα is on the blue side showing that the source of blue emission is much more ephemeral. The intensities of the blue and red emissions are also very different as we go from Hα to Hδ (see Fig. 2 in Appenzeller *et al.*, 1988). While the red decreases drastically, the blue remains almost constant. We also verified this behavior in our data.

The broad, weak symmetric outer wings of Hα may be due to magnetic turbulence. They are very well fitted by a Gaussian centered at the stellar rest frame, which strongly suggests a turbulent origin. Muzerolle *et al.* (1998b) suggest that Stark broadening effects might be responsible for the extended Hα wings. However, in the case of DR Tau, it is hard to imagine that the far wings of Hα are the result of Stark broadening of a strong centered emission component, since most of the Hα emission is obviously redshifted and there is no indication of such a component in most of the higher Balmer lines, where the influence of wind absorption should be weaker. The higher Balmer lines do not generally show this broad component, indicating it is optically thin there. If Stark broadening is important in the formation of the Balmer lines, its effects should be testable using the high lying members of the series where Stark broadening is more noticable. Such comparisons have clearly shown the role of Stark broadening in solar flares, permitting a determination of the local electron density in the line formation region (e.g. Johns-Krull *et al.*, 1997, and references therein).

The variety of profiles displayed by the Hα line of a single star like DR Tau indicates that many CTTSs that exhibit very different line profiles may indeed be star-disk systems with very similar characteristics. We may just be seeing them in some particular accretion or outflow configuration. Perhaps if we look at them long enough, like we did with DR Tau, we will find that most CTTSs show very diverse line profiles in different epochs.

The He I line is probably produced in the accretion flow or the shock region, since it correlates very well with the Hα red emission peak. The same kind of correlation is found between the Hβ red emission peak and the He I line. This confirms the trend shown by Alencar & Basri (2000) between the Hα , Hβ and He I veiling corrected equivalent widths of several CTTSs. The correlation between Hα and He I persists for 1 day, the effects of a change in accretion lasting longer in the He I line forming region than in Hα.

The narrow and broad He I components are expected to correlate with the veiling, the former because it is enhanced by accretion and the latter because it is thought to arise in the accretion flow or shock. However, the equivalent widths of the He I components corrected or not for veiling do not show, in general, a corre-

lation with the veiling itself. A slight correlation can be noticed between the BC corrected for veiling and the veiling itself, but nothing is apparent between the NC or the redshifted absorption component and the veiling. Anyway, we must keep in mind that our veiling values are not extremely reliable.

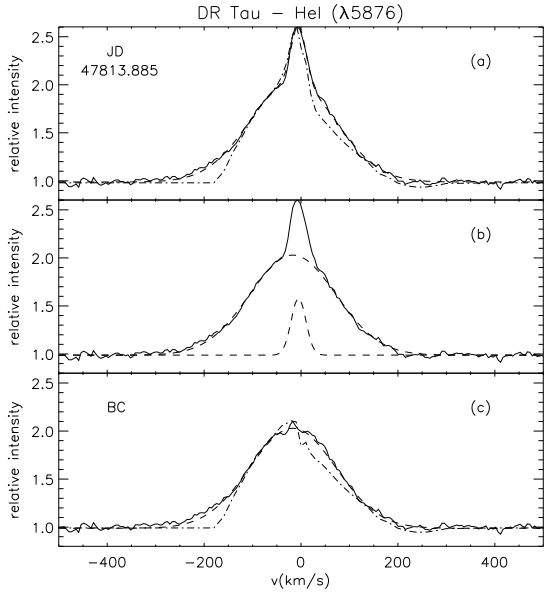

Figure 8.15: He I line profile decomposition and comparision with the theory. The solid line is the observed profile. In (*a*) the dashed line is the fitted profile obtained adding the two components shown in (*b*). The dash-dotted line is the theoretical profile with the fitted NC added to it. In (*c*) we show only the BC. The solid line is the observed profile with the NC subtracted, the dashed line is the BC fit and the dash-dotted line is the theoretical profile.

As pointed out by Hartmann *et al.* (1994), the He I line looks very much like the theoretical magnetospheric profiles. Since the He I line does not have any wind contribution and is not expected to have any significant Stark broadening, it is a good candidate to be compared to the theoretical profiles. We do not have these profiles for the He I line but decided to use scaled Hartmann *et al.* (1994) Hβ profiles in the comparison instead. While the He I source function will not look exactly like the Hβ one, the temperature structure in the magnetospheric flow is still poorly understood and is currently specified as adhoc functions. Our primary assumption is, then, that the *shape* of the He I theoretical profiles should be similar to those of Hβ .

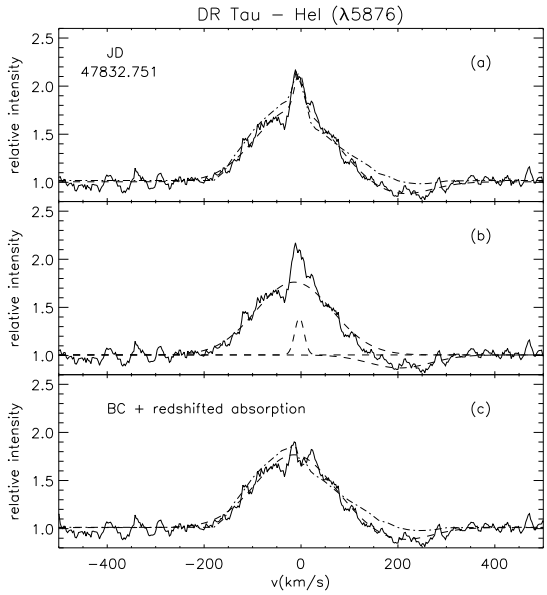

Figure 8.16: Asymmetric He I line profile decomposition and comparision with the theory. The lines have the same meaning as in Fig. 8.15 except that now there is a redshifted absorption present.

In Fig. 8.15*a* we show a typical He I line profile with a scaled theoretical profile overplotted. We have added to the theoretical profile our gaussian fit of the observed spectrum's NC. The theoretical profiles should only be compared to the BC and the occasional redshifted absorption since the NC, despite being affected by the accretion process, is not thought to be produced in the magnetospheric flow itself. We note that, although the entire He I line may look asymmetric, the individual components are very symmetric (Fig. 8.15*b*). The fact that the BC is normally found blueshifted, while the NC is not, gives a false impression of asymmetry to the line. The theoretical profile in Fig. 8.15 corresponds to an inclined magnetospheric model with $i = 60°$ and hot ring emission at the base of the magnetosphere (Fig. 9 in Hartmann *et al.*, 1994). In general, the published theoretical profiles tend to be very asymmetric, with a lack of redshifted low velocity material due to occultation by the disk of the material moving slowly away from the observer. Extended red wings are also commonly produced at lower inclinations or with different geometry assumptions (e.g. hot spot emission instead of a ring). In this case, the lack of blueshifted emission in the far wings is caused by occultation by the star of the high

velocity material moving toward the observer. We do not normally see any of these asymmetries in our sample.

An exceptionally asymmetric profile is shown in Fig. 8.16. This time the agreement with the theoretical profile shape is much better but unfortunately profiles like this one are quite rare in our sample for DR Tau.

The theoretical profiles tend to be either blueshifted and asymmetric (higher inclinations) or centered and symmetric (lower inclinations) but not really blueshifted and symmetric, like most of the He I BCs. In Hartmann *et al.* (1994) the case that comes closest to what we observed is a large magnetosphere, which favors the material starting out in the disk near co-rotation radius. The profiles look quite symmetric even at higher inclinations, but it is unclear that such profiles would also appear blueshifted.

Another possibility is that the He I and Ca II broad emission components are mainly produced by magnetospheric turbulence. Typical values of magnetic field measured in CTTSs (~ 2.5 kG) and theoretical gas densities used in magnetospheric accretion models ($\sim 1 \times 10^{-9}\,\mathrm{g/cm^3}$) yield Alfvén velocities of $\sim$200 km s^{-1}. This plausible turbulent origin would help explain the symmetry of these components.

The observed Hα profiles, on the other hand, do not look at all like the published theoretical ones at any inclination. Due to that, we decided to investigate the influence of the many geometrical parameters and the flux distribution along the field lines on the profile characteristics.

We computed a very simple dipole model, where material free-falls from the disk to the star along the field lines Fig. 8.17. The disk was considered to be opaque and black at all frequencies, and we did not take into account the emission from a hot ring or spot. We only calculated axisymmetric models, where the rotation and magnetic axis are aligned. The disk truncation radius was assumed to correspond to the corotation point where the keplerian angular velocity of the disk equals the angular velocity of the star.

We calculated the velocity vector and attributed a flux value to every point on the dipole streamlines. We had the option of adding a turbulent velocity component (v_{turb}) with a random Gaussian distribution to each velocity point and a rotation component. We calculated the projected velocities in the observer's direction and added up the flux of the points that fell in the same 10 km s^{-1} velocity bin. The intensity of this imaginary line profile does not have any physical meaning, but the shape of the profile reflects the geometry of the system and the flux distribution in the magnetosphere.

We obtained line profiles that present the same general characteristics as those of Hartmann *et al.* (1994), except for the sporadic redshifted absorption which is

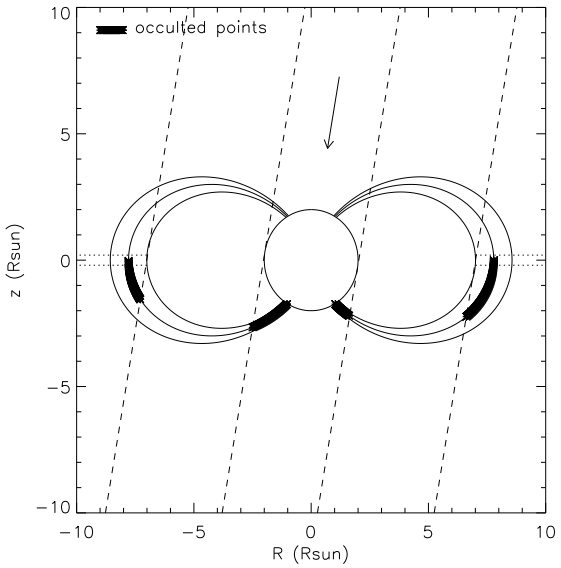

Figure 8.17: The dipole geometry in the poloidal plane with six streamlines. The dotted lines represent the disk and the arrow shows the direction of the line of sight. The inclination of the dashed lines correspond to the inclination of the line of sight and the occulted points are identified in the middle streamlines.

related to the presence of a hot ring (or spot) which we did not model. In Fig. 8.18 we show an example obtained with a constant flux along the field lines and a low inclination. It is very different from the observed Balmer lines of DR Tau, so we decided to vary the flux along a streamline. Results with a line emissivity that strongly increases near the star are presented in Fig. 8.19. This theoretical profiles justify the decomposition we adopted, since they show that we can produce a redshifted emission component from magnetospheric accretion even without a wind contribution. We obtained profiles strongly peaked in the red for $0^\circ < i < 20^\circ$ but for higher inclinations the profiles do not match the observed Balmer lines anymore. Longer periods shift the red emission peak towards higher velocities (P=6 days, peak at ~ 150 km s^{-1} and P=9 days, peak at ~ 165 km s^{-1}). We are still working to determine the temperature structure of the magnetosphere that would yield such a flux distribution. Although we do not know it yet, we also do not know the temperature structure of the magnetosphere at all. What Fig. 8.19 shows is that it is possible to obtain line profiles that look like the Balmer lines observed in DR Tau with a heuristically constructed magnetospheric accretion configuration.

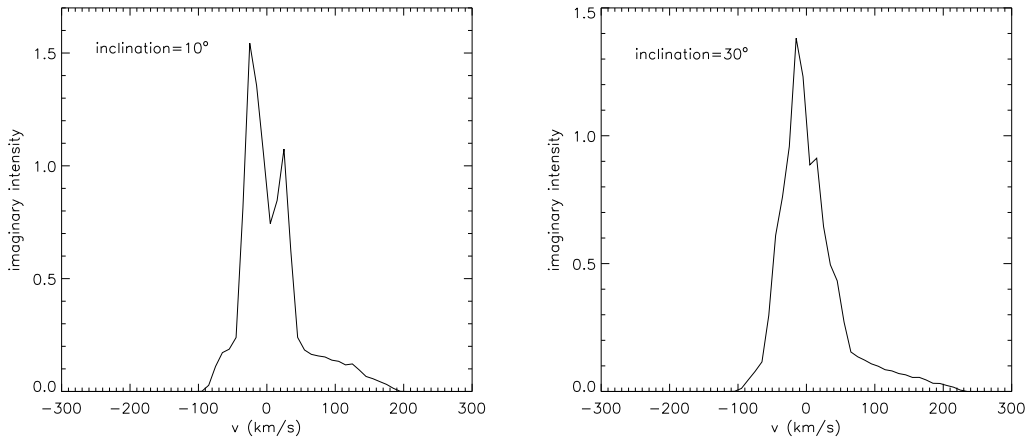

Figure 8.18: Theoretical line profiles computed with a constant flux, v_{turb} = 5 km s^{-1}, R_*=2 $R_\odot$, M_*=0.4 $M_\odot$ and period=4 days.

8.8 Conclusions

We analysed 103 spectra of the Classical T Tauri star DR Tau and showed that according to our interpretation the system is likely viewed more pole-on than edge-on, in agreement with previous results.

We showed that the emission line profiles vary constantly, but not with a unique period, implying that the variations are caused by non-steady accretion and outflow processes. Many different emission line changes are correlated showing that different line forming regions are affected by the same events. The published theoretical magnetospheric accretion profiles are very different from our observed ones. We propose, for DR Tau, that the very symmetric Ca II and He I broad components may be produced by magnetospheric turbulence while the Balmer lines originate in a magnetosphere with a line emissivity that increases strongly near the star. We computed simple dipole models and showed that the observed redshifted Balmer profiles can be produced in a magnetospheric accretion configuration with low inclinations.

This work is being completed and will be submitted to the Astronomical Journal.

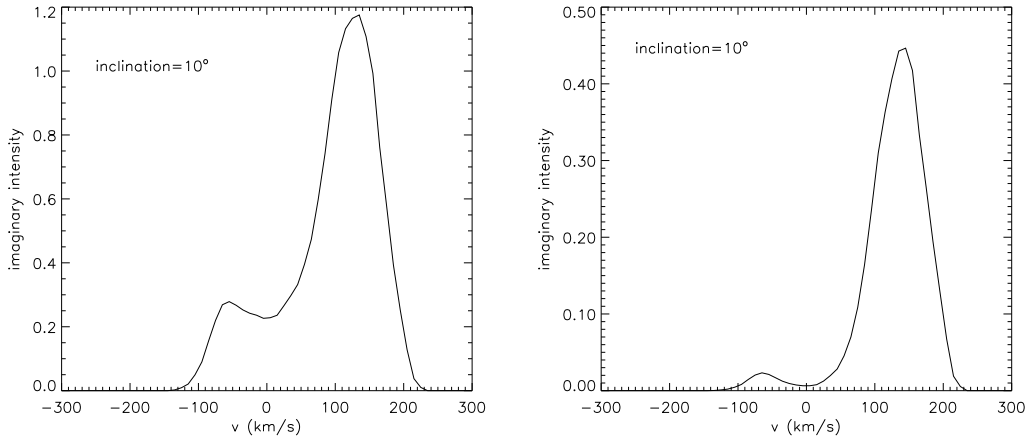

Figure 8.19: Theoretical line profiles computed with a power-law flux ($\propto r^{-5}$ and r^{-9}, respectively), $v_{turb} = 20$ km s^{-1}, R_*=2 $R_\odot$, M_*=0.4 $M_\odot$ and period=4 days. The profile was smoothed with a window width of 30 km s^{-1}.

Chapter 9

—

Conclusions and Perspectives

We established new and better theoretical values to parameters, such as the gravity-brightening exponents and the limb-darkening coefficients, that describe proximity effects in binary systems. These are usually fixed parameters in a light curve analysis and it is, therefore, very important that their values are consistent with the system being analysed. We showed the influence of illumination on these parameters and presented a new set of theoretical values that should be used when studying close binaries, since non-illuminated values fail to describe the proximity effects in this case.

We did a first successful observational test of the non-illuminated gravity-brightening exponents with the quadruple PMS system TY CrA. The new values of the gravity-brightening exponents are already implemented in the Wilson-Devinney light curve synthesis program and the implementation of the illuminated limb-darkening coefficients are on their way. New tests are needed in order to evaluate the importance of the results obtained, and close binary systems are the best candidates to be used.

We also tested observational and theoretical results of magnetospheric accretion models, in order to better understand the star-disk system interactions. We showed that the accretion and outflow seem to be related, and that evidence of accretion like redshifted absorption at free-fall velocities is sometimes present in the CTTS spectra. We showed that most of the emission components analysed are symmetric instead

of blueward asymmetric, as predicted theoretically, and that the broad emission components of different atomic lines thought to be formed in the accretion flow are not all strongly correlated to each other. We emphasize the need to add turbulence, winds and rotation to the models, in order to successfully compare the theoretical profiles to the observed ones.

We showed that magnetospheric models must be dynamic in order to fully describe the variety of profiles a CTTS may exhibit, and that magnetospheric turbulence may be responsible, at least partially, for some emission lines.

We intend to redetermine the absolute parameters of the close binary systems with high quality data in the literature using our proposed values of gravity-brightening exponents and limb-darkening coefficients in order to test the importance of these effects.

We hope that in the future the proximity effect results will be useful in the analysis of PMS close binary systems and that, together with the improvement of the magnetospheric accretion models, a complete description of the PMS star formation will arise. Some encouraging results have recently begun to appear, close binary systems such as RW Aur are now being studied, and several groups are currently working on the implementation of more realistic features in the magnetospheric models, like multipole non-axisymmetric fields and winds. The perspectives seem great!

Chapter 10

—

Síntese em português do trabalho

10.1 Introdução

O estudo da formação e evolução estelares é uma das áreas mais ativas em astrofísica e tem sido em grande parte auxiliado pela análise de estrelas binárias e estrelas jovens. Há poucos anos, a maioria dos testes de modelos evolutivos eram realizados com estrelas na Sequência Principal (SP). Os resultados foram encorajadores e, nas últimas décadas, dados observacionais de alta qualidade permitiram investigar a importância de efeitos como o "core overshooting" na convecção tradicional ("mixing length"), a influência da composição química na evolução estelar, ajudaram a aperfeiçoar as teorias de evolução de maré em sistemas binários, além de contribuirem na melhoria das tabelas de opacidade (Andersen, 1991). Recentemente, o desenvolvimento tecnológico de detectores de alta qualidade no infra-vermelho (IV) permitiu a descoberta de várias binárias entre estrelas Pré-Sequência Principal (PSP). Isto tornou possível estender estes testes para as fases PSP (Mathieu, 1994; Casey *et al.*, 1998; Basri *et al.*, 1997), assim como estudar estrelas solitárias para entender os processos que levam à formação de planetas, à acresção de matéria e que determinam a perda de momento angular nas fases iniciais da evolução estelar (Shu *et al.*, 1994; Johns & Basri , 1995a; Muzerolle *et al.*, 1998a).

Há alguns anos foi realizada a determinação de elementos absolutos de alta precisão do sistema binário eclipsante V906 Sco (Alencar *et al.*, 1997; Vaz *et al.*, 1997),

cujas componentes se encontram próximas à SP de idade terminal. Durante a análise de V906 Sco, cujas observações são de qualidade excepcional, ficou bastante claro a forte influência dos valores teóricos a serem adotados para parâmetros, tais como os coeficientes de escurecimento de bordo, dos expoentes de brilho por gravidade e também do tratamento do chamado "efeito reflexão" nos resultados finais. Então, utilizando recursos ao nosso alcance no momento, decidimos estudar o problema e tentar estabelecer valores teóricos mais rigorosos para esses parâmetros tendo em vista a análise de curvas de luz de sistemas binários eclipsantes (SBE).

A primeira parte do trabalho de Doutorado consistiu do estudo dos processos que afetam as atmosferas estelares como o efeito reflexão, o brilho por gravidade e o escurecimento de bordo, expressando esses efeitos de maneira adequada para que fossem aplicáveis a modelos de síntese de curvas de luz de SBE. Foram aperfeiçoados resultados teóricos clássicos como Lucy (1967) (brilho por gravidade em atmosferas convectivas) e Van Hamme (1993) (escurecimento de bordo), estendendo-os para atmosferas iluminadas, um cenário mais realista em se tratando de sistemas binários.

Na segunda parte do Doutorado trabalhou-se com aspectos da formação estelar em seus estágios preliminares de alta taxa de acresção, tendo como objetivo o controle dos modelos de formação, estrutura e evolução estelares na fase PSP.

Conseguiu-se, com este trabalho, estabelecer valores teóricos mais precisos e consistentes para parâmetros que descrevem efeitos de proximidade em sistemas binários, testando a validade e importância dos resultados teóricos obtidos. Testaram-se também resultados teóricos e observacionais de modelos de acresção magnetosférica com o objetivo de melhor entender a interação disco-estrela na fase PSP de estrelas T Tauri clássicas. O objetivo principal deste projeto foi aperfeiçoar teórica e empiricamente os métodos de análise e a base de dados de dimensões estelares absolutas precisas, assim como contribuir para a melhor compreensão dos vários processos que se desenvolvem em estrelas em formação.

Nas próximas seções será feito um resumo estendido dos resultados obtidos durante o doutorado que são apresentados de maneira detalhada nos capítulos seguintes.

10.2 Modelos de atmosferas

Devido à alta opacidade do interior estelar a luz emitida por uma estrela possui as características das camadas mais externas de sua superfície, a fotosfera.

Pode-se analisar esta luz medindo-se sua magnitude, uma quantidade relacionada ao fluxo integrado de radiação em uma determinada faixa de comprimentos de onda. Pode-se também estudar o espectro estelar, a energia liberada em função da frequência ou do comprimento de onda. Estas análises são fundamentais para o estudo de atmosferas estelares, podendo fornecer informações sobre a estrutura física da atmosfera como a distribuição das temperaturas, pressões e densidades encontradas. Tem-se também indicações da presença de turbulência, convecção e campos magnéticos e pode-se, ainda, deduzir a composição química existente.

Para que estas análises sejam feitas corretamente, o fluxo de energia através das camadas mais externas de uma estrela tem que ser descrito de maneira adequada, tornando possível prever características observáveis da radiação emergente. Isto é feito aplicando-se leis físicas fundamentais, que descrevem a interação da radiação com a matéria, e construindo modelos matemáticos dos quais calculam-se estimativas teóricas das observáveis físicas.

Os modelos de atmosferas devem descrever a estrutura física de uma atmosfera estelar e o seu espectro. Trata-se de um problema de grande complexidade do ponto de vista dos fenômenos físicos a serem analisados e dos cálculos necessários, por isso várias simplificações são usualmente feitas.

A geometria da atmosfera estelar é essencialmente esférica, mas em alguns modelos supõe-se que a atmosfera é composta de camadas homogêneas plano-paralelas. Isto é uma aproximação válida quando a profundidade da atmosfera é pequena comparada com o raio da estrela (Mihalas, 1978) e o fato dela ser considerada homogênea reduz o problema a uma dimensão.

Supor equilíbrio termodinâmico local (ETL) na atmosfera é outra simplificação importante. A hipótese de ETL implica que os números de ocupação de estados livres e ligados do material, a opacidade, a emissividade e todas as propriedades termodinâmicas tenham o valor que teriam no estado de equilíbrio termodinâmico descrito pelos valores locais de temperatura e densidade. Trata-se de uma suposição forte, pois tem-se uma teoria puramente local, não levando em consideração a interação de um elemento de gás com seus vizinhos, nem os gradientes normalmente presentes na atmosfera.

Costuma-se usar atmosferas cinzas, onde a opacidade é considerada como independente da frequência, como ponto de partida nos estudos, sendo o objetivo final sempre conseguir resultados aplicáveis a atmosferas não-cinzas e assim mais realistas.

Consideram-se geralmente atmosferas em equilíbrio hidrostático e radiativo, embora muitas vezes o interesse seja atmosferas convectivas e a simplificação acima não seja aplicável. Em atmosferas estelares o transporte de energia é feito pelo processo que for mais eficiente entre convecção e radiação. De maneira geral, o equilíbrio radiativo prevalece em estrelas de tipo espectral A e mais quentes, enquanto a convecção torna-se importante nas estrelas F e domina nos tipos espectrais frios. O fluxo convectivo é turbulento e, infelizmente, ainda não existe uma teoria definitiva para a convecção. A mais usada, teoria do comprimento de mistura, contém vários parâmetros físicos básicos e fornece uma visão no mínimo ilustrativa dos efeitos da convecção.

Em SBE uma componente ilumina a outra, afetando a distribuição de temperatura em ambas as atmosferas. Este efeito de irradiação mútua, historicamente chamado "efeito reflexão", pode ser descrito exatamente para atmosferas em equilíbrio radiativo. Eddington (1926) e Milne (1927) mostraram que, neste caso, o albedo bolométrico de reflexão é unitário, ou seja, que toda a energia incidente é localmente re-radiada/espalhada pelas camadas mais externas da atmosfera. Vaz & Nordlund (1985) mostraram ser possível, para a aproximação de atmosferas cinzas não convectivas, expressar em termos polinomiais um "albedo efetivo de reflexão" que leva em conta a dependência da reemissão com o comprimento de onda. Para atmosferas convectivas foram obtidas expressões numéricas aproximadas para o albedo efetivo de reflexão dependente da frequência. Entretanto a dependência do modelo em vários parâmetros, como o comprimento de mistura, o fluxo incidente e a direção de incidência, não permitiram uma generalização como a obtida no caso de atmosferas não convectivas. Estes resultados foram mais tarde estendidos para o caso de atmosferas não-cinzas (Nordlund & Vaz, 1990). Claret & Giménez (1992) estudaram albedos bolométricos de reflexão para o caso de irradiação mútua em sistemas tipo Algol (uma componente fria e uma quente). Eles mostraram a importância de levar em consideração a iluminação para evitar erros na análise dos espectros, mostrando, por exemplo, que em algumas regiões espectrais o espectro irradiado é bastante parecido com o não-irradiado com metalicidade mais baixa, o que poderia levar a conclusões errôneas sobre a metalicidade das componentes.

Outro efeito que afeta as atmosferas de SBE é o brilho por gravidade. Em sistemas binários onde as componentes se encontram relativamente próximas entre si, forças de maré acopladas com a rotação causam deformação nas estrelas. Essa distorção na forma da componente produz uma distribuição não uniforme da gravidade na superfície estelar, o que influencia a distribuição de brilho, tornando o disco estelar aparente mais brilhante nos pólos do que no equador. von Zeipel (1924) demonstrou que a distribuição de fluxo $\mathcal{F}$ radiativo ao longo da superfície estelar

deformada por rotação ou força de maré varia com a gravidade segundo

$$\mathcal{F} \ \alpha \ g^{\beta} \tag{10.1}$$

sendo β, o expoente de brilho por gravidade, igual a 1.0 para atmosferas radiativas. Em 1967, Lucy determinou β para o caso de atmosferas convectivas, obtendo 0.32. Entretanto estes valores nem sempre concordam com os obtidos através da análise de dados observacionais (Alencar & Vaz, 1997) e um estudo cuidadoso e diretamente voltado para SBE ainda se fazia necessário. Infelizmente poucos são os sistemas binários analisados de maneira sistemática e com dados de qualidade boa o suficiente (levando por exemplo à determinação de parâmetros absolutos com 1-2% de erro) que permitam obter valores confiáveis para grandezas como os expoentes de brilho por gravidade (Alencar, 1995).

O escurecimento de bordo, apesar de não ser um efeito de proximidade, foi estudado por ser afetado pelo efeito reflexão. O disco estelar de uma estrela é visto mais brilhante no centro do que nas bordas pois, apesar de enxergarmos a mesma profundidade óptica em ambas situações, corresponde a camadas mais profundas, e consequentemente mais quentes, no centro do que nas bordas. Trata-se de um efeito bastante estudado em atmosferas não-iluminadas, várias leis tendo sido propostas para descrever a distribuição de intensidades ao longo do disco estelar (Van Hamme, 1993; Díaz-Cordovés *et al.*, 1995). Entretanto, apesar deste efeito ser bastante afetado pelo efeito reflexão (Claret & Giménez, 1990), os modelos de síntese de curvas de luz usam coeficientes de escurecimento de bordo calculados por modelos de atmosferas não-iluminadas, o que é, no mínimo, uma inconsistência.

10.2.1 O programa UMA (Uppsala Model Atmospheres)

Usou-se o programa UMA (Uppsala Model Atmospheres), numa versão modificada por Vaz (1985) para levar em consideração a iluminação externa. O código foi desenvolvido para estrelas frias ($T_{\rm ef}$<8 000 K), atmosferas em equilíbrio hidrostático, usando uma estrutura plano-paralela, equilíbrio temodinâmico local e modelando a convecção através do comprimento de mistura.

Modelos não-iluminados são definidos pela temperatura efetiva $T_{\rm ef}$, a gravidade superficial g e a massa M da estrela, o parâmetro de comprimento de mistura $\alpha = l/H_P$ e a composição química (fixada no valor solar em todos os nossos trabalhos). Além dos parâmetros citados acima, modelos iluminados precisam da direção da iluminação ω (=cos(θ), onde θ é o ângulo de incidência em relação à normal à superfície), da temperatura efetiva do fluxo iluminante, T_h, e do raio aparente, r_h,

da estrela iluminante. O raio aparente corresponde à razão entre o raio da estrela fonte e a distância de seu centro ao ponto na superfície da estrela refletora. A Fig. 10.1 ilustra a geometria descrita acima.

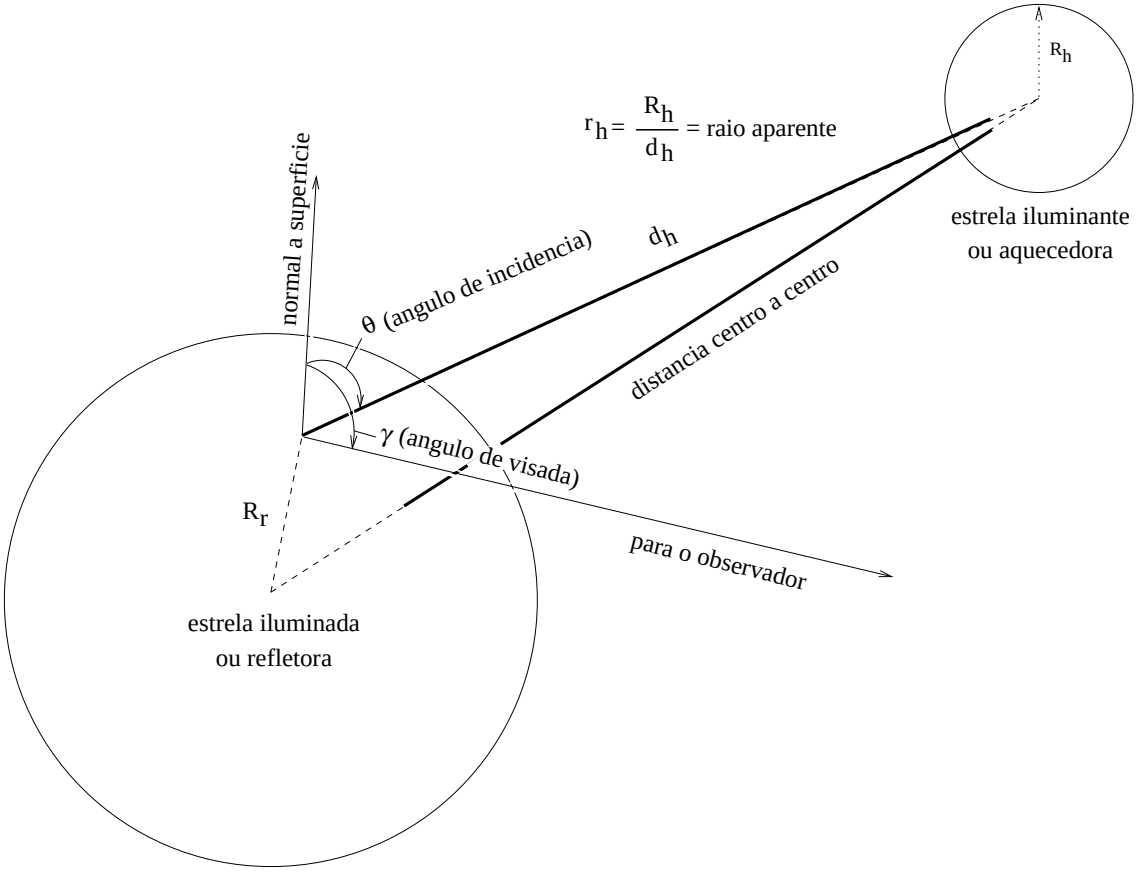

Figura 10.1: Geometria de iluminação em um sistema binário.

Usaram-se modelos estelares (Claret, 1995, X=0.70, Z=0.02) para associar $T_{\rm ef}$ com M para estrelas não deformadas na SP de idade zero. Referimo-nos a modelos com e sem absorção de linha como "não-cinzas" e "cinzas" respectivamente, incluindo nos modelos "cinzas" a variação da opacidade do contínuo com a frequência (como em Nordlund & Vaz, 1990). Estudaram-se atmosferas iluminadas cinzas (i.e. apenas com a opacidade do contínuo) e não-cinzas (com opacidade de linhas ou Funções de Distribuição de Opacidade – ODFs) no equilíbrio convectivo. As ODFs limitaram a faixa de temperaturas dos nossos estudos para aquelas correspondendo

a estrelas na SP de idade zero com massas de $0.6\,M_\odot$ a $1.5\,M_\odot$.

10.2.2 Efeito de brilho por gravidade

Inicialmente estudou-se com o programa UMA o comportamento do expoente de brilho por gravidade em atmosferas não-iluminadas cinzas e não-cinzas na faixa de temperaturas $3\,700\,\mathrm{K} < T_{\mathrm{ef}} < 7\,000\,\mathrm{K}$. A lei de brilho por gravidade, Eq. (10.1), foi válida com um alto grau de confiança para todos os modelos gerados. Os expoentes β foram calculados teoricamente para atmosferas convectivas forçando a entropia no fundo da atmosfera a ser igual em modelos que devem representar uma mesma estrela deformada (modelos com diferentes $\log g$, para simular deformações). Nosso modelo reproduz o resultado médio de Lucy (1967), mas o valor β=0.32 por ele proposto foi confirmado apenas para $T_{\mathrm{ef}} \sim 6\,500\,\mathrm{K}$. Vimos que β depende de T_{ef}, sendo bastante insensível a variações do parâmetro de comprimento de mistura, da massa da estrela e do uso de atmosferas cinzas ou não. Um polinômio de terceira ordem, $\beta(T_{\mathrm{ef}})$ (Eq. 3.2), foi proposto por ser uma maneira conveniente de expressar os resultados para o uso na análise de SBE (Fig. 10.2). Os coeficientes dos polinômios cinza e não cinza estão apresentados na Tabela 3.1. A existência de um máximo na relação $\beta(T_{\mathrm{ef}})$ é devida a mudanças em ambas as propriedades da convecção e opacidade dos modelos. Claret (1998) também realizou cálculos do expoente de brilho por gravidade em modelos não-iluminados usando uma versão modificada da técnica de triângulos (Kippenhahn *et al.*, 1967) em modelos de evolução estelar. Os resultados obtidos por ele concordam com os nossos, descrevendo o mesmo comportamento para β na região em comum dos parâmetros.

Um primeiro teste observacional foi realizado com o sistema PSP triplo e eclipsante TY CrA (Casey *et al.*, 1993, 1995, 1998), implementando-se o polinômio $\beta(T_{\mathrm{ef}})$ na versão modificada do modelo WD (Wilson & Devinney, 1971; Wilson, 1993) descrita por Vaz *et al.* (1995). As curvas de luz foram analisadas com o programa WD, usando o valor proposto por Lucy e nossa aproximação para β. Os resultados obtidos com o valor do expoente proposto ($\beta = 0.41$ na temperatura efetiva da secundária) foram mais consistentes do que usando β=0.32, gerando uma componente primária (B8-9 SP de idade zero) cujas dimensões absolutas estavam mais próximas do valor teórico esperado para uma estrela nesta fase.

Uma explicação detalhada dos passos descritos acima encontra-se no Capítulo 3.

A segunda parte do trabalho com o expoente de brilho por gravidade foi o estudo da influência exercida no expoente pelo efeito reflexão (iluminação mútua em binárias próximas). Usou-se o programa UMA com atmosferas cinzas e não-cinzas, iluminadas por fluxos cinzas e não-cinzas novamente para $3\,700\,\mathrm{K} < T_{\mathrm{ef}} < 7\,000\,\mathrm{K}$, e

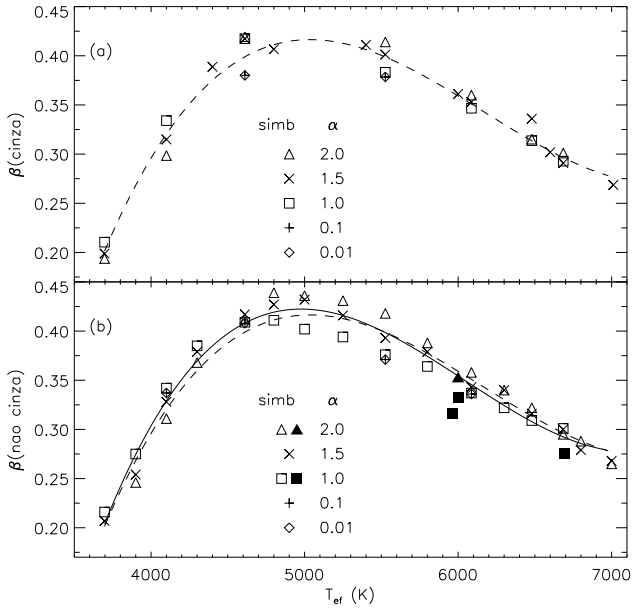

Figura 10.2: Variação de β com T_{ef} para modelos não-iluminados cinzas (**a**) e não-cinzas (**b**). Os símbolos cheios representam os cálculos de Lucy para uma composição química similar. Os polinômios de terceira ordem estão mostrados para os modelos cinzas (tracejado) e não-cinzas (linha contínua).

fluxos externos com temperaturas variando de $7\,000\,\mathrm{K}<T_\mathrm{h}<12\,000\,\mathrm{K}$. Os fluxos externos com $T_\mathrm{h}\geq 10\,000\,\mathrm{K}$ foram interpolados dos modelos de Kurucz (1979) disponíveis eletronicamente para os comprimentos de onda usados pelo programa UMA.

Os resultados obtidos para atmosferas cinzas iluminadas por fluxos cinzas e não-cinzas foram bastante similares, mostrando que, neste caso, β depende principalmente da quantidade de energia incidente e da direção da iluminação, além da dependência com a temperatura efetiva observada nos modelos sem iluminação. A iluminação externa aumenta o valor de β, quanto maior a quantidade de fluxo incidente, maior o valor do expoente, até ocorrer a saturação ao atingir o valor proposto por von Zeipel (1924) para atmosferas em equilíbrio radiativo. Este comportamento ocorre pois, ao iluminarmos a atmosfera, a convecção diminui à medida que se aumenta o fluxo externo, atingindo assintoticamente o equilíbrio radiativo. Decidimos apresentar o resultado final como expressões analíticas (polinômios) para facilitar

a implementação do efeito em programas de síntese de curvas de luz. A Fig. 10.3

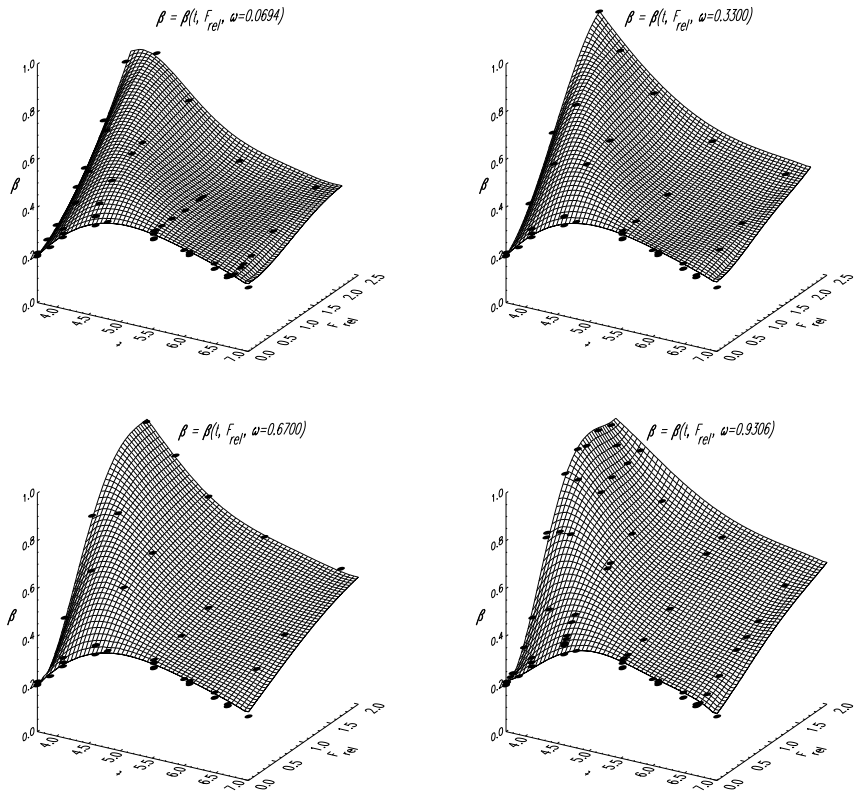

Figura 10.3: Variação de β com $T_{\rm ef}$, $F_{\rm rel}$ e ω para modelos iluminados. As grades representam a parametrização proposta e os pontos são os cálculos obtidos com os modelos de atmosferas.

ilustra o comportamento descrito acima.

Atmosferas não-cinzas iluminadas por fluxos cinzas e não-cinzas mostraram-se bem mais complexas, apresentando uma dependência extra do expoente com a temperatura de iluminação. Neste caso, quanto maior a temperatura da estrela iluminante, menor é o valor do expoente β para o mesmo valor de fluxo relativo ($F_{rel} = [T_{\rm h}/T_{\rm ef}]^4 {r_h}^2 \omega$), ou seja, existe uma dependência de β com T_h que não é descrita por F_{rel}. Isso ocorre devido à dependência da opacidade de linha espectral com o comprimento de onda. A medida que T_h aumenta, o fluxo externo desvia-se para o UV onde a opacidade de linha é tão grande que impede que grande parte

do fluxo externo atinja as camadas onde o contínuo se forma. A convecção é assim menos afetada pela iluminação e tem-se um valor de β menor, empurrando o efeito de aumentar o expoente para fluxos relativos maiores.

Os valores obtidos no caso de atmosferas cinzas iluminadas podem, entretanto, ser usados para atmosferas não-cinzas, desde que T_h não difira mais do que $\approx$25% de $T_{\rm ef}$. Para diferenças maiores entre as temperaturas é necessário corrigir o fluxo relativo incidente por um fator de penetração, correspondente à absorção do fluxo UV nas camadas superiores do modelo iluminado.

Um estudo detalhado dos resultados da influência do efeito reflexão nos expoentes de brilho por gravidade é mostrado no Capítulo 4.

10.2.3 Escurecimento de bordo

Estudou-se o efeito da iluminação nos coeficientes de escurecimento de bordo em atmosferas não-cinzas iluminadas por fluxos não-cinzas com o programa UMA. Foram realizados cálculos de coeficientes monocromáticos, bolométricos e para alguns filtros fotométricos (u, v, b, y, U, B, V, R, I), obtendo-se coeficientes para 5 leis de escurecimento de bordo (linear, quadrática, cúbica, logarítmica e raiz quadrada) segundo dois métodos diferentes, um proposto por Claret & Giménez (1990) (CG) e outro por Van Hamme (1993) (VH).

O programa UMA gera intensidades em 6 direções angulares diferentes (μ = 0.06943, 0.33001, 0.5, 0.66999, 0.93057 e 1.0) e 368 comprimentos de onda variando de 1500 Å a 124000 Å. O método de CG determina os coeficientes por ajuste de mínimos quadrados nas intensidades normalizadas e integradas, enquanto o segundo método segue o procedimento descrito por VH, onde um número de vínculos físicos, igual ao número de coeficientes a serem determinados, é estabelecido. Os coeficientes de escurecimento de bordo são obtidos solucionando as equações dos vínculos. Calculando leis de um parâmetro, o vínculo usado é a conservação do fluxo total e para leis de dois parâmetros adiciona-se o vínculo que a intensidade média da aproximação usada seja igual à do modelo de atmosferas.

A iluminação externa afeta fortemente as leis de escurecimento de bordo e os coeficientes tornam-se bem diferentes daqueles obtidos com atmosferas não-iluminadas. Vê-se na Fig. 10.4 que, ao aumentarmos a quantidade de energia incidente, por exemplo aumentando o raio aparente enquanto os outros parâmetros são mantidos fixos, a lei não-iluminada não representa mais as intensidades calculadas, mostrando que coeficientes não-iluminados geram leis de escurecimento de bordo erradas quando usados em estrelas iluminadas.

Optamos por fazer os cálculos finais com o método de VH, pois para alguns

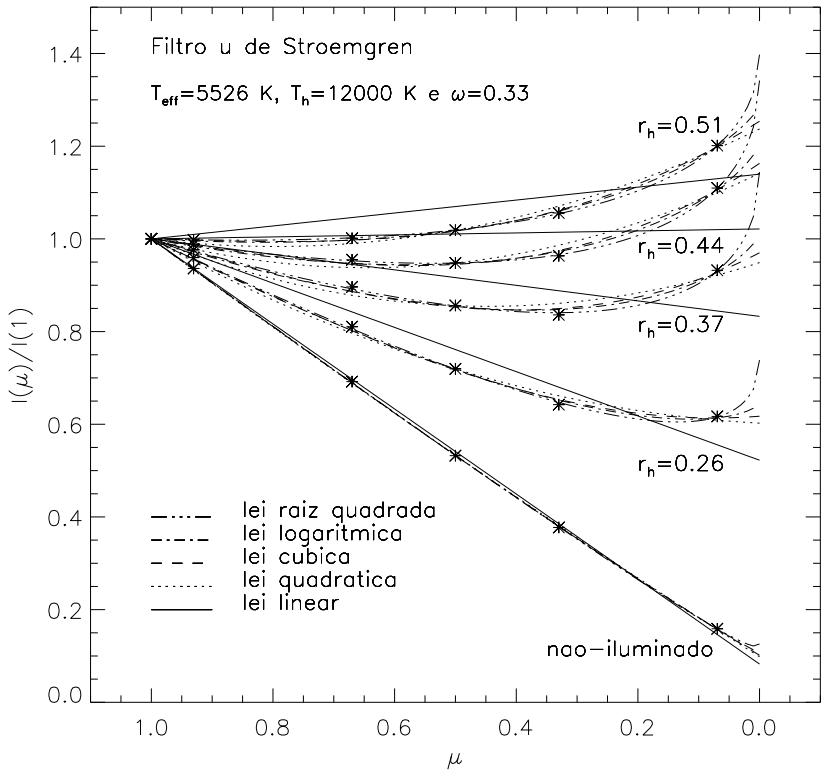

Figura 10.4: Ajuste de leis de escurecimento de bordo, um modelo não-iluminado e 4 iluminados (variando r_h).

modelos iluminados, mesmo escolhendo leis não lineares de ajuste, o fluxo total não se conservou usando o método de CG.

Um resultado interessante que apareceu durante os cálculos de escurecimento de bordo foi que, dependendo do conjunto de parâmetros escolhidos, observa-se um efeito de brilho de bordo ao invés de escurecimento (veja a Fig. 10.4). Este efeito pode ser compreendido da seguinte maneira: ao iluminarmos a atmosfera de uma estrela a distribuição de temperaturas torna-se mais homogênea a medida que aumentamos o fluxo externo incidente, até atingir um estado onde não existe escurecimento de bordo e o brilho do disco estelar é quase homogêneo. Se continuarmos a aumentar o fluxo externo, seja aproximando as estrelas ou aumentando a temperatura da estrela iluminante ou, ainda, simplesmente alterando a direção de

incidência da iluminação, atinge-se uma situação onde as camadas mais externas estão mais quentes do que as internas. Como vemos mais camadas externas nas bordas do que no centro, tem-se o efeito de brilho de bordo.

Apresentamos nossos resultados em tabelas que podem ser interpoladas em modelos de síntese de curva de luz de SBE. Ajustamos polinômios aos coeficientes calculados para faixas de comprimento de onda correspondentes aos filtros fotométricos como uma forma alternativa (e mais rápida) de utilizar os resultados obtidos.

Um estudo detalhado dos resultados da influência do efeito reflexão nos coeficientes de escurecimento de bordo é realizado no Capítulo 5.

10.3 Estrelas Pré-Sequência Principal

Acredita-se que a maioria das estrelas nascem em Nuvens Moleculares Gigantes (NMG) que são regiões interestelares frias (temperaturas cinéticas ~ 10 K) e densas ($\mathrm{n}(H_2) \sim 200 - 300\,\mathrm{cm}^{-3}$). Devido à baixa temperatura, a pressão térmica sozinha não é suficiente para impedir que o colapso da nuvem ocorra e pensa-se que o suporte contra a gravidade seja em parte devido a campos magnéticos e turbulência. As Nuvens Moleculares Gigantes são estruturas não uniformes constituídas de filamentos e de núcleos muito densos ($\sim 10^4\,\mathrm{cm}^{-3}$). Nestas altas densidades o colapso deveria ocorrer em algumas centenas de milhares anos, mas o processo de formação estelar é bastante ineficiente e de acordo com as observações apenas 2-3% do gás molecular em uma NMG forma estrelas. Acredita-se que isto seja causado em parte pela formação de estrelas massivas que rapidamente ionizam o meio e dispersam o gás molecular. A poeira também parece ser importante na formação estelar. A extinção devida à poeira deve facilitar a formação estelar ao diminuir a temperatura dos núcleos das nuvens (McKee, 1999). A absorção da radiação externa pela poeira deve reduzir a ionização na nuvem molecular, o que reduz o acoplamento entre íons e neutros e permite a difusão do gás através das linhas de campo magnético. Este efeito reduz o suporte magnético da nuvem e acelera o processo de formação estelar.

Quando um núcleo da nuvem se torna instável gravitacionalmente o colapso se inicia em velocidades próximas de queda-livre. Acredita-se que isto aconteça inicialmente de dentro para fora, a parte central e mais densa colapsando primeiro. Por menor que seja a velocidade rotacional inicial do núcleo, seu momento angular será transferido para a estrela em formação. Devido à rapidez do processo e à diferença em tamanho entre a nuvem e a estrela, é bastante provável que o material forme um disco, um sistema estelar múltiplo ou ambos ao invés de cair diretamente na massa central.

A protoestrela e o disco formam-se envoltos na nuvem que os deu origem. Daí em diante, no caso de estrelas de baixa massa, a maioria da massa estelar será adquirida por acresção do disco.

Ventos, jatos e outras formas de ejeção de material ("outflows" moleculares) são gerados pelo sistema jovem da estrela e disco, ajudando a dissipar a nuvem que os envolve. Quando uma estrela Pré-Sequência Principal se torna visível no óptico ela é chamada de estrela T Tauri se tiver baixa massa (M <2 $M_{\odot}$) e AeBe de Herbig no caso de massas intermediárias (2 $M_{\odot}$< M < 8 $M_{\odot}$). Nesta fase a estrela ainda recebe massa do disco, mas em taxas bem menores do que na fase protoestelar. Não se sabe ao certo o que provoca o fim do disco. Ele pode simplemente alimentar a estrela até acabar, mas pode também ser rompido por instabilidades de maré ou falhas criadas pela formação de planetas. Algumas estrelas T Tauri, chamadas de estrelas T Tauri fracas, não possuem disco de acresção desde muito cedo ($\sim 10^6$ anos) enquanto outras, as estrelas T Tauri clássicas (ETTC), em idades e tipo espectrais semelhantes ainda o têm.

Estrelas T Tauri clássicas possuem excesso de emissão no IV associado com o reprocessamento da radiação da estrela pelo disco. Elas também apresentam um contínuo em excesso no UV produzido em manchas quentes onde o material atinge a estrela no processo de acresção. ETTCs apresentam várias linhas permitidas e proibidas em emissão e Lítio (6707.8 Å) em absorção. Estas estrelas são variáveis fotométricas devido à presença de manchas quentes e frias nas suas superfícies. Acredita-se que as manchas frias são causadas por atividade magnética que é também responsável por fulgurações ("flares") e emissão no raio-X.

As estrelas T Tauri, por possuírem massas próximas à do Sol, oferecem a oportunidade única de estudar o passado do nosso Sol e tentar compreender o processo de formação do próprio sistema Solar.

10.3.1 Modelos de acresção magnetosférica

Vários modelos foram propostos para explicar as características observacionais das ETTCs. Os mais aceitos hoje em dia são os modelos de acresção magnetosférica (Shu *et al.*, 1994; Hartmann *et al.*, 1994; Muzerolle *et al.*, 1998a). Um desenho simplificado da configuração deste modelo é mostrado na Fig. 10.5 e uma visão do que acontece perto da estrela segundo o modelo de Shu está na Fig. 10.6. Nestes modelos um campo magnético intenso interrompe o disco circunstelar no ponto de co-rotação e trava a estrela ao disco. A estrela adquire massa através de linhas fechadas de campo magnético que a ligam ao disco. Linhas abertas do campo que se originam perto do raio de co-rotação carregam um vento e podem formar uma espiral criando um jato.

Linhas abertas de campo na própria estrela também contribuem para o fluxo de material para fora. Acredita-se que as linhas de emissão permitidas são produzidas no funil de fluxo magnético, onde o material é acelerado. Quando o material atinge a superfície da estrela uma mancha ou um anel quente se formam e produzem um contínuo em excesso no UV (conhecido como velamento). Linhas de emissão proibidas originam-se no fluxo para fora ou no jato e são observadas desviadas para o azul devido à ocultação pelo disco do fluxo que se afasta do observador.

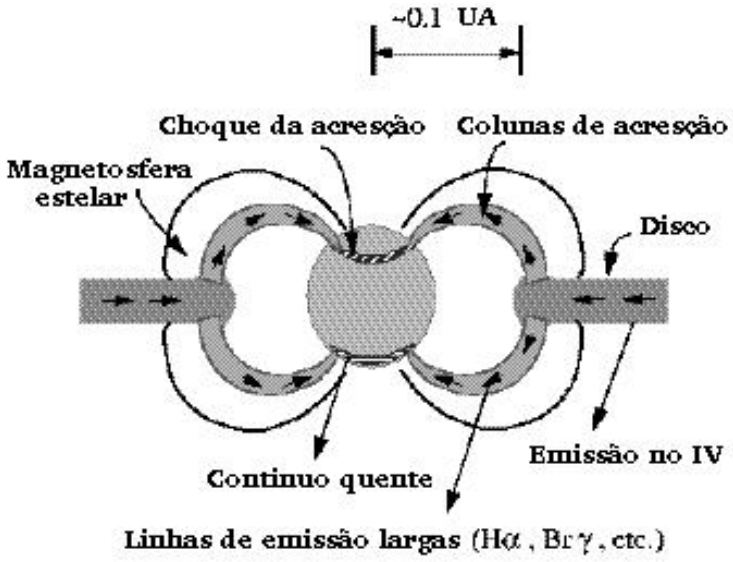

Figura 10.5: Representação simplificada do modelo magnetosférico (adaptado de Hartmann , 1999).

Vários trabalhos observacionais confirmaram características previstas pelos modelos de acresção magnetosférica, como linhas de emissão com perfis do tipo P Cygni invertido causadas pelo material caindo em queda livre na estrela (Edwards *et al.*, 1994), linhas de emissão assimétricas levemente desviadas para o azul devido à ocultação pelo disco de parte do material se afastando do observador (Muzerolle *et al.*, 1998a) e variações nas linhas com periodicidade igual ao período de rotação da estrela (Johns & Basri, 1995b) previstas pelo modelo magnetosférico de Shu *et al.* (1994).

Entretanto, os perfis de linha teóricos tendem a ser mais assimétricos e sempre menos alargados do que os observados e nem sempre as variações das linhas espec-

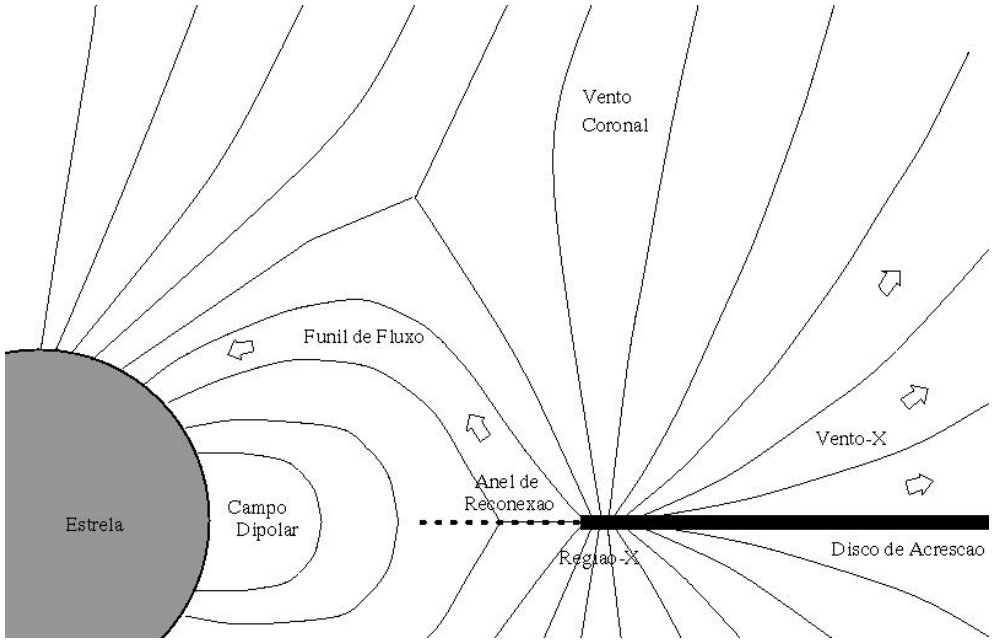

Figura 10.6: Configuração do modelo de acresção magnetosférica (Shu *et al.*, 1999).

trais são relacionadas ao período de rotação da estrela (Johns & Basri , 1995a).

A grande dificuldade em modelar ETTCs é que o processo de acresção é dinâmico e os perfis de linha podem mudar drasticamente em poucas horas. O fato de uma determinada estrela apresentar perfis de linhas que concordam com a teoria não significa que isto será sempre o caso e não é necessariamente um apoio irrefutável aos modelos. O verdadeiro desafio para os modelos será reproduzir todos os perfis de linha que uma determinada estrela possa exibir ou, de maneira equivalente, os vários perfis de linha apresentados por muitas ETTCs.

Uma maneira de testar os modelos magnetosféricos é investigar linhas de emissão observadas em várias estrelas T Tauri. Das relações entre as larguras equivalentes das linhas e das suas componentes podem-se inferir várias características dos modelos. Pode-se também investigar a simetria dos perfis de linha e seus formatos além de ajudar a calibrar os modelos com valores realistas para parâmetros como velocidade de vento e alargamento de linha. Uma outra maneira de testar os modelos é observar uma mesma estrela por várias noites consecutivas durante um período longo de tempo. Isto é importante para tentar entender todos os tipos de perfis que podem ser produzidos por uma única estrela, onde vários parâmetros têm que ser

mantidos fixos mas várias processos são dinâmicos. Decidimos fazer os dois tipos de testes.

10.3.2 Estudo de perfis espectrais de linhas de emissão de estrelas T Tauri clássicas.

Foram analisadas 15 linhas de emissão permitidas de 30 estrelas T Tauri clássicas observadas com o espectrógrafo Hamilton echelle acoplado ao telescópio de 3m do observatório Lick da Universidade da Califórnia. O objetivo foi testar as previsões do modelo de acresção magnetosférica levando-se em conta evidências observacionais publicadas anteriormente que dão suporte ao modelo. Discute-se também a relação entre diferentes regiões de formação de linhas e procuram-se bons indicadores de taxas de acresção.

As linhas selecionadas foram decompostas usando múltiplas gaussianas e as larguras equivalentes de todas as linhas e suas componentes foram medidas. Os valores obtidos foram usados para estudar as correlações entre "fluxos" (larguras equivalentes corrigidas do velamento) de diferentes linhas e entre "fluxos" e parâmetros como a taxa de acresção de massa. As correlações entre diferentes linhas podem indicar regiões de formação em comum ou implicar que um processo em comum está afetando as regiões de formação de ambas as linhas ao mesmo tempo.

Mostrou-se que linhas de emissão que fazem a transição para um mesmo nível de energia são muito bem correlacionadas, como é o caso de Hβ com Hα e entre o tripleto de Ca no infra-vermelho. Isto era esperado, pois essas linhas precisam das mesmas condições físicas para serem produzidas e tendem a ser afetadas pelos mesmos processos. Como mostrado em estudos anteriores a maioria das linhas tende a ser formada por mais de um componente - componentes largas e estreitas para o He I e o Ca II e em emissão e absorção para a série de Balmer e o Sódio D. Estas componentes são provavelmente formadas em regiões diferentes, pois suas características permanecem distintas em toda a nossa amostra de estrelas e várias correlações encontradas são válidas apenas para uma das componentes.

De acordo com os nossos dados a emissão das linhas de Balmer, as componentes largas do He I e do Ca II e as linhas de Ferro (quando em emissão) são formadas principalmente no funil magnetosférico. Alternativamente, a componente larga do He I pode também ter origem na região de impacto na estrela do material em acresção, onde as temperaturas são mais altas e assim mais apropriadas para a formação desta linha ao invés do próprio fluxo magnetosférico. As componentes estreitas do He I e do Ca II devem originar-se em parte na superfície da estrela

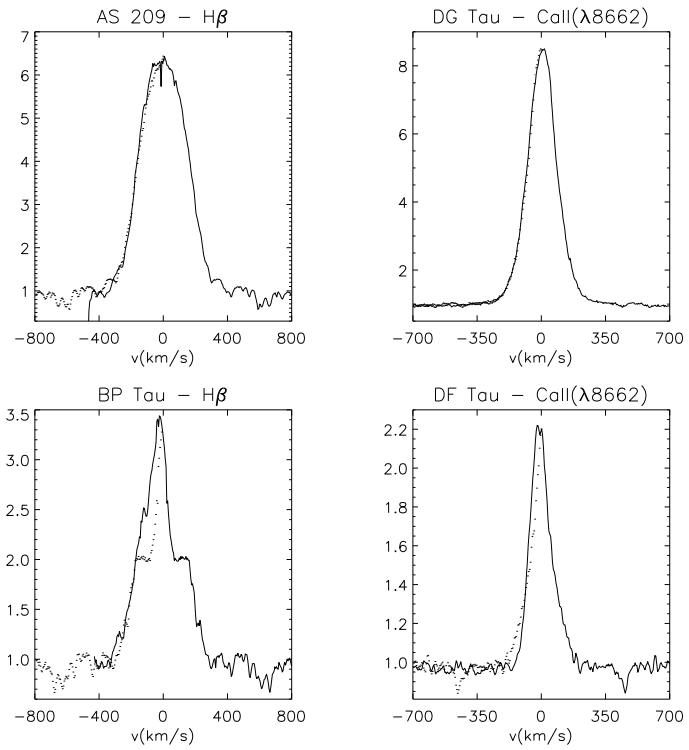

Figura 10.7: Linhas de emissão com os lados vermelhos refletidos (em pontilhado). As linhas de cima são simétricas e não previstas pelos modelos e as de baixo assimétricas concordam com as previsões gerais dos modelos de acresção magnetosférica.

onde a perturbação da acresção influencia a atmosfera estelar e em parte na cromosfera estelar não perturbada. O vento é a origem da absorção desviada para o azul facilmente vista nas linhas do Na D e de Balmer.

Neste trabalho foram confirmados vários pontos importantes dos modelos como a correlação entre acresção e perda de massa, a presença de componentes largas de emissão quase sempre centradas ou levemente deslocadas para o azul e ocasionais componentes vermelhas em absorção. Mostrou-se, entretanto, que as componentes largas em emissão, supostamente formadas no fluxo magnetosférico de acresção suportam apenas parcialmente os modelos. Diferentes das previsões, elas estão às vezes deslocadas para o vermelho e são geralmente simétricas (Fig. 10.7). Assim, os perfis de linhas teóricos não se parecem muito com os observados. Enfatiza-se a necessidade de incluir turbulência nos modelos de acresção para que os perfis teóricos

concordem com as observações. Rotação, assim como componentes devidas a perda de massa, são aspectos também necessários para reproduzir as observações.

Os resultados detalhados deste estudo são apresentados no Capítulo 7.

10.3.3 Estudo da variação temporal de linhas de emissão da estrela T Tauri clássica DR Tau

DR Tau é uma estrela que apresenta variações fotométricas grandes (1-3 mag), atribuídas a manchas quentes e frias (e.g. Bertout *et al.*, 1977; Bouvier *et al.*, 1993; Kenyon *et al.*, 1994; Ultchin *et al.*, 1997), assim como valores altos de velamento no óptico (Basri & Batalha , 1990; Valenti , 1994). Ela apresenta a linha proibida de [OI] (λ6300) em emissão com duplo pico (Hartigan *et al.*, 1995; Hirth *et al.*, 1997), sugerindo a presença de ejeção colimada de massa. A estrela parece exibir variabilidades quasi-periódicas, pois vários períodos (de 4 a 9 dias) foram encontrados em estudos fotométricos e espectroscópicos. Ela possui linhas de emissão prominentes que apresentam uma grande variedade e variabilidade de perfis (Appenzeller *et al.*, 1988; Guenther & Hessman , 1993; Johns & Basri , 1995a; Hessman & Guenther , 1997; Smith *et al.*, 1999). Apesar de ser uma das ETTCs mais estudadas, ainda faltava um estudo espectroscópico de alta resolução, com acompanhamento por um longo período de tempo, para tentar entender a origem e variabilidade de suas linhas.

O objetivo deste estudo é analisar um conjunto de 103 espectros echelle da estrela T Tauri clássica DR Tau obtidos na última década. Pretende-se investigar as regiões onde se originam as linhas de emissão, tentar compreender a relação entre diferentes regiões de formação estelar e testar as previsões dos modelos de acresção magnetosférica. Grande parte da análise das variações e possíveis periodicidades foi feita com uma série de programas desenvolvidos em IDL (Interactive Data Language).

Uma amostra dos perfis de linha observados está na Figura 10.8. As 2 primeiras observações estão separadas por 3 dias em Outubro de 1989 e as duas últimas por 2 dias em Dezembro de 1998. Hα apresenta perfis P Cygni tipo I em $\sim$ 75% dos casos (Figura 10.8*c* e *d*). Porém, as vezes, uma emissão no azul aparece, como nas Figuras 10.8*a* e *b*. A linha de Hβ tende a se comportar como a de Hα , mas apresentando a emissão no vermelho bem mais fraca. A linha de He I possui uma componente estreita e centrada na velocidade de repouso da estrela, uma larga um pouco deslocada para o azul e, esporadicamente, pode-se ver uma componente em absorção deslocada para o vermelho. Esta linha tende a variar simultaneamente com as linhas da série de Balmer. A linha de Ca II muda basicamente apenas em intensidade.

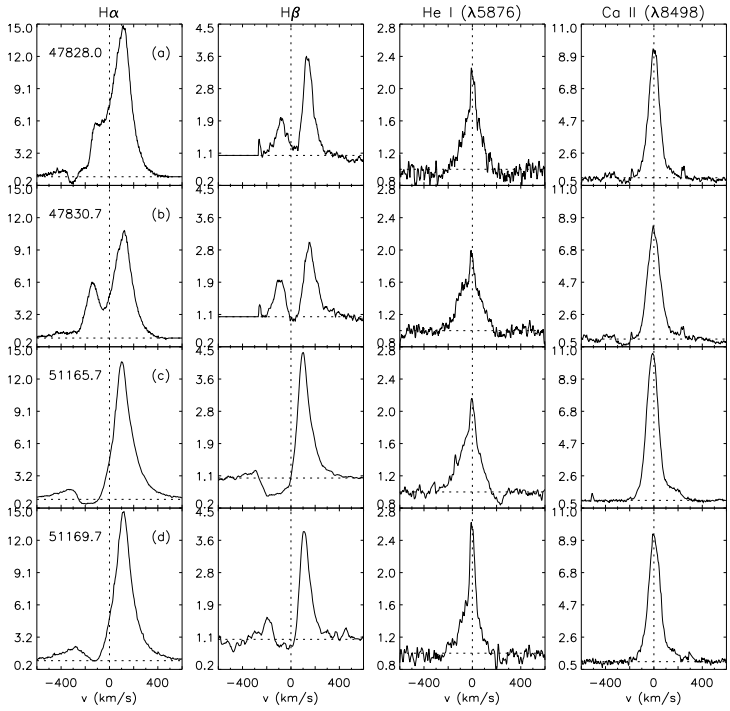

Figura 10.8: Amostra de perfis de linha. As linhas pontilhadas horizontais representam o nível do contínuo. As linhas pontilhadas verticais correspondem ao centro da linha espectral na velocidade de repouso da estrela. Os números nos panéis à esquerda são as datas julianas das observações menos 2400000.0.

O aparecimento da emissão no azul em Hα não é um processo periódico, como pode ser notado na Figura 10.9. As duas sequências correspondem a aproximadamente 1 semana de observações e, enquanto que na primeira série a emissão no azul aparece e desaparece em poucos dias, na segunda quase nada acontece.

Para explicar os espectros obtidos propomos que o sistema é visto mais de face do que de lado, como mostrado na Figura 10.10. Várias razões nos levam a favorecer este tipo de geometria. A decomposição que melhor se aplica à linha de Hα corresponde a uma emissão desviada para o vermelho, uma absorção desviada para o azul e uma emissão com pouca intensidade, largura a meia altura grande e centrada no comprimento de onda de repouso. A primeira componente seria produzida por

material nas linhas de fluxo magnetosférico que ligam o disco à estrela. A segunda teria origem no vento e a terceira corresponderia a uma componente de turbulência do próprio campo magnético. A emissão no azul que aparece esporadicamente deve ter origem em ejeções intensas de massa.

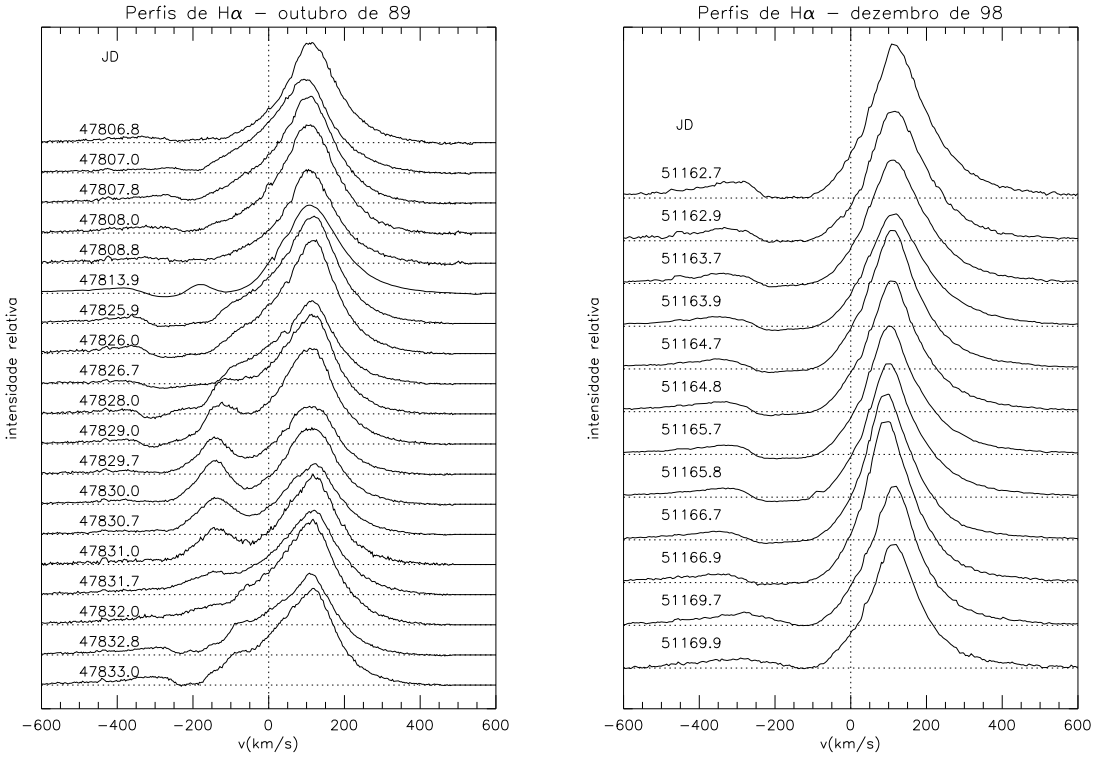

Figura 10.9: Sequência de observações em Outubro de 1989 e em Dezembro de 1998. As linhas pontilhadas têm o mesmo significado daquelas na Fig 10.8 e JD corresponde à data juliana das observações menos 2400000.0.

A linha de Hα apresenta variabilidade no lado azul muito maior do que no vermelho e interpretamos as variações como sendo devidas a processos de ejeção de matéria. O pico de emissão no vermelho é bastante simétrico em sua parte superior, o que indica que um mesmo fenômeno é responsável pelo lado direito e esquerdo desta parte do pico. Além disto esta parte da emissão apresenta ótima

autocorrelação e pouca correlação com outras partes da linha. Isto tudo indica que processos diferentes são responsáveis pela emissão no vermelho e pelas variações no azul da linha de Hα .

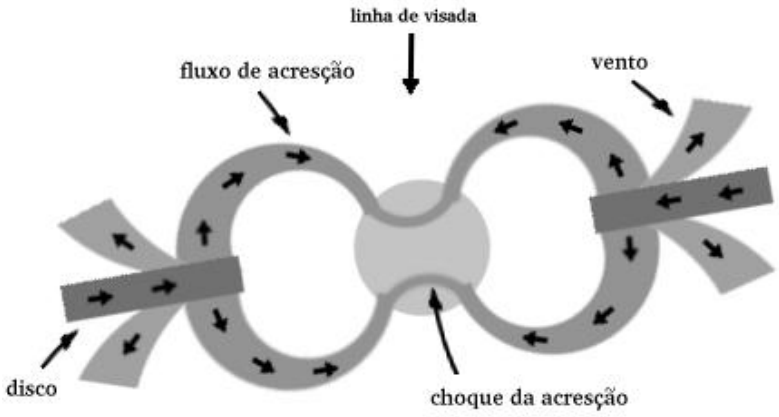

Figura 10.10: Representação simplificada do sistema DR Tau. As setas pequenas indicam o fluxo de material do disco.

Mostramos também que as componentes largas de linhas como as de He I e de Ca II podem ser produzidas em grande parte por turbulências do campo magnetosférico, já que para valores típicos de campo magnético medidos em ETTCs (∼2-3 kG) e densidades do gás usadas nos modelos de acresção ($\sim 10^{-9}$g/cm^3) tem-se velocidades de Alfvén da ordem de 200 km s^{-1}. Isto explicaria a simetria destas componentes, que geralmente não se parecem com os perfis de linha gerados por modelos de acresção magnetosférica.

Os períodos que obtivemos com os diversos conjuntos de dados variam bastante entre 4 e 9 dias, implicando que as variações são causadas por processos não estacionários de acresção e perda de massa.

O fato de DR Tau apresentar uma variedade muito grande de perfis de linha sugere que estrelas T Tauri com perfis de linhas de emissão bem diferentes podem, na verdade, ser sistemas muito parecidos, mas que foram observados em momentos distintos de atividade. Como as variações não são sempre periódicas, pode ser necessário observar uma estrela por longos períodos de tempo para que se tenha uma amostra razoável dos perfis de linha por ela apresentados.

Figuras animadas no formato Mpeg mostrando a variação de várias linhas de emissão de DR Tau encontram-se disponíveis no endereço
`http://sprg.ssl.berkeley.edu/~cmj/html/drtau.html`.

Os perfis das linhas de Balmer de DR Tau são bastante diferentes dos perfis magnetosféricos teóricos disponíveis na literatura. Por isso decidimos investigar a influência dos vários parâmetros geométricos e da distribuição de fluxo ao longo das linhas de campo nas características dos perfis de linhas. Calculamos um modelo de dipólo magnético bastante simples onde o material cai em queda livre do disco na estrela ao longo das linhas de campo magnético. A intensidade dos perfis de linha obtidos não tem nenhum significado físico, mas o formato da linha reflete a geometria do sistema e a distribuição de fluxo na magnetosfera. Usando funções fonte semelhantes às de Hartmann *et al.* (1994) obtivemos perfis de linha com as mesmas características gerais que os deles (Fig. 10.11). Estes perfis entretanto não se parecem com os observados em DR Tau.

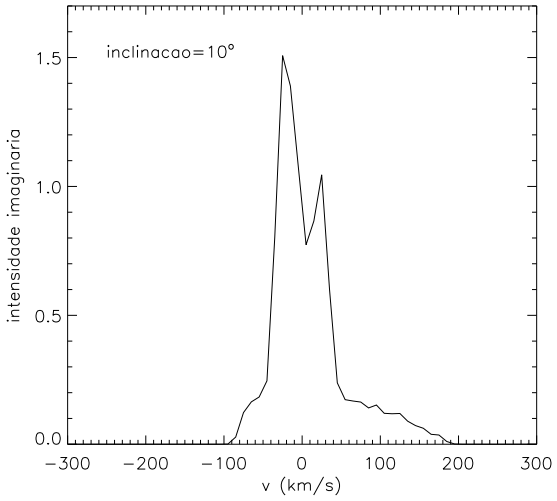

Figura 10.11: Perfil de linha teórico obtido usando função fonte semelhante à de Hartmann *et al.* (1994).

Um outro resultado obtido, com a emissividade de linha aumentando fortemente perto da estrela, pode ser visto na Figura 10.12. Obtivemos perfis semelhantes a este, com picos de emissão desviados para o vermelho com $0° < i < 20°$. Valores maiores de inclinação geram perfis que não se parecem mais com os observados em DR Tau. Ainda não sabemos com certeza qual a estrutura de temperaturas que geraria a distribuição de fluxo da Figura 10.12, mas, na verdade, ainda não se conhece a estrutura de temperatura na magnetosfera. O que a Figura 10.12 mostra é que é possível obter perfis de linha que se parecem com as linhas de Balmer observadas

em DR Tau com uma configuração magnetosférica heuristicamente construída.

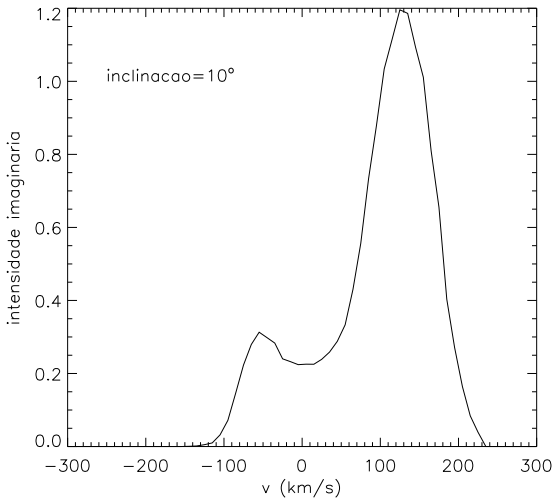

Figura 10.12: Perfil de linha teórico obtido com emissividade de linha aumentando fortemente perto da estrela.

Os resultados detalhados deste estudo são apresentados no Capítulo 8.

10.4 Conclusões

Estabelecemos valores teóricos novos e melhores para parâmetros como os expoentes de brilho por gravidade e os coeficientes de escurecimento de bordo que são importantes na análise de sistemas binários eclipsantes. Mostramos a influência da iluminação externa nestes parâmetros e apresentamos um novo conjunto de valores que devem ser usados no estudo de binárias próximas, onde os efeitos da iluminação externa são mais importantes.

Testamos resultados teóricos e observacionais dos modelos de acresção magnetosférica visando compreender melhor as interações do sistema estrela-disco em formação. Mostramos que a acresção e perda de massa estão relacionadas e que evidências do processo de acresção, como absorção desviada para o vermelho em velocidades de queda livre, estão presentes nos espectros. Mostramos que a maioria das componentes em emissão são simétricas ao invés de assimétricas, como previsto pela teoria e que as linhas de emissão largas de diferentes espécies atômicas,

que supostamente são produzidas no funil magnetosférico, nem sempre estão fortemente correlacionadas. Enfatizamos a necessidade de adicionar turbulência, ventos e rotação aos modelos, de maneira a comparar com sucesso perfis de linha teóricos e observados.

Chapter 11

—

Appendix - published papers

11.1 Gravity-brightening - non-illuminated models (Paper 1)

Astron. Astrophys. 326, 257–262 (1997)

ASTRONOMY
AND
ASTROPHYSICS

The gravity-brightening effect and stellar atmospheres

I. Results for models with 3700 K $<$ $T_{\rm eff}$ $<$ 7000 K

S.H.P. Alencar and L.P.R. Vaz

Departamento de Física-ICEx-UFMG, Caixa Postal 702, 30.161-970 Belo Horizonte MG, Brazil

Received 8 August 1996 / Accepted 18 March 1997

Abstract. The gravity-brightening exponent (β) is studied using the UMA (Uppsala Model Atmosphere) code in non-illuminated convective grey (in the sense of "continuum only" opacity) and non-grey (line blanketed) atmospheres, for 3 700 K $<T_{\rm eff}<$ 7 000 K. The value β=0.32 proposed by Lucy was confirmed only for $T_{\rm eff}\sim$ 6 500 K. β depends upon $T_{\rm eff}$ (an analytical expression is given), being rather insensitive to variations of the mixing length parameter, of the stellar mass and to the use of grey or non-grey atmospheres. A comparison with empirical determinations and a preliminary test of the use of the proposed β values in eclipsing binary light curve analysis are presented. A dependence of β on external illumination ("reflection effect") for convective models is evidenced for the first time, the larger the amount of incident flux the larger the β exponent.

Key words: atmospheres – stars: binaries: close – stars: binaries: eclipsing – stars: fundamental parameters – stars: general

1. Introduction

The analysis of eclipsing binary (EB) light curves (LC) involves a large number of parameters. To avoid multiple solutions, as many parameters as possible are kept fixed either at the observed values (e.g. mass ratio) or at the theoretical ones (limb-darkening coefficients, bolometric albedos, gravity-brightening exponents). LC generation models are able to directly adjust such parameters, but this may introduce correlations that make the convergence to physically acceptable solutions difficult or impossible.

The limb-darkening effect on EBLC is moderate (Popper 1984). Its coefficients for different laws (e.g. Al-Naimiy 1978, Wade & Ruciński 1985, Van Hamme 1993, Claret et al. 1995, amongst other) are satisfactorily used in the EB models, but the Strömgren u theoretical values seem not to correctly reproduce the observed u LC of early systems (Vaz et al. 1995 and references therein).

The bolometric albedos affect the LC of all types of close EB (Vaz 1984, 1985). The albedos for convective grey (Vaz & Nordlund 1985) and non-grey (Nordlund & Vaz 1990) atmospheres have been modeled. In non-grey models no convenient expression for the study of EBLC was found, and each case should be treated individually.

1.1. Basic works on the gravity-brightening effect

Von Zeipel (1924) showed that the local emergent flux of a star with an atmosphere in hydrostatic and radiative equilibrium and distorted by rotation or tidal effects is proportional to the local gravity acceleration (β = 1.0):

$$\mathscr{F} \propto g^{\beta} \tag{1}$$

Lucy (1967) found that Eq.(1) would hold for convective atmospheres if $\beta \simeq$0.32, a value obtained by coupling convective envelopes of models with different surface gravities at depths where the temperature gradient was adiabatic. He recognized that the entropy at the bottom of different models should be the same, in order to represent the same star: "inward integrations of the equations governing the atmospheric structure must always end up on the same adiabat" (Lucy 1967). Lucy made his calculations for the effective temperatures corresponding to stars with 1.00 $M_{\odot}$ (6 000 K) and 1.25 $M_{\odot}$ (6 700 K and 5 950 K), using atmosphere models by Baker & Temesváry (1966).

Anderson & Shu (1977) presented another formulation for convective atmospheres arguing that, for a contact star in hydrostatic equilibrium having a common convective envelope (the contact discontinuity model, Shu et al. 1976, Lubow & Shu 1977), the convective flux depends on the effective gravitational potential alone, and not on its gradient (i.e. the local acceleration of gravity). As for late-type stars $F_{\rm conv} \simeq F_{\rm total}$ and the photosphere must ultimately radiate $\sigma T_{\rm eff}^4$, this flux should be constant on equipotentials, with consequently β=0.

Send offprint requests to: L.P.R. Vaz

1.2. Empirical determinations and modern works

Rafert & Twigg (R&T, 1980) determined β by analysing a uniform sample of detached, semi-detached and contact EB with the WD (Wilson 1979) program. They found $\beta \approx 0.31$ for convective envelopes ($5\,400\,\mathrm{K} < T_{\rm eff} < 7\,100\,\mathrm{K}$) and $\beta \approx 0.96$ for the radiative ones ($T_{\rm eff} > 7\,900\,\mathrm{K}$). For $7\,100\,\mathrm{K} < T_{\rm eff} < 7\,900\,\mathrm{K}$ they found empirically $0.31 < \beta < 1$.

Hilditch (1981) found very small values of β (four contact EB), and that imposing β=0.32 yields a photometric mass ratio which is significantly different from the spectroscopic one, what does not happen with β=0. However, the obvious presence of star spots in all the 4 systems may render very difficult, and even spoil, attempts to determine temperature variations over the surfaces (Ruciński 1989).

Nakamura & Kitamura (1992 and references therein) did empirical studies on the β exponent (their distortion theory extended to a second order treatment, Kitamura & Nakamura, K&N 1983). For detached EB their values agree with those of von Zeipel (1924) and Lucy (1967), but for early-type both semi-detached (K&N 1987b, 1992) and contact EB (K&N 1988a,b), they obtained $\beta > 1.0$.

Sarna (1989), with a model of convective envelope for Roche lobe filling stars (W UMa-type), computed the distribution of effective temperatures and surface gravities for the stars and directly determined $\beta \approx$0.32.

Observation and theory thus generally agree with each other, with $\beta \approx$1.0 for radiative atmospheres and $\approx$0.32 for the convective ones, albeit exponents $>$1.0 were found by K&N. There is observational evidence for a transition between these two regimes (K&N and R&T), suggesting that β=0.32 is valid only for temperatures close to what Lucy (1967) used. "Whereas $\beta_{\rm rad}$=1 is a solid, physically well understood upper limit (...), $\beta_{\rm conv}$=0.32 is an approximate relation based on a small set of envelope models which used very crude physics" (Ruciński 1989). Further, there is only one empirical determination (Ruciński 1976) and no theoretical study for $T_{\rm eff} < 5\,400$ K up to now, all this being the motivation for the present study.

2. The atmosphere model

We use the Uppsala Model Atmosphere (UMA, Gustafsson et al. 1975, Bell et al. 1976) code, in a version by Vaz & Nordlund (1985). The code is designed for cool stars ($T_{\rm eff} < 8\,000$ K), atmospheres in hydrostatic equilibrium using plane-parallel structure, local thermodynamic equilibrium and modeling convection through mixing length.

The effective temperature $T_{\rm eff}$, the surface gravity g, the stellar mass M, the mixing length parameter l/H_P, and the chemical composition (fixed at solar abundance in this work) define a model. We use stellar models (Claret 1995, X=0.70, Z=0.02) to associate $T_{\rm eff}$ with M for undistorted stars at the ZAMS. We refer to models with and without line absorption as "non-grey" and "grey", respectively, including in the "grey" models, though, the continuum opacity variation with frequency (as in Nordlund & Vaz 1990). We study grey (i.e. "continuum only") and non-grey (line blanketed or ODF) atmospheres in convective equilibrium. The ODF tables limit the temperature range of this study to those corresponding to (ZAMS) stars with masses ranging from $0.6\,\mathrm{M}_\odot$ to $1.5\,\mathrm{M}_\odot$.

2.1. The method

Starting from a reference model ($\log g$=4.5) we adjust $T_{\rm eff}$ for models having another $\log g$ (distorted) until the adiabat at the bottom of the distorted model becomes equal to that of the reference one, i.e. these models must represent the same star by having the same entropy at the bottom. We then examine how the total flux varies with g, determining β by linear regression.

Taking the most distorted components of some high quality EB solutions we find $\Delta \log g$=0.28 for V Pup (detached, Andersen et al. 1983), 0.22 for LZ Cen (detached, Vaz et al. 1995) and 0.30 for RY Aqr (semi-detached, Helt 1987). Larger values for $\Delta \log g$ will certainly be found amongst the most deformed components of contact EB. In the beginning of this study we used equally spaced steps of 0.1 in $\log g$ over a large interval of $\Delta \log g$=1.5 to calculate β. Equation (1) proved to be valid to a very high degree all over the interval, with both the β exponents and the linear regression correlation coefficients practically equal no matter if we used $\Delta \log g$=1.5 or smaller intervals (e.g. 0.30). However, an uncertainty of $\pm$5 K in the effective temperatures of the models could affect the β values for small $\Delta \log g$ intervals. Then, we decided to use in our study of grey atmospheres (Sect. 2.2) an interval $\lesssim$5 times the one easily happening for the components of close EBS, in order to minimize the effect of uncertainties in $T_{\rm eff}$ on β and to have our studies valid even for very distorted stars. In Sect. 2.3 we give β for both the large and the small $\log g$ intervals, but adopt the more realistic $\Delta \log g$=0.30.

To have layers deep enough for the adiabatic regime to be fully established, we extended the temperature structure from $\log \tau = -4.2$ to +7.3, going as deep in the atmosphere as the program allowed. In these deep layers $F_{\rm rad}$ is in practice zero, but there is non-adiabaticity because of mixing. The opacity hence is of negligible importance, unless it becomes completely wrong, what does not happen: the continuum opacity is indeed quite reasonable at the temperatures reached. The equation of state is close to modern formulations, such as the one by Mihalas et al. (1988), and is reasonable as well (it lacks effects like Coulomb screening, but these should come into play only much further down). Other formulations for the equation of state exist now, driven by helioseismology (Guenter et al. 1996, Elliott 1996, Antia 1996), but the level of differences are not significant in the current context. Moreover, these differences are particularly small at the surface, where the traditional (ODF) model atmospheres are actually covering effects not included in these newer formulations. The thermodynamic variables are both internally and physically consistent, as they obey the thermodynamic relations in the code (i.e., they stem from the same thermodynamic potential) and are supported by reasonable values for the continuum opacity and by the use of a realistic equation of state. Besides, these deep models produce the same spectrum as mod-

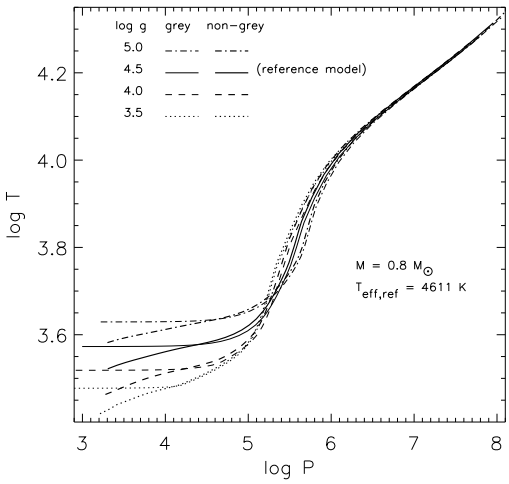

Fig. 1. $\log T$ vs. $\log P$ for convective grey (thin lines) and non-grey (thick lines) models with α = 1.5.

els (same parameters) having $\log \tau$ from -4.2 to $\sim$1.0. We are, therefore, still generating physically valid models.

The plane-parallel approximation means that we generate models for small regions over the distorted atmosphere (in terms of the geometrical depth our deep models have less than 0.6% of the star radius). Spherical symmetry models, apparently a better approach, would connect $\log g$ with M and R, and then have difficulties in generating a distorted star, where $\log g$ is larger precisely where the curvature radius is larger (but R is smaller). Both approximations, however, should lead to similar results for β with our method, as we compare models with the same approximation (in a way, β is a "differential" effect).

2.2. Convective grey (continuum only) atmospheres

Some models obtained with this method are shown in Fig. 1. The relation between $\log T$ and $\log P$ is the same at the bottom of the atmosphere in all the models that must represent different parts of the same distorted star.

We calculated models varying the values of α (=l/H_P), which is a measure of the degree of efficiency in the convective energy transport. However, β did not show a strong dependence on α, as shown in Table 1 and Fig. 2a. This was also noted by Sarna (1989). It can be seen, also, that the change in β with α is dependent on the model effective temperature. For some models (0.8 $M_\odot$, 1.0 $M_\odot$) we calculated β for very small α values (0.1, 0.01). The resulting values show that β does not change significantly from its value for a normal atmosphere (α=1.5).

The last lines of Table 1 list tests made with non-main sequence stars (i.e. with a $T_{\rm eff}$ very different from the one a normal star with the same mass should have on this phase). The cold 1.65 $M_\odot$ model with $T_{\rm eff}$=4800K does correspond to a real Pre-

Table 1. Values of β for convective grey models. Models marked with an * are non-Main Sequence stars, used to investigate the influence of the mass and temperature on β. All models have solar chemical abundance.

$T_{\rm eff}$	M	$\alpha = l/H_P$				
(K)	($M_\odot$)	2.0	1.5	1.0	0.10	0.01
3 697	0.60	0.194	0.199	0.210	-	-
4 100	0.69	0.299	0.334	0.315	-	-
4 611	0.80	0.419	0.417	0.417	0.380	0.380
5 526	1.00	0.414	0.401	0.383	0.378	0.378
6 087	1.18	0.360	0.353	0.347	-	-
6 480	1.33	0.315	0.336	0.314	-	-
6 685	1.41	0.301	0.291	0.293	-	-
7 011	1.50	-	0.269	-	-	-
4 400*	1.65	-	0.389	-	-	-
4 800*	1.65	-	0.411	-	-	-
5 400*	1.65	-	0.407	-	-	-
6 000*	1.65	-	0.361	-	-	-
6 600*	1.65	-	0.302	-	-	-

Table 2. Coefficients for Eq. (2) in convective models.

	a_0	a_1	a_2	a_3
grey	-5.00784	27.9838	-46.9701	25.5398
non-grey	-5.61111	31.6225	-54.0000	29.7779

Main Sequence (PMS) star (the secondary of TY CrA, Casey et al. 1993, 1995, 1997, see Sect. 3.2), while the other tests correspond to some different evolutionary PMS phases of that same star. These non-main sequence models show, however, that β depends mostly on $T_{\rm eff}$ for normal (i.e. non-illuminated, see Sect. 3.1) atmosphere models. Fig. 2a shows our theoretical values of β vs. $T_{\rm eff}$ listed in Table 1 and the third order polynomial adjusted with all the β values for grey atmospheres, given by the equation:

$$\beta = \sum_{i=0}^{3} a_i t_e^i \qquad (2)$$

with t_e =$T_{\rm eff}$ $\times$ 10^{-4} and the values of a_i given in Table 2.

2.3. Convective non-grey (line blanketed) atmospheres

In Fig. 1 we have models calculated for convective non-grey atmospheres: the non-grey models differ from the grey ones being colder in the upper layers, and slightly hotter in the deep ones. For $T_{\rm eff}$>6 400 K we were forced to diminish the extension in $\log \tau$ in order to be able to calculate for the same range of effective temperatures used for the grey models, due to limitations of the ODF files.

β turned out to be very close to those for grey models, showing that the phenomenon is more related to the constitutive equa-

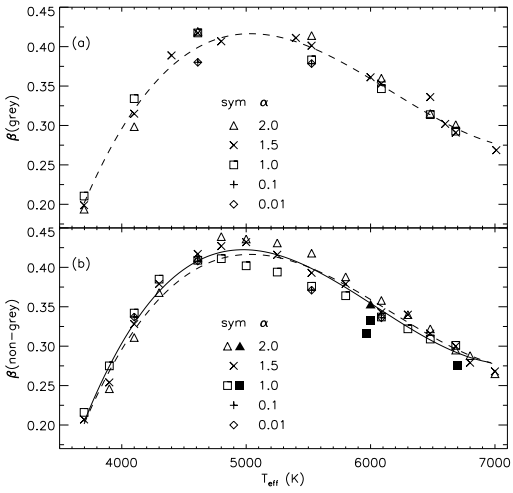

Fig. 2a and b. β vs. $T_{\rm eff}$ for convective (**a**) grey and (**b**) non-grey models (filled symbols are Lucy calculations for a similar chemical composition). The third order polynomials are shown.

Table 3. Values of β for convective non-grey models. The values for α=1.5* were calculated using $\Delta \log g$=1.5, while all other used $\Delta \log g$=0.3. In all cases the reference model has log g=4.5.

$T_{\rm eff}$	M	$\alpha = l/H_P$					
(K)	($M_\odot$)	2.0	1.5*	1.5	1.0	0.1	0.01
3 697	0.60	-	0.205	0.207	0.216	-	-
3 900	0.66	0.246	0.253	0.254	0.275	-	-
4 100	0.69	0.311	0.322	0.328	0.342	0.337	0.337
4 300	0.75	0.368	0.369	0.379	0.385	-	-
4 611	0.80	0.412	0.413	0.417	0.409	0.409	0.408
4 800	0.83	0.439	0.430	0.427	0.411	-	-
5 000	0.87	0.436	0.432	0.432	0.402	-	-
5 250	0.93	0.431	0.414	0.416	0.394	-	-
5 526	1.00	0.418	0.396	0.393	0.376	0.372	0.371
5 800	1.09	0.388	0.375	0.379	0.364	-	-
6 087	1.18	0.358	0.349	0.343	0.337	0.336	0.336
6 300	1.26	0.340	0.336	0.340	0.322	-	-
6 480	1.33	0.322	0.321	0.316	0.309	-	-
6 685	1.41	0.295	0.298	0.300	0.301	-	-
6 800	1.44	0.288	0.282	0.279	-	-	-
7 000	1.50	0.265	0.272	0.268	-	-	-

tions than to the ODF table used or to the value of the mixing length parameter, α.

The weak dependence of β on α is confirmed for non-grey models (Table 3), although some trends become evident: the maximum of β shifts slightly, but systematically, in $T_{\rm eff}$ with α (Fig. 2b). However, the influence of α on β (same $T_{\rm eff}$) is small if compared with the normal errors involved in the empirical determinations of β (see Sect. 3.1). Then, we used all values of α (calculated with $\Delta \log g$=0.3) in fitting the third order polynomial to the non-grey β (Table 2, Fig. 2b) which should be the best approximation for real stars.

The β values calculated by Lucy (1967) are shown in Fig. 2b, also. Although the procedure used to compute β was the same, our opacity tables and atmosphere model were different from those he used. Even then, our results are in very close agreement: the mean of the 16 values of Table 3 calculated with $\Delta \log g$=0.3 in the interval 6 000 K $\leq T_{\rm eff} \leq$ 6 800 K is $\beta = 0.320 \pm 0.006$.

3. Discussion

Our results for the β exponent in continuum only and line blanketed convective atmospheres are very similar to each other. The dependence of β for these models is mostly on the effective temperature, being very weak, albeit systematic, its dependence on the mixing length parameter (i.e. on the efficiency of convection in the energy transport).

For lower $T_{\rm eff}$, convection becomes very efficient due to the higher density caused by the lower opacity. The entropy jump at the surface becomes small and its changes even smaller (the convective zone reaches layers closer to the surface), yielding small β. For increasingly higher $T_{\rm eff}$, the top convective layers start deeper and deeper, increasing the entropy jump and its changes at the surface and, consequently, β. At high $T_{\rm eff}$, convection loses importance altogether, and the effect weakens again, although the adiabat still is a constraint at the bottom. In between these limits β reaches a maximum at $\sim$5 000 K.

Equation (1) was valid to a high degree in all the models. The β values were determined by linear regression with correlation coefficients very close to 1.0: the smallest value was r^2=0.994 for some models with α=2.0. The correlation coefficients for the β values calculated by using either $\Delta \log g$=0.30 or 1.5 (see Table 3) were essentially equal.

3.1. Comparison with empirical determinations

Figure 3 shows our results for β and empirical determinations found in the literature for the exponent. The 1σ error bars are given for the β exponent only, due to lack of information on the $T_{\rm eff}$ errors in most of the works used. However, we may assume that these errors are at least $\pm$500 K, a too optimistic figure for works using UBV, but reasonable for those using $uvby$ or DDO photometry.

Lucy's (1967) β=0.32 is a reasonable approximation for the data in Fig. 3. Our theoretical result agrees with Lucy's value in the temperature range he used and matches most of the empirical values for detached systems in Fig. 3, with only one determination showing a large discrepancy. Although the values for semi-detached and contact systems show a larger scattering, the theoretical curve still is a good approximation. One reason for the large scattering of the empirical β values for the more

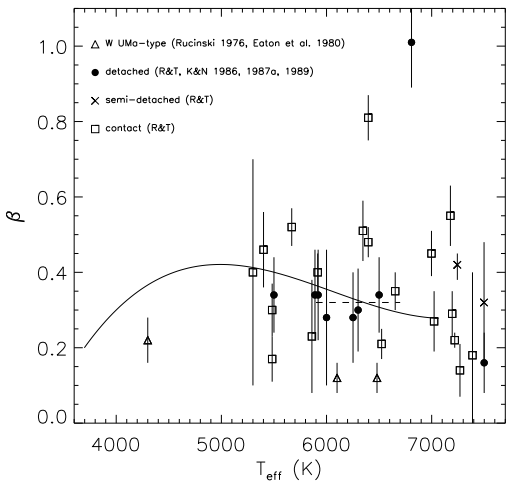

Fig. 3. The β theoretical curve and empirical results. The dashed line is Lucy's value in the temperature range he used.

deformed systems may be the large numerical correlation in the EB models between the exponent and the geometric parameters (inclination and star sizes) and, in some configurations, with the effective temperatures, too. Note that the above mentioned correlation has meaning exclusively for the empirical determinations of β; the theoretical values depend only on the atmosphere model parameters.

Contact and semi-detached EB should be better represented by illuminated atmospheres, since their components are closer to each other. Some calculations were made with an atmosphere grey model of $T_{\rm eff}$=4 611 K heated by sources with $T_{\rm h}$=4 500 K and 7 000 K, following Vaz & Nordlund (1985). The amount of incident flux may be changed through the value of $r_{\rm h}$, the ratio between the source star radius and the distance from its centre to the point at the surface of the reflecting star. The results (Table 4) show that the external heating increases the β values roughly in proportion to the amount of the incident flux. It would be then expected that contact and semi-detached systems would lie above our polynomial fit computed for non-illuminated atmospheres. The error estimations for β in Fig. 3 may be too optimistic, due to the correlations mentioned above and to the intrinsic difficulties in its empirical determinations. Better determinations of β are needed to confirm observationally the theoretically expected influence of external illumination[1].

The system CC Com (Ruciński 1976) has the only observational determination of β for $T_{\rm eff}$<5 400 K. W UMa (Eaton et al. 1980) has both components shown in Fig. 3 with $T_{\rm eff}$ by Hutchings & Hill (1973) and presents the lowest β value amongst

[1] Considering the □ and × symbols, there are more determinations above our curve (12, being 7 by more than 1σ) than below (7, 5 by more than 1σ) in Fig. 3.

Table 4. β for convective grey models with $T_{\rm eff}$=4 611 K illuminated by different stars in various degrees of approximation. The external flux incidence angle with the surface normal is 21°.5. No illumination is represented by $r_{\rm h}$=0.00.

$T_{\rm h}$	Apparent radius $r_{\rm h}$				
(K)	0.00	0.05	0.10	0.20	0.40
4500	0.417	0.422	0.427	0.439	0.494
7000	0.417	0.426	0.451	0.515	0.615

all the systems. Our model cannot reproduce the β=0 predicted by Anderson & Shu (1977) for $T_{\rm eff}\lesssim$6 400 K. The reason may be the fact that our method is unable to detect any horizontal entropy gradients, which are possibly significant in contact systems, but not in the (semi) detached ones. Our results, then, must be taken with care if applyed to contact systems, but should be valid for the detached and semi-detached ones.

3.2. One first observational test

Equation (2), with the non-grey coefficients of Table 2, was implemented in the modified version of the WD model (Wilson & Devinney 1971, Wilson 1993) described by Vaz et al. (1995). The triple PMS eclipsing system TY CrA (Casey et al. 1993, 1995) has its eclipsing secondary component early in the PMS evolutionary phase, at the very end of the Hayashi track. The light curves were analysed (Casey et al. 1997) with the WD model using both Lucy's value and our approximation for β. For the secondary's effective temperature (4 800 K) our value is 0.41, about 28% larger than Lucy's value. The results obtained with our β were more consistent than when using β=0.32, yielding a (B8-9 ZAMS) primary star with absolute dimensions closer to what theoretically expected for a star in such phase. The reason was the increase of surface brightness in the secondary polar regions, requiring a lower inclination to reproduce the minimum depth and, consequently, larger stellar radii to reproduce the minima duration. Even though this result is encouraging, TY CrA is not, however, the most adequate system for such a test, as it is in a problematic evolutionary phase. We are searching for more favorable EBS for a definite observational test of the impact of the proposed theoretical values for β on EBLC analysis, whose results will be published elsewhere.

4. Conclusions

The gravity-brightening law, Eq. (1), is valid to a high degree for all models generated in this work with a modified version of the UMA code (plane-parallel atmosphere model in both hydrodynamic and local thermodynamic equilibrium). The β exponents for convective atmospheres were calculated theoretically by forcing the entropy at the bottom of the atmosphere to be equal in models that should represent the same star. Our model reproduces the mean result of Lucy (1967) for the convective regime.

We extended the result of Lucy (1967, for three values of $T_{\rm eff}$) to the range 3 700 K$<T_{\rm eff}<$7 000 K and found that β practically only depends on $T_{\rm eff}$, being rather insensitive to the value of the mixing length parameter, to the use of grey or non-grey atmospheres, and to the model total mass. A third order polynomial, $\beta(T_{\rm eff})$, was given as a convenient way to use the results in the analysis of EBLC.

The influence of the "reflection effect" on the gravity-brightening exponent for convective atmospheres is evidenced for the first time: the external illumination increases the values of β significantly, indicating that in close systems, where the reflection effect is prominent, the standard β values might be too low. A detailed analysis including illuminated models and an extension of the present work to higher effective temperatures are in progress.

Acknowledgements. Support by FAPEMIG, CNPq, FINEP, CAPES (Brazilian institutions). Fruitful discussions with Dr. Å. Nordlund and Dr. J.V. Clausen are gratefully acknowledged. The comments of an anonymous referee were fundamental to bring this work to its final form.

References

Al–Naimiy H.M., 1978, Ap&SS 53, 181
Andersen J., Clausen J.V., Giménez A., Nordström B., 1983, A&A 128, 17
Anderson L., Shu F.H., 1977, ApJ 214, 798
Antia H.M., 1996, A&A 307, 609
Baker N., Temesváry S., 1966, Tables of Convective Stellar Envelope Models. 2d ed. New York: NASA, Goddard Inst. for Space Studies.
Bell R.A., Eriksson K., Gustafsson B., Nordlund Å., 1976, A&AS 23, 37
Casey B.W., Mathieu R.D., Suntzeff N.B., Lee C.W., Cardelli J.A., 1993, AJ 105, 2276
Casey B.W., Mathieu R.D., Suntzeff N.B., Walter F.M., 1995, AJ 109, 2156
Casey B.W., Mathieu R.D., Vaz L.P.R., Andersen J., Suntzeff N.B., 1997, AJ, submitted
Claret A., 1995, A&AS 109, 441
Claret A., Díaz–Cordovés J., Giménez A., 1995, A&AS 114, 247
Eaton J.A., Wu C.-C., Ruciński S.M., 1980, ApJ 239, 919
Elliott J.R., 1996, MNRAS 280, 1244
Guenther D.B., Kim Y.-C., Demarque P., 1996, ApJ 463, 382
Gustafsson B., Bell R.A., Eriksson K., Nordlund Å., 1975 A&A 42, 407
Helt B.E., 1987, A&A 172, 155
Hilditch R.W., 1981, MNRAS 196, 305
Hutchings J.B., Hill G., 1973, ApJ 179, 539
Kitamura M., Nakamura Y., 1983, Ann. Tokyo Astron. Obs. 2nd Series, 19, 413
Kitamura M., Nakamura Y., 1987b, Ann. Tokyo Astron. Obs. 2nd Series, 21, 387
Kitamura M., Nakamura Y., 1988a, Ap&SS 145, 117
Kitamura M., Nakamura Y., 1988b, Ann. Tokyo Astron. Obs. 2nd Series, 22, 31
Kitamura M., Nakamura Y., 1989, Publ. Natl. Astron. Obs. 1, 43
Mihalas D., Däppen W., Hummer D.G., 1988, ApJ 331, 815
Lubow S.H.,Shu F.H., 1977, ApJ 216, 517
Lucy L.B., 1967, Zeitschr. für Astrophys. 65, 89
Nakamura Y., Kitamura M., 1992, Ap&SS 191, 267
Nordlund Å., Vaz L.P.R., 1990, A&A 228, 231
Popper D., 1984, AJ 89, 132
Rafert J.B., Twigg L.W., 1980, MNRAS 193, 79
Ruciński S.M., 1989, Comments Astrophys. 14, 79
Ruciński S.M., 1976, PASP 88, 777
Sarna M.J., 1989, A&A 224, 98
Shu F.H., Lubow S.H., Anderson L., 1976, ApJ 209, 536
Van Hamme W., 1993, AJ 106, 2096
Vaz L.P.R., 1984, Ph. D. Thesis, Copenhagen University Observatory (unpublished)
Vaz L.P.R., 1985, Ap&SS 113, 349
Vaz L.P.R., Andersen J., Rabello Soares M.C.A., 1995, A&A 301, 693
Vaz L.P.R., Nordlund Å., 1985, A&A 147, 281
von Zeipel H., 1924, MNRAS 84, 665
Wade R.A., Ruciński S.M., 1985, A&AS 60, 471
Wilson R.E., 1979, ApJ 234, 1054
Wilson R.E., 1993, in New Frontiers in Binary Star Research, eds. K.C. Leung and I.-S. Nha, ASP Conf. Series 38, 91
Wilson R.E., Devinney E.J., 1971, ApJ 182, 539

This article was processed by the author using Springer-Verlag LaTeX A&A style file *L-AA* version 3.

11.2 Gravity-brightening - illuminated models (Paper 2)

For the sake of clarity in the thesis the symbol ν represents frequency, while the cosine of θ, the incidence angle of the external illumination, is ω. In Chapter 5 $\mu = \cos\gamma$, where γ is the line of sight angle. Unfortunately the symbols used in the papers are sometimes different. In the following paper $\mu = \cos\theta$.

Astron. Astrophys. 346, 556–563 (1999)

ASTRONOMY AND ASTROPHYSICS

The gravity-brightening effect and stellar atmospheres

II Results for illuminated models with $3\,700\,\mathrm{K} < T_{\rm eff} < 7\,000\,\mathrm{K}$

S.H.P. Alencar[1], **L.P.R. Vaz**[1], **and Å. Nordlund**[2]

[1] Departamento de Física, ICEX–UFMG, C.P. 702, 30.123-970 Belo Horizonte, MG – Brazil (silvia, lpv@fisica.ufmg.br)
[2] Niels Bohr Institute for Astronomy, Physics and Geophysics; Astronomical Observatory, Juliane Maries Vej 30, DK-2100 Copenhagen, Denmark (aake@astro.ku.dk)

Received 23 September 1998 / Accepted 18 February 1999

Abstract. The influence of the so–called "reflection effect" (mutual illumination in a close binary) on the gravity–brightening exponent (β) is studied using the UMA (Uppsala Model Atmosphere) code. The model is applied to convective grey (in the sense of continuum–only–opacity) and non–grey (line–blanketed) atmospheres with $3\,700\,\mathrm{K} < T_{\rm eff} < 7\,000\,\mathrm{K}$, illuminated by grey and non–grey fluxes. The results for grey atmospheres illuminated by grey or non–grey fluxes are very similar. In this case β mostly depends on the amount of incident energy and on the illumination direction, apart from the dependence on the effective temperature already discussed for non-illuminated models in a previous work (Alencar & Vaz 1997). The existence of a maximum in the $\beta(T_{\rm eff})$ relation is due to the interplay between the convection and opacity properties of the models. The external illumination increases the values of β, that is, the larger the amount of incident flux the larger the value of the exponent. This effect is caused by the "quenching" of convection as the external illumination heats the surface layers of the illuminated star, thus bringing it closer to radiative equilibrium, where β is close to unity. We provide a polynomial fit to the variation of β with the fundamental parameters, in order to make it possible to easily account for the effect in light curve synthesis programs.

For line–blanketed illuminated atmospheres there is an additional dependence on the effective temperature of the incident flux (the heating temperature). This is related to the overall wavelength dependence of the spectral line opacity. Particularly in the UV, the line opacity is so strong that it prevents a significant amount of the incident flux from penetrating to the continuum formation layers. The quenching of convection by the external illumination and the related increase of β are thus partly prevented.

Key words: stars: atmospheres – stars: binaries: close – stars: binaries: eclipsing – stars: fundamental parameters – stars: general

Send offprint requests to: L.P.R. Vaz

1. Introduction

In order to improve the results obtained by eclipsing binary light curve models, and to avoid the multiplicity of solutions, it is convenient to keep as many parameters as possible fixed at their observed or theoretical values. The gravity–brightening exponent (β) of convective atmosphere stars is usually assumed to be equal to the theoretical value $\beta = 0.32$ (Lucy 1967), β being defined by the equation

$$\mathcal{F} \propto g^{\beta}, \tag{1}$$

proposed by von Zeipel (1924) for radiative atmospheres.

In Alencar & Vaz (1997, hereafter Paper I) it was shown that the gravity–brightening exponent of a non-illuminated convective atmosphere depends on the star's effective temperature, Lucy's result being a good approximation only as a mean value for non-illuminated atmospheres. In Paper I, where a brief review of the observational and theoretical work on the gravity–brightening effect was presented, it was also demonstrated that external illumination tends to increase the value of β.

External illumination is significant in many eclipsing binaries, as evidenced by the conspicuous "reflection effect" in their light curves. Nevertheless, until now, no particular attention has been paid to its influence on the β exponent. Our goal in the present study is to clarify the dependence of β on external illumination.

In Sect. 2 we describe our method and study the cases of grey and non–grey convective illuminated atmospheres, presenting the results (for the grey case) as a polynomial expression. Further, we explain why β has a maximum in the $T_{\rm eff}$ interval studied. We discuss the results in Sect. 3, and summarize our conclusions in Sect. 4.

2. The atmosphere model

We use the Uppsala Model Atmosphere (UMA, Gustafsson et al. 1975, Bell et al. 1976) code, in a version by Vaz & Nordlund (1985), as described in Paper I. The code is intended for cool ($3\,500\,\mathrm{K} < T_{\rm eff} < 8\,000\,\mathrm{K}$) atmospheres, and assumes hydrostatic equilibrium, a plane–parallel structure, and local thermo-

dynamic equilibrium. Convection is modeled with the mixing length recipe.

An illuminated model is defined by its effective temperature $T_{\rm eff}$, its surface gravitational acceleration g, mixing length parameter $\alpha = l/H_P$, and chemical composition (fixed at solar abundance in this work). The external illumination is parameterized by the direction of illumination μ (the cosine of the incidence angle with respect to the surface normal), the effective temperature of the illuminating star $T_{\rm h}$ and its apparent radius $r_{\rm h}$ (the ratio between the radius of the illuminating star and the distance from its centre to the surface of the reflecting star). The mixing length parameter was kept fixed at $\alpha = 1.5$ for the illuminated models (in Paper I it was shown that the gravity–brightening exponent does not depend strongly on this parameter). We refer to models with and without spectral line absorption as "non–grey" and "grey", respectively. The "grey" models include the variation of continuum opacity with frequency (as in Nordlund & Vaz 1990). We study grey (continuum–only) and non–grey (line–blanketed) illuminated atmospheres in convective equilibrium. The spectral lines are treated in the ODF (Opacity Distribution Function) approximation. The limits of the ODF tables constrain the effective temperature of stars in this study to a range corresponding to (ZAMS) stars with masses in the interval $0.6\,{\rm M}_\odot$ to $1.5\,{\rm M}_\odot$.

2.1. The method

Starting from a reference ($\log g = 4.5$) non-illuminated model we adjust $T_{\rm eff}$ for illuminated models with the same $\log g$ until the adiabat at the bottom of the illuminated model becomes equal to that of the reference model. These models represent the illuminated and the non–illuminated sides of the same star, by having the same entropy at the bottom. We then use the illuminated model with $\log g$ = 4.5 as a reference and follow the procedure described in Paper I to determine β, by examining how the total flux of the illuminated models varies with g (Eq. 1).

Note that our method gives β as a function of parameters that were chosen primarily for convenience of computing stellar atmosphere models, rather than for their direct applicability to binary systems. The $\log g$, $r_{\rm h}$, and μ parameters, for example, are interrelated through the value of the radius of the star. When applying these results to the study of a particular binary system, it is necessary to interpolate in our parameter space to the particular combination of parameter values appropriate to a given point on the stellar surface. The resulting values of the gravity–brightening exponent will vary between points on the reflecting stellar surface, a property that is shared with the limb-darkening coefficients, which are also affected by external illumination (Alencar & Vaz 1999).

We used suitable values for the $\log g$ interval, to reproduce the range of distortions covered in Paper I. Eq. (1), proposed by von Zeipel (1924) for atmospheres in radiative equilibrium and applied by Lucy (1967) to stars with convection, proved to be a good approximation for all the intervals used. The correlation coefficients in the linear regressions used to determine β were always close to unity (the smallest one found was 0.987).

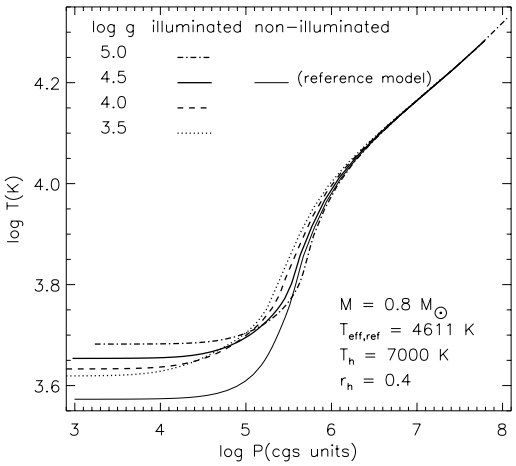

Fig. 1. $\log T$ vs. $\log P$ for convective grey non-illuminated (solid thin line) and illuminated models with $\alpha = 1.5$, $\mu = 0.93$.

The values of $T_{\rm eff}$, $T_{\rm h}$ and of the relative flux,

$$F_{{\rm rel},\mu} = [T_{\rm h}/T_{\rm eff}]^4 {r_{\rm h}}^2 \mu, \qquad (2)$$

used in the present work are representative of values for detached, semi–detached, and Algol systems found in the literature (Alencar & Vaz 1999).

In Sect. 2.2 we present the results obtained with grey atmosphere models illuminated by grey and non–grey fluxes. Initially we used $T_{\rm h}$ = 3 700 K, 4 500 K, 7 000 K and $T_{\rm h}$ = 10 000 K to check for a possible correlation between β and $T_{\rm h}$. However, the correlation turned out to be between β and the relative flux and we chose to compute most of the models with $T_{\rm h} = 7\,000\,{\rm K}$. The illuminating non–grey fluxes with $T_{\rm h} \leq 7\,000\,{\rm K}$ were generated with the UMA code, while for $T_{\rm h} = 10\,000\,{\rm K}$ we took the fluxes from Kurucz (1979). The grey fluxes were generated from a standard grey model (see, e.g. Mihalas 1978). It is worth mentioning that, even in our most extreme case of external illumination ($T_{\rm eff}$ = 6 700 K, $F_{\rm rel}$ = 1.5), the "heated" effective temperature of the illuminated models (keeping the constraint on the entropy at the bottom) did not exceed the validity limit of UMA, staying within $T_{\rm eff}^{\rm heated} \lesssim 8\,000\,{\rm K}$.

In Sect. 2.3 we give the results obtained with non–grey atmospheres illuminated by grey and non–grey fluxes. In this case β does depend on $T_{\rm h}$, and $F_{{\rm rel},\mu}$ alone is no longer sufficient to account for the correlations found.

2.2. Convective grey (continuum–only) atmospheres

Some of the models obtained with this method are shown in Fig. 1. The solid lines represent our reference models (with $\log g$ = 4.5); the thin line represents the non-illuminated model, while the thick line is the illuminated one. The other models are the illuminated and distorted ones. The relation of $\log T$ to $\log P$ is

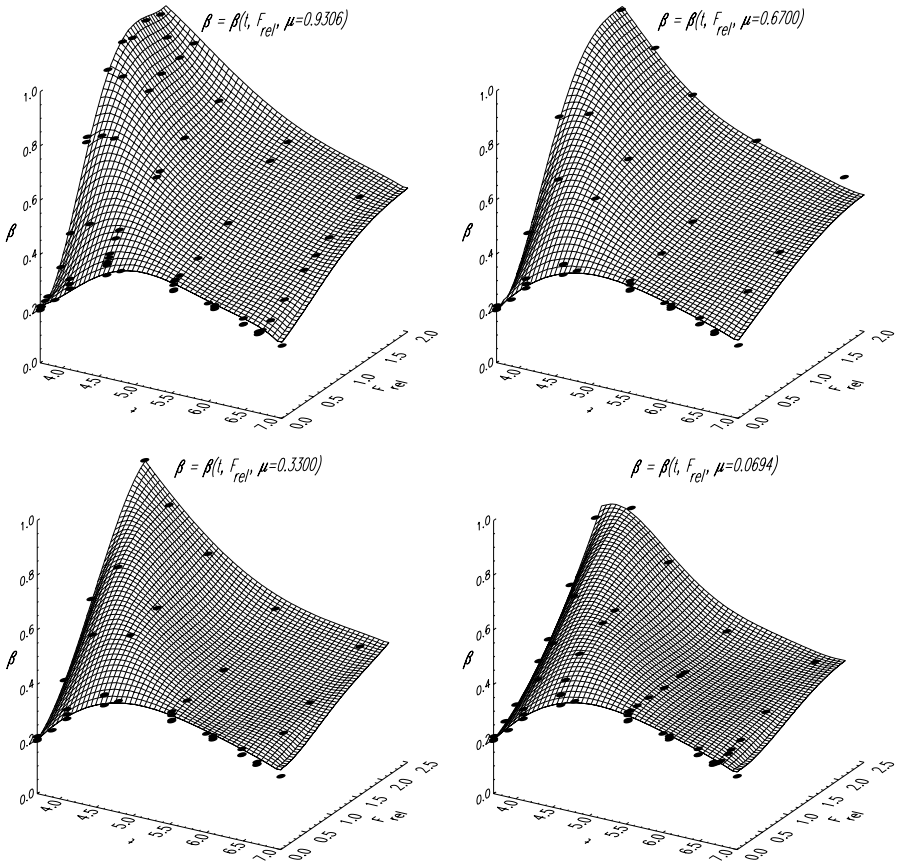

Fig. 2. $\beta(t, F_{\mathrm{rel},\mu}, \mu)$: calculations (grey models) and parametric surfaces (see Eq. (4) to (6)), presented for 4 values of μ. The curved grids represent the parameterization whose coefficients are shown in Table 1, and the points represent the calculations.

the same at the bottom of the atmospheres so that the different models have the same entropy at the bottom, as discussed above.

We calculated models by varying r_{h} and T_{h} for different values of T_{eff} (illuminated atmosphere), and four values of the angle of incidence of the radiation ($\mu = \cos\theta$ = 0.06943, 0.33001, 0.66999 and 0.93057). The corresponding β values are shown in Fig. 2, where $F_{\mathrm{rel},\mu}$ (Eq. 2), represents the influence of the parameters related to the illuminating flux, and $t = T_{\mathrm{eff}} \times 10^{-3}$ is the relevant parameter of the illuminated atmosphere. Note that in all panels of Fig. 2 the curve for $F_{\mathrm{rel},\mu}$ = 0 corresponds to the results of Paper 1 (no external illumination). Note also that β depends strongly on the amount of external illumination, represented by $F_{\mathrm{rel},\mu}$. A weaker dependence on the angle of incidence of the external radiation, μ, is also visible.

The β exponent increases with the incident flux, represented by $F_{\mathrm{rel},\mu}$ and saturates when β reaches its value for radiative atmospheres. This is most noticeable for models computed with incidence direction close to the surface normal (μ = 0.93 and 0.67) in Fig. 2.

The general trend revealed in Paper 1 of β having a maximum for a certain value of T_{eff} is repeated here for all values of $F_{\mathrm{rel},\mu}$. The maximum shifts to lower T_{eff} with increasing values of $F_{\mathrm{rel},\mu}$.

2.2.1. The behaviour of β for non-illuminated models

The maximum in $\beta(T_{\mathrm{eff}})$ is caused by changes in the convection and opacity properties of the models. For low T_{eff}, convection is rather efficient, because of the high mass densities and low total energy fluxes. The entropy jump at the surface is correspondingly small and its changes even smaller, yielding small β when we force the entropy at the bottom of the models to be

Table 1. c_{nlj} coefficients for Eqs. (4)-(6), corresponding to the parametric surfaces of Fig. 2 (grey models). All calculations were performed with double precision. The number inside parentheses is the power of 10 by which the entry must be multiplied (e.g. $c_{050} = -0.00186340$).

	a_0			
	c_{0l0}	c_{0l1}	c_{0l2}	c_{0l3}
b_{00}	1.24496 (0)	7.86878 (1)	–3.32836 (2)	3.26944 (2)
b_{01}	–3.37761 (0)	–7.49532 (1)	3.17539 (2)	–3.12273 (2)
b_{02}	1.96572 (0)	2.82025 (1)	–1.19617 (2)	1.17755 (2)
b_{03}	–4.55033 (-1)	–5.24475 (0)	2.22605 (1)	–2.19342 (1)
b_{04}	4.73747 (-2)	4.82560 (-1)	–2.04876 (0)	2.02029 (0)
b_{05}	–1.86340 (-3)	–1.75850 (-2)	7.46664 (-2)	–7.36785 (-2)
	a_1			
	c_{1l0}	c_{1l1}	c_{1l2}	c_{1l3}
b_{10}	–2.62765 (0)	3.38727 (3)	–1.01772 (4)	6.82868 (3)
b_{11}	–9.75380 (0)	–3.29553 (3)	9.81068 (3)	–6.56626 (3)
b_{12}	8.06846 (0)	1.26666 (3)	–3.73692 (3)	2.49471 (3)
b_{13}	–2.24768 (0)	–2.40423 (2)	7.03300 (2)	–4.68350 (2)
b_{14}	2.68404 (-1)	2.25419 (1)	–6.54300 (1)	4.34712 (1)
b_{15}	–1.17767 (-2)	–8.35587 (-1)	2.40850 (0)	–1.59682 (0)
	a_2			
	c_{2l0}	c_{2l1}	c_{2l2}	c_{2l3}
b_{20}	1.29112 (2)	–9.98733 (3)	2.78191 (4)	–1.86921 (4)
b_{21}	–1.12583 (2)	9.63611 (3)	–2.66734 (4)	1.79080 (4)
b_{22}	3.89523 (1)	–3.67200 (3)	1.01055 (4)	–6.77833 (3)
b_{23}	–6.70992 (0)	6.91170 (2)	–1.89208 (3)	1.26791 (3)
b_{24}	5.76212 (-1)	–6.42985 (1)	1.75181 (2)	–1.17284 (2)
b_{25}	–1.97307 (-2)	2.36651 (0)	–6.42031 (0)	4.29475 (0)
	a_3			
	c_{3l0}	c_{3l1}	c_{3l2}	c_{3l3}
b_{30}	–1.95456 (2)	7.51194 (3)	–2.01052 (4)	1.34888 (4)
b_{31}	1.80820 (2)	–7.19551 (3)	1.91845 (4)	–1.28727 (4)
b_{32}	–6.62234 (1)	2.72277 (3)	–7.23386 (3)	4.85339 (3)
b_{33}	1.20214 (1)	–5.09115 (2)	1.34832 (3)	–9.04429 (2)
b_{34}	–1.08251 (0)	4.70739 (1)	–1.24314 (2)	8.33660 (1)
b_{35}	3.87011 (-2)	–1.72301 (0)	4.53872 (0)	–3.04289 (0)
	a_4			
	c_{4l0}	c_{4l1}	c_{4l2}	c_{4l3}
b_{40}	5.85147 (1)	–1.64930 (3)	4.32086 (3)	–2.90577 (3)
b_{41}	–5.41777 (1)	1.57005 (3)	–4.10386 (3)	2.76141 (3)
b_{42}	1.98294 (1)	–5.90521 (2)	1.54029 (3)	–1.03671 (3)
b_{43}	–3.59233 (0)	1.09786 (2)	–2.85819 (2)	1.92392 (2)
b_{44}	3.22512 (-1)	–1.00971 (1)	2.62425 (1)	–1.76645 (1)
b_{45}	–1.14890 (-2)	3.67784 (-1)	–9.54449 (-1)	6.42438 (-1)

constant. This can be observed in Fig. 3, where we show $\log T$ vs. $\log P$ for a set of 5 values of $T_{\rm eff}$ and 4 values of $\log g$ ($F_{\rm rel}$ = 0). The effective temperature may be approximated by $T_{\tau=2/3}$ (marked in Fig. 3). The total flux is proportional to $\sigma T_{\rm eff}^4$ and, using Eq. (1), β is thus proportional to the total extension of $\Delta T_{\tau=2/3}$ obtained for each $T_{\rm eff}$ and models with $\log g$ varying between 3.5 and 5.0 (the vertical bars in Fig. 3).

The $T_{\rm eff}$ = 3900 K models are so adiabatic that β is small (the points at $T_{\tau=2/3}$ almost follow one adiabat). For intermediate $T_{\rm eff}$, convection becomes less efficient, with a correspondingly larger entropy jump near the surface. The stabilizing influence of convection thus diminishes, and the values of β increase (as

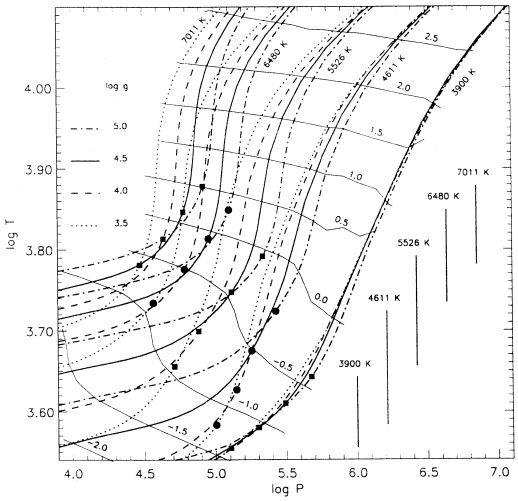

Fig. 3. $\log T$ vs. $\log P$ for convective non-grey non-illuminated models with $\alpha = 1.5$, $\mu = 0.93$ and different values of $T_{\rm eff}$. For each value of $T_{\rm eff}$ there are 4 models with different values of $\log g$, which match the entropy of the reference model ($\log g$ = 4.5) at the bottom. The ■ and ● symbols mark the $\tau_{\rm Ross}$ = 2/3 (Rosseland mean) layers. The vertical bars mark the extension of the temperature variation with the different $\log g$ for each $T_{\rm eff}$ at $\tau_{\rm Ross}$ = 2/3. The length of these bars is proportional to β. The thin continuous lines are contours of $\log \kappa$ (again shown as Rosseland mean) constant, labelled from $\log \kappa$ = -2.0 to 2.5 in equal steps of 0.5 dex.

illustrated by the increase of the extension of the vertical bars in Fig. 3 for $T_{\rm eff} \lesssim 5500$ K).

For even higher $T_{\rm eff}$ the influence of the opacity becomes significant. The temperature dependence of κ (i.e. $\partial \log \kappa / \partial \log T$) is much larger than its pressure dependence ($\partial \log \kappa / \partial \log P$). This is clear from Fig. 3, which shows that the contour levels of constant $\log \kappa$ tend to run parallel to the $\log P$ axis, especially as $\log T$ increases. The physical reason for this is that $T_{\rm eff}$ enters the regime where H is the dominant electron contributor and where, consequently, hydrogen ionization implies that the opacity (predominantly H^-) increases very rapidly with temperature. To appreciate how the temperature sensitivity of κ influences β it is useful to consider the approximation $\tau \sim \kappa P/g$, according to which, if g is increased, it does not take much of an increase in T to compensate for the change. One may derive

$$\beta \approx \frac{\Delta \log T^4}{\Delta \log g} \approx \frac{4}{\left[\frac{\partial \log \kappa}{\partial \log T}\right]_P + \left[1+\left[\frac{\partial \log \kappa}{\partial \log P}\right]_T\right] \Big/ \frac{d \log T}{d \log P}}, \qquad (3)$$

where $d \log T / d \log P$ is the logarithmic temperature gradient of the model at τ = 2/3, and the dependence of $d \log T / d \log P$ on g has been ignored. Eq. 3 shows that β does indeed become small for large values of $\left[\frac{\partial \log \kappa}{\partial \log T}\right]_P$.

As discussed further below (see Sect. 3), an increasing external flux tends to extinguish convection. Illuminated models thus tend to approach radiative equilibrium, and hence β increases as the amount of illumination increases.

After Paper I was published, Claret (1998) submitted a work dealing with the calculation of the gravity–brightening exponent (and of limb-darkening coefficients as well) using a different approach. By using a modified version of the triangles technique (Kippenhahn et al. 1967), Claret (1998) computed β values of non-illuminated models for a $T_{\rm eff}$ interval larger than in Paper I. His results are presented as a function of the logarithm of the model masses, starting at the Solar mass. Considering values at the ZAMS, the temperature interval of $3.56 < \log T_{\rm eff} < 3.85$, covered in our work, corresponds to $-0.222 < \log(m/{\rm M}_\odot) < 0.176$. Claret's (1998) results are in good agreement with those from Paper I with respect to the behaviour of β in the common region ($3.81 < \log T_{\rm eff} < 3.85$) covered by both works.

The lower limit in $\log T_{\rm eff}$ of Claret's models (3.81) is larger than the value for which we found a maximum in β (at $\log T_{\rm eff} \approx 3.74$, $F_{\rm rel} = 0$). However, his calculation of the evolution of β with age for two of the models does confirm the existence of such a feature (see his Fig. 5, for the evolution of a 2 $M_\odot$ model off the Main Sequence, and his Fig. 6. for the evolution of a 1 $M_\odot$ model from the Pre-Main Sequence phase). There is no specific comment about this behaviour in his work and Claret (1998) interprets the general trends in β changes in terms of convection only. However, as explained above, this behaviour is due to the interplay between the convection and opacity properties of the models.

2.2.2. A polynomial approximation for β

The variation of β for illuminated grey atmospheres is primarily a function of $T_{\rm eff}$, $F_{{\rm rel},\mu}$ and μ. In order to easily account for this dependence in light curve synthesis programs, we separate each variable using polynomials:

$$\beta = \sum_{n=0}^{4} a_n(t,\mu) F_{{\rm rel},\mu}^n \quad (4)$$

$$\text{where } a_n(t,\mu) = \sum_{l=0}^{5} b_{nl}(\mu) t^l \quad (5)$$

$$\text{and } b_{nl}(\mu) = \sum_{m=0}^{3} c_{nlm} \mu^m, \text{ with } t = T_{\rm eff} \times 10^{-3} \quad (6)$$

The theoretical grid obtained is shown in Fig. 2, with the values determined from the atmosphere model overplotted. The 120 c_{nlj} coefficients obtained with grey models are listed in Table 1. The standard deviation of the parametric fit is σ = 0.022 (26 models), with no systematic tendency of σ with the incidence angle. Due to the numeric operations involved, we advise the use of the full precision given in Table 1, in order to keep errors $\leq$0.1% when calculating β from Eqs. (4)-(6). Care must be taken in any attempt to extrapolate beyond the limits given in Fig. 2.

In Fig. 4 we show β calculated for grey atmospheres ($T_{\rm eff}$ = 3697 K, μ = 0.9306) illuminated by grey and non–grey fluxes for different values of $T_{\rm h}$ (3 700 K, 4 500 K, 7 000 K and 10 000 K). Our parametric approximation (Eqs. 4–6) is also included. One can see that β does not depend significantly on $T_{\rm h}$ for grey illuminated models. Similar results are obtained for grey models with other values of μ and of $T_{\rm eff}$.

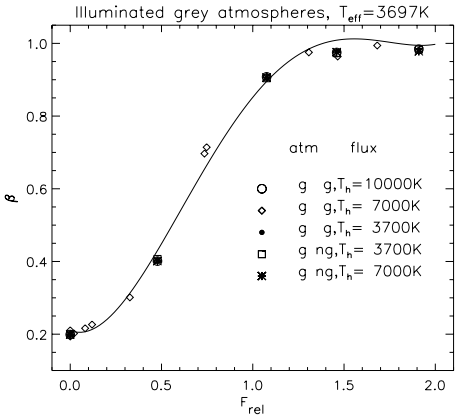

Fig. 4. $\beta(F_{{\rm rel},\mu=0.9306})$, for grey atmospheres illuminated with grey (g) and non–grey (ng) fluxes with different values of $T_{\rm h}$. The solid line corresponds to our parameterization given by Eqs. (4) to (6) and the coefficients in Table 1.

2.3. Convective non–grey (line–blanketed) atmospheres

Using the same procedure as in Sects. 2.1 and 2.2 we constructed non–grey atmosphere models illuminated by grey and non–grey fluxes. The gravity–brightening exponent values obtained are close to the grey ones for effective temperatures of the illuminating stars ($T_{\rm h}$) close to those of the illuminated stars ($T_{\rm eff}$). However, for a given illuminated star and a fixed incident flux, β decreases with the effective temperature of the illuminating star, showing that there is a dependence of β on $T_{\rm h}$ beyond the dependence through the incident flux ($\propto T_{\rm h}^4$).

The differences between model atmospheres illuminated by grey and non–grey fluxes are small relative to the differences between the grey and non–grey illuminated models. Thus, significant changes of β are not related to the use of line–blanketed illuminating fluxes, but rather to the interaction between a line–blanketed illuminated atmosphere and the overall spectral distribution of the illuminating flux. Representative results are shown in Fig. 5, for a particular line–blanketed illuminated atmosphere ($T_{\rm eff} = 3\,697$ K) and different illuminating fluxes (a result obtained with a grey illuminated model is shown for comparison).

It is clear from Fig. 5 that at least one more parameter is influencing the results in the case of non–grey illuminated models. By comparing the illuminated grey and non–grey models we realized that the main difference between them is that the spectral line opacity prevents part of the incident flux from reaching the continuum formation layers in the non–grey models. Because most of the spectral line opacity occurs in the UV, an increasing amount of the incident flux is intercepted for increasing effective temperatures of the illuminating star. The more of the incident

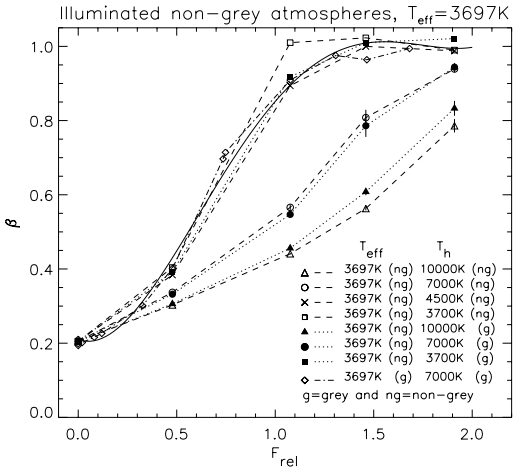

Fig. 5. $\beta(t, F_{\mathrm{rel},\mu})$, for non–grey atmospheres illuminated by grey (g) and non–grey (ng) fluxes with different values of T_{h}. The solid line has the same meaning as in Fig. 4.

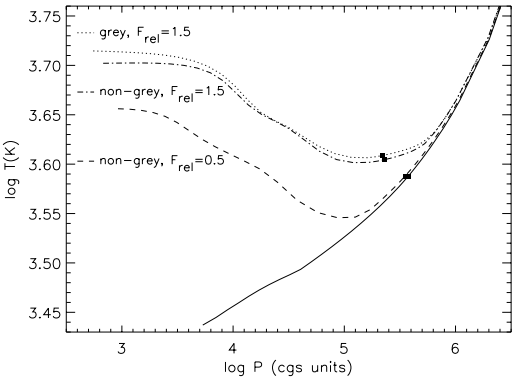

Fig. 6. $\log T$ vs. $\log P$ for convective non–grey non-illuminated (solid line) model with $T_{\mathrm{eff}} = 3\,697$ K and the same model illuminated by grey and non–grey fluxes with $T_{\mathrm{h}} = 10\,000$ K, $\mu = 0.93$ and different relative fluxes. The ■ signs mark the τ = 2/3 layers, as in Fig. 3.

flux that is intercepted, the smaller is the influence of the illumination on the convection. As a consequence, the increase of β with increasing illumination is reduced in non–grey models relative to grey models.

3. Discussion

The values of the β exponent in grey atmospheres illuminated by grey and non–grey fluxes are very similar. In these models β primarily depends on the effective temperature of the illuminated star, the relative flux and the illumination direction. The exponent increases as the relative flux increases, until it approaches the von Zeipel value ($\beta = 1$) for radiative stars.

Non–grey atmospheres illuminated by grey and non–grey fluxes also have similar β, but for these atmospheres β also depends on the effective temperature of the illuminating star, T_{h}. In line with the discussion above, this extra dependence may be thought of in terms of how much of the incident flux reaches the continuum formation layers of the illuminated atmosphere. As T_{h} increases, the β values decrease, following nevertheless a similar behavior as a function of the relative flux, as can be seen in Fig. 5.

Some models in Fig. 5 (e.g., T_{eff} = 3 697 K illuminated with T_{h} = 3 700 K and $F_{\mathrm{rel}} > 1$) have β values slightly larger than 1 (by $\lesssim$3%). These values are consistent with unity within the errors of our method, and may be a numerical artifact. For grey models the β values return to unity for even larger values of F_{rel}, and for non–grey models a similar asymptotic behavior may be expected. It is somewhat inconsistent to consider models with large values of F_{rel} and $T_{\mathrm{h}} \sim T_{\mathrm{eff}}$, though, since the geometrical parameters needed would not be physically meaningful (e.g. the apparent radius would imply one star touching or even intersecting the other). However, if one performs the calculation, the asymptotic behavior is indeed found also for the non–grey illuminated models, with $\beta \lesssim 1$ for $F_{\mathrm{rel}} \sim 2.2$. On the other hand, Eq. (3), in principle, does not prevent $\beta > 1$ values. For instance, for an adiabatic ideal gas with κ constant and $\frac{d\log T}{d\log P} = 2/5$, one would have $\beta = 8/5$. For a real gas, if the opacity increased sufficiently slowly with temperature and pressure, and $\frac{d\log T}{d\log P}$ was sufficiently large, Eq. (3) would allow $\beta > 1$ values, also.

The asymptotic approach to the von Zeipel value of the gravity–brightening exponent may be understood as follows: When a model atmosphere is heated by a large external flux, a significant part of the convection is extinguished (hence most of its original flux vanishes) and the model practically becomes one in radiative equilibrium, obeying the von Zeipel law asymptotically. This is illustrated in Fig. 6 where we show a non–grey model with $T_{\mathrm{eff}} = 3\,697$ K illuminated by grey and non–grey fluxes with $T_{\mathrm{h}} = 10\,000$ K and two $F_{\mathrm{rel},\mu}$ values. The greater the amount of external illumination, the more the model deviates from the $\log T$ vs. $\log P$ relation characteristic of convective equilibrium. This happens especially for $\tau \lesssim 1$ and affects deeper layers as the amount of external illumination increases.

However, as T_{h} increases, the external heating flux is shifted towards the UV. Due to the larger photospheric absorption in UV, the external flux penetrates less into the photosphere of the illuminated model, and hence convection is less affected. The smaller change in convection yields a smaller β value, and the effect of increasing the exponent is pushed to higher relative fluxes. An immediate consequence is that line–blanketed illuminated atmospheres have β values which must depend on the metal abundance [Fe/H] of the model.

Somewhat more subtle effects could result from the interference of spectral line patterns in the illuminating and illuminated stars. As a particular case, when similar stars orbit each other in

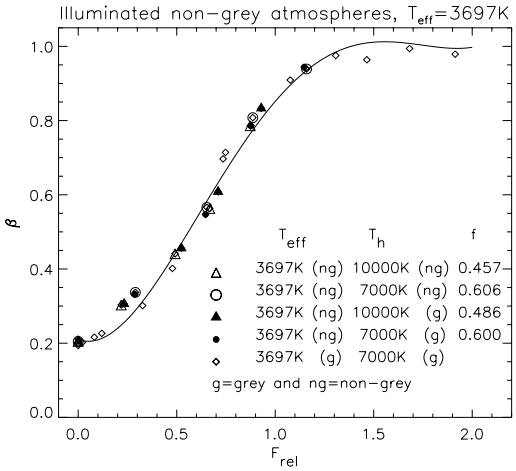

Fig. 7. Penetration factors (f) for the models presented in Fig. 5. The symbols are the same as in Fig. 5, the larger symbols correspond to the corrected relative fluxes. The solid line has the same meaning as in Fig. 4.

elliptical orbits, the spectral line patterns of the stars will match optimally at apogee and perigee, and there will be a corresponding maximum in the amount of illumination of the continuum layers. For non-zero Doppler shifts the illumination of the continuum layers will decrease. However, the size of this effect is only of the order of the difference between grey and non–grey illuminating models. As mentioned above, this difference is, in general, small.

3.1. The penetration factor

In light of the discussion of the non–grey results of Sect. 2.3, the results for grey models obtained in Sect. 2.2 are more general than they might seem at first sight. The relative fluxes in the non–grey case should be regarded as the effective amount of flux that penetrates to the continuum formation layers. We may describe this effect through a "penetration" factor, f, that, multiplied by the incident flux, gives a new corrected flux that may be used to interpolate β with the grey parameterization coefficients given in Table 1 ($F_{\mathrm{rel},\mu} = f F_{\mathrm{rel},\mu,\mathrm{Total}}$). For grey illuminated atmospheres $f = 1$, while $f < 1$ for line–blanketed illuminated models. This interpretation is strictly correct only if there exists a unique "penetration" factor for each set of parameters (T_{eff}, T_{h} and μ). Fig. 7 shows the models presented in Fig. 5. It illustrates that it is indeed possible to find a factor f that brings together all the points for each set of parameters T_{eff}, T_{h} and μ to be fitted by the parametric curves given by Eqs. (4) to (6) and the coefficients of Table 1.

Fig. 7 shows that f differs between cases where the incident flux is a continuum–only (g) or a line–blanketed (ng) one. This is due to minor differences in the amount of flux in the UV region. However, to a good approximation we may assume that the penetration factor is related only to the opacity distribution of the illuminated model. The surfaces presented in Fig. 2 may then be used to determine β even in the non–grey case, using appropriate values for the incident flux and the penetration factor.

In the present work we have concentrated on establishing the existence of such a penetration factor, by empirically calculating it and showing that it is the same for each family of models. However, it should be possible to calculate f from a knowledge of the effective temperature of the incident flux (amount of UV) and of the opacity properties of the atmosphere model in the upper layers (determining how much of the UV flux that is blocked). Studies of how to actually compute this factor for each situation are in progress and will be published elsewhere.

3.2. Possible tests

The secondaries of Algol-type systems are convective stars with effective temperatures around 5 000 K and may be used, with some caution, to test the gravity–brightening exponents determined here. The main problem with Algol systems is the transfer of mass between the components, which frequently causes distortion of the light curves due to spots on the stars. Nevertheless, some of these systems, whose absolute parameters are well-determined have been satisfactorily fitted with Lucy's value 0.32 kept fixed (e.g. TV Cas, Khalesseh & Hill 1992; AT Peg, Maxted et al. 1994; HU Tau, Maxted et al. 1995). In Algol-type systems T_{h} is much greater than the secondary's effective temperature ($T_{\mathrm{h}} \approx 10\,000$ K) yielding a large relative flux ($F_{\mathrm{rel},\mu} > 1.0$) and consequently a value of β much greater than 0.32, if we use the results obtained with grey atmospheres. But the results presented in the last section show that, in this case ($T_{\mathrm{h}} \gg T_{\mathrm{eff}}$), the value of the exponent decreases substantially from the value obtained with grey illuminated atmospheres. This is a reassuring point for our predicted β values, since, even taking into account the difficulties in modeling Algols, it is expected from the published results that β should not differ very much from Lucy's value. In most of the cases the authors had to let the reflection albedos vary in order to fit the light curves, and the results are albedos greater than those theoretically predicted for such stars. The β exponents assumed in these works are smaller than they should be according even to our non–grey results, possibly yielding an incorrect determination of the higher reflection albedos.

As stressed both in Paper I and by Claret (1998), comparisons between the theoretical calculations and the empirical determinations of β available at present are problematic and inconclusive, although promising (see Fig. 3 of Paper I and Fig. 7 of Claret 1998). A possible test of the results presented here is to fit the light curves of Algol-type stars using our predicted β values, to see if it is possible to improve upon earlier results. Such tests are currently underway, with our results (of this work and Paper1, for β, and of Alencar & Vaz 1999, for the limb-darkening coefficients) being implemented in a version of the WD model for light curve synthesis and solution of eclipsing systems (Wil-

son & Devinney 1971, Wilson 1979, Vaz et al. 1995, Casey et al. 1998).

4. Summary and conclusions

The most general result of the present paper is that we have demonstrated for the first time the influence of external illumination on the gravity–brightening exponent, showing that external illumination increases the value of β. This suggests that the classical value of $\beta = 0.32$ may be too small for binary systems with close components.

The results presented here extend our results from Paper I for illuminated convective atmospheres, providing β in the range $3\,700\,\mathrm{K} < T_{\mathrm{eff}} < 7\,000\,\mathrm{K}$, for varying amounts of external illumination and angles of incidence. For illuminated convective grey atmospheres the gravity–brightening exponent may be calculated from the effective temperature of the illuminated star, the external radiation angle of incidence, and the incident flux of radiation that reaches the continuum forming layers in the illuminated star. The general trend of β having a maximum in the T_{eff} range covered in this work is interpreted as being caused by an interplay between the convection and opacity properties of the atmosphere model.

For illuminated non–grey atmospheres the gravity–brightening exponent also depends on the spectral distribution of the incident flux. When T_{h} does not differ by more than $\sim 25\%$ from T_{eff}, the results obtained with illuminated grey atmospheres may be used. For larger relative temperature differences, one needs to correct the relative incident flux with a penetration factor, corresponding to the absorption of UV flux in the upper layers of the illuminated model. The penetration factor is necessarily a function of the metal abundance of the atmosphere, but this aspect has not been studied in the present paper.

Acknowledgements. SHPA and LPRV were supported in part by FAPEMIG, CNPq, FINEP, CAPES (Brazilian institutions). ÅN was supported in part by the Danish National Research Foundation, through its establishment of the Theoretical Astrophysics Center. Fruitful discussions with Drs. B.E. Helt and J.V. Clausen are gratefully acknowledged. The comments of an anonymous referee were fundamental to bring this work to its final form.

References

Alencar S.H.P., Vaz L.P.R., 1997, A&A 326, 257 (Paper I)
Alencar S.H.P., Vaz L.P.R., 1999, A&AS 135, 555
Bell R.A., Eriksson K., Gustafsson B., Nordlund Å., 1976, A&AS 23, 37
Casey B.W., Mathieu R.D., Vaz L.P.R., Andersen J., Suntzeff N.B., 1998, AJ 115, 1617
Claret A., 1995, A&AS 109, 441
Claret A., 1998, A&AS 131, 395
Gustafsson B., Bell R.A., Eriksson K., Nordlund Å., 1975 A&A 42, 407
Khalesseh B., Hill G., 1992, A&A 257, 199
Kippenhahn R., Weigert A., Hoffmeister E., 1967, in Computational Physics. Academic Press, New York, Vol. 7, p. 129
Kurucz, R.L., 1979, ApJS 40, 1
Lucy L.B., 1967, Zeitschr. für Astrophys. 65, 89
Maxted P.F.L., Hill G., Hilditch R.W., 1994, A&A 285, 535
Maxted P.F.L., Hill G., Hilditch R.W., 1995, A&A 301, 141
Mihalas D., 1978, in Stellar Atmospheres, W.H. Freeman and Co., Chapter 3
Nordlund Å., Vaz L.P.R., 1990, A&A 228, 231
Vaz L.P.R., Andersen J., Rabello Soares M.C.A., 1995, A&A 301, 693
Vaz L.P.R., Nordlund Å., 1985, A&A 147, 281
von Zeipel H., 1924, MNRAS 84, 665
Wilson R.E., 1979, ApJ 234, 1054
Wilson R.E., Devinney E.J., 1971, ApJ 182, 539

11.3 Limb-darkening (Paper 3)

For the sake of clarity in the thesis the symbol ν represents frequency, while the cosine of θ, the incidence angle of the external illumination, is ω. Unfortunately the symbols used in the papers are sometimes different. In the following paper $\nu = \cos\theta$.

ASTRONOMY & ASTROPHYSICS
SUPPLEMENT SERIES

Astron. Astrophys. Suppl. Ser. **135**, 555–564 (1999)

Limb-darkening coefficients of illuminated atmospheres

I. Results for illuminated line-blanketed models with $3\,700\,\mathrm{K} < T_{\mathrm{eff}} < 7\,000\,\mathrm{K}^{\star}$

S.H.P. Alencar[1] **and L.P.R. Vaz**[1]

Departamento de Física, ICEX–UFMG, C.P. 702, 30.123-970 Belo Horizonte, MG, Brazil

Received September 10; accepted November 24, 1998

Abstract. The effect of mutual illumination in a close binary on the limb-darkening coefficients is studied using the UMA (Uppsala Model Atmosphere) code in convective line-blanketed atmospheres illuminated by line-blanketed fluxes, for $3\,700\,\mathrm{K} < T_{\mathrm{eff}} < 7\,000\,\mathrm{K}$ and $7\,000\,\mathrm{K} < T_{\mathrm{h}} < 12\,000\,\mathrm{K}$. The results show that the limb-darkening coefficients of illuminated atmospheres are significantly different from the non-illuminated ones and mostly depend on four parameters: the amount of incident energy, the illumination direction, the effective temperature of the illuminated star and the temperature of the illuminating one. We present bolometric, monochromatic and passband specific coefficients and we give, for the latter, analytical expressions in order to easily account for the effect in light curve synthesis programs.

Key words: stars: fundamental parameters — stars: atmospheres — binaries: close; eclipsing

1. Introduction

Limb-darkening coefficients can only be directly determined for very few stars apart from the Sun. Due to that, when computing light curves (LC) synthesis programs, those coefficients are usually interpolated from tables of theoretical values calculated from atmosphere models.

Over the past decades many analytical approximations have been proposed to describe the variation of the intensity over a stellar surface. Initially, the most adopted was the linear limb-darkening law (Milne 1921):

$$R_\lambda(\mu) = \frac{I_\lambda(\mu)}{I_\lambda(1)} = 1 - x_\lambda(1-\mu) \tag{1}$$

where I_λ is the beam intensity at the wavelength λ, μ is the co-sinus of γ, the angle between the atmosphere normal and the beam direction (the line of sight angle, see Fig. 1) and x_λ is the so-called limb-darkening coefficient. This law gives a good description of the limb-darkening in the solar atmosphere that, due to its temperature and physical conditions, is reasonably well represented by a grey atmosphere (for which the limb-darkening is well adjusted by the linear law). Lately, mainly due to theoretical studies on stellar atmospheres, other non-linear laws were proposed, as the polynomial approximations, that better described the effect away from the solar temperature range:

$$R_\lambda(\mu) = \frac{I_\lambda(\mu)}{I_\lambda(1)} = 1 - x_\lambda(1-\mu) - y_\lambda(1-\mu)^n \tag{2}$$

where y_λ are the non-linear limb-darkening coefficients, $n = 2$ (Wade & Ruciński 1985, using the version 1979 of ATLAS by Kurucz 1979; Manduca et al. 1977 and Claret & Giménez 1990, using versions of UMA, see Gustafsson et al. 1975; Bell et al. 1976) for the quadratic case and $n = 3$ (Van't Veer 1960, quoted by Díaz-Cordovés & Giménez 1992) for the cubic law.

The logarithmic approximation, proposed by Klingesmith & Sobieski (1970) gave very good results in representing their theoretical models, valid for the interval $10\,000\,\mathrm{K} < T_{\mathrm{eff}} < 40\,000\,\mathrm{K}$:

$$R_\lambda(\mu) = \frac{I_\lambda(\mu)}{I_\lambda(1)} = 1 - x_\lambda(1-\mu) - y_\lambda\mu\ln\mu, \tag{3}$$

confirmed by Van Hamme (VH, 1993), with ATLAS (version 1991). Díaz-Cordovés & Giménez (1992, using ATLAS version 1979) proposed a new non-linear approximation, a square root limb-darkening law:

$$R_\lambda(\mu) = \frac{I_\lambda(\mu)}{I_\lambda(1)} = 1 - x_\lambda(1-\mu) - y_\lambda(1-\sqrt{\mu}). \tag{4}$$

Send offprint requests to: L.P.R. Vaz
e-mails: silvia@fisica.ufmg.br, lpv@fisica.ufmg.br

* Tables 1, 2 and 3 will be also accessible in electronic form at the CDS via anonymous ftp to cdsarc.u-strasbg.fr (130.79.128.5) or via http://cdsweb.u-strasbg.fr/Abstract.html

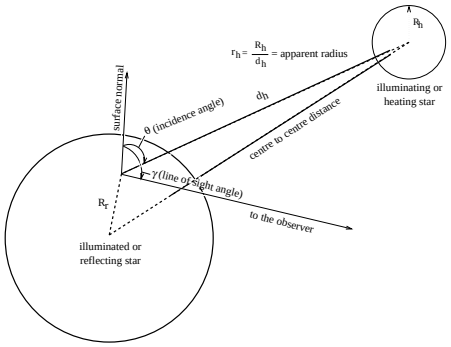

Fig. 1. Geometry of illumination in a double star system

In subsequent papers (Claret et al. 1995 and Díaz-Cordovés et al. 1995, both using ATLAS version 1991), studies are made only with the square root law and the quadratic and linear ones. In that case, the square root approximation seems almost always to be the best one.

According to VH, the logarithmic law gives the best approximation in the UV, while the square root law is the best in the IR and longer wavelengths. In the optical region, cooler stars are better represented by the logarithmic law and high temperature stars by a square root law.

In close binary systems, the mutual irradiation affects the light curves and the spectra of both stars. The reflection effect present in close binary systems has a strong influence on limb-darkening coefficients, as already noticed by Vaz & Nordlund (1985), Nordlund & Vaz (1990) and Claret & Giménez (CG, 1990). One effect concerns the values of the limb-darkening coefficients, which are changed by the infalling flux. In fact, even the limb-darkening law which best represents the variation of the flux with the line of sight angle may change due to the external illumination. Another important difference, as compared to the normal stellar atmospheres (for which the limb-darkening laws and coefficients are valid over the whole stellar surface), is that the illuminated atmospheres show different limb-darkening coefficients (and laws) for different points on the stellar surface, due to the dependence of these on the incidence angle of the infalling flux. Therefore, the best representation for the center-to-limb variation of the surface brightness of eclipsing binary components in the synthetic LC generation studies is to use the coefficients calculated for the local configuration (i.e. considering the apparent radius, the direction of illumination and the temperature of the companion, see below).

Our goal is to understand how the external illumination affects the limb-darkening laws and coefficients and to present the results in a way to easily account for the effect in LC synthesis programs. We made calculations of bolometric, passband-specific and monochromatic limb-darkening coefficients for all the laws presented above.

In real systems both stars are affected by the mutual illumination. However, in the present study we do not consider the effect of the irradiation from the illuminated (or reflecting) star on the illuminating one (also referred to as heating or source star), i.e. the small changing in the effective temperature of the illuminating star due to the "reflection effect" from its companion. As we are considering mostly systems for which the illuminated star is cooler than the illuminating one, this is probably a minor contribution. Consequently, we did not take second order effects into account (back reflection), either.

In Sect. 2 we describe the method and study the effect of illumination on the limb-darkening laws and coefficients (bolometric, monochromatic and for the passband specific filters of the Strömgren and of the Johnson-Morgan photometric systems), presenting the results as polynomial expressions and tables. We discuss the results in Sect. 3, and present our conclusions in Sect. 4.

2. The atmosphere model

We use the Uppsala Model Atmosphere (UMA, Gustafsson et al. 1975; Bell et al. 1976) code, in a version by Vaz & Nordlund (1985), as described in Alencar & Vaz (1997). The code is intended for cool ($3\,500\,\mathrm{K} < T_{\rm eff} < 8\,000\,\mathrm{K}$) atmospheres, and assumed hydrostatic equilibrium, a plane–parallel structure, and local thermodynamic equilibrium. Convection is modelled with the mixing length recipe.

An illuminated model is defined by its effective temperature $T_{\rm eff}$, its surface acceleration of gravity g, mixing length parameter $\alpha = l/H_P$, and chemical composition (fixed at solar abundance in this work). The external illumination is parametrized by the direction of illumination ν (the cosine of θ, the incidence angle with respect to the surface normal), the effective temperature of the heating star $T_{\rm h}$, and its apparent radius $r_{\rm h}$ (the ratio between the radius of the heating star and the distance from its centre to the point on the surface of the reflecting star). The geometry of illumination in a double star system is shown in Fig. 1. We kept $\alpha = l/H_P$ fixed at 1.5 for the reflecting star atmosphere.

We noticed that the effect caused by illumination on the limb-darkening was rather weakly dependent on the $\log g$ of the model. This can be seen in Fig. 2, where we show that the effect of changing the $\log g$ from 3.5 to 5.0 corresponds to only $\pm 7\%$ and $\pm 9\%$ of the overall effect of illuminating an atmosphere of $T_{\rm eff} = 3\,697\,\mathrm{K}$ by $T_{\rm h} = 3\,700\,\mathrm{K}$ and $10\,000\,\mathrm{K}$, respectively. Therefore, we did calculations only for $\log g = 4.5$, as for this value we achieve a representative mean effect of illumination for the interval $3.5 \leq \log\ g \leq 5.0$. We study illuminated atmospheres with line absorption (line-blanketed or ODF)

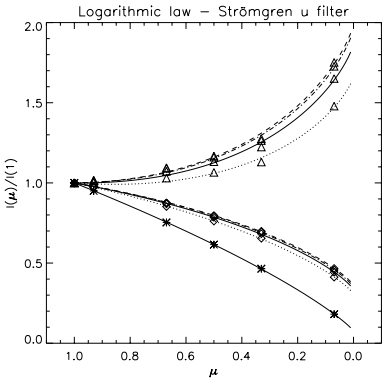

Fig. 2. Comparison between the effect of the surface gravity and of external illumination on the limb-darkening, here adjusted by the logarithmic law, see Eq. (3). The * symbols correspond to the non–illuminated model with $T_{\rm eff} = 3\,697$ K. The $\diamond$ and $\triangle$ symbols correspond to this model illuminated by $T_{\rm h} = 3\,700$ K and 10 000 K, respectively. The dashed lines correspond to models with $\log g = 3.5$, the dash-dotted ones to $\log g = 4.0$, the solid lines to $\log g = 4.5$ and the dotted lines to $\log g = 5.0$

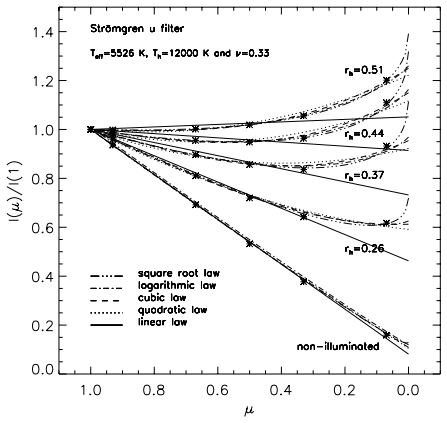

Fig. 3. Adjusted limb-darkening laws for a non-illuminated model and 4 illuminated models (varying $r_{\rm h}$). The asterisks represent the model results

in convective equilibrium. The ODF tables limit the temperature range of this study to those corresponding to (ZAMS) stars with masses ranging from $0.6\,M_\odot$ to $1.5\,M_\odot$.

This same model has been used to study, in another paper and for the first time in the literature, the effect of illumination on the gravity brightening exponent β, another important parameter for LC synthesis. That work (Alencar et al. 1998) is a continuation of the study of the β exponent using stellar atmospheres (Alencar & Vaz 1997).

2.1. The method

The atmosphere model generates intensities in six different angular directions ($\mu = 0.06943, 0.33001, 0.5, 0.66999, 0.93057$ and 1.0) and 368 wavelengths ranging from 1500 Å to 124000 Å. Starting from these data, monochromatic, passband-specific and bolometric limb-darkening coefficients can be calculated. We will present here the results obtained using two different calculation methods. The first one, described by CG, determines the coefficients by least square-fitting of the integrated and normalized model intensities. The second method follows the procedure outlined by VH where a number of physical constraints, equal to the number of coefficients to be determined, are assumed. The limb-darkening coefficients are obtained by solving the constraint equations. Using a one parameter law, the constraint is the conservation of the total flux and for a two parameter law, the additional constraint that the mean intensity of the approximation and the atmosphere model must be equal is applied. When calculating the passband coefficients we made a convolution of the intensities with the response functions corresponding to the Strömgren filters *uvby* (Crawford & Barnes 1970) and the *UBVRI* passbands (Bessel 1983). We used in the convolution the atmospheric mean transmission by Allen (1976), the reflection curve of two aluminum coated mirrors (Allen 1976), the sensitivity of a 1P21 photo-multiplier from Kurucz (1979) and for the Strömgren filters, the sensitivity function of the SAT photometer (Florentin-Nielsen 1983, personal communication).

We calculated models with relative fluxes ($F_{{\rm rel},\nu} = [T_{\rm h}/T_{\rm eff}]^4 {r_{\rm h}}^2 \nu$) ranging from 0 to 2, whenever possible ($r_{\rm h} < 1$). Those values are easily found in the literature amongst many types of binary systems. Using $\nu = 1$ we find $F_{\rm rel} = 0.446$ for V Pup (detached, Andersen et al. 1983), 0.338 for LZ Cen (detached, Vaz et al. 1995), 0.386 for RY Aqr (semi–detached, Helt 1987), 0.660 for DH Cep (detached, Hilditch et al. 1996), 1.35 for AT Peg (algol, Maxted et al. 1994), 2.39 for HU Tau (algol, Maxted et al. 1995) and 2.72 for TV Cas (algol, Khalesseh & Hill 1992).

Many of the binary systems above also have temperatures that fall in our selected ranges: RY Aqr ($T_{\rm eff} = 4\,500$ K and $T_{\rm h} = 7\,600$ K), AT Peg (4 898 K and 8 395 K), HU Tau (5 495 K and 12 022 K) and TV Cas (5 248 K and 10 471 K).

As with $T_{\rm h}$ close to $T_{\rm eff}$ we could not get large values of $F_{\rm rel}$ with reasonable values of $r_{\rm h}$, we studied models mostly ranging in the interval $7\,000\,{\rm K} < T_{\rm h} < 12\,000\,{\rm K}$.

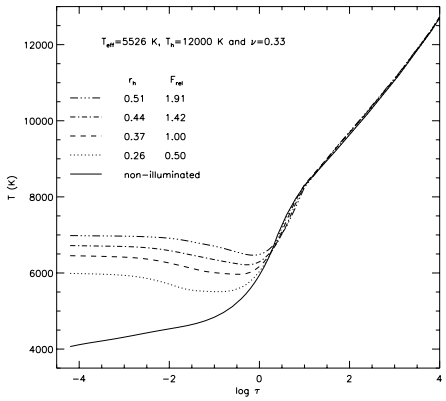

Fig. 4. The run of the temperature with the optical depth (Rosseland mean) for the models shown in Fig. 3

The illuminating non–grey fluxes with $T_{\rm h} \leq 7\,000\,{\rm K}$ were generated with the UMA code, while for higher $T_{\rm h}$ we took the fluxes from Kurucz (1979). We did calculate some models with $T_{\rm h}$ close to $T_{\rm eff}$ ($T_{\rm h} = 3700\,{\rm K}$, $4600\,{\rm K}$, $5500\,{\rm K}$, $6700\,{\rm K}$) and the results are in agreement with our studies with higher $T_{\rm h}$ so that our results do apply for lower heating temperatures, also. However, we advise caution in using those approximations extended to outside the limits proposed in this work.

In Sect. 2.2 we give the results obtained with line-blanketed atmospheres illuminated by line-blanketed fluxes, showing differences in the calculations with the two distinct methods.

2.2. Results

Figure 3 shows that the external illumination strongly affects the limb-darkening laws and coefficients of illuminated atmospheres as compared with the non-illuminated ones. These models are approximately equivalent to those calculated by CG and ν has a mean value between vertical and grazing incidence. In order to be consistent we will show the results for the Strömgren u filter, but the effects are similar for the other calculations done, bolometric, monochromatic and for all the Strömgren filters and the $UBVRI$ filters of the Johnson-Morgan system, as well. As we increase the amount of incident energy, for example by increasing the apparent radius while keeping the other parameters fixed, the law for non-illuminated models no longer represents the calculated intensities, showing that non-illuminated coefficients yield wrong limb-darkening laws when used with illuminated stars.

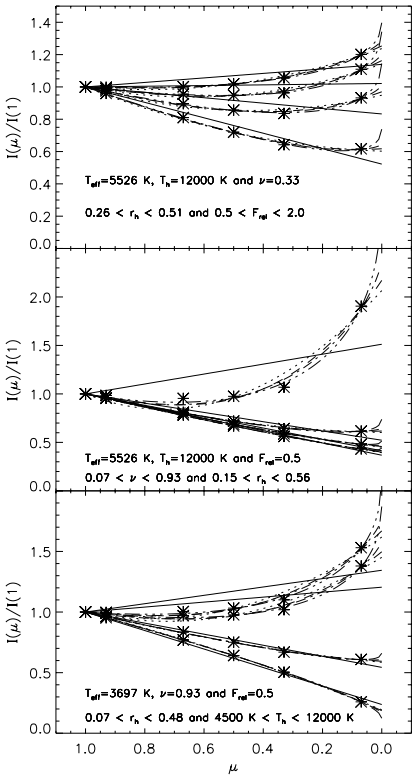

Fig. 5. $I(\mu)/I(1)$ vs. μ curves for the Strömgren u filter and various models, see the text for explanation. The meaning of the different linestyles and symbols is the same as in Fig. 3

A first interesting result from Fig. 3 is that, depending on the set of parameters chosen, we observe an effect of limb brightening instead of darkening. This can be understood as follows: when looking at a stellar disk we normally see the limb darker than the center because, despite of seeing the same optical depth in both, it corresponds to deeper, and consequently hotter, layers in the center than in the limb. In a illuminated star, the temperature distribution in the atmosphere becomes more and more homogeneous as we increase the illumination flux, until it reaches a state where there is no center-to-limb darkening and the star's brightness is the same throughout the stellar disk. This can be seen in Fig. 4, where we show the

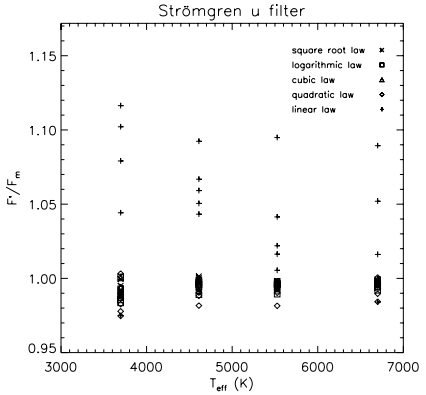

Fig. 6. $F'/F_{\rm m}$ calculated with the coefficients determined by the CG method. Models used: $\nu = 0.07$, $T_{\rm h} = 7000$ K

temperature structure for the models shown in Fig. 3. The larger the amount of infalling flux the higher the temperature of the external layers and the larger the region where it stays approximately constant.

If we keep increasing $F_{\rm rel}$, by changing either $r_{\rm h}$, $T_{\rm h}$ or ν, we reach a situation where the most external layers are hotter than the internal ones. As we see more external layers looking at the limb than looking at the center, we have a limb brightening effect. In Fig. 5 we illustrate that effect in three panels, each with four $I(\mu)/I(1)$ vs. μ curves, varying the many parameters. The effect is, though, dependent not only on the amount of the infalling flux. The first panel of Fig. 5 shows models that reach limb brightening with constant $T_{\rm h}$ and incident direction, but changing $F_{\rm rel}$ through changes in $r_{\rm h}$. Panels 2 and 3 show that limb brightening can also be achieved with constant $F_{\rm rel}$ (= 0.5), either by keeping $T_{\rm h}$ constant and using different pairs of $r_{\rm h}$ and ν, or by fixing ν and changing $r_{\rm h}$ and $T_{\rm h}$. We can also notice in Figs. 3 and 5 that the linear law (straight lines) is a poor approximation for the limb-darkening of illuminated atmospheres, while for $T_{\rm eff} \approx 5\,500$ K it fits well the non-illuminated case (Fig. 3). One should mention here that, although the models of Fig. 3 are similar to those calculated by CG, they do not report any evidence for the limb brightening effect in their work.

The methods by CG and VH, used here to calculate the coefficients, differ from each other in some important aspects. While CG emphasize the point of using coefficients that best match the relation $I(\mu)/I(1)$ vs. μ, even if the total flux is not perfectly conserved, VH says that the physical constraints of his method are introduced in order to avoid non-physical coefficients. In non-illuminated atmospheres CG find that the total emergent flux obtained by integrating the intensities calculated from the adjusted coefficients (F') does not differ more than 2% from the total flux obtained from the model intensities ($F_{\rm m}$), and that when choosing a non-linear law, the difference vanishes. We calculated the relation ($F'/F_{\rm m}$) for all our illuminated models, and the result for a set of models is shown in Fig. 6. As noticed, the linear law is not a good approximation when dealing with illuminated atmospheres. We find that the mean difference between the fluxes is around 4% (with a maximum of 26% in some models) in the case of a linear law and less than 1% (however with a maximum of 6%) for the non-linear ones. These results show that for an illuminated atmosphere the CG method should be used with care, as, for some models, even choosing a non-linear law, the flux is not conserved. Due to that we decided to adopt the VH method in our calculations of all the results presented in Tables 1 and 2.

Tables 1 and 2 are a sample of the tables with the monochromatic, bolometric and passband-specific limb-darkening coefficients than can be accessed electronically. We calculated coefficients for the linear, quadratic, cubic, logarithmic and square root laws, for stars with $3700\,{\rm K} \leq T_{\rm eff} \leq 6700\,{\rm K}$ heated by a companion with $7000\,{\rm K} \leq T_{\rm h} \leq 12000\,{\rm K}$, with relative fluxes ranging from 0.0 to 2.0 and the illumination direction, ν, varying from 0.07 to 0.97. The parameter Q in Table 1 has the same meaning as in VH. It is a quality factor that shows how good is the fitting to the model intensities, the smaller the Q the better the fitting:

$$Q_\lambda = \sqrt{\frac{\sum_{i=1}^{6}[R_\lambda(\mu_i) - \widehat{R_\lambda}(\mu_i)]^2}{6-m}} \tag{5}$$

where $m = 1$ for a one-parameter law (linear law) and $m = 2$ for a two parameter law (non-linear laws). $R_\lambda(\mu)$ stands for the ratio $I_\lambda(\mu)/I_\lambda(1)$ determined with the atmosphere model and $\widehat{R_\lambda}(\mu)$ for the same ratio determined with the limb-darkening approximation. When determining the bolometric coefficient, Q was calculated as:

$$Q = \frac{\int_{\lambda_i}^{\lambda_f} F(\lambda)Q(\lambda)}{\int_{\lambda_i}^{\lambda_f} F(\lambda)} \tag{6}$$

where $F(\lambda)$ is the monochromatic flux, λ_i is the shortest and λ_f the longest wavelength used in the UMA code.

When calculating with the CG method we do not determine the monochromatic limb-darkening coefficients, so Q cannot be obtained by integrating them. In order to be able to compare the results from the CG and VH methods, we used in Table 2, the following similar definition:

$$Q_{\rm filter} = \sqrt{\frac{\sum_{i=1}^{6}[R_{\rm filter}(\mu_i) - \widehat{R_{\rm filter}}(\mu_i)]^2}{6-m}}. \tag{7}$$

Although only the VH results are presented in Table 2, we performed calculations with both methods. In general, the CG method gives a smaller Q than VH, representing

Table 1. Sample of the table with the bolometric and monochromatic limb-darkening coefficients

Model 5, $T_{\rm eff} = 3697$ K, $F_{\rm rel} = 0.150$, $\nu = 0.06943$, $T_{\rm h} = 7000$ K

	Linear Law		Quadratic Law			Cubic Law			Logarithmic Law			Square Root Law			$I(\lambda, \mu = 1)$
λ (nm)	x	Q	x	y	Q	x	y	Q	x	y	Q	x	y	Q	$\left(\frac{erg}{s\,cm^2\,ster\,nm}\right)$
bolometric	0.240	(0.0300)	0.221	0.040	(0.0115)	0.230	0.033	(0.0088)	0.267	0.040	(0.0088)	0.181	0.099	(0.0080)	
153.20	−0.099	(0.0128)	−0.130	0.062	(0.0023)	−0.114	0.051	(0.0007)	−0.058	0.062	(0.0008)	−0.192	0.154	(0.0009)	7.100e+01
155.70	−0.091	(0.0120)	−0.121	0.059	(0.0021)	−0.106	0.050	(0.0005)	−0.052	0.059	(0.0006)	−0.180	0.149	(0.0007)	9.564e+01
158.90	−0.082	(0.0113)	−0.111	0.056	(0.0019)	−0.096	0.047	(0.0004)	−0.045	0.056	(0.0005)	−0.167	0.141	(0.0006)	1.389e+02
...															
600.70	0.398	(0.0153)	0.408	−0.021	(0.0144)	0.403	−0.018	(0.0138)	0.383	−0.021	(0.0138)	0.430	−0.053	(0.0137)	2.704e+06
603.30	0.395	(0.0154)	0.407	−0.023	(0.0145)	0.401	−0.019	(0.0139)	0.380	−0.023	(0.0139)	0.429	−0.057	(0.0135)	2.715e+06
606.70	0.392	(0.0158)	0.405	−0.025	(0.0147)	0.399	−0.021	(0.0140)	0.376	−0.025	(0.0140)	0.430	−0.063	(0.0137)	2.726e+06
...															
11691.20	0.028	(0.0200)	0.070	−0.084	(0.0076)	0.049	−0.070	(0.0054)	−0.028	−0.084	(0.0055)	0.155	−0.211	(0.0045)	1.332e+03
12153.40	0.026	(0.0208)	0.069	−0.087	(0.0077)	0.048	−0.073	(0.0054)	−0.032	−0.087	(0.0056)	0.157	−0.218	(0.0046)	1.146e+03
12432.30	0.024	(0.0209)	0.069	−0.089	(0.0077)	0.046	−0.074	(0.0053)	−0.035	−0.089	(0.0054)	0.158	−0.222	(0.0046)	1.050e+03

Table 2. Sample of the table with the passband-specific limb-darkening coefficients. We calculated the coefficients for the Strömgren *uvby* filters and for the Johnson-Morgan *UBVRI* filters. B2 and B3 are the response function of the *B* filter with and without the earth's atmosphere transmission function, respectively (see Buser 1978)

Model 5, $T_{\rm eff} = 3697$ K, $F_{\rm rel} = 0.150$, $\nu = 0.06943$, $T_{\rm h} = 7000$ K

	Linear Law		Quadratic Law			Cubic Law			Logarithmic Law			Square Root Law		
filter	x	Q	x	y	Q	x	y	Q	x	y	Q	x	y	Q
u	0.320	(0.0894)	0.575	−0.511	(0.0365)	0.448	−0.426	(0.0301)	−0.021	−0.511	(0.0296)	1.087	−1.279	(0.0259)
v	0.380	(0.0624)	0.518	−0.275	(0.0253)	0.449	−0.229	(0.0183)	0.197	−0.275	(0.0185)	0.793	−0.688	(0.0149)
b	0.317	(0.0563)	0.445	−0.256	(0.0250)	0.381	−0.214	(0.0188)	0.146	−0.256	(0.0189)	0.701	−0.641	(0.0156)
y	0.299	(0.0449)	0.396	−0.193	(0.0212)	0.348	−0.161	(0.0163)	0.171	−0.193	(0.0164)	0.589	−0.482	(0.0139)
U	0.265	(0.0887)	0.514	−0.498	(0.0356)	0.389	−0.415	(0.0287)	−0.068	−0.498	(0.0283)	1.012	−1.246	(0.0244)
$B2$	0.323	(0.0567)	0.456	−0.266	(0.0251)	0.389	−0.222	(0.0190)	0.145	−0.266	(0.0190)	0.722	−0.666	(0.0158)
$B3$	0.326	(0.0581)	0.460	−0.268	(0.0245)	0.393	−0.223	(0.0181)	0.147	−0.268	(0.0182)	0.728	−0.671	(0.0148)
V	0.307	(0.0410)	0.390	−0.166	(0.0201)	0.349	−0.139	(0.0159)	0.196	−0.166	(0.0159)	0.557	−0.416	(0.0138)
R	0.354	(0.0217)	0.383	−0.058	(0.0161)	0.368	−0.048	(0.0146)	0.315	−0.058	(0.0146)	0.441	−0.145	(0.0139)
I	0.291	(0.0195)	0.316	−0.049	(0.0147)	0.303	−0.041	(0.0135)	0.258	−0.049	(0.0135)	0.365	−0.124	(0.0129)

Table 4. Linear and quadratic limb-darkening coefficients for non-illuminated models. Our calculations were made with $T_{\rm eff} = 6700$ K while Claret & Giménez (1990) used $T_{\rm eff} = 6730$ K, both with $\log g = 4.5$. For the quadratic law, at the top is the linear coefficient and below it the non-linear one. Here CG stands for the results by Claret & Giménez (1990), CG′ and VH′ correspond to our calculations using the methods by CG and VH and, respectively, and, finally, VH correspond to the values by Van Hamme (1993), bi-linearly interpolated for $T_{\rm eff} = 6700$ K and $\log g = 4.5$

band	Linear				Quadratic		
	CG	CG′	VH′	VH	CG	CG′	VH′
u	0.78	0.76	0.70	0.64	0.65	0.65	0.63
					0.14	0.15	0.14
v	0.79	0.77	0.72	0.66	0.68	0.67	0.66
					0.13	0.13	0.14
b	0.74	0.72	0.69	0.60	0.63	0.63	0.62
					0.13	0.13	0.13
y	0.65	0.63	0.59	0.51	0.51	0.52	0.52
					0.16	0.16	0.15
U	0.79	0.76	0.70	0.64	0.66	0.64	0.61
					0.15	0.16	0.17
B	0.76	0.74	0.70	0.62	0.64	0.64	0.63
					0.13	0.13	0.13
V	0.63	0.63	0.60	0.51	0.48	0.51	0.52
					0.17	0.15	0.15

a better fit. That was an expected result as CG does not require any constraint to the fitting, the coefficients being calculated directly by applying the least squares method to the integrated intensities obtained with the atmosphere model. As VH applies the constraint of total flux conservation the fittings are often worse, but always physically correct. We observe that the worse the fitting with VH method the more the CG coefficients fail in conserving the total flux ($|(F'/F_{\rm m})| > 1$).

As already noticed by Claret & Giménez (1990), the limb-darkening coefficients of an illuminated atmosphere strongly depend on many parameters, making it difficult to find a simple function that describes the effect. We propose, for the passband specific coefficients, a solution to easily account for the effect in LC synthesis programs, parametrizing with polynomials the results obtained. In Eq. (8) K represents x_λ or y_λ of Eqs. (1) to (4) for the different limb-darkening laws:

$$K = a_0(t) + \sum_{n=1}^{3} a_n(t, \nu, t_{\rm h}) F^n \tag{8}$$

$$a_n = \sum_{m=0}^{3} b_{nm}(\nu, t_{\rm h}) t^m \tag{9}$$

Table 3. Sample of the table with the polynomial adjusted coefficients for the Strömgren u filter. See Eqs. (2), (8)-(11)

a0 - quadratic law												
	b00			b01			b02			b03		
	d00l0	d00l1	d00l2	d01l0	d01l1	d01l2	d02l0	d02l1	d02l2	d03l0	d03l1	d03l2
c0m0_L	10.93	−7.248	0.3957	−7.797	4.569	−0.2498	1.888	−0.9371	0.05130	−0.1432	0.06236	−0.003416
c0m1_L	−416.9	82.57	−4.093	254.7	−50.65	2.521	−50.50	10.09	−0.5041	3.259	−0.6536	0.03277
c0m2_L	891.2	−172.7	8.373	−541.8	105.4	−5.128	106.9	−20.86	1.019	−6.861	1.344	−0.06590
c0m3_L	−520.8	99.85	−4.792	315.9	−60.76	2.927	−62.15	12.00	−0.5800	3.982	−0.7710	0.03740
c0m0_NL	−34.82	13.11	−0.7404	25.86	−8.808	0.4929	−6.056	1.909	−0.1058	0.4440	−0.1320	0.007240
c0m1_NL	354.2	−85.30	4.891	−242.4	57.77	−3.283	53.71	−12.67	0.7140	−3.806	0.8899	−0.04969
c0m2_NL	−699.0	168.3	−9.626	475.2	−113.2	6.424	−104.9	24.75	−1.393	7.432	−1.737	0.09703
c0m3_NL	408.7	−98.24	5.601	−275.7	65.61	−3.714	60.54	−14.27	0.8019	−4.274	0.9982	−0.05570
a1 - quadratic law												
	b10			b11			b12			b13		
	d10l0	d10l1	d10l2	d11l0	d11l1	d11l2	d12l0	d12l1	d12l2	d13l0	d13l1	d13l2
c1m0_L	−10.58	8.848	−0.5346	4.765	−5.034	0.3140	−1.547	1.077	−0.06571	0.1549	−0.07678	0.004508
c1m1_L	371.0	−85.77	4.585	−231.9	53.70	−2.906	50.95	−11.61	0.6254	−3.682	0.8205	−0.04368
c1m2_L	−700.3	154.4	−8.303	469.9	−102.7	5.530	−106.3	22.91	−1.222	7.773	−1.647	0.08689
c1m3_L	403.4	−84.34	4.455	−278.3	57.94	−3.059	63.51	−13.12	0.6877	−4.649	0.9513	−0.04941
c1m0_NL	−822.9	165.6	−9.820	472.6	−98.62	5.918	−88.36	19.05	−1.161	5.385	−1.198	0.07424
c1m1_NL	6542.	−1373.	73.18	−3589.	769.6	−41.78	642.6	−140.8	7.799	−37.59	8.431	−0.4767
c1m2_NL	−1.102e+04	2297.	−120.9	5963.	−1269.	68.04	−1051.	228.5	−12.50	60.32	−13.43	0.7516
c1m3_NL	5652.	−1172.	61.22	−3033.	641.4	−34.15	528.2	−114.1	6.209	−29.93	6.625	−0.3688
a2 - quadratic law												
	b20			b21			b22			b23		
	d20l0	d20l1	d20l2	d21l0	d21l1	d21l2	d22l0	d22l1	d22l2	d23l0	d23l1	d23l2
c2m0_L	88.11	−19.03	0.9265	−49.12	10.90	−0.5373	10.17	−2.244	0.1103	−0.7167	0.1547	−0.007510
c2m1_L	−688.2	135.5	−6.444	415.8	−83.28	4.019	−88.61	17.84	−0.8650	6.285	−1.262	0.06110
c2m2_L	1032.	−202.5	9.791	−674.3	134.4	−6.580	152.2	−30.48	1.496	−11.21	2.243	−0.1098
c2m3_L	−511.1	96.06	−4.551	352.7	−67.97	3.276	−82.33	16.06	−0.7789	6.178	−1.212	0.05883
c2m0_NL	1247.	−237.2	12.57	−649.2	126.0	−6.796	109.8	−21.75	1.199	−6.061	1.226	−0.06922
c2m1_NL	−9325.	1806.	−89.12	4747.	−928.4	46.37	−779.6	154.1	−7.806	41.49	−8.294	0.4270
c2m2_NL	1.595e+04	−3051.	147.8	−7998.	1538.	−75.21	1285.	−248.5	12.28	−66.37	12.91	−0.6460
c2m3_NL	−8268.	1566.	−74.97	4099.	−778.6	37.54	−648.1	123.3	−5.992	32.75	−6.234	0.3057
a3 - quadratic law												
	b30			b31			b32			b33		
	d30l0	d30l1	d30l2	d31l0	d31l1	d31l2	d32l0	d32l1	d32l2	d33l0	d33l1	d33l2
c3m0_L	−139.2	26.62	−1.250	77.80	−15.04	0.7118	−14.43	2.818	−0.1343	0.8846	−0.1742	0.008362
c3m1_L	825.5	−159.8	7.534	−476.3	93.27	−4.439	91.39	−18.10	0.8690	−5.795	1.160	−0.05615
c3m2_L	−1339.	261.1	−12.39	793.1	−156.5	7.499	−156.0	31.15	−1.505	10.12	−2.042	0.09950
c3m3_L	693.2	−134.1	6.334	−418.1	81.99	−3.912	83.57	−16.60	0.7991	−5.492	1.104	−0.05361
c3m0_NL	−1003.	190.1	−9.209	546.8	−104.4	5.076	−98.27	18.88	−0.9212	5.820	−1.124	0.05502
c3m1_NL	6296.	−1191.	56.17	−3357.	636.8	−30.09	586.9	−111.6	5.278	−33.72	6.420	−0.3039
c3m2_NL	−1.065e+04	1995.	−93.00	5615.	−1052.	49.05	−967.2	181.2	−8.435	54.64	−10.22	0.4749
c3m3_NL	5512.	−1026.	47.43	−2884.	535.9	−24.75	491.9	−91.20	4.198	−27.48	5.078	−0.2327

$$b_{nm} = \sum_{l=0}^{3} c_{nml}(t_{\rm h})\nu^l \qquad (10)$$

$$\text{and} \quad c_{nml} = \sum_{k=0}^{2} d_{nmlk} t_{\rm h}^k, \qquad (11)$$

with $F = F_{\rm rel}$, $t = T_{\rm eff}\ 10^{-3}$ and $t_h = T_{\rm h}\ 10^{-3}$.

In Table 3 we give a sample of the adjusted polynomial coefficients obtained from the data in Table 2 and in Fig. 7 we show the adjusted polynomial surface for one chosen model. In the case of a non-linear law, we give in Table 3 the linear adjusted polynomial coefficients ($cnm0\_L$, $cnm1\_L$, $cnm2\_L$, $cnm3\_L$) followed by the non-linear ones ($cnm0\_NL$, $cnm1\_NL$, $cnm2\_NL$, $cnm3\_NL$). A complete version of Table 3 with the adjusted polynomial coefficients for the 9 chosen photometric filters (see Sect. 2.1) can be accessed in electronic form at the CDS.

2.3. A control

It is important to compare limb-darkening coefficients calculated from different atmosphere models and computational methods. Claret & Giménez (1990) have also used the UMA code in their calculations, and our results can be easily compared. In Table 4 we show the coefficients for the linear and quadratic laws for non-illuminated atmospheres, obtained by Claret & Giménez (1990), Van Hamme (1993, only for the linear law, because VH did not include the quadratic law in his study) and by us, using

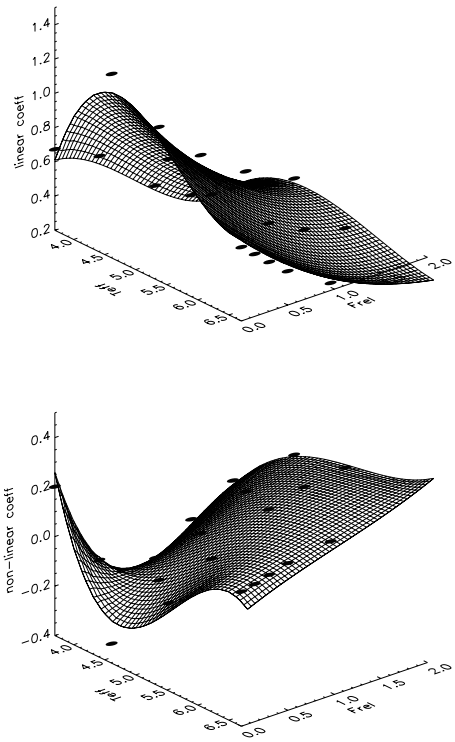

Fig. 7. Polynomial fittings to the quadratic law coefficients. Strömgren u filter, $\nu = 0.97$, $T_{\rm h} = 7000$ K. The x axis corresponds to $F_{\rm rel}$ and the y to $T_{\rm eff}$. The theoretical grid was calculated using the coefficients in Table 3

both VH and CG methods. As can be noticed, our values are very similar when using the same method but show a little expected difference with those determined by the VH method. Actually, Díaz-Cordovés & Giménez (1992) had already found that differences between tabulations by different works are normally due to the computational method rather than to the adopted model atmospheres themselves. This makes us confident that our calculations are correct for the non-illuminated case and that our results probably would be similar if we used another atmosphere model, instead of UMA. Note that the calculations with VH's method yield values somewhat systematically smaller for the linear law and that the limb-darkening coefficients given in VH (using ATLAS) are the smallest in each passband.

This control in the case of illuminated atmospheres is more problematic. To the best of our knowledge only CG worked on the effect of external irradiation on the limb-darkening coefficients using numerical atmosphere models (UMA in that case), but their results are only presented in a qualitative way, making impossible a numerical comparison. We do not know of any other work on the effect of external illumination on the limb-darkening coefficients with models other than UMA.

However, if the theoretical approximations used are similar to those used in this work we expect that the results will be similar to ours, irrespective of the atmosphere model used in the study. And we are confident that the results derived here are better, even used as a first order approximation, than the use of constant limb-darkening coefficients overall in the analysis of eclipsing binary LC.

3. Discussion

Until now the light curve synthesis programs have mostly used non illuminated limb-darkening tables to evaluate the center to limb brightness variation. In fact, the LC models use non-illuminated atmosphere results even to calculate the so-called "reflection effect", what is not strictly correct since the spectrum of an illuminated atmosphere is different from that of a standard one (Vaz & Nordlund 1992). The effect of the external irradiation on the coefficients themselves is ignored even when it is recognized that the limb-darkening coefficients should vary due to variations of the local effective temperature and surface gravity across the surface of a tidally distorted binary star, as in Van Hamme & Wilson (1994), who calculated position-dependent limb-darkening on computed light curves.

However, it is clear from Fig. 7 that the limb-darkening coefficients vary not only with the atmosphere's effective temperature, but show a strong dependence on the characteristics of the external illumination (the incidence angle, the amount of infalling flux, the spectrum of the infalling energy or, in other words, the temperature of the illuminating star), also. This dependence is well represented by the approximating Eqs. (8) to (11) for each of the 9 different limb-darkening laws reviewed in the present work. Even though the effect of the limb-darkening coefficients on the light curve analysis is small, it is large enough to allow attempts of empiric determination of the coefficients from precise observed light curves (as for DM Vir, Andersen et al. 1984), while the adoption of incorrect coefficients may affect systematically the determination of the orbital inclination, having also influence on the determination of other parameters (Popper 1984).

As the orbital configuration is fully known during the analysis of an eclipsing binary LC, Eqs. (8) to (11) can

be used to calculate the limb-darkening coefficients which are position-dependent on the surface of the components, taking into account not only the variation of $T_{\rm eff}$ and $\log g$, but also the effect of the external irradiation. The parametrization attained is very convenient for this purpose, which can be implemented in the existing computer models for eclipsing binary light curve synthesis. This extra calculation will represent a relatively easy task for the modern CPU's and certainly will improve the quality and reliability of the determination of the other parameters as, for instance, the orbital inclination. In fact, the treatment of both the limb-darkening and the gravity brightening, with respect to the effect of the mutual illumination, should be done consistently, and this is our goal. In Alencar et al. (1998) we present the continuation of the work on the gravity brightening exponent (Alencar & Vaz 1997) extended to illuminated atmospheres. The implementation of these results in the WD model (Wilson & Devinney 1921; Wilson 1979; Vaz et al. 1995) is in progress and its application to real systems will be published elsewhere. While this is not the complete integration of atmosphere model calculation with the light curve synthesis programs, yet, a desirable feature of the next generation of the LC programs, this is a significant step towards the improvement of these models with respect to the proximity effects on the theoretical light curves.

4. Conclusions

We determined monochromatic, bolometric and passband specific limb-darkening coefficients for illuminated atmospheres. Our results show that illuminated coefficients are significantly different from the non-illuminated ones and that illuminated atmospheres may present limb brightening instead of darkening, depending on the set of parameters chosen. We tested two different methods (Claret & Giménez 1990 and Van Hamme 1993) to calculate the coefficients and showed that in the illuminated case the method proposed by Van Hamme is recommended in order to obtain coefficients that preserve the total emergent flux from the atmosphere. For the passband specific coefficients we also present our results in a polynomial form, which is convenient for implementation of the use of these "illuminated" coefficients in the analysis of eclipsing binary light curves.

Acknowledgements. Support by FAPEMIG, CNPq, FINEP, CAPES (Brazilian institutions). Fruitful discussions with Dr. J.V. Clausen are gratefully acknowledged.

Appendix: Acronyms

Following a suggestion of the referee, we present here the definition of the many acronyms used in this paper.

$T_{\rm eff}$: effective temperature of the atmosphere to be illuminated
$T_{\rm h}$: heating star's effective temperature
γ: line of sight angle (see Fig. 1)
μ: $\cos\gamma$
θ: incidence angle (see Fig. 1)
ν: $\cos\theta$
λ: wavelength
$I_\lambda(\mu)$: beam intensity at the wavelength λ, direction μ
$R_\lambda(\mu)$: limb-darkening law
x_λ: linear limb-darkening coefficient
y_λ: non-linear limb-darkening coefficient
$r_{\rm h}$: the apparent radius of the illuminating star (see Fig. 1)
g: local surface gravity acceleration
α: the mixing length parameter
β: the gravity brightening exponent
Q: the quality factor of the limb-darkening law adjustment
$F(\lambda)$: the monochromatic flux
$F_{{\rm rel},\nu}$: bolometric incident flux relative to the one emitted by the illuminated star at the illuminated point of its surface
F': total emergent flux obtained by integrating the intensities calculated from the adjusted limb-darkening coefficients
$F_{\rm m}$: total flux obtained from the model intensities.

References

Allen C.W., 1976, Astrophys. Quantities, 3rd edition. Athlone, London
Alencar S.H.P., Vaz L.P.R., 1997, A&A 326, 257
Alencar S.H.P., Vaz L.P.R., Nordlund Å., 1998, A&A (submitted)
Andersen J., Clausen J.V., Giménez A., Nordström B., 1983, A&A 128, 17
Andersen J., Clausen J.V., Nordström B., 1984, A&A 137, 281
Bell R.A., Eriksson K., Gustafsson B., Nordlund Å., 1976, A&AS 23, 37
Bessel M., 1983, PASP 95, 480
Buser R., 1978, A&A 62, 411
Claret A., Giménez A., 1990, A&A 230, 412 (CG)
Claret A., Díaz–Cordovés J., Giménez A., 1995, A&AS 114, 247
Crawford D.L., Barnes J.V., 1970, AJ 75, 978
Díaz–Cordovés J., Giménez A., 1992, A&A 259, 227
Díaz–Cordovés J., Claret A., Giménez A., 1995, A&A 259, 227
Gustafsson B., Bell R.A., Eriksson K., Nordlund Å., 1975, A&A 42, 407
Helt B.E., 1987, A&A 172, 155
Hilditch R.W., Harries T.J., Bell S.A., 1996, A&A 314, 165
Khalesseh B., Hill G., 1992, A&A 257, 199
Klinglesmith D.A., Sobieski S., 1970, AJ 75, 175
Kurucz, R.L., 1979, ApJS 40, 1
Manduca A., Bell R.A., Gustafsson B., 1977, A&A 61, 809
Maxted P.F.L., Hill G., Hilditch R.W., 1994, A&A 285, 535

11.4 Profiles of strong permitted lines in Classical T Tauri stars (Paper 4)

THE ASTRONOMICAL JOURNAL, 119:1881–1900, 2000 April

PROFILES OF STRONG PERMITTED LINES IN CLASSICAL T TAURI STARS[1]

SILVIA H. P. ALENCAR[2,3] AND GIBOR BASRI[2]
Received 1999 September 26; accepted 2000 January 4

ABSTRACT

We present a spectral analysis of 30 T Tauri stars observed with the Hamilton echelle spectrograph over more than a decade. One goal is to test magnetospheric accretion model predictions. Observational evidence previously published supporting the model, such as emission-line asymmetry and a high frequency of redshifted absorption components, are considered. We also discuss the relation between different line-forming regions and search for good accretion rate indicators. In this work we confirm several important points of the models, such as the correlation between accretion and outflow, broad emission components that are mostly central or slightly blueshifted, and only the occasional presence of redshifted absorption. We also show, however, that the broad emission components supposedly formed in the magnetospheric accretion flow only partially support the models. Unlike the predictions, they are sometimes redshifted and are mostly found to be symmetric. The published theoretical profiles do not have a strong resemblance to our observed ones. We emphasize the need for accretion models to include a strong turbulent component before their profiles will match the observations. The effects of rotation, as well as the outflow components, will also be needed to complete the picture.

Key words: stars: formation — stars: pre–main-sequence

1. INTRODUCTION

Classical T Tauri stars (CTTSs) are young, almost solar-mass stars that exhibit a wide range of permitted and sometimes also forbidden emission lines, together with an excess continuum emission that goes from the infrared to the ultraviolet. Their spectral energy distribution is consistent with the presence of a circumstellar disk that appears to play a major role in the regulation of both the infall and outflow of material from the star-disk system. A strong wind component is also thought to be present and to cause the blueshifted absorption features commonly seen in the Balmer lines.

In the past years many attempts have been made to explain those characteristics. The permitted line emissions were discussed in terms of outflowing winds (Hartmann, Edwards, & Avrett 1982; Hartmann et al. 1990; Natta & Giovanardi 1990), turbulence in a boundary layer between the disk and the stellar surface (Bertout, Basri, & Bouvier 1988; Basri & Bertout 1989), and chromospheric activity (Calvet, Basri, & Kuhi 1984; Calvet et al. 1985). More recently, magnetospheric accretion models were proposed (Hartmann, Hewett, & Calvet 1994; Shu et al. 1994; Hartmann 1998). In these models the circumstellar disk is truncated by stellar magnetic field lines and the strong broad emissions arise from the accelerated infalling material channeled through the lines that connect the disk to the star. At the base of the magnetospheric accretion column, where the accreted material hits the star, hot spots and the hot continuum emission (veiling) are produced.

Edwards et al. (1994) showed observational evidence in a sample of 15 CTTSs that they claimed confirm some of the magnetospheric predictions, such as blueward asymmetric emission lines (due to disk occultation of the receding flow) and redshifted absorption components at typical free-fall velocities (inverse P Cygni profiles), which are naturally explained by the magnetospheric infall. The line profiles of several stars were also well reproduced by magnetospheric calculations (Muzerolle, Hartmann, & Calvet 1998a; Najita, Carr, & Tokunaga 1996), but often the theoretical profiles are more asymmetric and always less broadened than the observed ones. However, we must keep in mind that the models of Hartmann et al. (1994) do not include rotation and winds that would certainly influence both the asymmetry and the broadening of the theoretical profiles.

The CTTSs were initially found to be slow rotators, based on observational surveys that reported a bimodal distribution of stellar rotation periods among TTSs (Choi & Herbst 1996), where the slow rotators ($P > 4$ days) seemed to exhibit disk signatures, as near-infrared excess emission, that the fast rotators did not (Edwards et al. 1993). It has always been a challenge to understand the spin-down of those stars, but the magnetospheric model predicts that the magnetic interaction between the star and the disk could regulate the stellar rotation. This could explain why weak T Tauri stars (WTTSs), that do not have disks present a wider range of rotational periods. Recently, Stassun et al. (1999), analyzing the rotation period distribution of young stars in the Orion nebula region, showed that this bimodal distribution does not seem to exist and that the conclusion of the earlier work was also statistically consistent with a uniform distribution. Herbst, Rhode, & Hillenbrand (1999) suggest this recent result, however, may be confined to low-mass TTSs.

In view of the many points still under discussion, we present in this paper the spectral analysis of an observed sample of 30 TTSs with a large spectral coverage, which are used to analyze the magnetospheric model's predictions and test the previous observational results. The observations and reduction procedures are described in § 2, and the equivalent width and veiling measurements are detailed in § 3. We analyze the many features in our spectra in § 4,

[1] Based on observations obtained at Lick Observatory.

[2] Department of Astronomy, University of California at Berkeley, Berkeley, CA 94720-3411; silvia@crater.berkeley.edu, basri@soleil.berkeley.edu.

[3] Departamento de Física, Instituto de Ciências Exatas, Universidade Federal de Minas Gerais, C.P. 702, 30123-970, Belo Horizonte, MG, Brazil.

discuss the results in § 5, and draw our final conclusions in § 6.

2. OBSERVATIONS

We present the spectral analysis of a sample of 30 TTSs listed in Table 1. The observations, which span over more than a decade, were carried out at Lick Observatory with the 3 m Shane Telescope and the Hamilton echelle spectrograph (Vogt 1987) coupled either to a TI 800 × 800 CCD or a Ford 2048 × 2048 CCD. With the smaller detector, two settings were established: a red setting covering 52 orders from 4900 up to 8900 Å and a blue setting covering 38 orders from 3900 up to 5200 Å. The spectral coverage, however, is not complete, with a gap of a few dozens of angstroms between orders. Whenever possible, blue and red observations were obtained in the same night or within one night of difference, but for some stars we only have the red setting. The bigger CCD installed in 1992 permits a full spectral coverage of approximately 92 orders ranging from 3900 to 8900 Å. The mean resolution of the spectrograph is $\lambda/\Delta\lambda \approx 48{,}000$ and the exposure times varied from 15 minutes to 1 hr 15 minutes, depending on the target and on the CCD used.

The reduction was performed in a standard way described by Valenti (1994), which includes flat fielding with an incandescent lamp exposure, background subtraction, and removal of cosmic rays. Wavelength calibration is made by observing a thorium-argon comparison lamp and performing a two-dimensional solution to the thorium lines. Radial and barycentric velocity corrections are applied and all the data shown are in the stellar rest frame. The spectra are not flux calibrated, so each spectrum has been continuum normalized. Due to differences in weather conditions, exposure times, and efficiency between different chips, there is a wide range of signal to noise in the data. However, not only strong emission-line profiles were reliably extracted, but also many absorption-line profiles as shown in Figure 1. After the reduction procedure the spectra have been binned and smoothed with a window width of 3. A weak-line T Tauri star was included in the sample (V410) (Tau Herbig & Bell 1988), as a reference to stars without disk accretion. DQ Tau is a known binary system (Basri, Johns-Krull, &

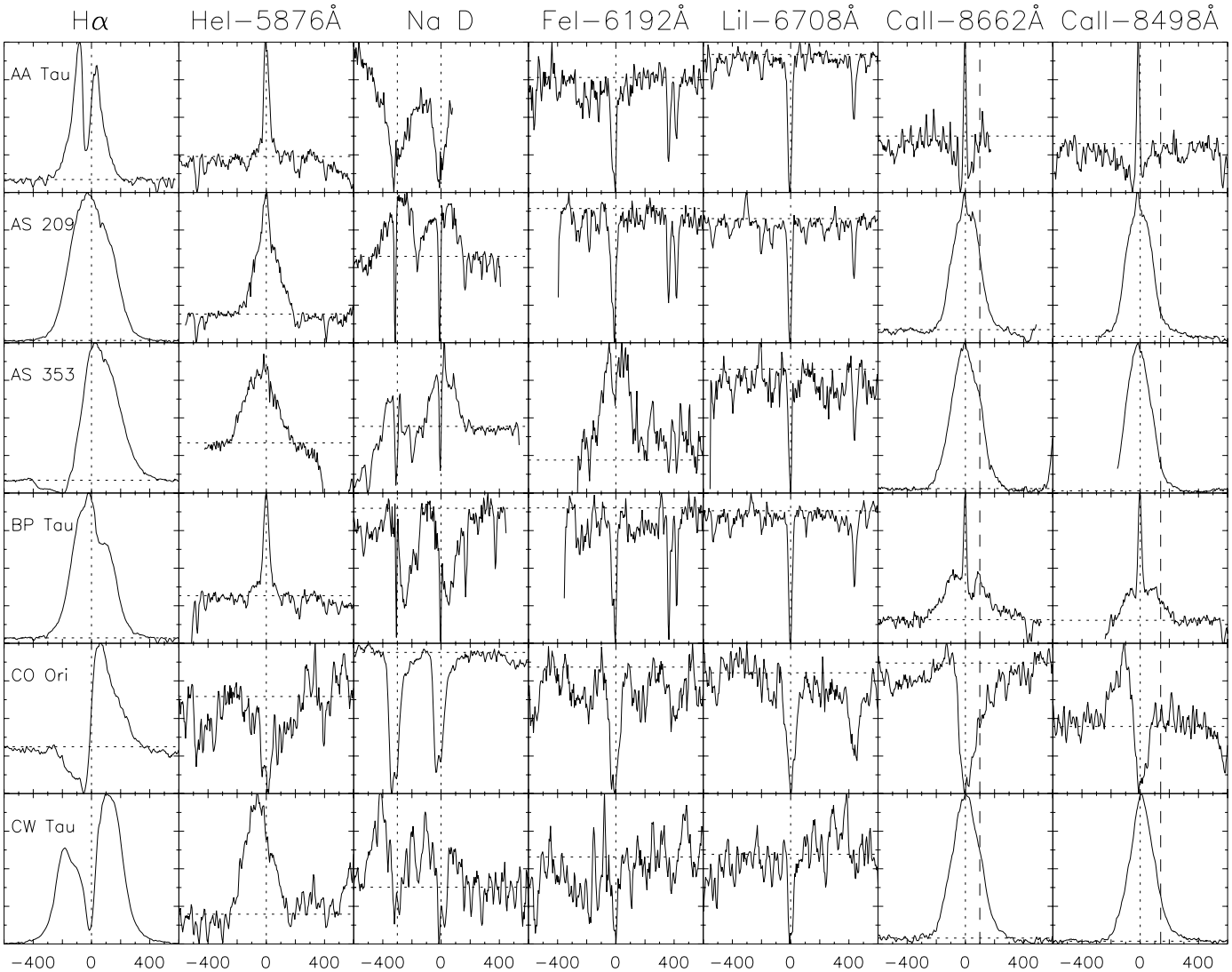

FIG. 1.—Line profiles. All data have been continuum normalized, binned, and smoothed with a window width of 3. The horizontal dotted lines represent the continuum level at 1. The vertical dotted lines are the spectral line's center at the stellar rest frame. The contamination of the Na D lines by the vapor lamps of the city of San Jose has been removed. The dashed lines close to the IRT profiles are the velocity position of the blended Paschen emission lines. The *x*-axes are radial velocities in km s^{-1} and the *y*-axes correspond to relative intensities.

TABLE 1

LINE EQUIVALENT WIDTHS (Å) AND VEILINGS

STAR	UT DATE Red/Blue	Hα	Hβ	Hγ	Hδ	He I	NaD1+D2	Fe I λ6192	Li I λ6708	Ca II λ8662	Ca II λ8498	Ca K	Fe I λ5497	Fe II λ4924	Fe II λ4352	VEILING red	VEILING blue
AA Tau.....	1989 Oct 13/13	14.2	2.2:	3.5:	2.7	1.2	−4:	−0.3	−0.6	0.5	0.7	2.2	−0.3	x	x	0.3	0.2
AS 205.....	1987 Jun 10/	111.1				1.6	2.5	−0.2	−0.1	20.4	39.7		−0.1			0.2	
AS 209.....	1987 Oct 6/6	113.4	33.5	11.5	7.9	3.3	2.9	−0.3	−0.4	16.6	21.0	21.6	−0.2	x	x	0.3	0.3
AS 353.....	1987 Sep 6/6	56.0	12.6	5.9:	−2.9	2.6	2.9	0.7	−0.1	37.9	36:	x	0.0	5.6	3.8	1.7	2.4
BP Tau	1986 Dec 21/21	48.6	10.7	4.5	4.8	1.0	−1.1	−0.2	−0.4	4.1	3.5	11.6	−0.2	x	x	0.5	0.9
CI Tau.....	1987 Oct 12/	110.1				3.4	−0.5	−0.3	−0.4	19.7	19:		−0.2	3:		0.2	
CO Ori	1992 Nov 15	2.9	−2.2	−3:	−2.9	−0.1:	−2.2	−0.2	−0.2	x	0.2	x	−0.2	x	x	0.2	0.2
CW Tau	1998 Nov 3	109.6	12.3	x	x	1.9	x	−0.1	−0.1	21.5	28.3	3:	x	2.2	x	1.5	x
DE Tau	1988 Feb 4/4	66.5	44.0	34.6	x	2.6:	x	x	−0.4	7.1	7.9	76.4	x	x	1.7	x	x
DF Tau	1992 Nov 14	61.0	6.8	3.0	3.2	3.0	0.8	x	−0.2	4.9	5.3	7.5	x	0.8:	0.1:	1.8	1.8
DG Tau	1993 Oct 30	60.5	17.7	8.2	5.4	2.4	2.5	0.3	−0.2	41.4	44.2	20.8	−0.1	5.0	3.0	2:	2:
DK Tau	1987 Oct 12/12	16.7	4.4	0.9	2.1	1.0	−2.1	−0.2	−0.4	2.1	2.7	3.5	−0.2	x	x	0.4	0.7
DL Tau	1998 Nov 3	110.2	24.8	7.2	3.4	5.4	7.0	−0.1	−0.2	39.9	46.5	8.5	x	7.3	x	1.9	x
DN Tau	1986 Nov 12/12	15.7	5.6	1.9	3.9	0.3	−3.4	−0.3	−0.6	0.4	0.5	10.6	−0.3	x	x	0.1	0.2
DO Tau	1998 Nov 3	58.2	5.3	x	x	2.1	2.4	x	−0.2	8.8	7.9	0.9:	x	1.9	x	0.9	x
DQ Tau	1993 Dec 24	157.1	23.4	3.3	2:	2.7	1.8	−0.1	−0.3	2.7	2.3	x	x	2.0	x	1.5	1.5
DR Tau	1998 Nov 3	81.0	5.3	1.0	1.5	4.2	4.0	x	−0.1	23.3	25.4	11.2	x	2.4	0.7	2.5	x
DS Tau.....	1987 Oct 11/11	27.3	7.2	4.6	3.7	0.9	−0.5:	−0.2	−0.2	0.4	0.3	19.9	−0.1	x	x	0.6	0.5
GG Tau	1989 Jan 17/18	40.2	8:	4:	2:	0.8	−2:	−0.2	−0.5	2.3	2.4	x	−0.2	x	x	0.3	1.1
GK Tau	1988 Feb 4/4	34.0	9.6	6:		1:	x	x	−0.6	4:	1.1	6.9	−0.3	x	x	x	0.1
GM Aur....	1987 Oct 11/11	63.5	12.4	4:	4.8	0.7	−2.1	−0.3	−0.4	0.3	0.4	32.5	−0.3	x	x	0.2	0.1
GW Ori	1993 Dec 23	31.5	2.9	x	x	x	1.4	−0.2	−0.2	4.7	5.2	x	−0.1	x	x	0.2	x
HL Tau	1986 Nov 12/	34.7				1.2	3.8	−0.2:	−0.2	28.2	30.6		x	2.5:		0.9	
RW Aur	1986 Dec 21/21	45.9	4.1	−2.1	−1.2	0.6:	−8.3	0.6	−0.2	27.5	37:	14.0	x	x	x	2.0	2.9
RY Tau.....	1986 Dec 21/21	12.4	−1.4:	−0.8:	−0.9	−0.3	0.2	−0.2:	−0.2	4.7	5.2	2.2	−0.2	x	x	0.1	0.0
SU Aur	1986 Nov 14/14	6.1	−1.7	−1.1:	−1.6:	−0.3	−1.0	−0.2	−0.2	−1.0	−0.7:	x	−0.3	x	x	0.0	0.0
T Tau.....	1989 Oct 13/13	63.1	9.8	3:	3.3	0.5	0.7:	−0.2	−0.4	11.2	13.7	27.7	−0.2	1.4:	x	0.1	0.1
UX Tau	1986 Dec 22/	3.5				x	−2.0	−0.3	−0.4	0.2	0.2		−0.3			0.0	
UY Aur	1988 Feb 4/4	97.0	20.8	10.7		2.6	x	x	−0.4	7.8	12:	96.2	x	x	x	0.1	0.8
V410 Tau...	1992 Nov 14	2.9	x	x	x	x	−3.4	−0.3	−0.5	0.2	0.2	2.2	−0.3:	x	−1:	0.1	0.2

NOTE.—When the lines could not be reliably used, the equivalent width and veiling were not measured (marked with an "x") and when we did not have a spectrum at a given wavelength the cell is left blank.

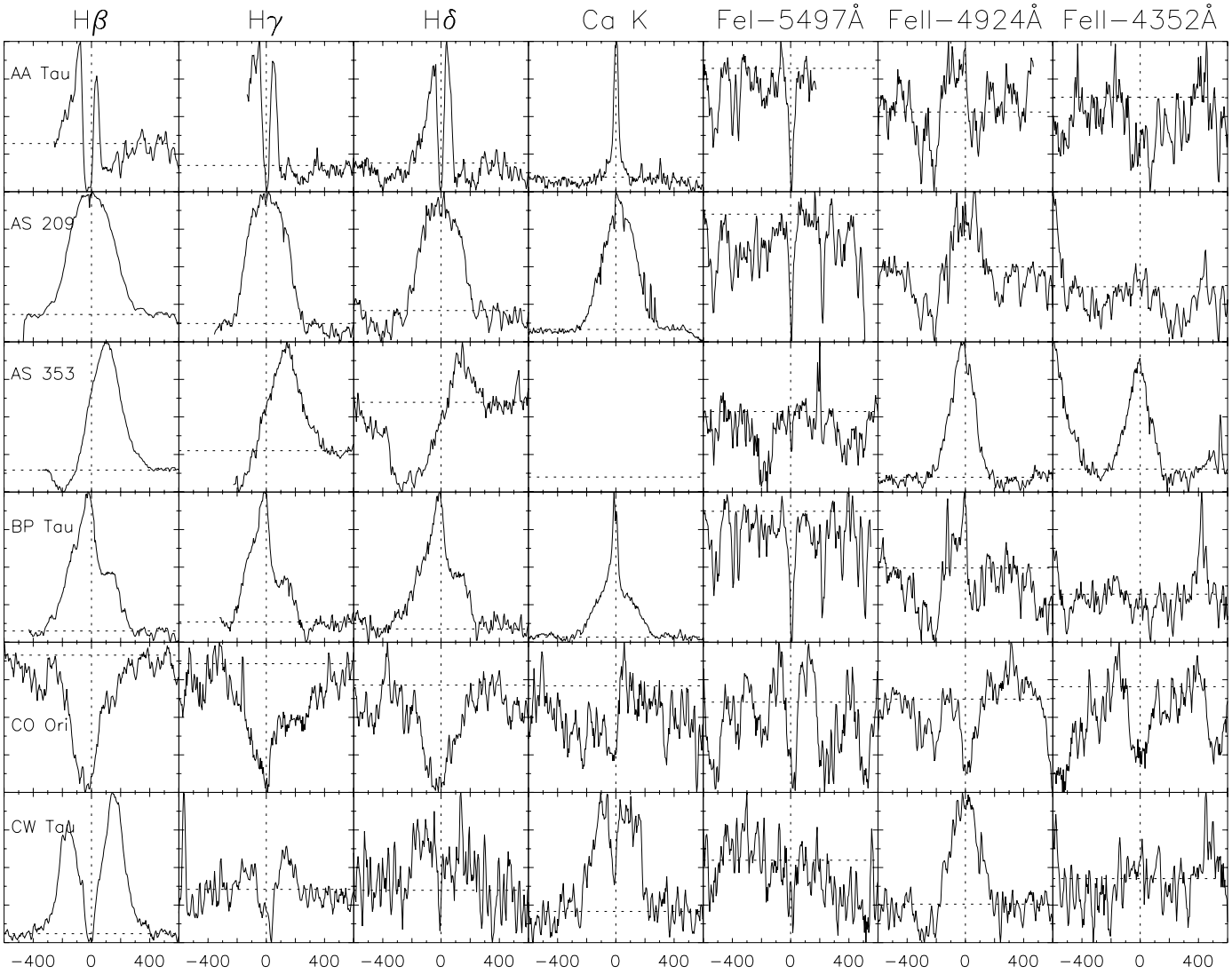

FIG. 1.—*Continued*

Mathieu 1997); the chosen spectrum corresponds to an outburst event when the lines are stronger and to a phase ($\phi = 0.02$) where there is no separation between the lines of the two components.

3. MEASUREMENTS

3.1. *Equivalent Widths and Profile Decomposition*

We first measure the equivalent width of all the lines in Figure 1 that could be reliably identified. The results are presented in Table 1 and will be used in the following sections to study the relations between "fluxes" (veiling-corrected equivalent widths) from different lines and between fluxes and parameters such as the mass-accretion rate.

The line profiles were also decomposed with a multiple Gaussian procedure based on the Marquardt method, so that we could also study correlations between line components. Most of the lines were very well fitted by one or two Gaussians and only sometimes required a third component. Some exceptions are the flat-topped profiles of T Tau, SU Aur, and DE Tau, which are clearly non-Gaussians. The fitting procedure was not always straightforward, since some lines are contaminated by nonstellar emission, some are blended by other lines, and some can be fitted with more than one Gaussian combination (such as two emissions instead of one emission and one absorption, for example). We explain below how we dealt with those problems.

The Hα line often exhibits a double-peaked profile, which in most cases was better fitted by a broad emission and a blue absorption than two emissions. The Hα wings are not steep and seem to belong to a very broad emission line rather than to two narrow ones. It is often possible to confirm that a true absorption is present by looking at the upper Balmer lines, where the feature is enhanced relative to the emission and dips below the continuum.

The Na D lines are strongly contaminated by the vapor lamps of the city of San Jose but our decomposition procedure was able to reliably subtract that contamination with a simultaneous Gaussian fit while decomposing the line profiles.

The Ca II and He I lines exhibit profiles typically with narrow and broad emission components; some lines show only one of the components. In some Ca II lines the narrow component is present inside a photospheric absorption core and, in that case, the emission-line equivalent width was measured from the base of the absorption core instead of the continuum. The Ca II infrared triplet (IRT) lines are also

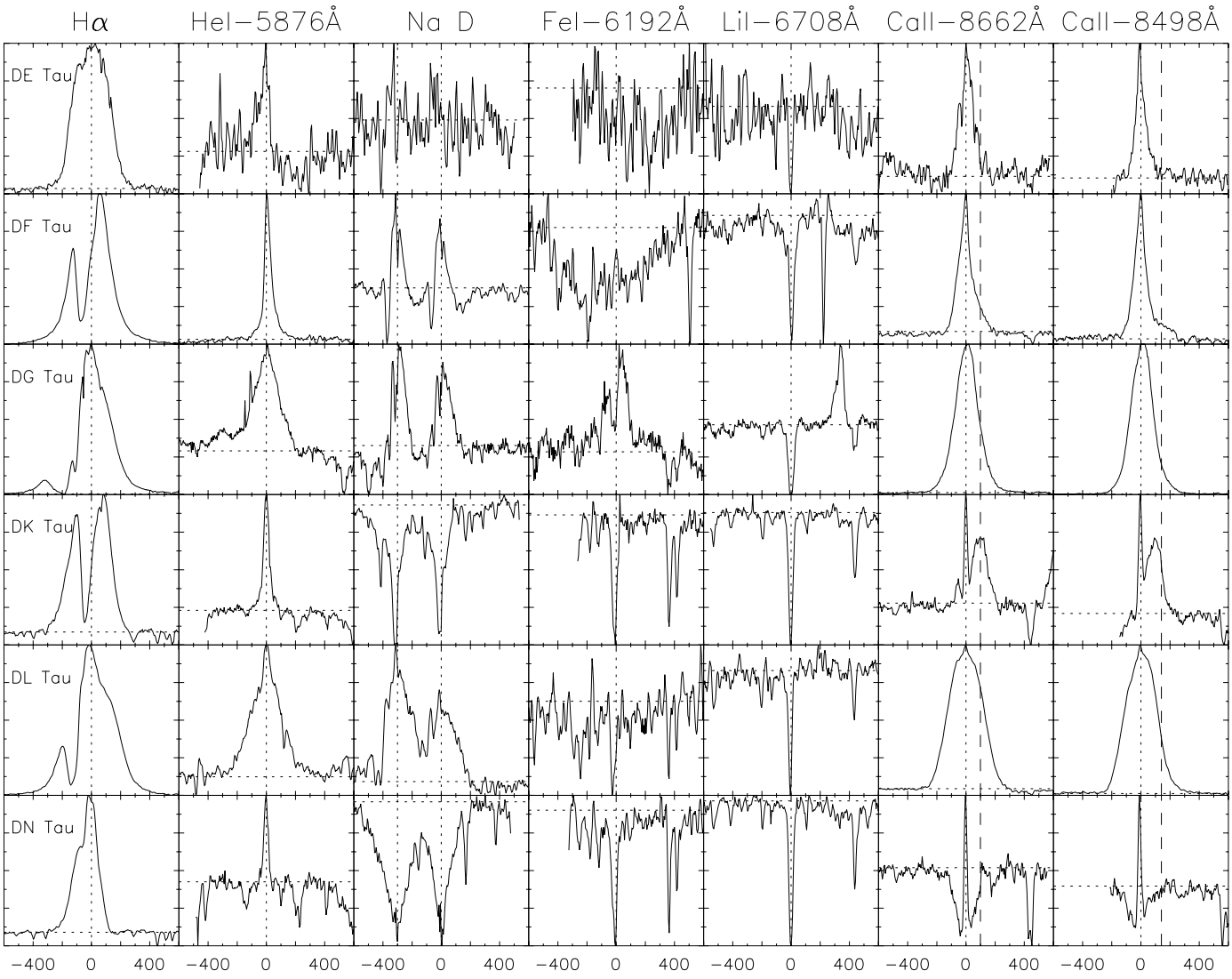

FIG. 1.—*Continued*

blended with a Paschen emission line, which usually has strengths less than 20% of the IRT, as also noted by Hamann & Persson (1992). Whenever the Ca II lines are weak or narrow, the Paschen contamination is significant and has been extracted from the equivalent width measurements.

Finally, the Fe II equivalent widths were only measured when the line was in strong emission and could surely be distinguished from the lines nearby.

3.2. *Veiling*

The equivalent widths presented in Table 1 are contaminated by the variable continuum against which they were measured. They need to be corrected for the veiling in order to represent a true emission strength that can be regarded as a "flux" measurement. Some of our spectra have measured veilings in previous papers (Basri & Batalha 1990; Johns-Krull & Basri 1997) but in order to be consistent we decided to measure all the veilings again. The new values are presented in the last columns of Table 1, and the common measurements agree within the errors with the previously published ones.

In order to calculate the veilings we chose spectral orders with many photospheric absorption lines, both in the blue and red settings. The red orders correspond to the wavelength ranges 5557 Å $< \lambda <$ 5642 Å and 5668 Å $< \lambda <$ 5755 Å and the blue orders to 4571 Å $< \lambda <$ 4641 Å and 4763 Å $< \lambda <$ 4836 Å. The idea is to compare the spectrum of a CTTS with that of a standard star with the same spectral type that has been broadened to the CTTS rotational velocity and veiled. The choice of suitable standard stars is important, and we followed, whenever possible, the suggestion of Basri & Batalha (1990) to use the Hyades dwarfs as reliable standards. We also used the standard and CTTS spectral types determined by them.

We first rotationally broadened the continuum-normalized spectrum of the standard star and then applied the veiling to the standard's spectrum, comparing it with the observed CTTS spectrum until a good match was found. The best adjustment was determined by eye, but a unique veiling value did not perfectly match all the photospheric lines and the results presented in Table 1 correspond to a mean value obtained with all the lines in the selected orders. The errors in the veiling determination are bigger for the higher veiling values, as the photospheric lines of highly veiled stars are extremely shallow and hard to match. Typically, we have errors of 0.1 for veilings smaller than 1.0 and up to 0.5 for the higher ones. Most of the rotational veloci-

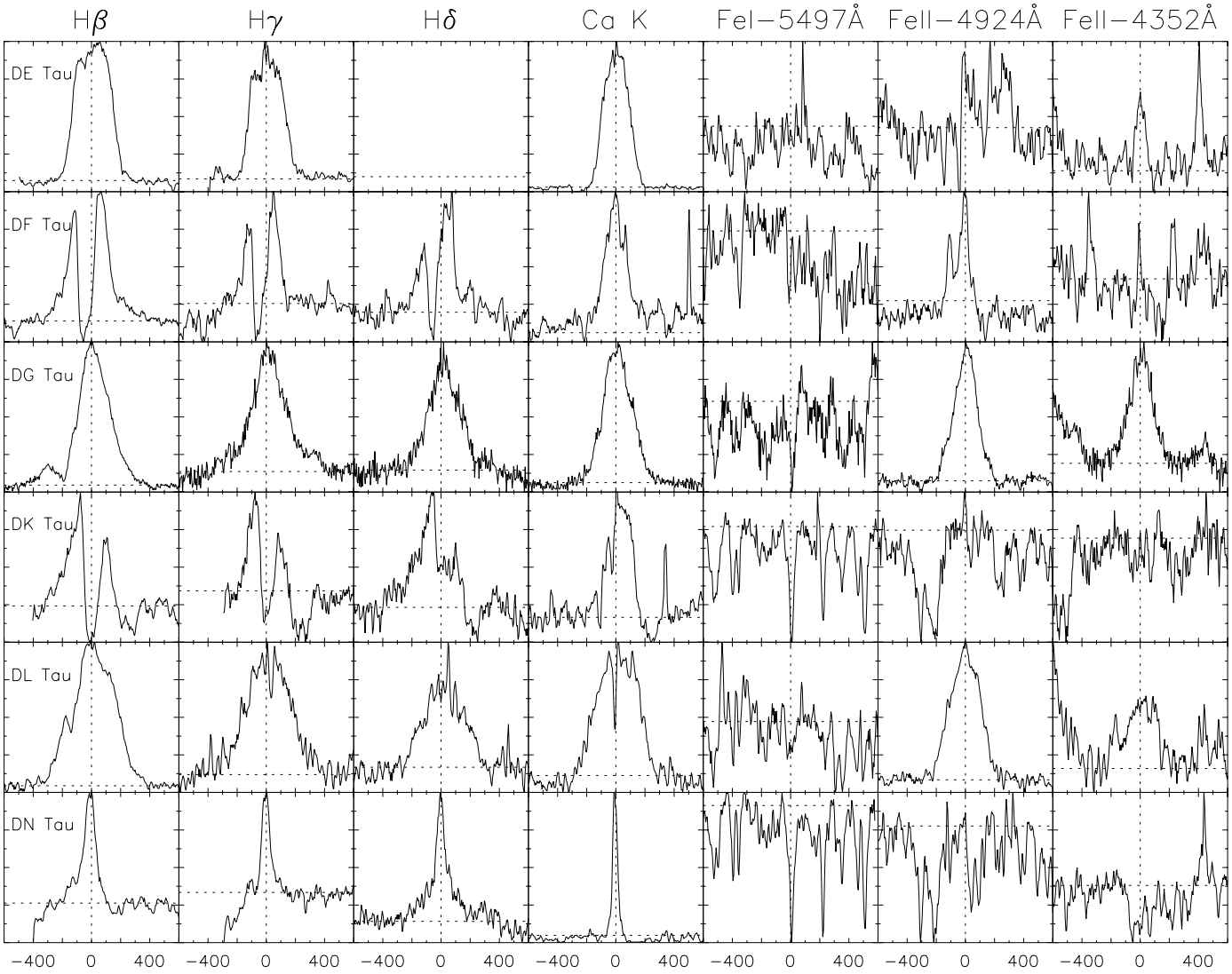

FIG. 1.—*Continued*

ties were taken from Basri & Batalha (1990), although we verified them by checking the match between the FWHM of the cross-correlation normalized profiles of the original standard with the CTTS spectra and of the original standard with the broadened and veiled standard.

The veiling values obtained are used to search for correlations between veiling-corrected line equivalent widths, defined as in Johns-Krull & Basri (1997):

$$W^0_{\rm eq} = W_{\rm eq}(V + 1)\,, \qquad (1)$$

where $W_{\rm eq}$ is the measured equivalent width and V is the veiling.

4. ANALYSIS

4.1. *General Characteristics*

The magnetospheric accretion model is the current consensus model to describe the accretion processes in CTTSs. These models predict general trends, such as central or blueshifted asymmetric broad emission lines, sometimes with redshifted absorption components (Hartmann et al. 1994; Muzerolle, Calvet, & Hartmann 1998b), that we should be able to verify in our large sample of stars and lines. The magnetospheric accretion scenario may also include winds that would cause further emission and blueshifted absorption (Shu et al. 1994). Some theoretical predictions have been confirmed by observational results (Edwards et al. 1994; Muzerolle et al. 1998a), but there is still a long way to go in order to fully understand the nature of the processes taking place in CTTSs. Below are some general profile characteristics from our sample of stars that we will analyze in detail in the next sections.

Many of our emission lines show broad components (BC) that tend to have blueshifted centroids (Hα, Hβ, the He I BC, the IRT BC, Na D, and Fe II λ4923) following the magnetospheric predictions, but the centroids are also redshifted in some stars and exhibit a wide range of shift values. The broad emission components are also generally well fitted by Gaussians, which may have a turbulent origin (Basri 1990) rather than the infall scenario. Redshifted absorption is not commonly present. The clearest example is BP Tau, where it appears in the Balmer lines, the Na D, and the Ca II (λ8662). Blueshifted absorption is a much more common feature that can be seen in many Balmer and Na D lines and sometimes in lines such as Ca K in RW Aur. Many lines show a multiple-component profile that can often be decomposed either as narrow and broad components, e.g., He I, Ca, and Fe lines (Basri & Batalha 1990;

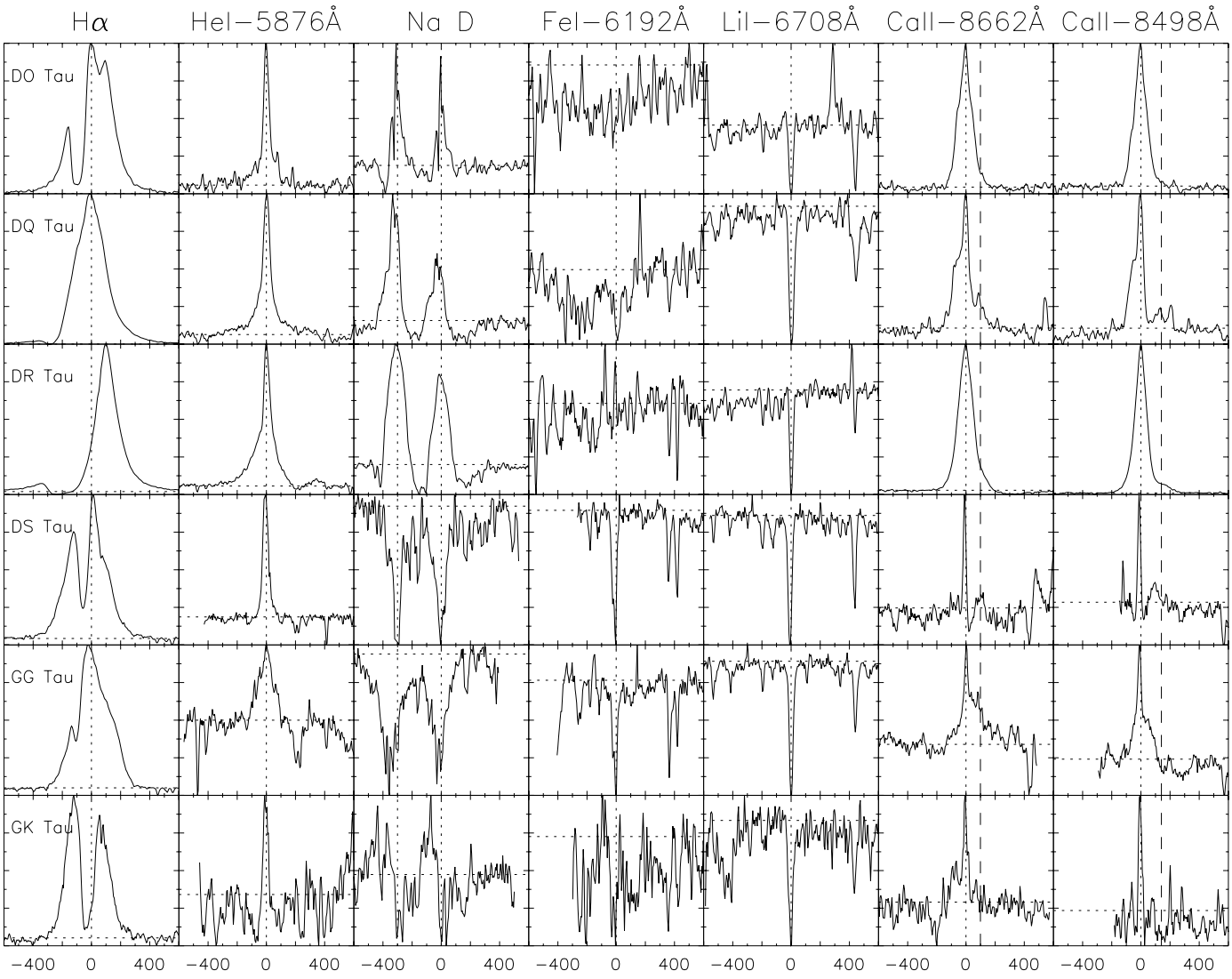

FIG. 1.—*Continued*

Beristain, Edwards, & Kwan 1998), or as emission and absorption components, such as the Balmer lines. The different components often show distinct characteristics (such as broadening and shifts), suggesting that the lines may originate in distinct regions. The Fe I lines are mostly in absorption but can be found in strong emission in very active stars (as in AS 353, DG Tau, and RW Aur) always with a double-peaked profile that could be due to NLTE chromospheric core inversion (inversion of the source function) or disk rotation.

4.2. *Line Strengths*

The study of the correlations between the fluxes of different lines is an important tool that gives insight on the relations between different line formation regions. Correlations can indicate common forming regions, but they can also mean that a common process is affecting both regions at the same time. In this section we discuss the correlations that appear in our data, as well as those that do not.

The Balmer lines emission components are well correlated with each other, as are the IRT lines with each other, which is expected as they should be formed in regions with the same physical characteristics. The difference between them should arise mainly because of differences in line optical depths. In the Balmer lines case, the correlation seems to decrease as we compare lines that are farther apart in the series; e.g., Hα and Hβ show a strong correlation with each other (Fig. 2, *top*) with a false alarm probability (FAP) of 3.24×10^{-7}, but Hα and Hδ do not (FAP = 0.168). This behavior is biased by stars with strong wind contribution, where the emission component is sometimes almost absent because of large absorption components and/or a hot underlying photosphere. By eliminating those stars, the good correlations are partially recovered (Fig. 2, *bottom*), with the FAP of the Hα and Hδ emission components decreasing to 3.55×10^{-4} and presenting a linear correlation coefficient $r = 0.880$.

The entire Hα and He I lines are also well correlated (Fig. 3; FAP $= 1.26 \times 10^{-6}$), except for DQ Tau, which has a very high Hα equivalent width in the outburst spectra we chose, and CW Tau, which has a high uncertainty in the veiling measurement (we get FAP $= 4.65 \times 10^{-10}$ without DQ Tau and CW Tau). The same kind of correlation is verified with Hβ, but Hγ and Hδ do not show a well-defined correlation with He I. The apparent lack of correlation with Hγ and Hδ may be due to the small number of spectra

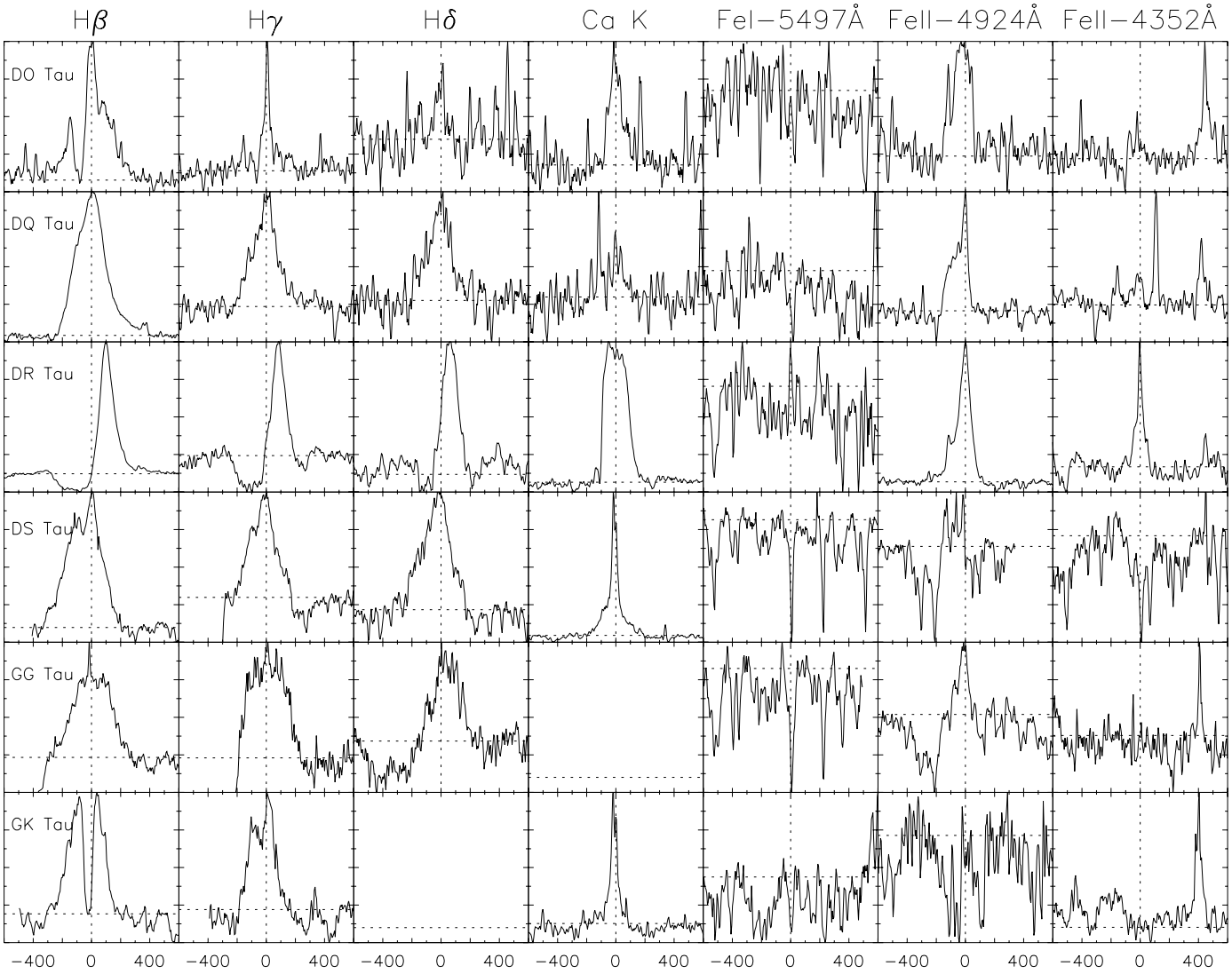

FIG. 1.—*Continued*

where those lines could be reliably measured and the lower signal to noise present in our spectra in that region. Apart from the correlation with the entire lines, we also verified a good correlation between the Hα emission component and the He I BC (FAP = 4.68×10^{-4} with DQ Tau and CW Tau and FAP = 8.32×10^{-6} without them). The He I line is believed to form in high-temperature regions (20,000 to 50,000 K), and, together with the large width of its BC, it suggests that the BC comes either from the highly turbulent shock region or the magnetospheric flow, where the broad emission component of the Balmer lines is also supposed to be formed. Due to their larger optical depths, the Balmer lines probe a much larger volume of gas than the He I lines, but the correlations between the entire lines and the components show that their formation regions are strongly related to each other.

Also thought to be formed in the accretion flow, because of its large widths and blueshifted center, the broad IRT component does not strongly correlate with the He I BC (FAP = 1.97×10^{-3} and $r = 0.678$ for $\lambda 8498$) or with the Hα emission (FAP = 6.12×10^{-3} and $r = 0.590$ for $\lambda 8498$). For the He I BC, no correlation is found for small equivalent width values and a tendency for the equivalent widths to increase together exists, although with much scatter. For the Hα, however, a correlation seems to exist, except for the higher Hα flux values (where the scatter is really large). Although the Ca II line is formed at much lower temperatures, it is expected to strongly correlate with Hα and He I, if the accretion flow is sufficiently organized that a global change in accretion rate is felt by all diagnostics.

Batalha et al. (1996) showed that the narrow components (NC) of CTTSs have a flux excess when compared with the WTTSs, and this was attributed to the reprocessing of radiation produced in accretion shocks as the accreting material hits the stellar atmosphere. However, neither the He I NC nor the Ca II NC correlate with the Balmer emission, which implies that although both the NCs and the Balmer lines are related to accretion, they are probably probing regions that are far away from each other and consequently not equally influenced by the same physical processes, or the time delay for changes that affect one region to reach the other is too large for the changes to show up in simultaneous spectra of both components.

We also confirmed the trend noticed by Batalha et al. (1996), that the IRT and the He I NCs are positively correlated (Fig. 4 and FAP = 1.41×10^{-5}; unsurprisingly, since

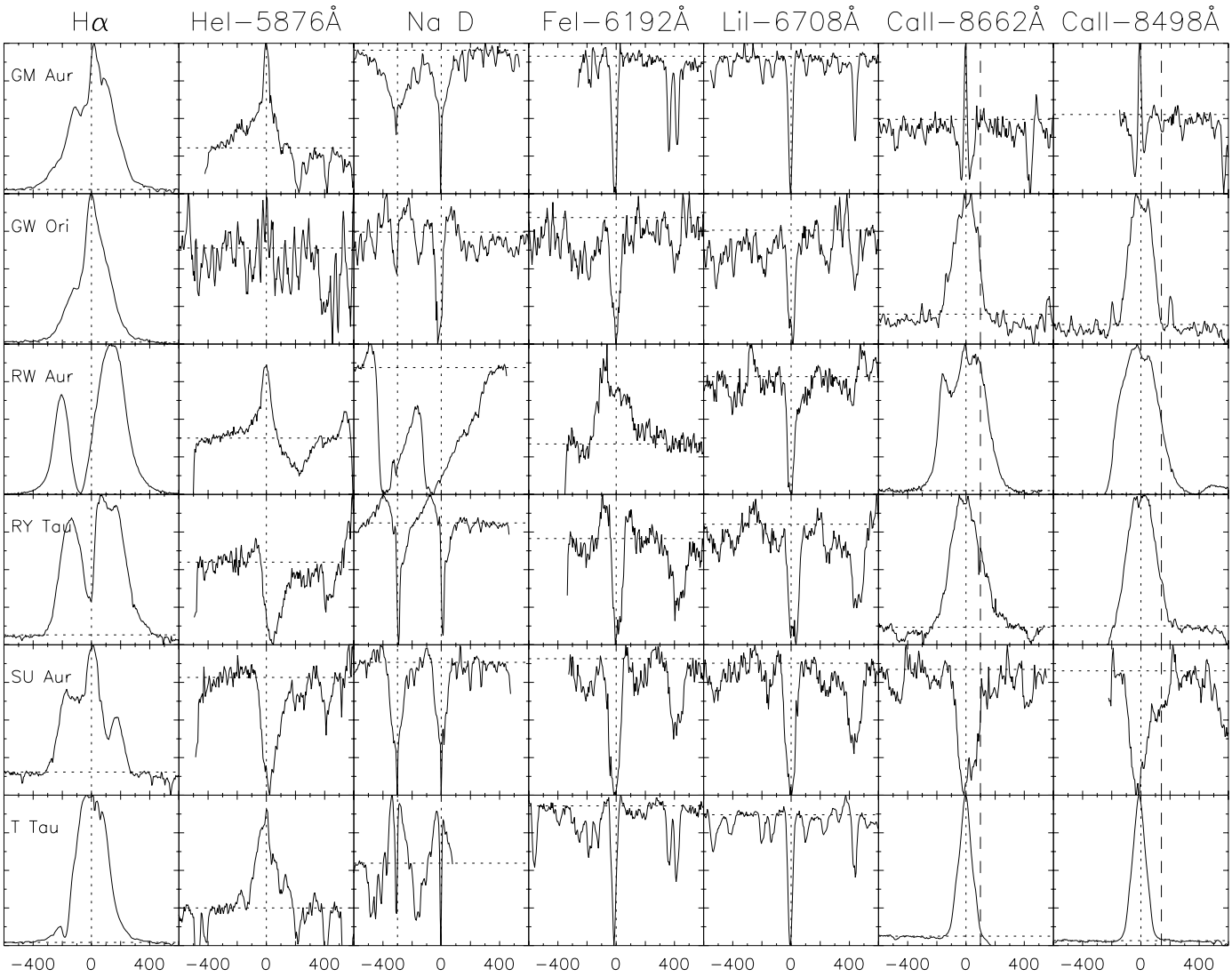

FIG. 1.—*Continued*

we have a lot of data in common), while Muzerolle et al. (1998a) found that they were uncorrelated. Those lines are generally thought to sample quite different temperature regions—the He I is formed in high temperatures (>20,000 K) while the IRT is a chromospheric line formed at 4000 K < T < 7000 K. The correlation found is probably related to the excess emission due to the influence of the accretion shock on the stellar atmosphere, a common feature in both of them.

Iron lines are quite common in CTTSs, so we decided to analyze the behavior of four of them (two Fe I and two Fe II) in our sample. The Fe II (λ4923) line was only fitted when in emission. Only 40% of the sample presented this line in emission, and we were able to measure the veiling for just some of them, but before applying the veiling corrections it shows a good correlation with the He I BC and with the IRT BC. These correlations may indicate that the Fe II lines, at least when in strong emission, share a common emitting region with the BCs of He I and the IRT.

The Fe I absorption lines (λ6192 and λ5497), with excitation energies of 4.43 eV and 3.27 eV, respectively, are not correlated with each other. Although visually they both have some resemblance to the Li I line, nothing was found between the Fe I (λ6192) and Li I, while a strong correlation exists between the Fe I (λ5497) and Li I lines. This is due to a temperature effect: the cooler stars show the deepest lines.

Another important aspect of the correlation measurements is the quest for good accretion rate indicators that would later provide an easy way to obtain these rates for other stars. Using the mass-accretion rates in Hartmann et al. (1998), there is a very good correlation between the IRT veiling-corrected equivalent widths (Ca II λ8498 and λ8662) and mass-accretion rates (Fig. 5, *top*, and FAP = 1.80×10^{-4}), as in Muzerolle et al. (1998a) for Ca II (λ8542). The only exception is DQ Tau, which has a $\log \dot{M} = -9.4\ M_{\odot}\ \mathrm{yr}^{-1}$, according to Hartmann et al. (1998), but $-7.3\ M_{\odot}\ \mathrm{yr}^{-1}$ according to Hartigan, Edwards, & Ghandour (1995) (the largest discrepancies between their values). DQ Tau is known to have a variable accretion rate that depends on the orbital phase of the binary system and on events such as outbursts that may occur when the stars approach each other (Basri et al. 1997). We decided not to use this star.

The Balmer lines and their components are also correlated to the mass-accretion rates (Fig. 5, *middle and bottom* with FAP = 3.40×10^{-4} and 7.09×10^{-3}, respectively).

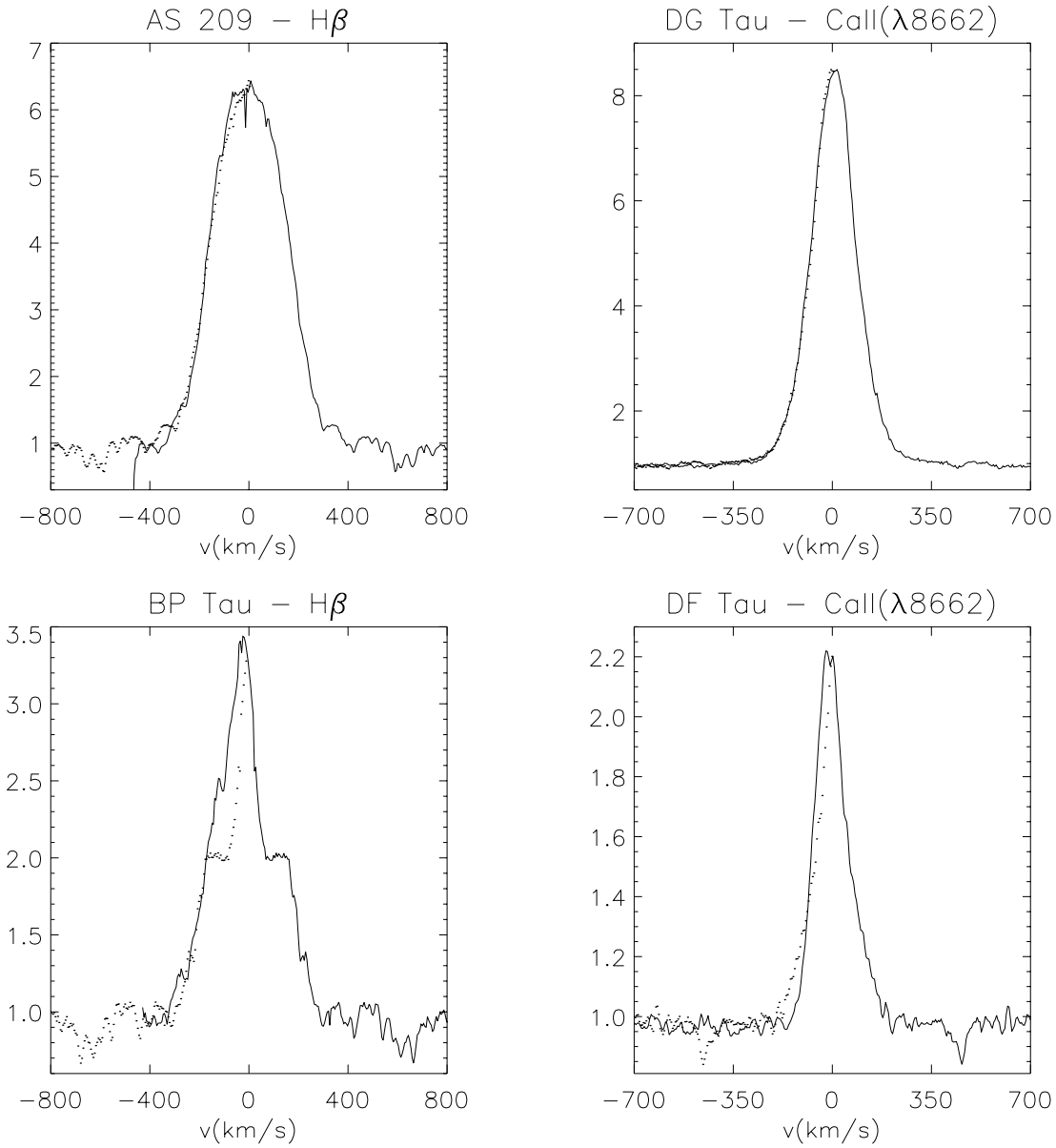

FIG. 10.—Emission lines with red wings (*dotted lines*) reflected. The top lines are symmetric and the bottom ones are asymmetric and in agreement with the magnetospheric model predictions.

In general, the symmetry predictions of the magnetospheric model cannot be strongly confirmed with our sample. Contrary to them, most of the BCs are found to be symmetric; among the asymmetric ones many are not blueward asymmetric, and about 20% of the broad emission components present centroids redshifted by more than 5 km s^{-1}.

5. DISCUSSION

Many aspects of the line formation of a CTTS can be inferred from the correlations found with the veiling-corrected equivalent widths in the previous sections.

We showed that lines coming from a common lower level are very well correlated, such as Hβ with Hα and the IRT lines with each other. This is expected, as they need the same physical conditions to be produced and tend to be affected by the same physical processes. As previous studies also showed, most lines have more than one component (BC and NC for the He I and the Ca II and emission and absorption components for the Balmer and Na D lines). These are likely formed in distinct regions, as the characteristics of those components are very different from each other throughout our sample and many correlations found were valid for one of the components but not for the other. According to our data, the Balmer emission, the He I BC, the IRT BC, and the iron lines (when in strong emission) are mainly formed in the magnetospheric flow. Alternatively, the He I BC may also come from the shock region, where the temperatures are high and more appropriate for the formation of that line instead of the magnetospheric flow itself. The NCs of the Ca and He I lines are thought to be formed at the stellar surface, where it is perturbed by the

infall of material and partly in the normal stellar chromosphere. The wind is the origin of the blueshifted absorption commonly seen in the Na D and Balmer lines.

We also verified that the effect of accretion on the line components sometimes probably produces the correlations, as lines formed in regions with physically distinct properties (very different temperatures, for example) but both affected by accretion can be found to correlate very well, such as the He I and the IRT NCs.

Somewhat puzzling is the lack of strong correlation between the IRT BCs and the Hα emission or the He I BCs, if all broad emission lines are supposed to share a common forming region. Johns-Krull & Basri (1997), analyzing DF Tau, confirm the lack of correlation found between the IRT BC and the Hα emission, but they found a correlation between the He I BC and the IRT that neither we nor Muzerolle et al. (1998a) confirm in our samples of various CTTSs.

We showed that the IRT lines and Hα are good mass-accretion indicators in our sample. We also confirmed that the same mechanism that powers the accretion also seems to influence the outflow, as the emission and absorption components of Hα are well correlated with the mass-accretion rates and with each other. Other good evidence for the accretion-wind connection is that the Fe lines in strong emission seem to be related to both processes, occurring when the wind and the veiling are prominent.

The blueshifted absorption components are thought to be formed in low-density winds. There is strong evidence that the NCs are formed at the stellar surface (Batalha et al. 1996). Although they are both influenced by the accretion process, they should not be compared to the theoretical magnetospheric profiles.

Some of the observations tend to support the fact that the accretion affects the relatively quiet stellar atmosphere, and lines produced in that region suffer the influence of such changes. The models also predict that accretion and outflow should be related to each other—the former occurring through closed magnetic field lines that connect the disk to the star and the latter through the open field lines escaping from the disk itself.

However, the results presented in the previous sections also show that some of the general characteristics of the magnetospheric accretion models are not always confirmed by our data. The idea that the broad emission components mainly arise from a common emitting region, the infalling magnetospheric gas according to those models (Hartmann et al. 1994), must be taken with care, as the observational evidence is not yet conclusive. We must also keep in mind that the magnetospheric predictions do not do particularly well for the broad emission components to which they primarily apply. We find observed profiles to be generally fairly symmetric, with centroids distributed through a range of blueshifted to redshifted velocities. Sometimes they have redshifted absorption components, but often not at free-fall velocities. Only about 20% of the BC profiles support the specific predictions of the models.

Hartmann et al. (1994), Muzerolle et al. (1998b), and Muzerolle et al. (1998a) presented line profiles generated with magnetospheric models and compared them with observational ones. They obtained good agreement between the observed and theoretical profiles of many lines for some stars, such as BP Tau. But, comparing their BP Tau observed profiles with ours, many differences can be seen. This is expected, as CTTSs are known to exhibit line profile variability sometimes even within a few hours (Johns & Basri 1995a), and Gullbring et al. (1996) showed that this is the case for BP Tau, a typical CTTS. The problem that arises with the rapid profile variation is that, even if the magnetospheric models can reproduce one of the profile types of a star, it does not mean that all the profiles that a line may exhibit will be reproduced without changing basic model characteristics. As an example, the model used to compare the observed and theoretical profiles of BP Tau cited above does not fit our observations of that star well.

Some years ago, Shu et al. (1994) proposed a new version of their X-celerator mechanism whose natural period was the rotational period of the star. Lines formed in magnetospheric accretion flows that are controlled by the stellar field might also show periodicity at the stellar rotation period in the presence of an inclined dipole field. In this case, the line variations would certainly be due to geometrical effects, and a model with the same basic parameters should be able to describe the various line profiles. SU Aur presented this kind of variations in Hβ and Hα (Johns & Basri 1995b), but unfortunately its profiles do not resemble the published theoretical ones very much.

In general, however, the line variations do not seem to be related to orbital motion as they do not usually correlate with the stellar rotational period. Different parts of a line may vary differently, as Johns & Basri (1995a) showed by analyzing time variations of Hα for several CTTSs. They suggest the line-emission region is composed of discrete, stochastically varying blobs with a range of velocities and turbulence, which the Sobolev treatment used in the actual magnetospheric models does not take into account.

Najita et al. (1996), analyzing Brγ emission profiles, showed that WL 16, an obscured low-luminosity YSO, presented profiles that were remarkably similar to the theoretical Balmer line calculations by Hartmann et al. (1994). Later, Muzerolle et al. (1998b) calculated profiles for the Brγ emission and showed that, in fact, the WL 16 Brγ emission line was very well reproduced. However, some of the stars in the sample of Najita et al. (1996) also present very symmetric emission profiles, such as AS 353, DG Tau, and SVS 13, that cannot be explained only by magnetospheric accretion. Although the magnetospheric model can generically explain part of the large line widths and the occasional redshifted line absorptions, it does not predict symmetric profiles, because the magnetospheric infalling material is subjected to occultation effects by the star-disk system.

Most of our broad emission profiles were found to be symmetric and the few asymmetries occur on both the blue and the red side. Due to these differences, the profiles presented in the theoretical papers generally do not match our observed ones. Many authors have speculated on the origin of the rather symmetric broad line wings in TTS profiles. Basri (1990) suggested that the wings were formed in a turbulent region near the star, and Edwards et al. (1994) pointed out that Alfvén waves could generate the necessary turbulent broadening. Johns & Basri (1995b) managed to reproduce some of the Balmer line symmetric features of SU Aur by adding a range of turbulent high-velocity components at the base of spherically symmetric wind models, and Johns & Basri (1995a) could also fit the DF Tau wings with a similar procedure.

Most of the stars discussed here rotate slowly ($v \sim 10$ km s^{-1}) at velocities that are much smaller than the velocities of

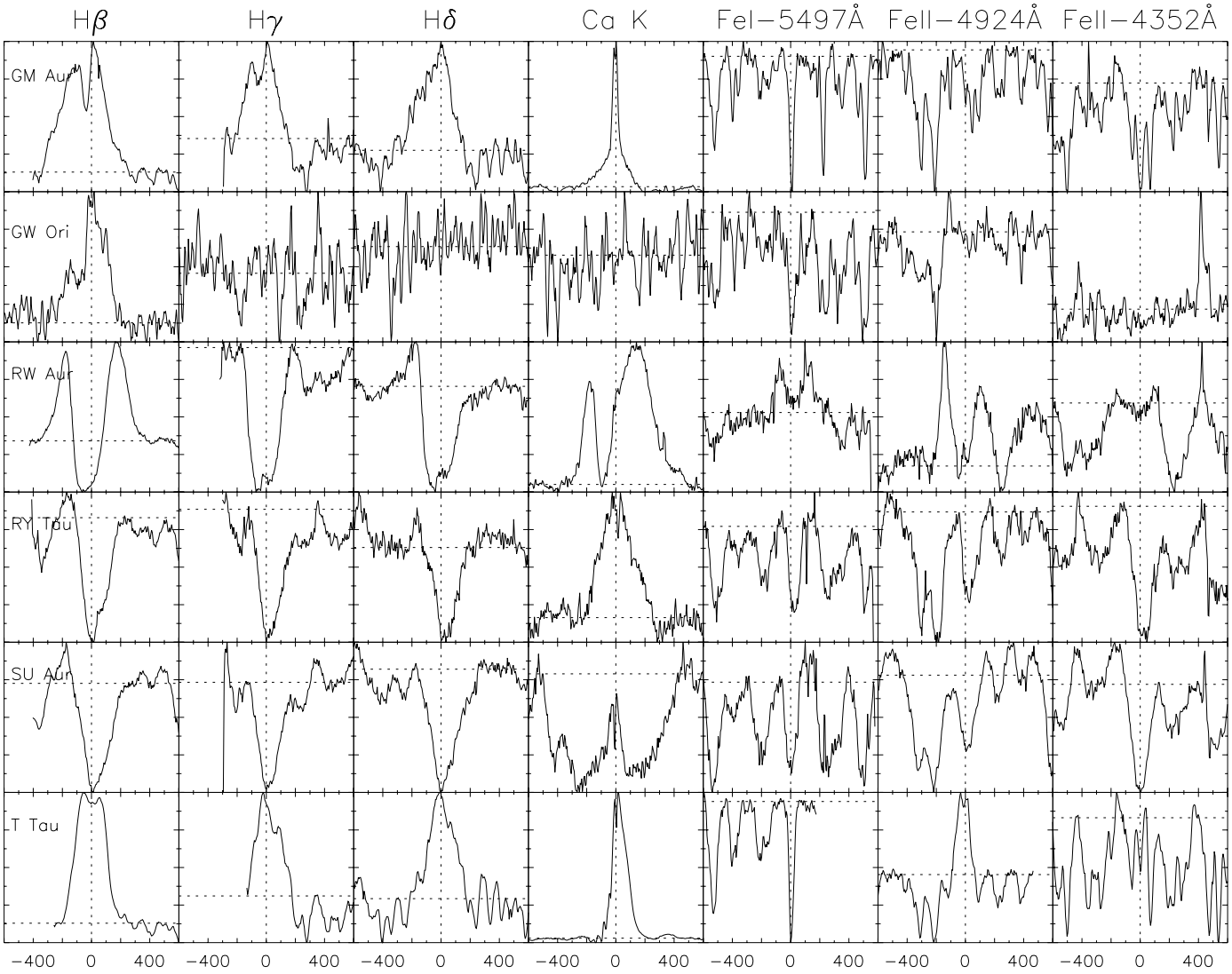

FIG. 1.—*Continued*

The results for the absorption component are not as reliable as the others, mainly because of the small number of stars that exhibit a clear absorption and for which there are published mass-accretion rates. The flux of the emission and absorption components increases as the accretion rate increases, showing that the accretion may be powering both the emission and the outflow. This would be consistent with theoretical results (Shu et al. 1994) that suggest that the wind mass-loss rate and the disk-accretion rate are directly proportional (but see below for caveats).

4.3. *Evidence for Outflows*

Winds are expected to be present in CTTS and help carry away angular momentum. If cool, they should appear mainly as absorption components. Due to the presence of the disk the absorption is expected to be blueshifted; the receding part of the wind is blocked by the disk from the observer's line of sight. The emission components of CTTS were thought for some time to be produced in optically thick winds, but these models also generated upper Balmer line profiles with very deep absorptions that were not consistent with observations.

The Balmer and Na D blueshifted absorption components are the clearest evidence in Figure 1 that a strong wind is present in our sample of CTTSs. Almost 80% of our stars show blueshifted absorption components in at least one line, the most common being Hα (see Table 2 for Hα and Tables 2 and 3 for a complete listing). The number of blueshifted components decrease as we look at the upper Balmer lines, appearing only in about 35% of the Hδ profiles (where they tend to be weak). This suggests that the blueshifted absorptions arise from a region that is optically thin, at least in the upper Balmer lines, and distinct from the emission component that is believed to arise mainly in the optically thick accretion flow. Some stars, like DR Tau and AS 353, present P Cygni profiles in all the Balmer lines. These are normally associated with strong winds, and other stars, such as CO Ori, RW Aur, SU Aur, and RY Tau, have such a strong absorption component that it sometimes suppresses the emission in the upper Balmer lines of the stars with the hottest underlying photospheres. A number of these stars are known to be jet sources.

The eight stars in our sample that exhibit blueshifted absorption components in the Na D lines (presumably indicating high mass-loss rates; Hartmann 1998) also do in Hα. The lack of P Cygni profiles in the Na D lines does not necessarily mean low mass-loss rates, as the star may present a deep photospheric absorption that prevents the

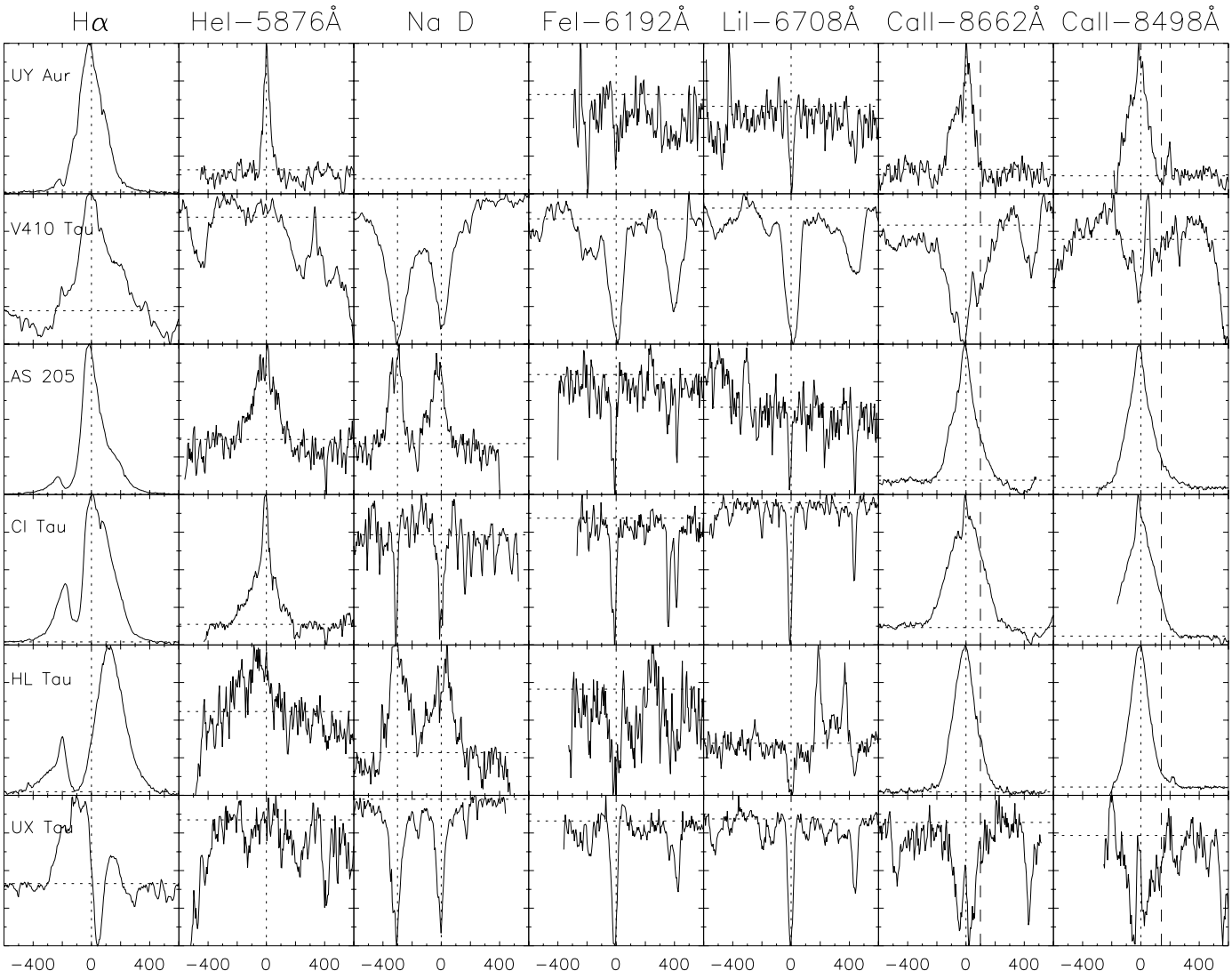

FIG. 1.—*Continued*

detection of the blue absorption due to the wind (Natta & Giovanardi 1990). Due to the difference in their optical depths, the Balmer and Na lines will sample different wind volumes. As resonance lines, the sodium probes the coolest part of the wind. The blueshifted components of both lines tend to be centered at approximately the same velocities (Tables 2 and 3), likely meaning that different wind regions share some common kinematic component. The Na D blueshifted absorptions bear no other resemblance to the Hα ones, being much weaker in intensity and width. The position of blueshifted absorption centers in these lines vary from star to star, suggesting that the wind velocities can occur with a wide range of values (from 0 to -270 km s^{-1} in our sample; see Fig. 6). There may well be projection effects that must be taken into account; these would imply the outflow is not spherical.

After decomposing the profiles we can also investigate the correlations that appear between different wind components and between wind components and other features in order to better understand the wind-forming region. The Hα and Hβ blueshifted absorptions are very well correlated (FAP $= 2.39 \times 10^{-8}$), showing that they both probe the same wind region, and although there is apparently no correlation with the blueshifted absorptions of Hγ and Hδ, this may be due to the small number of cases. Where the absorption does appear in the upper lines, the wind component is often very weak and consequently hard to fit.

The Hα and Hβ blueshifted absorptions also show some correlation with their line's emission components: the stronger the emission, the stronger the absorption. Unfortunately, that does not have a unique interpretation. One possibility is that the same mechanism that is powering the emission is also powering the wind in the sense that when more material is accreted there is more to outflow. This is predicted by the accretion model and also means that the absorption region is outside the emission region. A second possibility is that if both emission and absorption were formed in winds, the absorption component would be due only to the decay of the source function in the outer regions of the atmosphere and not to the accretion itself. If the first possibility is correct, this relation could also explain the trend seen between the Hα emission and absorption components and the mass-accretion rates.

Finally, the present result may also be an effect of line optical depth; if the wind is optically thick the central depth of the blueshifted absorption is fixed and the changes that

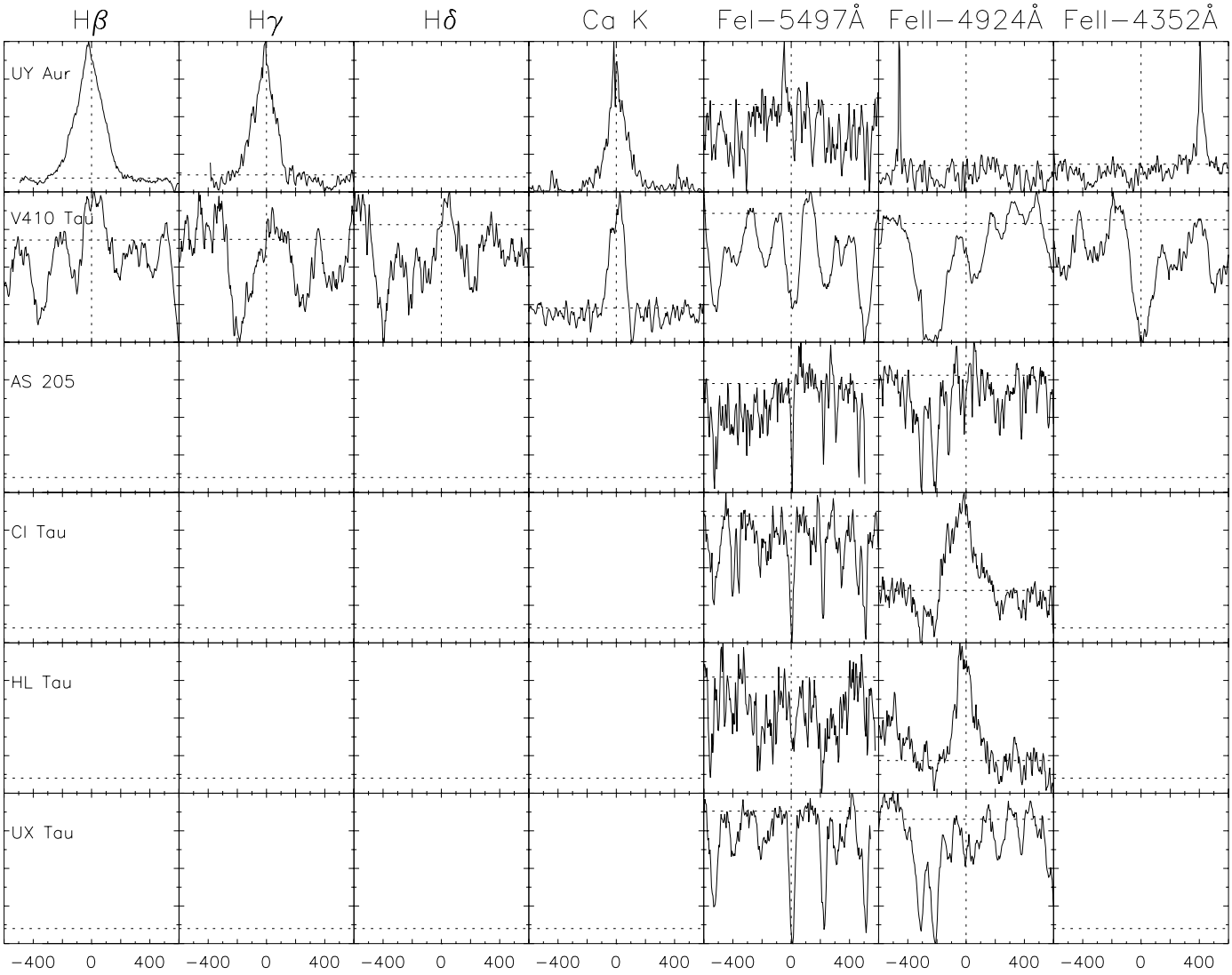

FIG. 1.—*Continued*

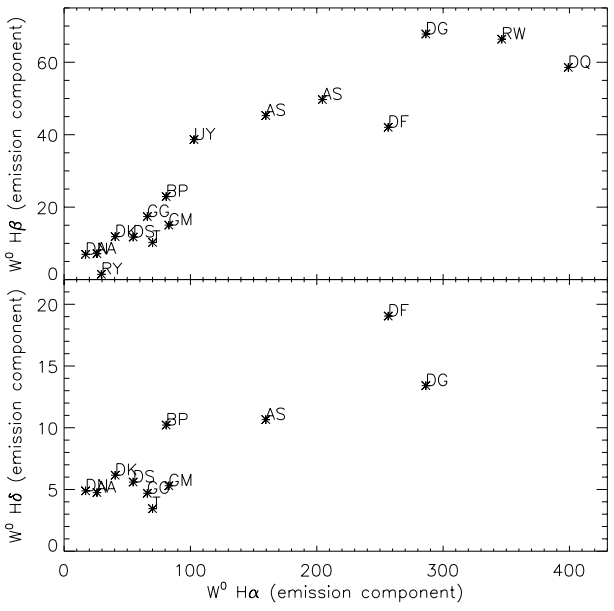

FIG. 2.—Veiling-corrected equivalent widths of emission components: $W^0_{H\alpha}$ vs. $W^0_{H\beta}$ and vs. $W^0_{H\delta}$.

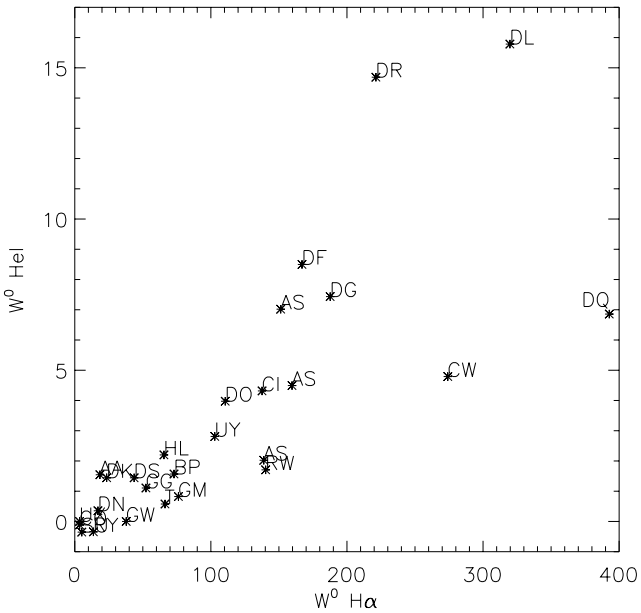

FIG. 3.—$W^0_{H\alpha}$ vs. W^0_{HeI}

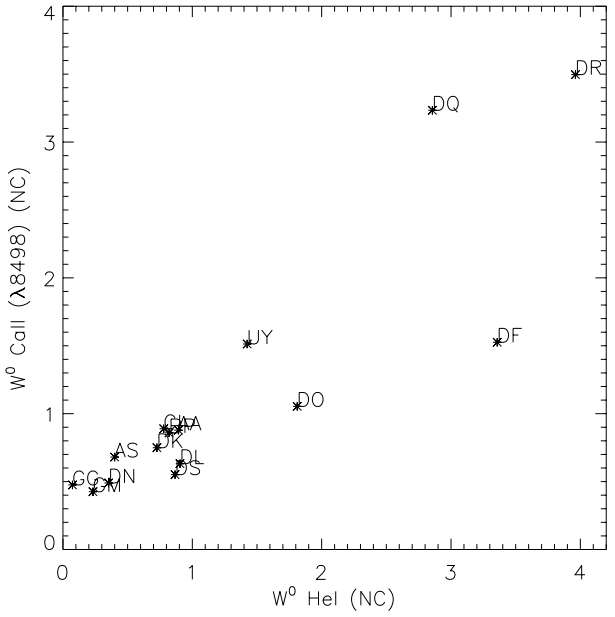

FIG. 4.—$W^0_{\text{He I}}$ (NC) vs. $W^0_{\text{Ca II}(\lambda 8498)}$ (NC)

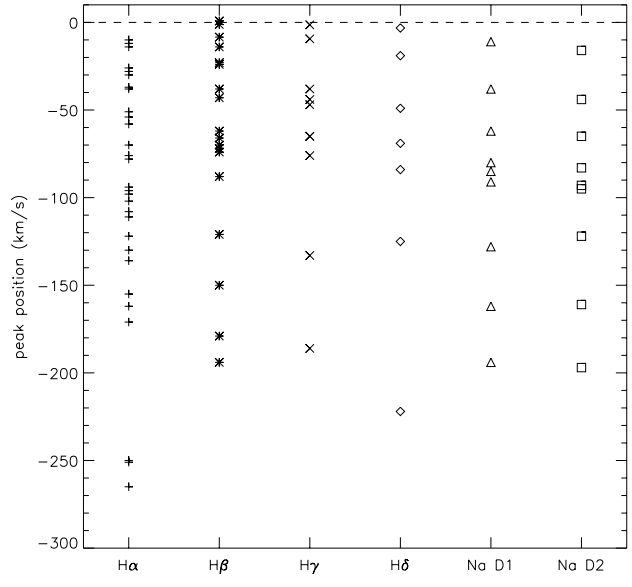

FIG. 6.—Blueshifted absorption component's peak position

appear are in fact only due to the emission component variations as shown by Johns & Basri (1995b) in the case of SU Aur. Johns-Krull & Basri (1997) also found that the Hα absorption and emission strengths of many DF Tau spectra were correlated and that the absorption component strength correlated with the veiling.

A curious fact about the absorption components can be noticed in the stars that show an absorption component in the four analyzed Balmer lines. This component tends to be shifted toward the red as we go from Hα to Hδ, and in Figure 7 we plot the absorption centers versus the Balmer lines oscillator strengths for those stars. It seems that we may be seeing the acceleration of the flow. This shift of the absorption component can also be noticed in Edwards et al. (1994) in the residual profiles of DK Tau and in Appenzeller, Reitermann, & Stahl (1988) in the DR Tau spectra, showing that this behavior may be quite common among CTTSs.

Another feature that is associated with strong activity, presumably both inflow and outflow, concerns the iron lines in strong emission. These lines are often in absorption in our sample, but Fe II (λ4923) is also found in emission in about 40% of our stars. When this happens, a wind component is present at least in Hα, sometimes also in the other

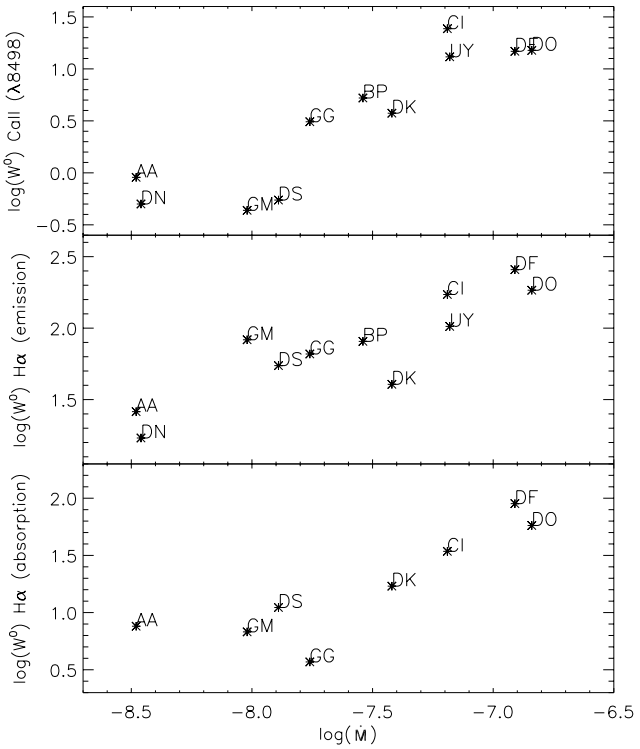

FIG. 5.—$\dot{M}$ vs. $W^0_{\text{Ca II}(\lambda 8498)}$ and vs. $W^0_{\text{Hα}}$ (emission and absorption components).

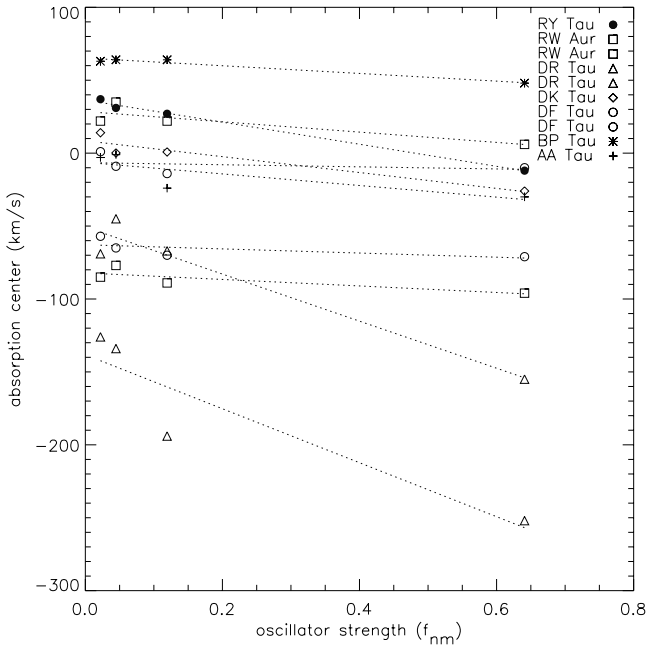

FIG. 7.—Balmer line absorption center vs. oscillator strength. RW Aur, DR Tau, and DF Tau are plotted twice as two wind components were measured.

TABLE 2

VELOCITY CENTROID (km s^{-1}) OF LINE PROFILE COMPONENTS

	Hα			Hβ			Hγ			Hδ			He I	
STAR	c1	c2	c3	c1	c2	c3	c1	c2	c3	c1	c2	c3	NC	BC
AA Tau.....	−30.1*	−34.1	x	−23.9*	−26.9	87.9*	−1.4*	−13.1	103.5*	−3.2*	0.3	101.0*	−0.4	9.0
AS 205.....	−109:*	−46.4	174.5										x	−14.3
AS 209.....	−4.7	x	x	1.3:	x	x	8.1	x	x	−1.4	x	x	−4.2	0.6
AS 353.....	−137:*	−266:*	30.1	−179.2*	97.7	x	−186:*	131.6	x	−222.5*	136:	x	x	−41.2
BP Tau	4.4	48.1*	x	−6.1	63.8*	x	−0.9	63.8*	x	−4.5	63.4*	x	0.4	−10.5
CI Tau.....	−98.3*	−9.2	x										−5.1	−23.0
CO Ori	−37.0*	−111.6*	22.7	−38.1*	x	x	−38.4*	115:*	x	−19.9*	x	x	6:*	x
CW Tau	−14.3*	−130.9*	−0.8	−1.2*	8.3	x	x	x	x	x	x	x	x	−58.0
DE Tau	−0.4	x	x	12.3	x	x	8.2	x	x				−2:	−53:
DF Tau	−70.8*	−10.4*	−5.3	−70.2*	−14.2*	−17.9	−65.3*	−9.4*	−28.3	−57.3*	1.0*	−22.3	4.6	21.8
DG Tau	−102.9*	−162.2*	−38.4	−150.1*	−50.1	x	17.7	x	x	21.0	x	x	x	−4.2
DK Tau	−26.3*	−13.7	x	0.8*	−14.3	213.8*	0.1*	−7.8	234.1*	14.2*	−30.6	213.6*	−0.2	0.4
DL Tau	−122.0*	2.1	59.1*	−121.4*	8.3	x	14.7	x	x	21.0	x	x	4.2	−2.5
DN Tau	−58.2*	−38.8	x	−43.1	−7.7	149.3*	−2.4	x	x	0.9	−3.2	x	−2.8	x
DO Tau	−76.0*	−3.3	43.1*	−72.1*	−6.3	50.7*	x	x	x	x	x	x	−0.5	5.6
DQ Tau	−250.0*	−8.2	262.9	−7.2	297.	x	−6.7	x	x	−12.1	x	x	2.3	−4.2
DR Tau	−155.0*	−251.8*	100.9	−66.8*	−194.0*	100.6	−44.7*	−133.8*	81.2	−69.3*	−125.8*	58.3	0.1	−14.5
DS Tau.....	−54.8*	−35.4	x	−62.1*	−49.4	x	−65.7*	−28.3	x	−33.9	x	x	−7.4	6.0
GG Tau	−94.8*	14.9	57:*	6.1	x	x	10:	x	x	42.2	x	x	3.0	−5.1
GK Tau	−28.3*	−33.3	x	−24.4*	−32.0	x	x	x	x				−4.7	x
GM Aur....	−51.8*	7.5	x	−43.7*	−49.7	x	−45.9*	−33.4	249.3*	−40:	189:*	x	2.4	−17:
GW Ori	−78.7*	−5.2	x	−74.4*	−22.6	x	x	x	x	x	x	x	x	x
HL Tau	−38.7*	−2.3	x										x	x
RW Aur	−96.0*	4.5	5.7*	−88.7*	9.5	21.6*	−76.8*	34.9*	x	−84.6*	−72:	21.8*	0.5	−15.0
RY Tau.....	−12.2*	14.3	118.*	28:*	x	x	31:*	x	x	36.7*	x	x	54:*	x
SU Aur	−22.4	10.7	103.1*	38.9*	x	x	20.4*	x	x	23.6*	x	x	29.2*	x
T Tau.....	−171.*	−2.68	x	−4.3	x	x	9:	x	x	2.7	x	x	x	−9.3
UX Tau	−48.8	42.5*	269.4*										x	x
UY Aur	−30.6	5.4	x	−15.0	−21.9	x	−18.3	−7.7	x				0.1	10.1
V410 Tau...	60.7	102:*	x	x	x	x	x	x	x	x	x	x	x	x

NOTE.—Lines for which the cell is left blank were not available, and those marked with an "x" were not present or could not be reliably measured in the observed spectrum. Velocities marked with an asterisk represent absorption components. The notations c1, c2, and c3 represent the emission and absorption components of the lines that could not be decomposed as NC and BC.

TABLE 3

VELOCITY CENTROID (km s^{-1}) OF LINE PROFILE COMPONENTS (CONTINUED)

	Na D1			Na D2			Fe I λ6192	Li I λ6707	Ca II λ8662			Ca II λ8498			Ca K		Fe I λ5497	Fe II λ4924	Fe II λ4352
STAR	c1	c2	c3	c1	c2	c3	c1	c1	NC	BC	c3	NC	BC	c3	NC	BC	c1	c1	c1
AA Tau.....	4.3*	x	x	−4.4*	x	x	−13.1*	−5.4*	−3.3	x	x	−14:	x	x	2.3	−5.7	5.6*	x	x
AS 205.....	−12.4	x	x	−28.2	x	x	−16.3*	−7.5*	−6.1	−9.7	375.1*	−15.4	−7.8	x			5.9*	x	
AS 209.....	11.4	x	x	11.0	x	x	−15.0*	−5.2*	−10.0	4.6	x	−20.0	−6.4	x	x	25.7	4.8*	x	x
AS 353.....	−197.1*	−28.3	x	−194.4*	16.3	x	0.7	−2.9*	x	0.3	x	x	−10.6	x	x	x	x	−21.4	−14.4
BP Tau	62.9*	x	x	53.7*	x	x	−10.4*	−1.6*	−1.8	0.4	37.9*	−2:	25:	x	−7.7	−9.0	7.5*	x	x
CI Tau.....	x	x	x	x	x	x	−16.0*	−6.9*	−3.6	−1.0	x	−16.4	−4.5	x			2.5*	−27.5	
CO Ori	−44.8*	−13.4 *	x	−38.5*	−5.2 *	x	−9.3*	3.2*	x	x	x	x	−66.0	−3.0*	x	x	11:*	x	x
CW Tau	x	x	x	x	x	x	−5.7*	1.6*	x	4.6	x	3.4	13.0	x	−11.1*	−3.7	x	−0.4	x
DE Tau	x	x	x	x	x	x	x	−2.8*	6.9	6.8	x	−10.8	1.5	x	x	3.4	x	x	2.4
DF Tau	−65.2*	−13.1	141.6	−62.2*	−23.2	136.4	x	4.1*	−1.4	−11.7	x	−0.7	−7.2	x	−5.7	−1.6	x	−7.5	−5.5:
DG Tau	−95.4*	−6.8	x	−91.9*	6.9	x	−2.5	−0.2*	x	4.9	x	x	8.2	x	x	10.2	7.2*	2.9	5.9
DK Tau	−16.3*	x	x	−11.9*	x	x	−11.3*	−2.2*	−1.4	93.7	x	−5.3	91.2	x	200:*	32.6	6.7*	x	x
DL Tau	−122.7*	−18.1	x	−128.1*	13.2	x	−20.1*	−6.2*	−3.5	−1.6	x	−6.0	2.9	x	x	15.1	x	−1.8	x
DN Tau	−8.9	x	x	1.9	x	x	−10.9*	−0.8*	−2.7	x	x	−9.1	x	x	−5.5	x	8.0*	x	x
DO Tau	−84.6*	−4.2	x	−80.0*	1.0	x	x	−0.2*	−3.3	−6.4	x	−5.1	−3.6	x	x	−3.1	x	−20.3	x
DQ Tau	−24.4	100:*	x	−23.6	101:*	x	9.1*	4.0*	0.3	−45.6	x	−1.4	−54.9	x	x	x	x	−0.2	x
DR Tau	−9.74	162.9*	x	−4.14	108.7*	x	x	−1.3*	x	−2.5	350.7*	x	−4.4	x	x	−3.1	x	−1.7	−2:
DS Tau	−4.1*	x	x	−4.0*	x	x	−11.6*	−7.9*	−9.7	x	x	−11.9	x	x	−10.4	−19.3	7.2*	x	x
GG Tau	x	x	x	x	x	x	−7.0*	1.0*	1.0	50.7	x	−10:	4:	x	x	x	8.2*	x	x
GK Tau	x	x	x	x	x	x	x	−1.7*	−4.8	−30:	x	−5:	x	x	−12.0	−42:	3.5*	x	x
GM Aur	5.4*	x	x	0.8*	x	x	−11.0*	−4.3*	−3.0	x	x	−6.7	x	x	−4.1	−15.4	7.1*	x	x
GW Ori	−15.0	x	x	4.9	x	x	−2.8*	3.4*	x	−1.6	x	x	−1.6	x	x	x	12.0*	x	x
HL Tau	2.3	x	x	6.3	x	x	−8.6*	−0.6*	x	−10.1	x	x	−8.5	x			x	−11.9	
RW Aur	−93.0*	12.1*	x	x	−85.0*	10.7*	−13:	0.2*	x	x	x	x	−11.0	285.8*	−52.0*	37.3	x	x	x
RY Tau.....	27.2*	−98.0	x	40.4*	−84.2	x	9.1*	17.8*	x	−2.3	x	x	5.3	x	x	5.0	27.1*	x	x
SU Aur	−4.3*	x	x	0.2*	x	x	−11.8*	−3.4*	x	x	11.5*	x	x	−10.6	x	x	2.2*	x	x
T Tau	−161.6*	−7.76	x	−161.9*	−9.73	x	−14.6*	−5.4*	x	−4.46	x	−13:	−12:	x	x	25.2	5.7*	−16.4	x
UX Tau	−9.8*	x	x	−5.9*	x	x	−12.8*	−3.2*	−9.0	x	x	−13.1	x	x			6.3*	x	
UY Aur	x	x	x	x	x	x	x	2.6*	18.9	−35.6	x	0.9	−23.1	x	−10.6	10.4	x	x	x
V410 Tau...	5.2*	x	x	2.7*	x	x	−1.3*	7.8	49.2	x	x	46.5	x	x	5.2	x	10.5	x	22.8

NOTE.—Markings same as Table 2.

Balmer lines and in the Na D lines, and the IRT lines always show a BC. The Fe lines in emission seem to be related to both the presence of outflow and high veiling, as some stars that show blueshifted absorption in Hα but no BC in the IRT do not present Fe I (λ4923) in emission. DG Tau, AS 353, and RW Aur, that also exhibit Fe I (λ6192) and Fe II (λ4352) in strong emission, also have associated jets (Edwards et al. 1994; Mundt & Eislöffel 1998). But unlike the forbidden lines that tend to be blueshifted, the iron lines when in emission are centered at the stellar rest frame. They are probably not produced in the outflow (wind or jet), since the occultation of the receding part of the flow by the disk would yield a blueshifted line.

4.4. *Evidence for Infall*

Redshifted absorption components in the line profiles (inverse P Cygni profiles) can be the clearest spectral evidence that infall of material is occurring, and they are naturally predicted by the magnetospheric accretion models. These models, however, require special conditions for the redshifted absorption component to be visible, such as low line thermalization, low emission damping wings, and proper inclination values. The inclination dependence arises from the contrast of the line source function of the infalling gas and the continuum source function where the gas stream is projected (Hartmann et al. 1994). If the projection is against the cool photosphere (low inclinations) no absorption is found, but if it is against the hot shock material, such as a ring or spots (higher inclinations), the absorption can be produced.

Edwards et al. (1994) presented an analysis of 15 CTTSs included in our sample, and showed that 87% of their stars had redshifted absorption components in at least one line at approximately 200 to 300 km s^{-1}, a range of velocities that is consistent with the ballistic infall predicted by the magnetospheric models for a typical CTTS. Only about 40% of our stars have redshifted absorption components in at least one line and generally not at approximately 200 to 300 km s^{-1}. BP Tau, for example, shows redshifted absorption in many lines at about 50 km s^{-1} and UX Tau has a strong redshifted absorption in Hα at 43 km s^{-1}. The difference in the absorption centroid position of the stars from the values predicted by the models could partially be due to inclination effects. The difference in the number of redshifted absorption occurrences found in the two different analyses could be due to the fact that Edwards et al. (1994) analyzed residual profiles instead of the original ones. This gives, according to them, a high sensitivity in defining features such as the Balmer lines wings, where the redshifted absorption lies. However, in the residual profiles showed by Muzerolle et al. (1998a) of 11 CTTSs, redshifted absorption at typical free-fall velocities can be found in less than half of their sample, which is more in agreement with the predictions of the magnetospheric accretion models.

In order to compare our results with the ones cited above we decided to generate residual profiles from our sample, choosing eight lines commonly found in emission: Hα, NaD, He I, Ca II (λ8498 and λ8662), Hβ, Hγ, and Fe II (λ4352). Hδ was excluded as most of our spectra present low signal to noise in that region, making it hard to obtain reliable information about small absorption features. We generated the residual profiles by subtracting from each observation a broadened and veiled standard spectrum, using as standard stars the ones previously selected for the veiling calculations.

Although the residual method often enhances features such as weak emission lines (see Fig. 8, *top*), care must be taken during the subtraction, as a small difference in continuum normalization between the two spectra can also introduce false features. The uncertainty in the veiling determination and the difficulty of choosing suitable standard stars are other factors that can introduce errors in the process. Finally, the legitimacy of the concept itself is dubious when the overlying emitting region is optically thick over most of the profile.

The residual profile calculation suppresses, in principle, all the photospheric contribution that is present in the spectra, generating smoother profiles, as the broad lines are no longer superposed with narrow absorption ones. However, we noticed that it did not a priori enhance the redshifted absorptions present in our unsubtracted spectra; indeed, some of the redshifted absorption components turned out to be mainly photospheric (for example, the Na D lines of BP Tau, DF Tau, DQ Tau, and RY Tau; see Fig. 8, *bottom*). In general, most of the redshifted absorptions became shallower, although less noisy, and we did not find many new ones. Our residual profiles show that about 50% of our stars present at least one line with a redshifted absorption component, a result in agreement with the original (unsubtracted) data, with the magnetospheric models, and with the results by Muzerolle et al. (1998a), but not with Edwards et al. (1994). Although very weak features such as the iron emission lines and the redshifted absorptions at free-fall velocities are strongly affected by the underlying photospheric spectrum, one may notice that the general characteristics of the line profiles discussed in this work are weakly affected by the subtraction of the photospheric features and that our results are also valid for residual profiles.

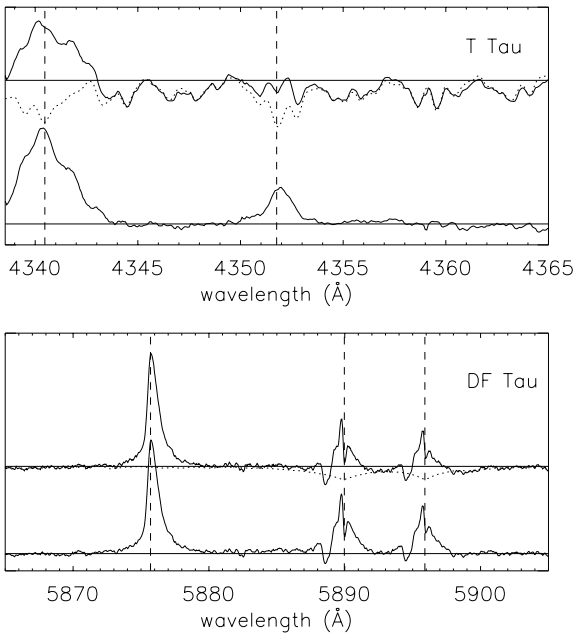

FIG. 8.—Residual profile determination. The upper solid lines correspond to the original spectra, the dotted lines to the standard spectra, and the lower solid lines to the residual CTTS profiles. *Top*: Fe II (λ4352) is dramatically enhanced by the residual method. *Bottom*: the redshifted absorption that appears in the unsubtracted spectrum in the Na D lines turns out to be mainly photospheric.

Finally, in agreement with both the model predictions and with Edwards et al. (1994), we see less evidence of redshifted absorption in Hα at high velocities than in the upper Balmer lines, probably because of thermalization effects and the Stark damping of the Hα wings.

4.5. *Profile Symmetry*

The magnetospheric accretion models predict that the BC emission is formed in the magnetospheric infalling material. It should then exhibit a central or slightly blueshifted peak and blueward asymmetry due to occultation by the disk and star of part of the flow moving slowly away from the observer. By blueward asymmetry we mean that there is an excess of blue emission compared to the red emission. Some theoretical profiles published by Hartmann et al. (1994) also show redshifted absorption at free-fall velocities, while others show extended red wings caused by the occultation of the high-velocity blueshifted material by the star; both effects add up to enhance the line asymmetry.

One way to search for asymmetries is to reflect one of the line wings about the broad emission centroid, as done by Johns-Krull & Basri (1997) for DF Tau. If the wings match each other, the line is considered symmetric, and this avoids a confusion between lines that are only shifted and lines that are really asymmetric. P Cygni profiles are more difficult to evaluate, since the blue emission wing is sometimes completely absent, and it may be hard to determine the correct shift to be applied.

In Table 4 we show the velocities that produced the best agreement between the opposite wings, and we also indicate which parts of the line are symmetric and which are not in the case of partially symmetric profiles. The BCs that showed blueward asymmetry are labelled "ASb" in Table 4, but they comprise only about 20% of the analyzed lines. Most of the BCs are symmetric (well fitted by a Gaussian) and about 75% of them have a central or slightly blueshifted peak. In Figure 9 we show the velocity position of the broad emission peak for several lines and we notice that, although most of them are indeed blueshifted, a substantial number present a redshifted peak. This is not seen in the published theoretical magnetosphere profiles. Lines with P Cygni profiles and those where the emission component was not reliably extracted are not included in this plot.

TABLE 4

WING SYMMETRY REFLECTION VELOCITIES (km s^{-1})

Star	Hα	Hβ	Hγ	Hδ	Ca II λ8662	Ca II λ8498
AA Tau.....	−30	ASb	ASb:	ASb	0[a]	−14[a]
AS 209.....	2	2	10	0	5	−7
AS 205.....	0[b]				−10	−10:
AS 353.....	0	20:	0:	0:	0	−10
BP Tau	ASb[b]	ASb[b]	ASb[b]	ASb	0	0
CI Tau.....	−10				0	−5
CO Ori	23	x	x	x	x	x
CW Tau	0	10	x	x	5	ASr[c]:
DE Tau.....	0	12	ASb[b]		7:	0
DF Tau.....	0	−18	−27	ASb:	ASb:	ASb:
DG Tau	−33	−33	20	20	5	ASr[d]
DK Tau	ASr[b]	ASb:	ASb	ASb	ASr:	ASr:
DL Tau.....	0	8	10	20	0	ASr[d]
DN Tau	AS*	ASb[c]	0	0	0[a]	−8[a]
DO Tau	0	−3	x	x	−6	−4
DQ Tau	ASr[d]	ASr[d]	−6	−10	ASb	ASb
DR Tau	0	0	−20	0	ASr[c]:	ASr[c]:
DS Tau	−35	−50	−30	−35	−9[a]	−12[a]
GG Tau	ASb[b]:	0	5	40	ASr	0
GK Tau	ASb[b]	−35	−25		−4[a]:	−5[a]
GM Aur.....	ASb[d]	−50:	−30	ASb	0[a]	−5[a]
GW Ori	0	−22	x	x	ASb[c]:	0
HL Tau.....	0				ASb[b]	−8
RW Aur	ASr[c]:	10	x	x	ASb[b]	ASb
RY Tau.....	ASr[d]	x	x	x	ASr	5
SU Aur	−13:	x	x	x	x	x
T Tau.....	0	−5	15:	0	−5	−10
UX Tau	−42				−8[a]	−15[a]
UY Aur.....	ASb[b]	−15	−20		ASb:	ASb:
V410 Tau....	ASb	x	x	x	x	x

NOTE.—Lines for which the cell is left blank were not available and as "x" were not reliably measured or observed in absorption. ASb means that the line is blueward asymmetric and ASr redward asymmetric.

[a] Only the narrow component is present.

[b] Only the high velocity is symmetric; the rest of the line is asymmetric.

[c] Only the low velocity part is symmetric; the wings at high velocities are asymmetric.

[d] The high and low velocities are asymmetric; the line part between those is symmetric.

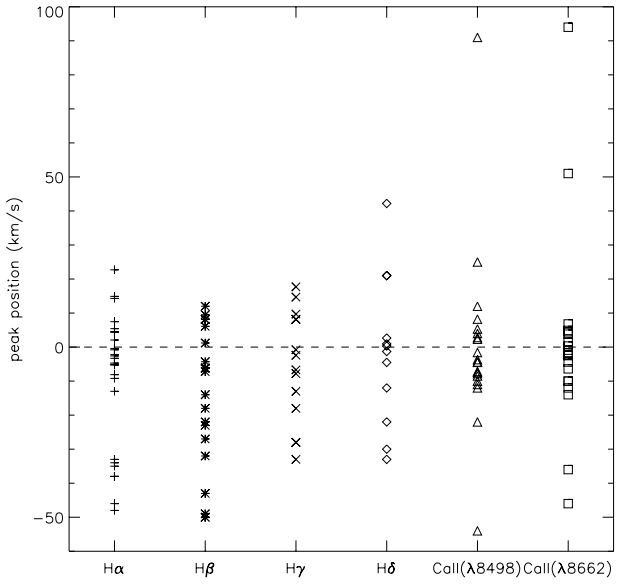

FIG. 9.—Broad emission component's peak position. Lines with P Cygni profiles and those not reliably measured are not included.

Among the lines that presented asymmetries, the ones identified as "ASb[c]" have symmetric low velocity material and a blueward excess of high-velocity emission, and those identified as "ASr" show redward asymmetries. Neither type is predicted by the magnetospheric model. Some lines do present profiles with the characteristics described by the magnetospheric models, corresponding to "ASb" and "ASb[b]" in Table 4. Examples of profiles in agreement and opposite to the magnetospheric symmetry predictions are shown in Figure 10 with the reflected wings overplotted.

Each Ca II IRT line is blended with a Paschen emission line, and this could lead to a wrong asymmetry classification. However, from the 13 stars that presented IRT asymmetries, only four could be due to the Paschen contribution, which affects the high-velocity wing redward of the line center. These stars are quoted as uncertain asymmetry measurements in Table 4.

the infalling material ($v \sim 200$–300 km s^{-1}) and the inclusion of rotation in the theoretical models will not significantly alter the profiles in this case. Even in the case of a stiff magnetosphere, material coming from a disk at $3R_\star$ would have $v \sim 30$ km s^{-1} and would not influence the entire line. The addition of winds to the theoretical models will certainly change the line shapes, but stars such as AS 209 and DE Tau, which do not always exhibit blueshifted absorption and are rather slow rotators, will still need some further explanation of their broad symmetric line profiles (Fig. 1).

Stark broadening may explain the low very broad far wings in Hα (Hartmann et al. 1994 and Muzerolle et al. 1998b), but it will not produce the main Gaussian shape commonly present in many different lines. A better treatment of the radiative transfer (actually done with the Sobolev method) could also alter the theoretical line profiles and would properly take into account Stark and opacity broadening effects.

Magnetospheric accretion probably does occur in CTTS. Evidence for it includes hot spots at the stellar surface of these stars, thought to be due to the magnetic accretion shock, redshifted absorption components at free-fall velocities that would be hard to explain without magnetospheric infall, as well as cases like SU Aur and WL 16 that give more explicit support to the theory. However, it may not be the only important mechanism. The symmetry of the line profiles and the lack of correlation of the variation among different line regions suggest an important turbulent process may be occurring together with the magnetospheric infall.

6. CONCLUSIONS

We have presented the spectral analysis of a sample of CTTSs covering a wide range of optical wavelengths and veilings. We tested the predictions of the magnetospheric accretion model and previously published results supporting them. We confirm that many CTTSs exhibit central or blueshifted broad emission lines but a substantial minority show redshifted centroids. The accretion and outflow seem to be related and redshifted absorption components are sometimes present in the spectra. We found that the analysis and interpretation of these is not straightforward. We could not reproduce the observational results that showed a very high frequency of redshifted absorption in the lines of CTTSs. We also show that most of our emission components are symmetric, instead of blueward asymmetric as predicted by the theory or suggested by previous observational studies. We saw that the broad components of different atomic lines are not strongly correlated to each other, while we would expect them to be if they were all formed in the accretion flow.

Our results do not refute the general magnetospheric accretion scenario, but rather indicate that it is only part of the important processes that produce the strong permitted line emission in CTTSs. Our intent is to point out that the case has not yet been strongly made, and that much more observational and theoretical work is required. Part of the emission-line profiles may also be produced in winds, and rotation and turbulence must be added to the models.

Synoptic observations are critical to understanding the full range of profiles produced by a single star, where some underlying parameters do not change but others do, and many structures are dynamic.

This research is based on data collected on the Shane 3 m telescope at Lick Observatory run by the University of California. We would like to thank Christopher Johns-Krull, Anthony Misch, Michael Bisset, Claude Bertout, Natalie Stout-Batalha, and Celso Batalha who helped gather the profiles presented here. S. H. P. A. acknowledges support from the Conselho Nacional de Desenvolvimento Científico e Tecnológico, Brazil.

REFERENCES

Appenzeller, I., Reitermann, A., & Stahl, O. 1988, PASP, 100, 815
Basri, G. 1990, Mem. Soc. Astron. Italiana, 61, 707
Basri, G., & Batalha, C. C. 1990, ApJ, 363, 654
Basri, G., & Bertout, C. 1989, ApJ, 341, 340
Basri, G., Johns-Krull, C. M., Mathieu, R. D. 1997, AJ, 114, 781
Batalha, C. C., Stout-Batalha, N. M., Basri, G., & Terra, M. A. O. 1996, ApJS, 103, 211
Beristain, G., Edwards, & S., Kwan, J. 1998, ApJ, 499, 828
Bertout, C., Basri, G., & Bouvier, J. 1988, ApJ, 330, 350
Calvet, N., Basri, G., Imhoff, C. L., & Giampapa, M. S. 1985, ApJ, 293, 575
Calvet, N., Basri, G., & Kuhi, L. V. 1984, ApJ, 277, 725
Choi, P. I., & Herbst, W. 1996, AJ, 111, 283
Edwards, S., Hartigan, P., Ghandour, L., Andrulis, C. 1994, AJ, 108, 1056
Edwards, S., et al. 1993, AJ, 106, 372
Gullbring, E., Petrov, P. P., Ilyin, I., Tuominen, I., Gahm, G. F., & Lodén, K. 1996, A&A, 314, 835
Hamann, F., & Persson, S. E. 1992, ApJS, 82, 247
Hartigan, P., Edwards, S., & Ghandour, L. 1995, ApJ, 452, 736
Hartmann, L. 1998, Accretion Processes in Star Formation (Cambridge: Cambridge Univ. Press)
Hartmann, L., Calvet, N., Avrett, E., & Loesler, R. 1990, ApJ, 349, 168
Hartmann, L., Calvet, N., Gullbring, E., & D'Alessio, P. 1998, ApJ, 495, 385
Hartmann, L., Edwards, S., & Avrett, E. 1982, ApJ, 261, 279
Hartmann, L., Hewett, R., & Calvet, N. 1994, ApJ, 426, 669
Herbig, G. H., & Bell, K. R. 1988, Lick Obs. Bull., 1111, 1
Herbst, W., Rhode, K., Hillenbrand, L. A. 1999, AAS Meeting, 194, 68.03
Johns, C. M., & Basri, G. 1995a, AJ, 109, 2800
———. 1995b, ApJ, 449, 341
Johns-Krull, C. M., & Basri, G. 1997, ApJ, 474, 433
Mundt, R., & Eislöffel, J. 1998, AJ, 116, 860
Muzerolle J., Calvet N., & Hartmann L. 1998b, ApJ, 492, 743
Muzerolle J., Hartmann L., & Calvet N. 1998a, AJ, 116, 455
Najita, J., Carr, J., & Tokunaga, A. T. 1996, ApJ, 456, 292
Natta, A., & Giovanardi, C. 1990, ApJ, 356, 646
Shu, F., Najita, J., Ostriker, E., Wilkin, F., Ruden, S., & Lizano, S. 1994, ApJ, 429, 781
Stassun, K. G., Mathieu, R. D., Mazeh, T., & Vrba, F. J. 1999, AJ, 117, 2941
Valenti, J. A. 1994, Ph.D. thesis, Univ. California, Berkeley
Vogt, S. S. 1987, PASP, 99, 1214

References

Alencar S.H.P., 1995, Dissertação de Mestrado, Depto. de Física, Universidade Federal de Minas Gerais, Brasil

Alencar S.H.P., Vaz L.P.R., Helt B.E., 1997, A&A, 326, 709

Alencar S.H.P., Vaz L.P.R., 1997, A&A, 326, 257

Alencar S.H.P., Vaz L.P.R., 1999, A&AS, 135, 555

Alencar S.H.P., Vaz L.P.R., Nordlund Å, 1999, A&A, 346, 556

Alencar, S.H.P., Basri, G. 2000, AJ, April

Allen C.W., 1976, Astrophys. Quantities, 3rd edition. Athlone, London

Andersen J., Clause J.V., Giménez A., Nordström B., 1983, A&A, 128, 17

Andersen J., 1991, A&A Rev., 3, 91

Anderson L., Shu F., 1977, ApJ, 214, 798

Appenzeller I., Reitermann A., Stahl O., 1988, PASP, 100, 815

Basri G., 1990, Mem. Soc. Astron. Ital., 61, 707

Basri G. & Batalha C.C., 1990, ApJ, 363, 654

Basri G., Johns-Krull C., Mathieu R.D., 1997, AJ, 114, 781

Basri G., 1998, "The Lithium Chronometer for Young Open Clusters" in *Cool Stars in Open Clusters and Associations: Magnetic Activity and Age Indicators*, Mem. S.A. It. (Pallavicini, ed.)

Batalha C.C., Stout-Batalha N.M., Basri G., Terra M.A.O., 1996, ApJS, 103, 211

Bertout C., Krautter J., Möllenhoff C., Wolf B., 1977, A&A, 61, 737

Bessel M., 1997, PASP, 95, 480

Bevington P.R., 1969, Data Reduction and Error Analysis for the Physical Sciences, 1st edition, McGraw-Hill, New York

Bouvier J., Cabrit S., Fernandez M., Martin E.L., Matthews J.M., 1993, A&AS, 101, 485

Bouvier J., Covino E., Kovo O., Martin E.L., Matthews J.M., Terranegra L., Beck S.C., 1995, A&A, 299, 89

Casey B.W., Mathieu R.D., Suntzeff N.B., Lee C.W., Cardelli J.A., 1993, AJ, 105, 2276

Casey B.W., Mathieu R.D., Suntzeff N.B., Walter F.M., 1995, AJ, 109, 2156

Casey B.W., Mathieu R.D., Vaz L.P.R., Andersen J., Suntzeff N.B., 1998, AJ, 117, 1617

Chavarria-K. C., 1979, A&A, 79, L18

Choi P.I. & Herbst W., 1996, AJ, 111, 283

Claret A., 1995, A&AS, 109, 441

Claret A., Giménez A., 1990, A&A, 230, 412

Claret A., Giménez A., 1992, A&A, 256, 572

Claret A., Díaz-Cordovés J., Giménez A., 1995, A&AS, 114, 247

Claret A., 1998, A&A, 131, 395

Crawford D.L., Barnes J.V., 1970, AJ, 75, 978

Díaz-Cordovés J., Giménez A., 1992, A&A,

Díaz-Cordovés J., Claret A., Giménez A., 1995, A&A,

Eddington A.S., 1926, MNRAS, 86, 320

Edwards S., Hartigan P., Ghandour L., Andrulis C., 1994, AJ, 108, 1056

Gray D., 1992, *The Observation and Analysis of Stellar Photospheres*, 2nd edition, Cambridge University Press, New York

Guenther E. & Hessman F.V., 1993, A&A, 268, 192

Gullbring E., Petrov P.P., Ilyin I., Tuominen I., Gahm G.F., Lodén K., 1996, A&A, 314, 835

Gustafsson B., Bell R.A., Eriksson K., Nordlund Å, 1975, A&A, 42, 407

Hamann F. & Persson S.E., 1992, ApJS, 82, 247

Hartigan P., Edwards S., Ghandour L., 1995, ApJ, 452, 736

Hartmann L., Edwards S., Avrett E., 1982, ApJ, 261, 279

Hartmann L., Calvet N., Avrett E., Loesler R., 1990, ApJ, 349, 168

Hartmann L., Hewett R., Calvet N., 1994, ApJ, 426, 669

Hartmann L., Calvet N., Gullbring E., D'Alessio P., 1998, ApJ, 495, 385

Hartmann L., 1998, *Accretion Processes in Star Formation*, Cambridge University Press

Hartmann L., 1999, "Disks Around YSOs and the FU Ori Phenomenon" in *Electronic Proceedings of the SOFIA - Star Formation Workshop* (http://www.astro.ucla.edu/meetings/SOFIA_Star_Formation99/proceedings.html)

Helt B., 1987, A&A, 172, 155

Herbig G.H., 1962, Advances in A&A, 1, 47

Hessman, F.V., Guenther, E.W. 1997, A&A, 321, 497

Hilditch R.W., 1981, MNRAS, 196, 305

Hilditch R.W., Harries T.J., Bell S.A., 1996, A&A, 314, 165

Hirth, Mundt, Solf, 1997, A&AS, 126, 437

Hofmann K.-H., Scholz M., Wood P.R., 1998, A&A, 339, 846

Horne, J.H., & Baliunas, S.L. 1986, ApJ, 302, 757

Johns C.M. & Basri G., 1995a, AJ, 109, 2800

Johns C.M. & Basri G., 1995b, ApJ, 449, 341

Johns-Krull C.M., Basri G., 1997, ApJ, 474, 433

Johns–Krull C.M. & Hatzes A.P., 1997, ApJ, 487, 896

Johns–Krull C.M., Hawley S.L., Basri G., Valenti J.A., 1997, ApJS, 112, 221

Johns-Krull C.M., Valenti J.A., Saar, A.H. 1999, "New Measurements of Magnetic Fields on T Tauri Stars" in *Electronic Proceedings of the SOFIA - Star Formation Workshop* (http://www.astro.ucla.edu/meetings/SOFIA_Star_Formation99/PosterList.htm)

Johns-Krull C.M., Valenti J., 1999, in *Stellar Clusters and Associations: Convection, Rotation and Dynamos*, eds. R Pallavicini, G. Micela, & S. Sciortino, in press

Joy A.H., 1945, ApJ, 102, 168

Kenyon S.J., Hartmann L., Hewett R., Carrasco L., Cruz-Gonzalez I., Recillas E., Salas L., Serrano A., Strom K.M., Strom S.E., Newton G., 1994, AJ, 107, 2153

Khalesseh B., Hill G., 1992, A&A, 257, 199

Kippenhahn R., Weigert A., Hoffmeister E., 1967, in *Computational Physics*, Academic Press, New York, Vol.7, p.129

Kitamura M., Nakamura Y., 1983, Ann. Tokyo Astron. Obs. 2nd Series, 19, 413

Kitamura M., Nakamura Y., 1987, Ann. Tokyo Astron. Obs. 2nd Series, 21, 387

Kitamura M., Nakamura Y., 1988a, Ap&SS, 145, 117

Kitamura M., Nakamura Y., 1988b, Ann. Tokyo Astron. Obs. 2nd Series, 22, 31

Klingesmith D.A., Sobieski S., 1970, AJ, 75, 175

Kurucz R.L., 1979, ApJS, 40, 1

Lada C.J., 1999, "The Formation of Low Mass Stars" in *The Origins of Stars and Planetary Systems*, Kluwer Academic Press, eds. C.J. Lada & N.D. Kylafis

Lubow S.H., Shu F., 1977, ApJ, 216, 517

Lucy L.B., 1967, ZAp, 65, 89

Lynden-Bell D., Pringle J.E., 1974, MNRAS, 168, 603

Manduca A., Bell R.A., Gustaffsson B., 1977, A&A, 61, 809

Maxted P.F.L., Hill G., Hilditch R.W., 1994, A&A, 285, 535

Maxted P.F.L., Hill G., Hilditch R.W., 1995, A&A, 301, 141

Mathieu R.D., 1994, ARA&A, 32, 465

McKee C.F., 1999, "The Dynamical Structure and Evolution of Giant Molecular Clouds" in *The Origins of Stars and Planetary Systems*, Kluwer Academic Press, eds. C.J. Lada & N.D. Kylafis

Mihalas D., 1978, Stellar Atmospheres, 2nd edition, W.H. Freeman and Co., San Francisco

Milne E.A., 1927, MNRAS, 87, 43

Mundt R., Eislöffel J., 1998, AJ, 116, 860

Muzerolle J., Hartmann L., Calvet N., 1998a, AJ, 116, 455

Muzerolle J., Calvet N., Hartmann L., 1998b, ApJ, 492, 743

Najita J., Carr J., Tokunaga A.T., 1996, ApJ, 456, 292

Nakamura Y., Kitamura M., 1992, Ap&SS, 191, 267

Natta A., Giovanardi C., 1990, ApJ, 356, 646

Nordlund Å, 1974, A&A, 32, 407

Nordlund Å, Vaz L.P.R., 1990, A&A, 228, 231

Palla F., 1999, "The Evolution of Pre-Main Sequence Stars" in *The Origins of Stars and Planetary Systems*, Kluwer Academic Press, eds. C.J. Lada & N.D. Kylafis

Pauls Th.A., Mozurkewich D., Armstrong J.T., Hummel C.A., Benson J.A., Hajian A.R., 1998, "Observations of stellar limb darkening with the Navy Prototype Optical Interferometer" in *Astronomical Interferometry*, Proc. SPIE, 3350, 467

Popper D.M., 1987, ApJ, 313, L81

Rafert J.B., Twigg L.W., 1980, MNRAS, 193, 79

Richter M., Basri G., Perlmutter S., Pennypacker C., 1992, PASP, 104, 1144

Ruciński S.M., 1989, Comments Astrophys. 14, 79

Sarna M.J., 1989, A&A, 224, 98

Scargle J.D., 1982, ApJ, 263, 835

Shu F., Lubow S.H., Anderson L., 1976, ApJ, 209, 536

Shu F., Najita J., Ostriker E., Wilkin F., Ruden S., Lizano S., 1994, ApJ, 429, 781

Shu F., 1999, "Low-Mass Star Formation: Theory" in *The Origins of Stars and Planetary Systems*, Kluwer Academic Press, eds. C.J. Lada & N.D. Kylafis

Smith, Lewis, Bonnel, Bunclark, Emerson, 1999, MNRAS, 304, 367

Stassun K.G., Mathieu R.D., Mazeh T., Vrba F.J., 1999, AJ, 117, 2941

Stout-Batalha, N.M., Batalha, C.C., Basri, G. 2000, ApJ(in press)

Ultchin, Regev, Bertout, 1997, ApJ, 486, 397

Valenti J.A., Basri G., Johns C.M., 1993, AJ, 106, 2024

Valenti J.A., 1994, Ph.D. Thesis, Univ. of California, Berkeley

Vogt S.S., 1987, PASP, 99, 1214

Van Hamme W., 1993, AJ, 106, 2096

Van't Veer F., 1960, Rech. Astr. Obs. Utrecht 14, No. 3

Vaz L.P.R., 1985, Ap&SS, 113, 349

Vaz L.P.R., Nordlund Å, 1985, A&A, 147, 281

Vaz L.P.R., Andersen J., Rabello Soares M.C.A., 1995, A&A, 301, 693

Vaz L.P.R., Andersen J., Garcia J.M., Giménez A., Helt B.E., Clausen J.V., Alencar S.H.P., 1997, A&AS, 125, 471

Vaz L.P.R., Andersen J., Casey B.W., Clausen J.V., Mathieu R.D., Heyer I., 1998, A&AS, 130, 1

von Zeipel H., 1924, MNRAS, 84, 665

Wade R.A., Ruciński S.M., 1985, A&AS, 60, 471

Wilson R.E., Devinney E.J., 1971, ApJ, 166, 605

Wilson R.E., 1979, ApJ, 234, 1054

Wilson R.E., 1993, in *New Frontiers in Binary Star Research*, eds. K.C. Leung e I.-S. Nha, ASP Conf. Series 38, 91